Optical and Magneto-Optical Investigations on 3D Dirac- and Weyl-Semimetals

Von der Fakultät Mathematik und Physik
der Universität Stuttgart zur Erlangung der Würde eines Doktors
der Naturwissenschaften (Dr. rer. nat.) genehmigte Abhandlung

vorgelegt von
David Johannes Neubauer
aus Filderstadt

Hauptberichter: Prof. Dr. Martin Dressel
Mitberichter: Jun. Prof. Dr. Andreas W. Rost

Tag der mündlichen Prüfung: 02.06.2017
Prüfungsvorsitzende: Prof. Dr. Maria Daghofer

1. Physikalisches Institut der Universität Stuttgart
2017

You can't expect to reach the top without a little climbing

Roni Size/Reprazent - Dirty Beats - Talkin' Loud (2000)

To Lilli

Zusammenfassung

Eine neuartige Materialklasse beschäftigt seit kurzem die Gemüter der Wissenschaftler im Bereich der kondensierten Materie. Diese Materialklasse umfasst neben Graphen auch topologische Isolatoren, d-Wellen Supraleiter, supraflüssiges ^{3}He und erst kürzlich entdeckte Familien dreidimensionaler Halbmetalle [1, 2]. Auf den ersten Blick haben diese eben erwähnten Materialien wenig gemein. Sie teilen jedoch das fundamentale Merkmal, dass ihr niedrig energetisches fermionisches Quasiteilchenspektrum an bestimmten Punkten im reziproken Raum keine Energielücke besitzt und in der Umgebung dieser Punkte mit dem Diracschen Hamilton-Operator beschrieben werden kann, was sich markant von der sonst üblichen Schrödinger Beschreibung von Fermionen in Festkörpern abhebt. Trotz all ihrer Unterschiede können diese Materialien aufgrund der eben erwähnten Gemeinsamkeit unter dem Begriff 'Dirac Materialien' zusammengefasst werden.
Interessant aus fundamentaler Sicht, so wie auch im Hinblick auf mögliche Anwendungen der Dirac Materialien, ist die topologisch nicht triviale elektronsiche Struktur, die vielen dieser Materialien inhärent ist, was ebendiese *a fortiori* in den Vordergrund der heutigen Festkörperforschung rückt [3, 4].
Für die vorliegende Arbeit sind insbesondere Materialien von Interesse, welche Berührungspunkte von Valenz- und Leitungsband in ihrer Volumenbandstruktur (konträr: Oberflächenbandstruktur) aufweisen. In der unmittelbaren Umgebung dieser Berührungspunkte verlaufen die Bänder linear, weshalb die niederenergetischen Anregungen als masselose, relativistische Quasiteilchen angesehen werden können. Es gibt zwei Materialfamilien, die diese Voraussetzungen erfüllen. Zum einen, die Familie der Weyl Halbmetalle, welche sich durch die Existenz mindestens zweier Bandberührungspunkte in der Brillouin Zone, welche als Weyl Punkte tituliert werden, auszeichnet. Die elektronische Struktur in der Umgebung dieser Weyl Punkte wird durch den 2×2 Weyl Hamilton-Operator beschrieben. Die Weyl Punkte selbst, sowie die linearen Bänder die von ihnen ausgehen, sind chiral, was hier bedeuted, dass der (Pseudo-) Spin an die Richtung des Impulses gekoppelt ist. Diese Art der Weyl

Bandkreuzungspunkte erfordern, dass entweder die Zeitumkehr- oder Punktspiegelsymmetrie gebrochen sind.
In der zweiten Familie, den Dirac Halbmetallen, fallen zwei Weyl Punkte gegensätzlicher Chiralität auf einen einzigen Punkt im reziproken Raum bei der selben Energie. Damit sind die Bänder um diesen, als Dirac Punkt bezeichneten, Kreuzungspunkt entartet und werden nunmehr durch einen 4×4 Dirac Hamilton-Operator beschrieben. Eine solche Situation bedarf einer erhaltenen Zeitumkehr und Punktspiegelsymmetrie, sowie einer zusätzlichen Symmetrie welche das öffnen einer Bandlücke am Dirac Punkt verhindert.

Zur Untersuchung von Dirac und Weyl Halbmetallen werden weitläufig Techniken wie winkelaufgelöste Photoelektronenspektroskopie oder Quantenoszillationen angewandt, da sie Einblick in die Bandstruktur gewähren. Die winkelaufgelöste Photoelektronenspektroskopie ist jedoch „blind“ bei Energien oberhalb der Fermienergie und erlaubt nur eine grobe Auflösung. Quantenoszillationen hingegen, erlauben lediglich einen Einblick bei Energien an der Fermikante.
Um ein vollständigeres Bild über Dirac und Weyl Halbmetalle zu erlangen, wird deshalb in dieser Arbeit Infrarotspektroskopie, eine zu den letzteren beiden komplementäre Technik, eingesetzt. Diese Technik ermöglicht einen Einblick in die elektronische Struktur auch oberhalb der Fermienergie und ist ein mächtiges Instrument, welches, kombiniert mit theoretischen Modellen, erlaubt, die effektive Bandstruktur in der Umgebung der Dirac oder Weyl Punkte zu ermitteln, wie in dieser Arbeit dargelegt wird. Mit der Installation eines neuartigen experimentellen Aufbaus für optische Messungen in hohen Magnetfeldern und bei tiefen Temperaturen ebnet diese Arbeit darüber hinaus den Weg zur Beobachtung von außergewöhnlichen Quantenphänomenen, wie der chiralen Anomalie in Weyl Halbmetallen, oder anderen ungewöhnlichen Magnetfeld induzierten Effekten auch abseits der Dirac Materialien.

Im Rahmen dieser Arbeit werden vier verschiedene Materialien untersucht, wovon zwei der Familie der Weyl Halbmetalle angehören und die anderen beiden Diracsche Bandkreuzungspunkte aufweisen.
Die erstern beiden, NbP und TaAs, gehören zu einer kürzlich entdeckten Familie von Monopniktiden mit gebrochener Punktspiegelsymmetrie, welche die zur Zeit einzige Realisierung von Weyl Fermionen beherbergt [5, 6]. Dies ist insbesondere faszinierend, da Weyl Fermionen auch in der Hochenergiephysik bis heute noch nicht als Teilchen entdeckt wurden. Mit der Realisierung als Quasiteilchen in der

o.g. Materialfamilie bietet sich somit die einzigartige Möglichkeit die Eigenschaften von Weyl Fermionen in vergleichsweise einfachen experimentellen Aufbauten zu untersuchen.

TaAs und NbP besitzen die gleiche Kristallstruktur mit einer tetragonalen Einheitszelle und fehlendem Spiegelzentrum. Die Brillouin Zone beinhaltet zwei, im Hinblick auf die Symmetrie ungleichwertige, Spezies von Weyl Punkten W1 und W2. Beide Verbindungen werden in dieser Arbeit mit Hilfe von Transport, Optik, Magneto-Optik und im Fall von NbP aud mit Magneto-Transport untersucht. Die Modellierung der ohne Magnetfeld aufgenommenen optischen Spektren mit einem Vier-Band-Modell erlaubt es, die effektive Bandstruktur um die Weyl Punkte zu extrahieren, wie exemplarisch für NbP in Fig. 0.0.1 dargestellt. Die sorgfältige Analyse erlaubt es die einzelnen Übergänge, welche in Fig. 0.0.1 mit ω_i $(i = 1 - 5)$ bezeichnet sind, einzelnen Signaturen in den Spektren zuzuweisen.

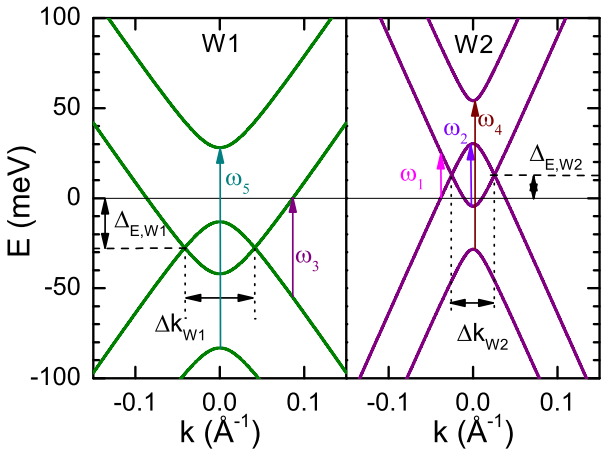

Abbildung 0.0.1: Die effektive Dis-persionsbeziehung $\epsilon_{eff,W1}$ and $\epsilon_{eff,W2}$ um die W1 und W2 Weyl Punkte in NbP. Die Übergänge zwischen den Bändern, welche für feine Details in den Spektren verantwortlich sind, sind mit Pfeilen markiert und mit ω_i $(i = 1 - 5)$ bezeichnet.

In den Spektren, aufgenommen in hohen Magnetfeldern, finden sich klare Anzeichen von Landau Level Übergängen die sich mit $\sqrt{B}$ entwickeln, was die Linearität der Bänder in NbP und TaAs beweist. Die erreichte Übereinstimmung aller Werte für die Fermigeschwindigkeit und das chemische Potential, welche aus Daten verschiedener experimenteller Techniken (Optik, Magneto-Optik und Magneto-Transport) extrahiert wurden, ist bemerkenswert und belegt die exzellente Konsistenz der Auswertung.

In TaAs wird ein ungewöhnliches vierfaches Aufspalten des niedrigsten Landau Level Übergangs bei sehr hohen Magnetfeldern oberhalb von 20 T beobachtet. Dieses hochinteressante Verhalten ist äusserst ungewöhnlich, da in einem Weyl Halbmetal die Spin-Entartung der Energienieveaus für einen gegeben k-Punkt bereits aufgehoben ist und damit das Aufspalten der magnetischen Unterniveaus augenscheinlich

nicht mit dem Zeeman Effekt erklärbar ist. Das dennoch beobachte Aufspalten der Übergänge in TaAs deutet auf eine schwach definierte Chiralität hin. Weitere Untersuchungen dieses Sachverhalts sind von Nöten, um dessen Ursprung im Detail zu klären.

Das erste der beiden hier untersuchten Dirac Halbmetalle ist Cd_3As_2, ein Material, das schon viele Jahrzehnte als Halbleiter mit kleiner Bandlücke gehandelt wurde. Erst kürzlich erlangte Cd_3As_2 neue Aufmerksamkeit, da sich eine 3D Dirac Bandstruktur, in dem die Bänder linear entlang aller drei Richtungen des reziproken Raums verlaufen, in diesem Material erhärtete [7, 8].

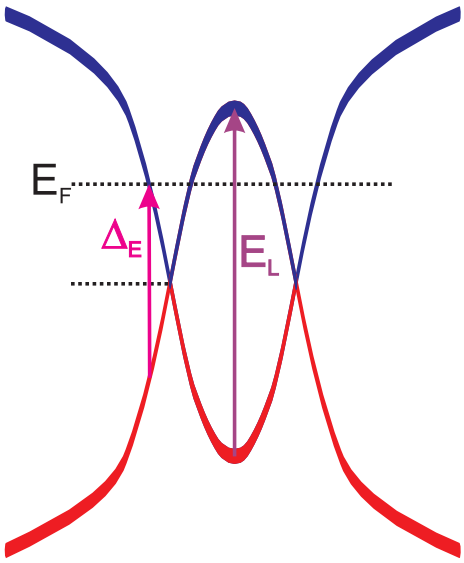

Abbildung 0.0.2: Schematische Bandstruktur der Dirac Bänder in Cd_3As_2. Die Bänder verjüngen sich zu den Dirac Punkten hin und erfahren einen Knick im Bereich der Lifshitz Energie E_L. Die Dirac Interbandüberänge sind mit einem pinken Pfeil markiert, wohingegen die Übergänge zwischen den Lifshitzpunkten mit einem lila Pfeil gekennzeichnet sind.

Die Untersuchung dieses Materials in dieser Arbeit deckt neue Details der Bandstruktur auf. Die zentrale Erkenntnis ist, dass die Bänder nicht linear, sondern tatsächlich sub-linear verlaufen, d.h. $\epsilon(k) = k^{0.6}$, wie schematisch in Fig. 0.0.2 dargestellt. Die Übergänge zwischen den zwei Lifshitz Punkten, in bisherigen Experimenten unentdeckt, hinterlassen eine klare Signatur in den optischen Spektren.

Das zweite der Dirac Halbmetalle, FeSe, gehört zur Familie der eisenbasierten Supraleiter. Erst kürzlich wurden in diesem Material Dirac ähnliche Bänder bei tiefen Temperaturen entdeckt [9, 10]. FeSe erfährt einen strukturellen Übergang beim Abkühlen unter $T_s = 86\,\mathrm{K}$, welcher die Symmetrie von tetragonal zu orthorhombisch reduziert und mit einer deutlichen Änderung der Bandstruktur einhergeht, was sich in den optischen Spektren niederschlägt. Die Dirac Physik in diesem Material stellte sich *a posteriori* als zwei dimensional, ähnlich wie in Graphen oder Graphit [11,

12], heraus. Der deutlichste Hinweis, dass 2D Dirac Bänder vorliegen, findet sich in der Schichtleitfähigkeit, welche über einen ausgedehnten Frequenzbereich konstant ist und im Rahmen des Genauigkeit der Quantenleitfähigkeit $G_0 = \frac{e^2}{4\hbar}$ entspricht, wie in Fig. 0.0.3 dargestellt. Die Existenz der Dirac Bänder, welche kleine Ladungsträgertaschen bilden, wird durch Hinweise für die Formierung einer hoch mobilen Ladungsträgerspezies in den Spektren unterhalb von T_s gestützt. Sowohl das chemische Potential, als auch die Fermigeschwindigkeit der Dirac Bänder kann aus den Daten extrahiert werden.

Abbildung 0.0.3: Die Schichtleitfähigkeit von FeSe ist quasi konstant über einen ausgedehnten Frequenzbereich und entspricht im Rahmen des Fehlers der Quantenleitfähigkeit $G_0 = \frac{e^2}{4\hbar} = 6.08 \times 10^{-5}\,\Omega^{-1}$. Dies entspricht der Erwartung für die Schichtleitfähigkeit durch Interbandübergänge zwischen zweidimensionalen Dirac Bändern. Der Fehlerbalken steht für den absoluten systematischen Fehler in den durchgeführten optischen Experimenten.

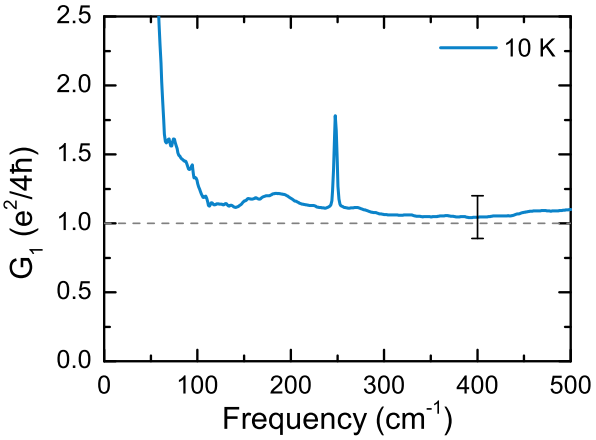

Die supraleitenden Eigenschaften von FeSe werden mit Hilfe eines Modells analysiert, das im Bereich der eisenbasierten Supraleiter häufig zum Einsatz kommt und von zwei Energielücken ausgeht. Die Verhältnisse der extrahierten supraleitenden Energielücken zur Energieskala, die der Sprungtemperatur entspricht, deuten darauf hin, dass eine Energielücke in FeSe anisotrop ist, während die andere keinerlei Anzeichen dafür zeigt.

Abstract

Recently a novel class of materials is getting vivid attention of the condensed matter community. This class of materials is comprising, next to graphene, also topological insulators, d-wave superconductors, superfluid ^{3}He and two very recently discovered families of three dimensional semimetals [1, 2]. At first sight the commonalities of the aforementioned materials are minor. However, they share the essential similarity, that their low energy fermionic quasiparticle spectrum is gapless and can be described by the Dirac Hamiltonian, instead of behaving like Schrödinger fermionic spectrum. Even though all materials are vastly different, by this commonality this collection of matter is dubbed 'Dirac materials'.

Many of the Dirac materials host a topological non-trivial electronic structure, which is interesting from a fundamental point of view and promising for applications, pushing them even more to the fore of condensed matter research [3, 4].

Of particular interest in this work are materials, that posses touching points of valence and conduction bands in their bulk band structure. In the vicinity of these touching points the bands disperse linear, and hence, the low energy excitations can be viewed as relativistic, massless quasiparticles. There are two families that fulfill this prerequisite. The family of Weyl semimetals is characterized by the existence of at least two band touching points, dubbed Weyl nodes (or points), in the Brillouin zone. The electronic structure around these Weyl points is described by the 2×2 Weyl Hamiltonian. The Weyl nodes and the bands dispersing linearly from this node are chiral, where chirality refers to the locking of the (pseudo) spin to the momentum. The Weyl type band crossings require either time reversal or inversion symmetry to be broken.

In the second family of Dirac semimetals two Weyl points happen to merge at a single point in reciprocal space and at the same energy. Then the bands around the crossing points, dubbed Dirac nodes, are degenerate and described by the 4×4 Dirac Hamiltonian. This situation requires preserved time reversal and inversion symmetry, as well as an additional symmetry that prevents a gapping of the Dirac point.

In the field of Dirac and Weyl semimetals, techniques that are sensitive to the bandstructure, like angle resolved photoemission spectroscopy or quantum oscillations are widely applied, to learn about their electronic structure. Angle resolved photoemission spectroscopy is, however, "blind" above the Fermi energy and only provides a poor resolution. Quantum oscillations only allow to obtain information at the Fermi energy. Experimental results of these two techniques are frequently reported and plenty of information is available.
To get a more complete picture and add valuable information to the full picture of Weyl and Dirac semimetals, in this work, infrared spectroscopy, a complementary technique to the latter two, is applied. This technique allows to probe the electronic structure also across the Fermi energy and, combined with theorethical models, it is extremely powerful in determining effective band structures around the Dirac or Weyl nodes, as will be demonstrated in this thesis. With the implementation of a novel installation in the lab for optical measurements at low temperatures and high magnetic fields, this work paves the way towards the observation of anomalous quantum phenomena, as the chiral anomaly in Weyl semimetals, and further magnetic field induced peculiarities, not only in the area of Dirac materials.

Four different materials are investigated in the framework of this thesis, two out of the family of Weyl semimetals, and two where the band structure exhibits Dirac type crossings.
The former two, NbP and TaAs belong to a recently discovered family of noncentrosymmetric mono pnictides, which host the only confirmed realizations of a Weyl fermions, yet [5, 6]. This is in particular fascinating, considering, that Weyl fermions are lacking any realization as a particle in high energy physics to date. Hence, the realization as quasiparticle in this material class offers the opportunity to investigate Weyl fermions in comparably simple table top experiments.
NbP and TaAs share the same crystallographic structure with a tetragonal unit cell which lacks an inversion center. The Brillouin zone hosts two symmetry inequivalent species of Weyl nodes W1 and W2. Both compounds are investigated by the means of transport, optics and magneto-optics, while NbP is also probed with magneto-transport techniques. The modeling of the zero field optical spectra with a four-band model yields the quantitative effective bandstructure around the Weyl nodes, exemplary depicted in Fig. 0.0.4 for NbP. The careful analysis allows the assignment of the transitions labeled ω_i $(i = 1 - 5)$ to features in the optical spectra.

The observation of inter Landau level transitions depending on $\sqrt{B}$ in the magneto

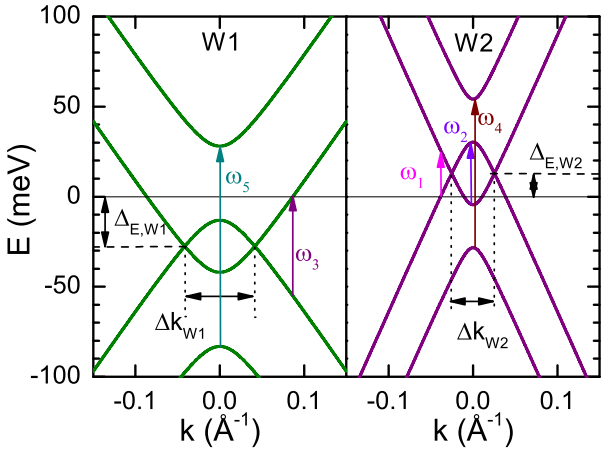

Figure 0.0.4: The effective dispersions $\epsilon_{eff,W1}$ and $\epsilon_{eff,W2}$ around the W1 and W2 Weyl nodes in NbP. The transitions between the bands responsible for subtle details in the spectra are marked with arrows and labeled ω_i $(i = 1 - 5)$.

optical experiments prove the linear dispersion in TaAs and NbP. The agreement of all values for the Fermi velocities, as well as for the chemical potentials, deduced from various techniques (optics, magneto-optics, magneto-transport) is remarkable and demonstrates excellent self-consistency.

In TaAs an anomalous fourfold splitting of the lowest Landau level transition is observed in very high magnetic fields above 20 T. The spin degeneracy of the energy levels at a given k-point in a Weyl semimetal is already lifted. Therefore a Zeeman term can not generate an additional gap at a given k-point. Therefore, the observed behavior in TaAs is possibly arising due to a poorly defined chirality. Further investigations are required to elucidate this issue.

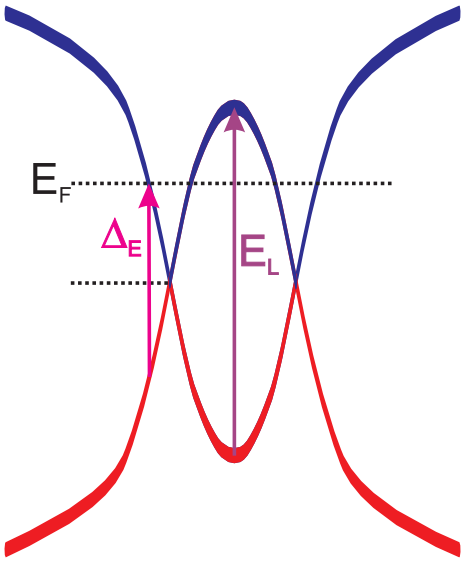

Figure 0.0.5: Schematic bandstructure of the Dirac bands in Cd_3As_2. The bands narrow towards the Dirac nodes and exhibit a kink at an energy around E_L. The onset of the Dirac interband transitions is marked with a pink arrow, while the transitions at the Lifshitz transition points are depicted in purple.

The first of the Dirac semimetals under investigation is Cd_3As_2 which is known for decades as a narrow gap semiconductor, and was recently confirmed to be a 3D Dirac

semimetal, with bands dispersing linearly along all three directions in reciprocal space [7, 8]. The investigation of this material in this work unearths novel details on the bandstructure. The key finding is, that the bands disperse sub-linear, i.e. $\epsilon(k) = k^{0.6}$, schematically depicted in Fig. 0.0.5. The transitions between the two Lifshitz points, undiscovered in previous experiments, are detected with the optical methods applied in this work.

The second of the Dirac semimetals, FeSe, belongs to the family of iron based superconductors, and was only recently found to host Dirac like bands at low temperatures [9, 10]. FeSe exhibits a structural transition from tetragonal to orthorhombic at $T_s = 86\,\mathrm{K}$, accompanied by considerable bandstructure reconstruction, which is directly reflected in the spectra. The Dirac physics in this material below T_s is found *a posteriori* to be rather two dimensional, similar to the well known graphene or graphite [11, 12]. The most striking evidence for the 2D Dirac bands is found in form of a quasi constant sheet conductance of the order of the conductance quantum $G_0 = \frac{e^2}{4\hbar}$ in FeSe over a wide frequency range, as depicted in Fig. 0.0.6. The formation of Dirac bands, forming small pockets below T_s is further supported by the emergence of a high mobility carrier species found in the analysis of the low temperature spectra. The chemical potential, as well as the Fermi velocity of the Dirac bands is extracted from the data.

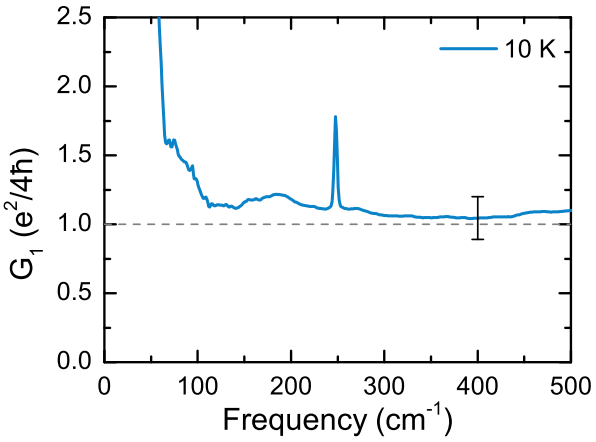

Figure 0.0.6: The sheet conductance of FeSe is quasi constant over an extended frequency range and of the order of $G_0 = \frac{e^2}{4\hbar} = 6.08 \times 10^{-5}\,\Omega^{-1}$. *This arises from the Dirac interband transitions and proves the two dimensional nature of the Dirac bands in FeSe. The errorbar indicates the systematic absolute error in the optical experiments.*

The superconducting properties of FeSe are also analyzed in the framework of a two gap model, which is widely applied to the iron based superconductors. The BCS gap ratios indicate, that on gap is anisotropic and the other is not.

Publications

Some of the results presented in this thesis have already been published

- **D. Neubauer**, J. P. Carbotte, A. A. Nateprov, A. Löhle, M. Dressel, and A. V. Pronin,
  "Interband optical conductivity of the [001]-oriented Dirac semimetal Cd_3As_2"
  In: *Phys. Rev. B*, vol. 93, no. 12, p. 121202, (2016).

Additional scientific publications which are not presented here

- **D. Neubauer**, A. V. Pronin, S. Zapf, J. Merz, H. S. Jeevan, W. H. Jiao, P. Gegenwart, G. H. Cao, and M. Dressel,
  "Optical properties of superconducting $EuFe_2(As_{1-x}P_x)_2$"
  In: *Phys. status solidi (b)*, vol. 254, no. 1, p. 1600148, (2017).

- S. Zapf, **D. Neubauer**, K. W. Post, A. Kadau, J. Merz, C. Clauss, A. Löhle, H. S. Jeevan, P. Gegenwart, D. N. Basov, and M. Dressel,
  "Electronic scattering effects in europium-based iron pnictides"
  In: *Comptes Rendus Phys.*, vol. 17, no. 1-2, pp. 188-196, (2016).

- S. Zapf, C. Stingl, K. W. Post, J. Maiwald, N. Bach, I. Pietsch, **D. Neubauer**, A. Löhle, C. Clauss, S. Jiang, H. S. Jeevan, D. N. Basov, P. Gegenwart, and M. Dressel,
  "Persistent Detwinning of Iron-Pnictide $EuFe_2As_2$ Crystals by Small External Magnetic Fields"
  In: *Phys. Rev. Lett.*, vol. 113, no. 22, p. 227001, (2014).

- A. Baumgartner, **D. Neubauer**, S. Zapf, A. V. Pronin, W. H. Jiao, G. H. Cao and M. Dressel,
  "Reentrant phases in electron-doped $EuFe_2As_2$: spin glass and superconductivity"
  In: *arXiv preprint*, arXiv:1702.04104,2 (2017)

- M. B. Schilling, A. Löhle, **D. Neubauer**, C. Shekhar, C. Felser, M. Dressel and A. V. Pronin,
  "Two-channel conduction in YbPtBi"
  In: *Phys. Rev. B*, vol. 95, no. 15, p. 155201, (2017)

- K. Sedlmeier, S. Elsässer, **D. Neubauer**, R. Beyer, D. Wu, T. Ivek, S. Tomić, J. A. Schlueter and M. Dressel,
  "Absence of charge order in the dimerized κ-phase BEDT-TTF salts"
  In: *Phys. Rev. B*, vol. 86, no. 24, p. 245103, (2012).

Contents

Zusammenfassung **v**

Abstract **xi**

1 Introduction **1**
1.1 Dirac Materials 1
1.2 3D Dirac and Weyl semimetals 2
1.3 Motivation and Outline 5

2 Theoretical background:Basic models for optical response functions 7
2.1 Light matter interaction 8
2.2 Kramers-Kronig relations 11
2.2.1 Sum rules 11
2.3 Drude model 12
2.4 Lorentz model 13
2.5 The impact of the bandstructure 15
2.5.1 Martix elements 15
2.5.2 Critical points 18
2.6 Models for the optical response of3D Dirac and Weyl semimetals . . . 19
2.6.1 Model for a single cone 19
2.6.2 Four-band model 24
2.7 Influence of magnetic field 26
2.7.1 Magneto plasma effects 27
2.7.2 Interband effects 28
2.8 Optical models for superconductors 31

3 Experimental Techniques **39**
3.1 Fourier transform infrared spectroscopy 40
3.2 Far-infrared technique 43

3.2.1 The spectrometer . . . 43
3.2.2 The cryostat . . . 45
3.2.3 The measurement . . . 46
3.3 Setup for mid-infrared,near-infrared and visible . . . 48
3.3.1 The spectrometer . . . 48
3.3.2 The cryostat . . . 49
3.3.3 The measurement . . . 49
3.4 Magneto-optical setup . . . 50
3.4.1 The magnet . . . 51
3.4.2 The optics . . . 54
3.4.3 The cold finger . . . 56
3.4.4 Setup operation and characterization . . . 58
3.5 Further techniques applied . . . 67
3.6 Data treatment and errors . . . 67

4 The Dirac semimetal Cd_3As_2 69
4.1 The material . . . 69
4.2 Cd_3As_2: Results and Discussion . . . 70
4.2.1 Transport properties . . . 70
4.2.2 Optical experiments . . . 72
4.3 Conclusions . . . 84

5 The Weyl semimetal NbP 87
5.1 The material . . . 87
5.2 NbP: Results and Discussion . . . 92
5.2.1 Transport properties . . . 92
5.2.2 Optical experiments . . . 102
5.2.3 Results: Magneto-Optics . . . 112
5.3 Conclusions . . . 123

6 The Weyl semimetal TaAs 125
6.1 The material . . . 125
6.2 TaAs: Results and Discussion . . . 127
6.2.1 Transport properties . . . 127
6.2.2 Optical experiments . . . 128
6.2.3 Results: Magneto-Optics . . . 135
6.3 Conclusions . . . 143

7 The iron based superconductor FeSe **145**
7.1 The material 145
7.2 FeSe: Results and Discussion 148
7.2.1 Transport properties 148
7.2.2 Optical experiments 150
7.3 Conclusions 165

8 Summary and Outlook **169**

A Interband optical conductivity in the four-band model **172**

Appendices **172**

B Magneto optical conductivity for a single isolated Weyl cone **174**

C Influence of the extrapolation in Cd_3As_2 **175**

D Magneto-optical setup - details **177**

E Acknowledgments **183**

Bibliography **205**

Declaration of originality **206**

1. Introduction

This chapter provides an introduction to the basic electronic structure of Dirac materials. Specifically a look is taken on three dimensional systems with a gapless energy spectrum, and the classification of these systems into Dirac and Weyl semimetals will be examined.

1.1 Dirac Materials

Analogies between high-energy particle physics and low-energy condensed matter physics are generally very fruitful for both fields [13]. With the discovery of massless fermions in graphene [11], that can be described by the Dirac equation, a new chapter in modern physics was opened where exactly such close resemblance led to fast breakthroughs towards a deep understanding [14].
This equation was published in 1928 by Paul Dirac on his search why there is the necessity to artificially introduce a 'spin' to the quantum mechanical description of the electron in order to explain experimental observations [15]. Ingeniously he introduced Einstein's theory of relativity to the quantum mechanics, which not only yielded the spin but also led to the prediction of antimatter.
The discovery of graphene was only the starting point towards a whole new family of materials, classified by the fermionic low-energy excitations that behave like Dirac particles. This fastly growing family of so-called Dirac materials comprises next to the archetypical graphene also topological insulators, d-wave superconductors, superfluid phases of ^{3}He and the only recently discovered three dimensional Dirac and Weyl semimetals [1, 2].
In condensed matter systems, as for instance simple metals (such as Cu) and doped semiconductors, usually the concept of nearly free quasiparticles that obey the Schrödinger equation holds. The Schrödinger Hamiltonian $\mathbf{H}_S = \mathbf{p}^2/2m^*$, with the momentum operator $\mathbf{p}$ and the effective quasiparticle mass m^*, leads to an energy spectrum that depends on the square of the momentum $p^2 = (\hbar k)^2$ (see Fig. 1.1.1).

Each band is described by a different Schrödinger Hamiltonian.

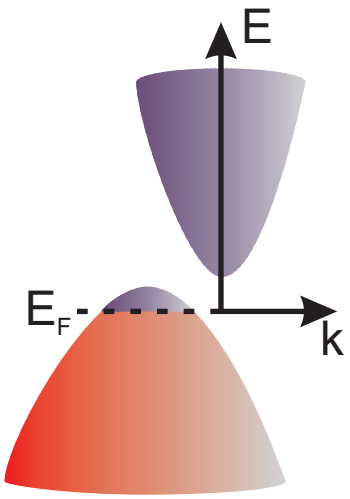

Figure 1.1.1: Schematic representation of Schrödinger type parabolic bands. Each band (conduction, blue; valence=red) is described by a Schrödinger Hamiltonian with a different effective mass parameter m^*.

In contrast to that, for the quasiparticles of Dirac materials the energy and momentum are directly proportional. This situation can be realized in a solid where a conduction band crosses a valence band, and hence in the vicinity of the crossing point the dispersion relation can be viewed as linear (see Fig. 1.2.1). Band crossings have been viewed to be very unusual to occur, even though the possibility was pointed out as early as 1937 [16], but are ubiquitously reported in materials of current interest.
Many of the Dirac materials host a nontrivial topological electronic structure [17, 18], and are discussed to open new perspectives for applications as, for instance, spintronics and quantum computing (see Refs. [1–4, 19, 20] for reviews).

1.2 3D Dirac and Weyl semimetals

For graphene, or similar two dimensional Dirac materials, the low energy effective (Dirac) Hamiltonian has the form (following Ref. [1])

$$\mathbf{H}_D = \hbar v_{\mathrm{F}} \boldsymbol{\sigma} \cdot \mathbf{k} + m^* v_{\mathrm{F}}^2 \sigma_z, \tag{1.2.1}$$

with the Pauli matrices $\boldsymbol{\sigma} = (\sigma_x, \sigma_y)$, σ_z and the Fermi velocity v_{F} (which replaces the speed of light). The bands touch at a single point when the mass vanishes, since a gap Δ in the spectrum and the effective mass m^* of the quasiparticles are equivalent, i.e. $\Delta = 2mv_{\mathrm{F}}^2$. Hence, it is clear, that because of the second term in Eq. 1.2.1 the

Dirac points[1] are not robust and can be gapped.
In a three dimensional analogue of the above Hamiltonian (Eq. 1.2.1), the second term is absent

$$\mathbf{H}_W = \hbar v_\mathrm{F} \boldsymbol{\sigma} \cdot \mathbf{k}, \tag{1.2.2}$$

because all three Pauli matrices are occupied in the first term [1, 21]. This Hamiltonian is the 2×2 Weyl Hamiltonian and has a gapless linear energy spectrum. The massless quaiparticles described by the Hamiltonian in Eq. 1.2.2 are chiral, where the chirality $\chi = \pm$ is set by the sign of the velocity $\mathbf{v} = \pm v_\mathrm{F} \boldsymbol{\sigma}$ [1, 22].

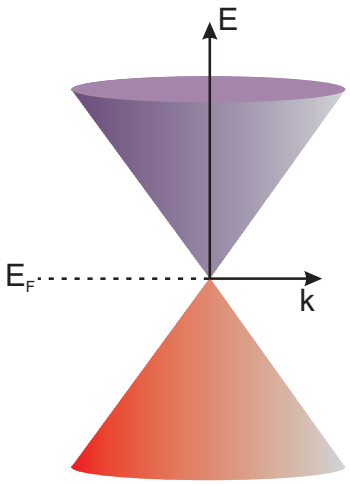

Figure 1.2.1: Schematic representation of a Dirac or Weyl cone. Conduction (blue) and valence (red) bands are both described by one Dirac Hamiltonian. The bands touch at a single Dirac or Weyl point.

The crossing points always appear in pairs of opposite chirality at two points $\mathbf{k}_\pm$, and require either a broken time reversal or inversion symmetry to exist. Then, these Weyl points are topologically protected and can not be gapped [1, 3]. The only way for a Weyl point to disappear is, to annihilate with a Weyl point of opposite chirality, which requires, that these two points are shifted to the same point in momentum space [1, 18]. A material is a Weyl semimetal, when it hosts at least two band crossing points in the vicinity of the Fermi energy, and when the low energy excitations around these crossing points are described by the Weyl Hamiltonian (Eq. 1.2.2).
When an electron travels a closed loop in momentum space in a Weyl semimetal, its wave function receives a geometrical (or Berry) phase, because the Weyl nodes are sources or sinks of the Berry curvature and can be viewed as magnetic monopole-like objects [3, 20, 23]. The edges of a Weyl semimetal in real space host exotic edge

[1]The crossing (or touching) points of the bands will be referred to as Dirac/Weyl points or nodes. The linear dispersing bands, due to their conic shape, will be referred to as Dirac or Weyl cones (just like in graphene).

states, the Fermi arcs. They are open Fermi surface curves which connect the projections of the bulk Weyl points of opposite chirality to the surface Brillouin zone. Another outstanding consequence of the 3D Weyl bandstructure is, that these materials exhibit the chiral anomaly in magnetic and electric fields applied to the material parallel to each other [4, 24, 25]. Under these circumstances the charge of a given chirality is not conserved, meaning the charges of a cone with one chirality are pumped to the cone of opposite chirality. Experimentally this effect is resulting in a negative longitudinal magneto resistance. The chiral anomaly is known in the high energy physics context as the Adler-Bell-Jackiw anomaly.

The first theoretical suggestions for a Weyl semimetal state in a solid focused on the time reversal symmetry broken case in systems with magnetic order, as pyrochlore iridates [23], complicated stacks of magnetically doped topological insulators [26] or ferromagnetic $HgCr_2Se_4$ [27]. However, all attempts for experimental confirmation of a time reversal broken Weyl semimetal are yet inconclusive [20]. In contrast to that, recently the realization of an inversion symmetry broken Weyl semimetal state was theoretically predicted in the family of non-centrosymmetric mono pnictides around TaAs [28, 29], which are also investigated in this work in form of TaAs and NbP. The experimental confirmation followed soon, by the observation of Fermi arcs and Weyl nodes in angle resolved photoemission experiments [5, 30], and a negative longitudinal magneto resistance, indicative for the chiral anomaly [6, 31]. Yet, there is controversy in the community about the negative longitudinal magneto resistance and its interpretation, since such behavior can be also induced by current jetting effects [32].

As mentioned above, a Weyl semimetal requires the breaking of inversion or time reversal symmetry. If both symmetries are preserved all bands are degenerate, and the 4×4 Hamiltonian, describing this situation is of the form [1, 3]

$$\mathbf{H}_W = \begin{pmatrix} \hbar v_\mathrm{F} \boldsymbol{\sigma} \cdot \mathbf{k} & m \\ m & -\hbar v_\mathrm{F} \boldsymbol{\sigma} \cdot \mathbf{k} \end{pmatrix}. \tag{1.2.3}$$

This describes two Weyl points of opposite chirality at the same point in the Brillouin zone, and the mass entries m mix the two Weyl fermions and open a gap. The case, when $m = 0$ is the situation that describes a 3D Dirac semimetal. At the Dirac node, there is degeneracy of four bands, in contrast to the twofold degeneracy at a Weyl node. The Dirac node is not protected by topology anymore, and to stabilize

a 3D Dirac point with $m = 0$, an additional symmetry is needed.
To date there are only two 3D Dirac semimetals that are experimentally well confirmed by the means of ARPES [7, 8, 33, 34], and signatures of chiral quasiparticles in magnetic fields [35, 36], namely Cd_3As_2, which is investigated in this work, and Na_3Bi. A gapped 3D Dirac state is discussed e.g. in $ZrTe_5$ (see e.g. [37]).

In an increasing number of materials, though maybe known for quite some time, Dirac and Weyl physics is discovered to be of relevance, for instance in iron based superconductors in general [38, 39], and FeSe in particular [10, 40], which is investigated in this work.

The latest suggestions for topologically interesting material classes in the field of Dirac materials comprise type II Weyl semimetals, that break the Lorentz invariance, and hence the Weyl cones are tilted [4, 41], and line node semimetals which host lines of Dirac nodes [42].

1.3 Motivation and Outline

Despite their great potential for applications, there is a keen interest to investigate 3D Dirac and Weyl semimetals from a fundamental point of view. There are three types of fermionic particles in quantum field theory, Dirac, Weyl and Majorana fermions (for a pedagogical review see Ref. [43]). Yet, Weyl and Majorana fermions are lacking confirmation via the observation of the specific characteristics on a real particle in high energy physics.
Now, at least Weyl fermions are realized in condensed matter systems as quasiparticles, which enables investigations of their properties in table top experiments. The existence of Weyl quasiparticles additionally paves the way towards a Majorana type quasiparticle, which is predicted to exist in Weyl or topological insulator superconductors [44–46].

For experimental investigations on Dirac and Weyl semimetals a technique is desirable, which is sensitive to the bandstructure of the material. In this field widely applied is the angle resolved photoemission spectroscopy (ARPES) (see e.g. Refs. [7, 30, 47]). Though, this technique is extremely powerful, it lacks any possibility to apply magnetic fields, has only a rather poor energy resolution, and can not gather any information of the bandstructure above the Fermi energy E_F.

Another technique, widely applied to probe the bandstructure, is the analysis of quantum oscillations in high magnetic fields (see e.g. [48–50]). This technique only allows the determination of the Fermi surface at the Fermi energy.
To add beneficial details on the full picture of the bandstructure of Dirac and Weyl semimetals, in this work optical spectroscopy at infrared frequencies with and without magnetic fields is applied, as a complementary technique to the latter discussed. In contrast to the aforementioned, infrared spectroscopy allows to achieve extremely high resolutions, giving access to subtle details of the bandstructure, and permits to probe above E_F. Combined with theoretical models for the optical response of Dirac and Weyl semimetals, quantitative effective bandstructures around the Dirac and Weyl nodes can be deduced.

After introducing the basic theoretical concepts and details of the experimental technique, four materials are explored in the course of this thesis.

- The 3D Dirac semimetal $\mathbf{Cd_3As_2}$.
- Two Weyl semimetals, of the family of non-centrosymmetric mono pnictides, with different amounts of spin orbit coupling, **NbP** and **TaAs**.
- The iron based superconductor **FeSe**, where the Dirac-like bands *a posteriori* are found to be rather of two dimensional nature.

In the final chapter a summary of the key findings, and a future perspective for further investigations will be given.

2. Theoretical background: Basic models for optical response functions

Infrared optical experiments are a powerful tool in condensed matter physics to gain insight into, and obtain understanding of the specific electrodynamic properties of a material. Optical transitions of diverse origin can directly be identified from such experiments. Since optical spectroscopy in the linear regime is nothing more than the excitation of states by photons, the electrodynamic behavior of the specimen under investigation is determined by the bandstructure of the material. Therefore, from the outset, one can differentiate between intraband transitions within one band, that can be excited by arbitrary small amounts of energy, and interband transitions between two separate bands, where a certain energy threshold has to be overcome. If the material undergoes a phase transition (e.g. structural, magnetic, superconducting), the optical response can be altered drastically at the transition. From these changes, valuable information on the nature of the phase transition can be gained.

Commonly, optical experiments are performed at different temperatures down to liquid-helium temperatures. Applying additionally high magnetic fields leads to the splitting of the bands into magnetic sub-levels, namely the Landau levels. In some cases the Landau levels are split further due to the Zeeman effect. For now the Zeeman splitting will, however, be ignored.
The transitions between the Landau levels, seen in the optical spectra, can unveil subtle details of the bands and their shape.
In real space, the conduction electrons experience restrictions of their motion under the influence of a magnetic field by the Lorentz force. From the so called cyclotron frequency of the circular movement, transport characteristics (e.g. the effective mass of the carriers) can be deduced.

This chapter is dedicated to the basic theoretical concepts that describe the electrodynamics of the electronic sub-system in a solid with and without applied magnetic fields. Focus will lie on models for the optical properties. In Secs. 2.1 and 2.2 the complex response functions of solids to varying electromagnetic fields, and the relations between the real and imaginary parts of these response functions are introduced. In Secs. 2.3, 2.4 and 2.5 general models describing the optical properties arising from free carriers, oscillatory phenomena, and the impact of the bandstructure on the optical absorption process are introduced. In Sec. 2.6 theoretical models specifically for the electrodynamic response of Weyl and Dirac semimetals are presented. Sec. 2.7 sums up the magneto-optical effects, that are relevant for this work, and finally, Sec. 2.8 deals with the optical properties of a superconductor.

2.1 Light matter interaction

In this section the basic concepts of the interaction between light and matter shall be briefly recapitulated. Secs. 2.1, 2.2, 2.3 and 2.4 are following Refs. [51] and [52]. The starting point are the Maxwell equations in presence of a medium. These read as[1]:

$$\nabla \times \mathbf{E} + \frac{1}{c}\frac{\delta \mathbf{B}}{\delta t} = 0 \tag{2.1.1a}$$

$$\nabla \cdot \mathbf{B} = 0 \tag{2.1.1b}$$

$$\nabla \times \mathbf{H} + \frac{1}{c}\frac{\delta \mathbf{D}}{\delta t} = \frac{4\pi}{c}\mathbf{J} \tag{2.1.1c}$$

$$\nabla \cdot \mathbf{D} = 4\pi\rho \tag{2.1.1d}$$

Eqns. 2.1.1 connect the electrical current $\mathbf{J}$ and the charge density ρ with the magnetic and electric field strengths $\mathbf{H}$ and $\mathbf{E}$, as well as to the material dependent electric displacement field $\mathbf{D}$ and magnetic flux density $\mathbf{B}$ (c is the speed of light). The electric displacement field $\mathbf{D}$ and the magnetic flux $\mathbf{B}$ are connected to the corresponding electric and magnetic field strengths $\mathbf{E}$ and $\mathbf{H}$ via the material parameters

[1] The theoretical considerations will be done in Gaussian (cgs) units, as widely applied in optical spectroscopy. In figures sometimes also mixtures between SI and cgs units will occur. At this point the reader is referred to the useful conversion tables between units in Ref. [51].

namely the dielectric constant ε_1 and the magnetic permeability μ_1.

$$\mathbf{D} = \varepsilon_1 \mathbf{E} = (1 + 4\pi\chi_\mathrm{e})\mathbf{E} = \mathbf{E} + 4\pi\mathbf{P} \tag{2.1.2a}$$

$$\mathbf{B} = \mu_1 \mathbf{H} = (1 + 4\pi\chi_\mathrm{m})\mathbf{H} = \mathbf{H} + 4\pi\mathbf{M} \tag{2.1.2b}$$

The material equations 2.1.2 can be understood as follows: upon applying external fields $\mathbf{E}$ and $\mathbf{H}$, inside of the material, electrical and magnetic dipoles get oriented leading to an electric polarization $\mathbf{P}$ and magnetization $\mathbf{M}$. For small fields, in the linear regime, constants of proportionality, namely the electric and magnetic susceptibilities χ_e and χ_m can be utilized to characterize the response. These susceptibilities directly relate to ε_1 and μ_1, respectively.
Note, that the magnetic susceptibility χ_m is orders of magnitude smaller than χ_e in non-ferromagnetic materials, and therefore the magnetic response to electromagnetic waves will henceforth be neglected in this work.
Assuming a harmonically oscillating displacement[2] $\delta\mathbf{D}/\delta t = -\mathrm{i}\omega\mathbf{D}$ and assuming Ohm's law holds for the currents in the material (which states the proportionality between electric field and current $\mathbf{J} = \sigma_1\mathbf{E}$ with the materials conductivity σ_1), Eq. 2.1.1c can be rewritten as:

$$c\nabla \times \mathbf{H} = -\mathrm{i}\omega\varepsilon_1 + 4\pi\sigma_1\mathbf{E} \tag{2.1.3}$$

Eq. 2.1.3 involves the complex dielectric function,

$$\widehat{\varepsilon}(\omega) = \varepsilon_1(\omega) + \mathrm{i}\frac{4\pi\sigma_1(\omega)}{\omega} = \varepsilon_1(\omega) + \mathrm{i}\varepsilon_2(\omega) \tag{2.1.4}$$

which accounts for the change of amplitude and phase shift between $\mathbf{E}$ and $\mathbf{D}$. The dielectric function can be related to the complex refractive index $\widehat{N}(\omega) = n(\omega) + \mathrm{i}k(\omega)$ with the real refractive index $n(\omega)$ and the extinction coefficient $k(\omega)$ as:

$$\widehat{N}(\omega) = \sqrt{\widehat{\varepsilon}(\omega)} \tag{2.1.5}$$

For this thesis the quantities that are mainly discussed aside from the dielectric function are the optical conductivity $\widehat{\sigma}(\omega) = \sigma_1(\omega) + \mathrm{i}\sigma_2(\omega)$ which can be defined by the complex dielectric function as

[2] This is reasonable since the electric field of the light $\mathbf{E}$ as obtained from the solution of the Maxwell equations in vacuum is harmonic in time and space $\mathbf{E}(\mathbf{r}, t) = \mathbf{E}_0 \mathrm{e}^{\mathrm{i}(\mathbf{qr} - \omega t)}$.

$$\widehat{\varepsilon}(\omega) = 1 + \frac{4\pi \mathrm{i}}{\omega}\widehat{\sigma}(\omega), \tag{2.1.6}$$

and the reflection coefficient at the surface of a medium. Equal to the dielectric function $\widehat{\varepsilon}$ (Eq. 2.1.4) the refractive index $\widehat{N}$ (Eq. 2.1.5) and the optical conductivity $\widehat{\sigma}$, the reflection coefficient is also a complex quantity $\widehat{r} = r(\omega)e^{\mathrm{i}\phi_r(\omega)}$. It consists of an amplitude change $r(\omega)$ as well as a change in phase $\phi_r(\omega)$ between incident and reflected wave. The experimentally determined part of the complex reflection coefficient $\widehat{r}$ is the square of the amplitude, from now on referred to as reflectivity[3] $R(\omega) = r(\omega)^2$. For the experimental approach employed in this thesis, the phase $\phi_r(\omega)$ is lost[4].

In this work, the reflectivity at near normal incidence is measured. With this technique one can probe the bulk properties of a specimen due to the finite penetration of the light.

For the reflection at a surface of a medium in vacuum the reflectivity $R(\omega)$ and phase $\phi_r(\omega)$ relate to the real and imaginary part of the complex refractive index $\widehat{N}(\omega)$, namely $n(\omega)$ and $k(\omega)$, as:

$$R(\omega) = \frac{(1 - n(\omega))^2 + k(\omega)^2}{(1 + n(\omega))^2 + k(\omega)^2} \tag{2.1.7a}$$

$$\phi_r(\omega) = \arctan\left[\frac{-2k(\omega)}{1 - n(\omega)^2 - k(\omega)^2}\right] \tag{2.1.7b}$$

It has to be noted, that in the most general case, the optical constants are tensors. In this thesis, only a scalar response can be measured. However, all investigated materials posses tetragonal symmetry[5] and only the in-plane response is probed. Hence, the observed response can basically be boiled down to the leading diagonal element of the tensor.

[3] In the course of this thesis mainly the real parts of $\widehat{\varepsilon}$, $\widehat{\sigma}$ and the reflectivity are discussed. These quantities will be simply referred to as dielectric function $\varepsilon_1(\omega)$, optical conductivity $\sigma_1(\omega)$ and reflectivity $R(\omega)$, without emphasizing the fact, that these are the real parts of the complex response functions.

[4] This is not true for all optical techniques. In ellipsometry, for instance, the real and imaginary part of an optical response function can be measured.

[5] Except from FeSe, which is orthorhombic at low temperatures. However the orthorhombicity is masked by the formation of twin domains.

2.2 Kramers-Kronig relations

It is desired, to not only analyze the measured reflectivity $R(\omega)$. Especially the real part of the optical conductivity $\sigma_1(\omega)$ is of interest in this work. The Kramers-Kronig transformation can be applied to calculate the imaginary part $\phi_r(\omega)$ of the complex reflection coefficient. Having both, real and imaginary part of any of the optical constants, one can calculate all others.
For this thesis, the relation to obtain the optical constants from pure reflectivity measurements connects the phase shift $\phi_r(\omega)$ to the reflection amplitude $r(\omega) = \sqrt{R(\omega)}$ and reads as [51, 52]:

$$\phi_r(\omega) = -\frac{2\omega}{\pi}\mathcal{P}\int_0^\infty \frac{\ln r(\omega')}{\omega'^2 - \omega^2}d\omega' \tag{2.2.1}$$

$\mathcal{P}$ denotes the Cauchy principal value.

The integration in Eq. 2.2.1 is performed from zero to infinity. For this reason it is necessary to perform the measurements of $R(\omega)$ over a frequency range as wide as possible. Nevertheless it is indispensable to extrapolate the data to high and low frequencies. The extrapolation towards zero frequency is described in Sec. 2.3. Towards high frequencies an extrapolation method suggested by D. Tanner is applied [53]. This method treats a solid as a linear combination of atoms, and computes a reflectivity for frequencies from $10\,\mathrm{eV} \approx 80\,000\,\mathrm{cm}^{-1}$ up to $34\,\mathrm{keV} \approx 2.7 \times 10^8\,\mathrm{cm}^{-1}$ from the x-ray atomic scattering functions [54]. The only things needed to compute this extrapolation are the chemical formula of the material and it's density.

2.2.1 Sum rules

From the Kramers-Kronig relations together with physical arguments some powerful sum rules for the optical constants can be deduced. Of particular importance is the so called f-sum rule, which relates the area below the real part of the complex conductivity to the number of carriers involved in any kind of transition contributing to the optical response. This means the total area below $\sigma_1(\omega)$ can be related to the total carrier density N in the material by:

$$\int_0^\infty \sigma_1(\omega)\mathrm{d}\omega = \frac{\omega_p^2}{8} = \frac{\pi N e^2}{2m} \tag{2.2.2}$$

Here m denotes the carrier mass. Note, that Eq. 2.2.2 is valid independent of the

model or whether bound or free carriers are involved in the absorption process. Often it is however used, to determine information on the plasma frequency ω_p of the free carrier response described in Sec. 2.3, by only integrating up to a cutoff frequency ω_c that is assumed to be sufficiently high to capture all carriers contributing to intraband absorptions.

2.3 Drude model

For a meaningful analysis of the data obtained in optical experiments, some models are needed that give insight into the behavior of the optical constants in various circumstances. The optical response of free carriers can be well described by the phenomenological Drude model. The carriers of a metal are treated as a classical gas of electrons. This means that each electron travels freely, until it experiences a scattering event. This motion is characterized by the mean time between scattering events, the scattering time τ, or its inverse, the scattering rate $\Gamma = \frac{1}{\tau}$. If light hits this free electron gas, the electrons are excited by the electric field $E(t) = E_0 \mathrm{e}^{\mathrm{i}\omega t}$, with the amplitude E_0, and the equation of motion becomes:

$$m\frac{d^2r}{dt^2} + \frac{m}{\tau}\frac{dr}{dt} = -eE(t) \tag{2.3.1}$$

Note, that the italic e denotes the electron charge while e represents the Euler number in the course of this thesis. The solution of Eq. 2.3.1 yields the frequency dependent conductivity of the Drude model:

$$\widehat{\sigma}(\omega) = \sigma_1(\omega) + \mathrm{i}\sigma_2(\omega) = \frac{Ne^2\tau}{m}\frac{1}{1-\mathrm{i}\omega\tau} \tag{2.3.2}$$

with the carrier density N. The real and imaginary parts can be represented as:

$$\sigma_1(\omega) = \frac{\omega_p^2\tau}{4\pi}\frac{1}{1+\omega^2\tau^2} \tag{2.3.3a}$$

$$\sigma_2(\omega) = \frac{\omega_p^2\tau}{4\pi}\frac{\omega\tau}{1+\omega^2\tau^2} \tag{2.3.3b}$$

In the zero frequency limit the real part of the optical conductivity corresponds to the DC conductivity σ_{DC}, which relates to the plasma frequency ω_p as:

$$\sigma_1(\omega = 0) = \sigma_{\mathrm{DC}} = \frac{Ne^2\tau}{m} = \frac{1}{4\pi}\omega_p^2\tau \tag{2.3.4}$$

To account for the fermionic nature of electrons and to get a more realistic treatment of the interactions among them, the Sommerfeld extension of the Drude model includes the concept of a Fermi surface. The mean free path l of an electron depends under this conditions on the Fermi velocity v_{F}, instead of the thermal velocity, and can be expressed as $l = v_{\mathrm{F}}\tau$. The interactions lead to a renormalization of the electron mass, hence an effective mass m^* has to replace the mass m in Eqns. 2.3.1 to 2.3.4.

Fig. 2.3.1 (a) depicts the typical Drude reflectivity of a metal. Over a wide frequency range, the reflectivity remains constant and close to unity. At the plasma frequency $\nu_p = \frac{\omega_p}{2\pi c}$ a sharp edge occurs, where the reflectivity rapidly drops to zero. At low frequencies, $\omega \ll \gamma = \frac{1}{2\pi c\tau}$, the electrodynamic response is dominated by the DC conductivity σ_{DC} and the reflectivity can be approximated by the Hagen-Rubens relation (Eq. 2.3.5) as displayed in the insert of Fig. 2.3.1 (a):

$$R(\omega) = 1 - \sqrt{\frac{2\omega}{\pi\sigma_{\mathrm{DC}}}} \tag{2.3.5}$$

The Hagen-Rubens relation is utilized for the low frequency extrapolations in the course of this thesis, if not stated else.

Panel (b) of Fig. 2.3.1 displays the real part of the optical conductivity $\sigma_1(\omega)$. The low-frequency response is nearly constant and adapts the value of σ_{DC}, until $\sigma_1(\omega)$ rolls off at higher frequencies, where the inflection point marks the scattering rate γ. In panel (c) of Fig. 2.3.1, $\varepsilon_1(\omega)$ is displayed, which exhibits large negative values at low frequencies. The plasma frequency ν_p can be identified as the zero crossing $\varepsilon_1(\omega) = 0$, as visualized in the insert of panel (c).

2.4 Lorentz model

The classical Lorentz oscillator model and its quantum-mechanical analogue can be used to describe the optical properties of oscillating phenomena in solids. It is often applied to model the optical response of lattice vibrations (phonons), as well as electronic transitions, where the initial and final states lie in different bands (interband transitions). In the classical Lorentz model, the starting point is the equation of motion of electrons that are bound to ions by a restoring force, acting

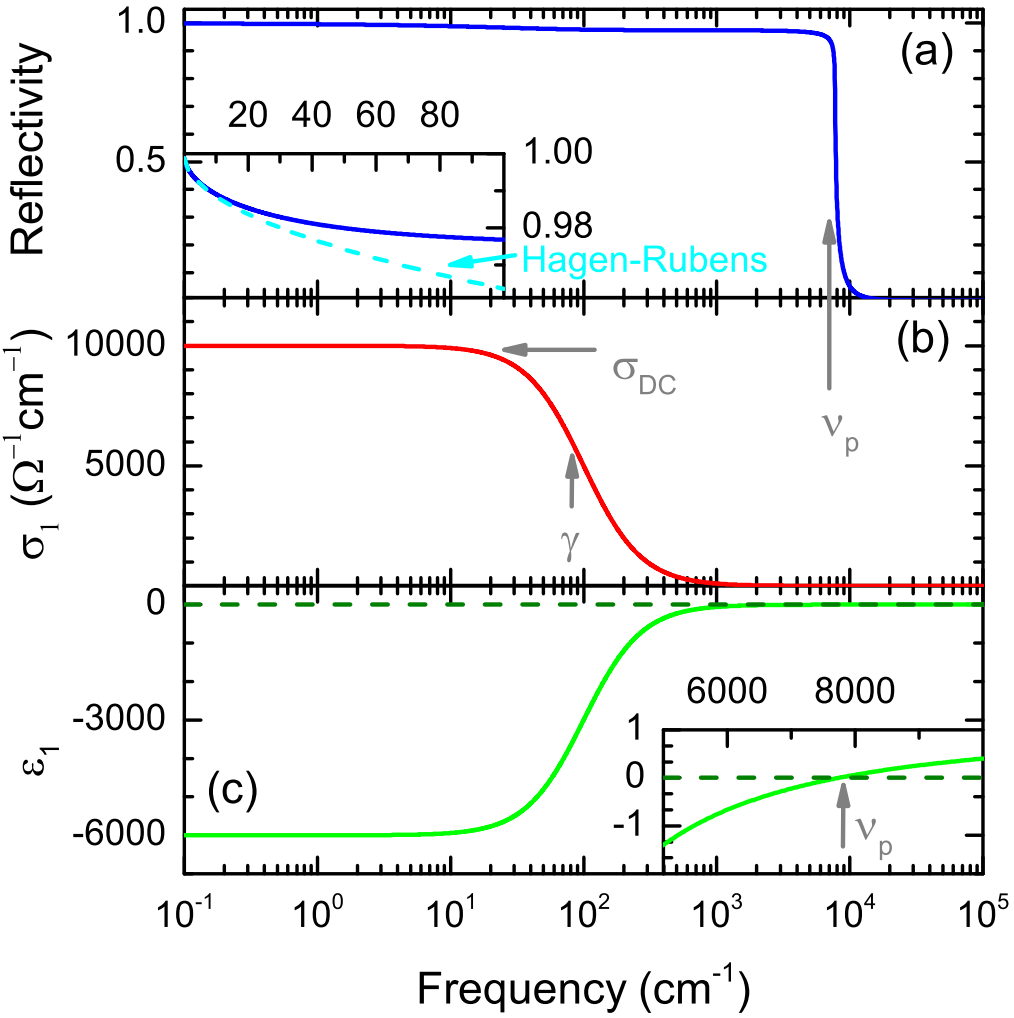

Figure 2.3.1: Optical properties of the Drude model in bulk reflectivity $R(\omega)$ (a), real part of the optical conductivity $\sigma_1(\omega)$ (b) and real part of the dielectric function $\varepsilon_1(\omega)$ (c). The plasma frequency ν_p can be identified in panel (a) as the sharp edge, where $R(\omega)$ drops to zero, as well as in the inset of panel (c) as the zero crossing of $\varepsilon_1(\omega)$. Scattering rate γ and DC-conductivity σ_{DC} are revealed in panel (b) as the inflection point of $\sigma_1(\omega)$ and the zero frequency limit $\sigma_1(\omega \to 0)$, respectively. The inset of panel (a) enlarges the low frequency reflectivity region, where $R(\omega)$ can be approximated by the Hagen-Rubens relation (see text).

like a spring. In presence of an oscillating electric field as in Sec. 2.3 the motion is described by,

$$m\frac{d^2r}{dt^2} + \frac{m}{\tau}\frac{dr}{dt} + m\omega_0^2 r = -eE(t) \tag{2.4.1}$$

where the term with $\Gamma = \frac{1}{\tau}$ can be interpreted as damping or scattering and ω_0 is the center frequency (or resonance frequency) of the oscillator. The solution yields a complex optical conductivity,

$$\widehat{\sigma}(\omega) = \frac{Ne^2}{m}\frac{\omega}{\mathrm{i}(\omega_0^2 - \omega^2) + \omega/\tau} \tag{2.4.2}$$

which can be split into the real and imaginary parts σ_1 and σ_2:

$$\sigma_1(\omega) = \frac{\omega_p^2}{4\pi}\frac{\omega^2/\tau}{(\omega_0^2 - \omega^2)^2 + \omega^2/\tau^2} \tag{2.4.3a}$$

$$\sigma_2(\omega) = -\frac{\omega_p^2}{4\pi}\frac{\omega(\omega_0^2 - \omega^2)}{(\omega_0^2 - \omega^2)^2 + \omega^2/\tau^2}. \tag{2.4.3b}$$

Fig. 2.4.1 (a-c) display the optical response of a Lorentz oscillator in terms of $R(\omega)$, $\sigma_1(\omega)$ and $\varepsilon_1(\omega)$. The reflectivity $R(\omega)$ is flat at low frequencies and starts to rise around ν_0. After a flat region at elevated amounts of reflection, $R(\omega)$ drops sharply at the plasma frequency ν_p similar to the Drude reflectivity, see Fig. 2.3.1 (a). The absorptive part of the optical conductivity $\sigma_1(\omega)$ exhibits a peak at ν_0. The full width at half maximum of this peak corresponds to the damping γ. The dielectric function $\varepsilon_1(\omega)$ is positive at low frequencies, in contrast to the Drude behavior revealed in Fig. 2.3.1 (c). $\varepsilon_1(\omega)$ remains positive up to frequencies around ν_0. Two zero crossings are apparent in 2.4.1 (c), one in the vicinity of ν_0 and another one at ν_p.

2.5 The impact of the bandstructure

2.5.1 Martix elements

The interaction of the electrons with the periodic potential of the ion cores in a crystalline solid leads to the formation of Bloch bands (see any textbook on solid state physics). The Drude and Lorentz models described above, though extremely useful for the analysis of optical spectra, do not take into account any bandstructure, which, particularly for semiconductors, can have considerable impact on the

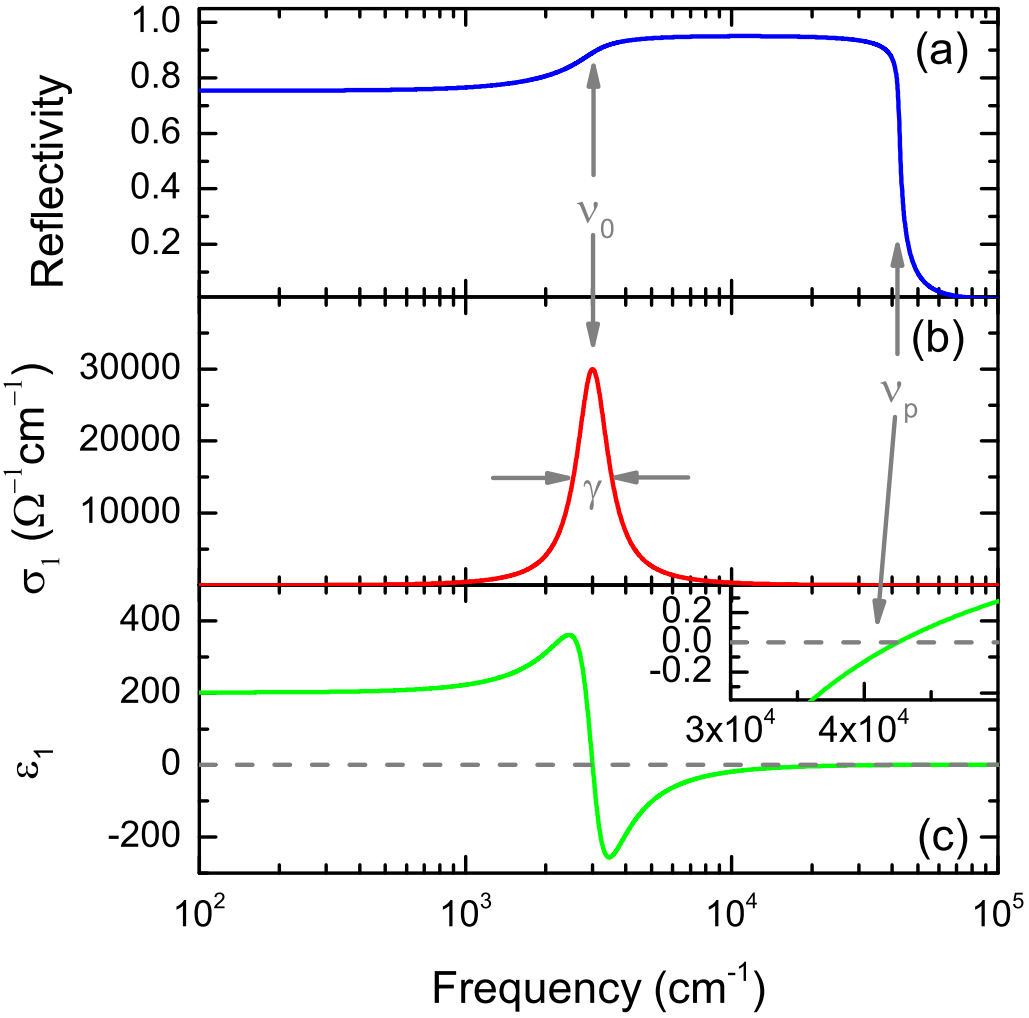

Figure 2.4.1: Optical properties of a Lorentz oscillator in the reflectivity $R(\omega)$ (a), the real part of the optical conductivity $\sigma_1(\omega)$ (b) and the real part of the dielectric function $\varepsilon_1(\omega)$ (c). The plasma frequency ν_p can be identified the same way as in the Drude model: in panel (a) as the sharp edge, where $R(\omega)$ drops to zero, and in panel (c) as a zero crossing from negative to positive values of $\varepsilon_1(\omega)$. The damping of the Lorentz oscillator γ is the full width at half maximum of the peak in the optical conductivity $\sigma_1(\omega)$ in panel (b). The center frequency $\nu_0 = \frac{\omega_0}{2\pi c}$ can be identified in $R(\omega)$ at the inflection point of the rise, in $\sigma_1(\omega)$ as the maximum of the peak and it can also be found in close vicinity of the first zero crossing of $\varepsilon_1(\omega)$ (positive to negative change in $\varepsilon_1(\omega)$).

optical response at infrared frequencies. The main effects will be introduced here in a nutshell following Refs. [51, 55–57].

The absorption of a photon by a solid can be treated with the time-dependent perturbation theory. With $\mathbf{H}_{em} = H'$, the perturbation operator of the electromagnetic field, the probability per time w_{fi} for an electron to perform a transition from an occupied initial (i) to an unoccupied final (f) state is given (with certain approximations) by Fermi's golden rule

$$w_{fi}(\hbar\omega) = \frac{2\pi}{\hbar} \left|H'_{fi}\right|^2 \delta(E_f - E_i - \hbar\omega). \tag{2.5.1}$$

Here, $\hbar\omega$ is the energy of the photon, E_i is the energy of the initial state and E_f the energy of the final state.

$$H'_{fi} = \langle \psi_f \left|\mathbf{H}'\right| \psi_i \rangle \tag{2.5.2}$$

is the matrix element with the wavefunctions of the unperturbed initial and final states, $\langle\psi_f|$ and $|\psi_i\rangle$ (in a solid the Bloch functions for conduction band $\langle c|$ and valence band $|v\rangle$). The Hamiltonian for an electron in the electromagnetic field (neglecting quadratic terms) is given by

$$\mathbf{H}_{em} = \frac{e}{mc}\mathbf{A}\cdot\mathbf{p}, \tag{2.5.3}$$

with the vector potential of the electromagnetic radiation $\mathbf{A} = A\cdot\hat{\mathbf{e}}$ ($\hat{\mathbf{e}}$ = unit vector $\|$ $\mathbf{A}$) and the momentum operator $\mathbf{p}$ for the electrons.
In the electric dipole approximation (for small wavevectors $\mathbf{q}$ of the electromagnetic radiation), the matrix element is given by:

$$|\langle c|\mathbf{H}_{em}|v\rangle|^2 = \frac{e^2|A|^2}{m^2}\,|\langle c|\hat{\mathbf{e}}\cdot\mathbf{p}|v\rangle|^2 = \frac{e^2|A|^2}{3m^2}|\mathbf{p}_{cv}|^2. \tag{2.5.4}$$

Often $\mathbf{p}_{cv} = \langle c \left|\mathbf{p}\right| v\rangle$ is used as a $\mathbf{k}$-independent matrix element.
The electric field amplitude E is connected to the vector potential amplitude via $A = \frac{E}{2\omega}\left[e^{i(\mathbf{qr}-\omega t)} + e^{-i(\mathbf{qr}-\omega t)}\right]$. With this, the electric dipole transition probability $\Re$ for the absorption of a photon is

$$\Re(\hbar\omega) = \frac{2\pi}{\hbar}\left(\frac{e}{m\omega}\right)^2 \left|\frac{E(\omega)}{2}\right|^2 |\mathbf{p}_{cv}|^2 \int_{\mathbf{k}} \delta(E_c(\mathbf{k}) - E_v(\mathbf{k}) - \hbar\omega)d\mathbf{k}. \tag{2.5.5}$$

Via the power loss per unit volume which is simply $\Re\hbar\omega$ when the integral in Eq. 2.5.5 runs over all allowed $\mathbf{k}$ in the unit volume of the crystal the expression for the

imaginary part of the dielectric function can be obtained (and the real part via Kramers-Kronig). These read

$$\varepsilon_1(\omega) = 1 + \frac{4\pi e^2}{m} \int_{\mathbf{k}} \frac{2|\mathbf{p}_{cv}|^2}{m\hbar\omega_{cv}} \frac{1}{1-\omega/\omega_{cv}} d\mathbf{k} \tag{2.5.6a}$$

$$\varepsilon_2(\omega) = \left(\frac{2\pi e^2}{m\omega}\right)^2 |\mathbf{p}_{cv}|^2 \int_{\mathbf{k}} \delta(E_c(\mathbf{k}) - E_v(\mathbf{k}) - \hbar\omega) d\mathbf{k}, \tag{2.5.6b}$$

with $\hbar\omega_{cv} = E_c(\mathbf{k}) - E_v(\mathbf{k})$.

2.5.2 Critical points

The dispersion relation $E(\mathbf{k})$ identifies, how the energy of a (quasi-)particle depends on the $\mathbf{k}$-vector. The quantity how many states are available at a given energy is called density of states $D(E)$. Relevant for the optical transitions between conduction and valence band edges is the joint density of states $D_j(E)$, which defines, how many states are available for a given transition with energy $\hbar\omega$. This joint density of states corresponds to the integration over the delta function $\delta(E_c(\mathbf{k}) - E_v(\mathbf{k}) - \hbar\omega)$ in Eq. 2.5.6 and can be converted to an integration over energy as

$$D_j(\hbar\omega) = \frac{2}{(2\pi)^3} \int \frac{dS_{\mathbf{k}}}{|\nabla_{\mathbf{k}}(E_{cv})|}, \tag{2.5.7}$$

where $E_{cv} = E_c - E_v$, and $S_{\mathbf{k}}$ is the constant energy surface where $E_{cv}(\mathbf{k}) = const.$ The factor 2 arises from the spin degeneracy. The critical points where the dispersions of conduction and valence bands are parallel and $\nabla_{\mathbf{k}}(E_{cv}) = 0$ are called van Hove singularities.

Since $\varepsilon_2(\omega)$ is directly proportional to the joint density of states, the van Hove singularities leave prominent signatures in the optical response.
There are four types of van Hove singularities in three dimensions usually dubbed M_0-M_3, where M_0 refers to a minimum in band separation, M_1 and M_2 are saddle points and M_3 is a maximum in band separation. Each of the van Hove singularities leaves a distinct signature in the optical response.

The shapes of $\varepsilon_1(\omega)$ and $\varepsilon_2(\omega)$ around the band edge with a M_0 van Hove singularity is schematically depicted in Fig. 2.5.1 (for direct transitions). For the shape of the dielectric function in the cases of M_1-M_3, the reader is referred to Refs. [55, 56].

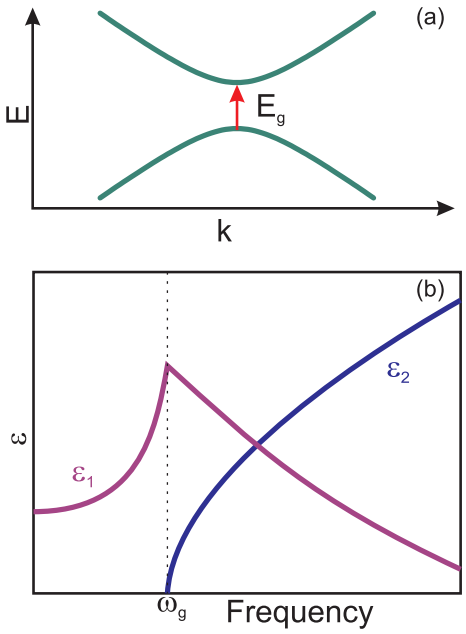

Figure 2.5.1: Illustration of a M_0-type van Hove singularity in the bandstructure (a). Conduction and valence band exhibit a minimum gap E_g. The shape of $\varepsilon_1(\omega)$ and $\varepsilon_2(\omega)$ are schematically depicted in panel (b). The dashed line marks the frequency ω_g corresponding to the gap energy E_g.

2.6 Models for the optical response of 3D Dirac and Weyl semimetals

2.6.1 Model for a single cone

The linear dispersing bands in three-dimensional Dirac and Weyl semimetals give rise to peculiar hallmarks in the optical constants. Interpretation of these characteristics enable a deep insight into the band dispersions, and the energy scales, relevant for Dirac or Weyl physics.

Soon after the discovery of graphene [58], in addition to transport investigations, optical experiments became important for understanding its electronic properties [12, 59–61]. The finding was, that the interband optical absorbance is independent of frequency, and only determined by the fine structure constant $\alpha = e^2/\hbar c$. The universality and flatness of this response was assigned to the linear momentum dependence of the 2D Dirac quasiparticle energy.

For two band systems, with quasiparticles possessing a (pseudo) spin degree of freedom, whose direction is solely determined by the direction of the momentum, Bácsi and Virosztek derived an expression for the optical conductivity [62]. With a pseudo spin locked to the momentum, the system possesses some generalized chirality. As a consequence, the band dispersion has to have a powerlaw dependence, i.e. $\epsilon(\mathbf{k}) \propto k^z$. Furthermore, the conduction and valence bands need to cross at the Fermi level and there is no energy gap. Under such circumstances, their model not only cap-

tures graphene, but can also be applied to more general cases. Utilizing the Kubo formula, they arrive at an expression for the real part of the optical conductivity,

$$\sigma_1(\omega) \propto \omega^{\frac{d-2}{z}}, \tag{2.6.1}$$

with the dimensionality of the system d and the dispersion exponent z.

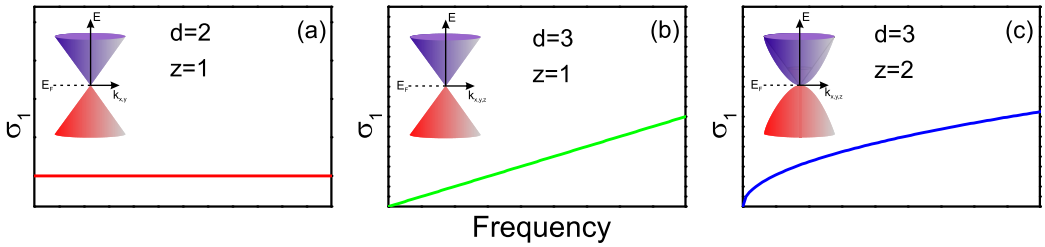

Figure 2.6.1: The interband optical conductivity $\sigma_{1,IB}(\omega)$ according to Eq. 2.6.1 [62]. Panel (a) displays the constant interband conductivity of a system with linear dispersing bands in two dimensions as it is found in graphene. Panel (b) exhibits the ω-linear $\sigma_{1,IB}(\omega)$ of a 3D Dirac cone, while panel (c) reveals the optical response of a hypothetical 3D system with parabolic bands touching at E_F. Sketches of the respective bands are displayed as insets in each panel.

It is clear, that for the graphene case, where the dispersion is linear and the dimensionality is 2, i.e. $z = 1$ and $d = 2$, the proportionality given in Eq. 2.6.1 yields a frequency independent $\sigma_1(\omega)$ as depicted in Fig. 2.6.1 (a)[6]. In this work, systems with $d = 3$ were investigated. For this case, Eq. 2.6.1 provides an optical conductivity $\sigma_1(\omega)$, linear in frequency and starting from the origin (Fig. 2.6.1 (b)). In a similar manner, one can think about bands with other shapes, and therefore different optical conductivities arising from this model. An exemplary $\sigma_1(\omega)$ for a 3D system with parabolic bands touching at E_F is displayed in Fig. 2.6.1 (c).
A linear or quasilinear optical conductivity was indeed observed in various compounds and ascribed to the linearly dispersing bands [63–69]. To date, various theoretical studies on the electrodynamics of Weyl and Dirac semimetals are available [70–76], each of those treating different models with subtle variations of the band shapes and varying amounts of disorder. At this point, first a simple phenomenological analytic expression for the interband optical conductivity $\sigma_{1,IB}(\omega)$ for three dimensional systems with linear bands shall be introduced. This expression provides a first insight into the hallmarks in the spectra arising from transitions between Dirac

[6] Actually, if $d = 2$, the band exponent z does not matter, in any case $\sigma_1(\omega) \propto \omega^0$ will hold.

or Weyl bands.
The simplest case of a 3D Dirac cone where the node is at the Fermi energy, is treated in Refs. [75, 77, 78] with the Kubo formula. It is found, that the interband conductivity can be represented as,

$$\sigma_{1,\mathrm{IB}}(\omega) = \frac{e^2 N_{\mathrm{W}}}{24\hbar^2 v_{\mathrm{F}}}\omega. \tag{2.6.2}$$

This includes the known ω-linear increase of σ_1 with a slope inversely proportional to the Fermi velocity v_{F}. N_{W} denotes the number of non-degenerate cones. For the more general case, when the chemical potential Δ_{E} (=distance Dirac node-Fermi energy)[7] is not necessarily at the Dirac or Weyl node the interband optical conductivity $\sigma_{1,\mathrm{IB}}(\omega)$ reads as [75],

$$\sigma_{1,\mathrm{IB}}(\omega) = \frac{e^2 N_{\mathrm{W}}}{24\hbar^2 v_{\mathrm{F}}}\frac{(\omega - 2\Delta_{\mathrm{g}})^2}{\omega}\Theta(\omega - \max[2\Delta_{\mathrm{E}}, 2\Delta_{\mathrm{g}}]). \tag{2.6.3}$$

In Eq. 2.6.3 a massless gap Δ_{g} can be included. Generally, the possibility of having a massless gap is questionable. It can probably be caused by self energy effects that push the upper and lower cone apart [75], or by electron-electron interactions [79]. A frequency independent scattering γ can be included in Eq. 2.6.3 by replacing the Θ-function, for instance with $\frac{1}{2} + \frac{1}{\pi}\mathrm{arctan}\frac{\omega - 2\max[\Delta_{\mathrm{E}},\Delta_{\mathrm{g}}]}{\gamma}$ [68, 75].

Fig. 2.6.2 illustrates the interband optical conductivity $\sigma_{1,\mathrm{IB}}(\omega)$ for various circumstances according to Eq. 2.6.3. Sketches of the bandstructures are displayed in each panel. When the chemical potential Δ_{E} is zero, i.e. the nodes are at the Fermi energy E_{F}, and no gap Δ_{g} is included (panel (a) of Fig. 2.6.2), Eq. 2.6.3 reduces to Eq. 2.6.2 and the conductivity is linear and starts from the origin, as it was already discussed in regard of Eq. 2.6.1. It is obvious from the sketch in panel (b), that for finite chemical potential, the interband transitions start at $\omega = 2\,|\Delta_{\mathrm{E}}|$, while the linear $\sigma_{1,\mathrm{IB}}(\omega)$ still extrapolates to $\omega = 0$. For increasing scattering γ, the sharp step gets smeared out, indicated by the black arrows. For large scatterings (purple dash dotted line), the deviations from the $\gamma = 0$ case (blue line) start to appreciably affect the linear part.

In contrast, introducing a gap Δ_{g}, as indicated in the left cone depicted in Fig. 2.6.2 (c), results in an intersection of $\sigma_{1,\mathrm{IB}}(\omega)$ at finite frequencies $\omega = |2\Delta_{\mathrm{g}}|$, as long as

[7] Note, that traditionally the chemical potential is referred to as μ. However in this work the notation Δ_E will be used, to avoid confusion with the carrier mobility μ.

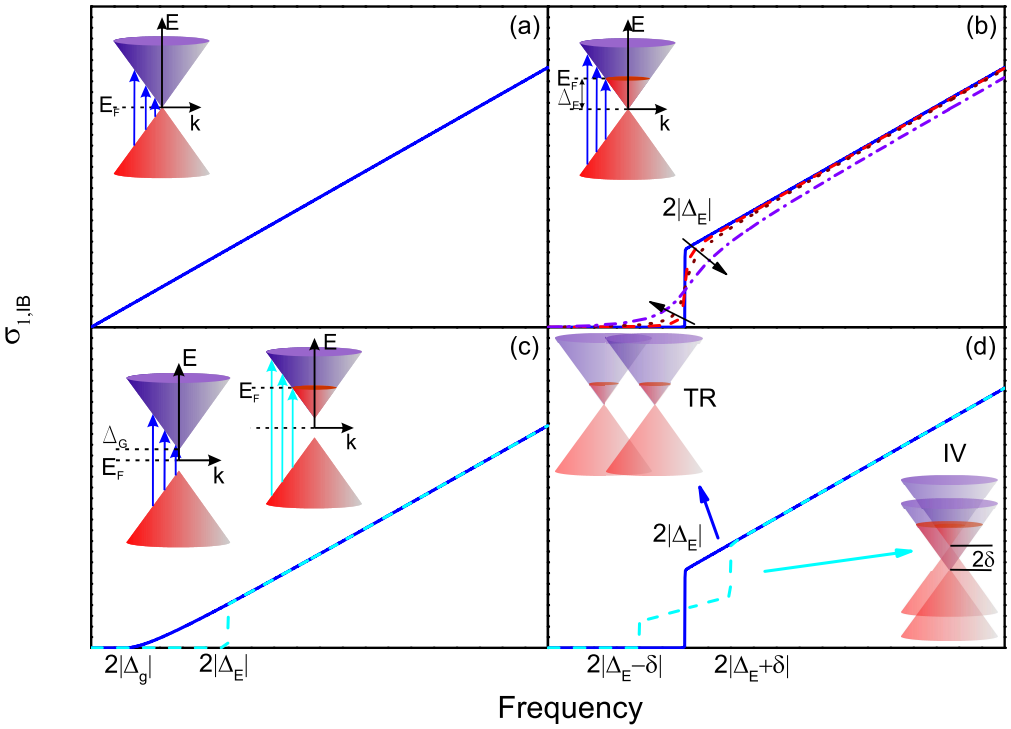

Figure 2.6.2: The interband optical conductivity $\sigma_{1,IB}(\omega)$ of Dirac (a-c) and Weyl (d) semimetals according to Eq. 2.6.3 [75]. Panels (a) and (b) reveal the linear response in case of zero and finite chemical potential, respectively. The finite chemical potential is reflected in the step at $\omega = 2\,|\Delta_E|$, which becomes smeared out by increased scattering (dotted curves in panel(b)). Including a massless gap Δ_g (i.e. a gap which preserves the bands to deviate from linearity) leads to a finite intersection of the ω-linear conductivity at $\omega = 2\,|\Delta_g|$ as long as $|\Delta_E| < |\Delta_g|$, otherwise a step appears in the spectrum (c). The interband absorption of a Weyl semimetal depends on the kind of symmetry breaking applied to the Dirac Hamiltonian in the simple model utilized in Ref. [75]. The broken time reversal (TR) symmetry leads to the same response as for the Dirac cone, in case of broken inversion (IV) symmetry, however, two steps are supposed to occur in $\sigma_{1,IB}(\omega)$ at $2\,|\Delta_E \pm \delta|$, where 2δ denotes is the energy distance between the two nodes (d). The respective bandstructures are sketched in each panel.

the Fermi energy remains in the gap. Such behavior was indeed observed in various compounds with Dirac physics [63, 66, 69]. While the massless-gap scenario phenomenologically captures the behavior, the real physical origin remains unresolved to date. The right cone in Fig. 2.6.2 (c) represents the situation, when the chemical potential exceeds the gap. In this case, a step occurs at $\omega = 2\,|\Delta_\mathrm{E}|$, but the linear part still extrapolates to a finite intersection with the abscissa. Note, that for all aforementioned considerations the number of cones was set to $N_\mathrm{W} = 2$ since a Dirac cone is twofold spin degenerate.

Breaking time reversal (TR) or inversion (IV) symmetry in the simple model of a Dirac cone in Ref. [75], leads to degeneracy lifting. The emerging state corresponds to two Weyl cones of opposite chirality (see Sec. 1). In the case of a broken TR symmetry, the two Weyl cones are separated in momentum, while for broken IV symmetry they are shifted in energy, as sketched in Fig. 2.6.2 (d). Therefore, in the case of a broken IV symmetry, two steps must appear at $2\,|\Delta_\mathrm{E} \pm \delta|$, if one defines Δ_E as the distance of Fermi energy E_F from the center between the nodes. In case of a broken TR symmetry, only one step occurs[8].

The real part of the dielectric function arising from the Dirac interband transitions $\varepsilon_{1,\mathrm{IB}}(\omega)$, is found to be logarithmically dependent on a cutoff energy Λ, beyond which the Dirac bands are assumed to be not linear anymore [70, 72, 80]. A simple expression for a qualitative treatment is satisfactory for the spectral analysis in this thesis and reads as [80]

$$\varepsilon_{1,\mathrm{IB}}(\omega) \propto \log\left(\frac{\Lambda^2 - \omega^2}{(2\Delta_\mathrm{E})^2 - \omega^2}\right). \tag{2.6.4}$$

In Fig. 2.6.3 the important aspect of $\varepsilon_{1,\mathrm{IB}}(\omega)$ of the Dirac interband transitions is highlighted. The cutoff is beyond the displayed range, and not of relevance here. The onset of the Dirac interband transitions in Fig. 2.6.3 is marked by a cusp in $\varepsilon_{1,\mathrm{IB}}(\omega)$ at $\omega = 2\,|\Delta_\mathrm{E}|$, corresponding to the step in $\sigma_{1,\mathrm{IB}}(\omega)$ discussed above.

[8] Strictly speaking, the effect of time reversal symmetry breaking can also lead to a nodal line in the bandstructure depending on the exact nature of the TR breaking perturbation [17]. The scenario discussed here is just the simpest one.

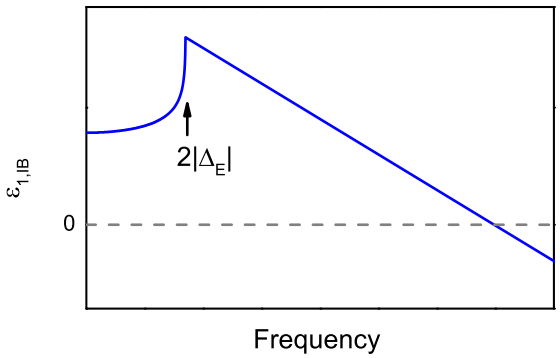

Figure 2.6.3: The cusp in the interband dielectric function, $\varepsilon_{1,IB}(\omega)$, of the Dirac cone at $\omega = 2\,|\Delta_E|$ marks the onset of the interband transitions.

2.6.2 Four-band model

A more realistic bandstructure and the arising optical interband conductivity $\sigma_{1,\mathrm{IB}}(\omega)$ of a Weyl semimetal are treated in Ref. [74] (see Appendix A). Instead of a single Dirac or Weyl cone four particle-hole symmetric conduction and valence bands are utilized for the calculations. The energy dispersion can be represented as

$$\epsilon_{s,s'}(\mathbf{k}) = s\sqrt{m^2 + b^2 + (v_\mathrm{F}\hbar\mathbf{k})^2 + 2bs'\sqrt{(v_\mathrm{F}\hbar k_z)^2 + m^2}}. \tag{2.6.5}$$

The parameters m and b thereby introduce a mass gap and control the spacing between the bands, respectively. $s = \pm$ accounts for conduction and valence bands while $s' = \pm$ yields the lower and higher branches of the conduction and valence bands (see Fig 2.6.4). For $b = m = 0$ a single fourfold degenerate cone is obtained, whereas for finite m a mass gap is created leading to twofold degenerate massive Dirac particles. The interesting range of parameters for this work are however the cases, where $b > m$ which yields the Weyl-type bandstructures. Resulting bands for various values of m and b are displayed in Fig. 2.6.4 (a) in arbitrary units along k_z. In case of $m = 0$ but finite b, Eq. 2.6.5 yields two identical cones separated in k symmetrically around $k_z = 0$. Increasing m leads to a gapping of the band crossings at $k_z = 0$ and finite E, while the crossings at $E = 0$ persist. Further increase of m urges the crossings of the $s' = -$ bands to shift towards $k_z = 0$ and for $m = b$ the bands only have a single touching point left, similar to the situation displayed in Fig. 2.6.1 (c). Further increasing m leads to a fully gapped bandstructure.

To highlight the key features of the optical conductivity arising for a bandstructure as described by Eq. 2.6.5 the interband optical conductivity $\sigma_{1,\mathrm{IB}}(\omega)$ is computed according to Eqns. A.0.4 and A.0.5 presented in Appendix A of this work and in

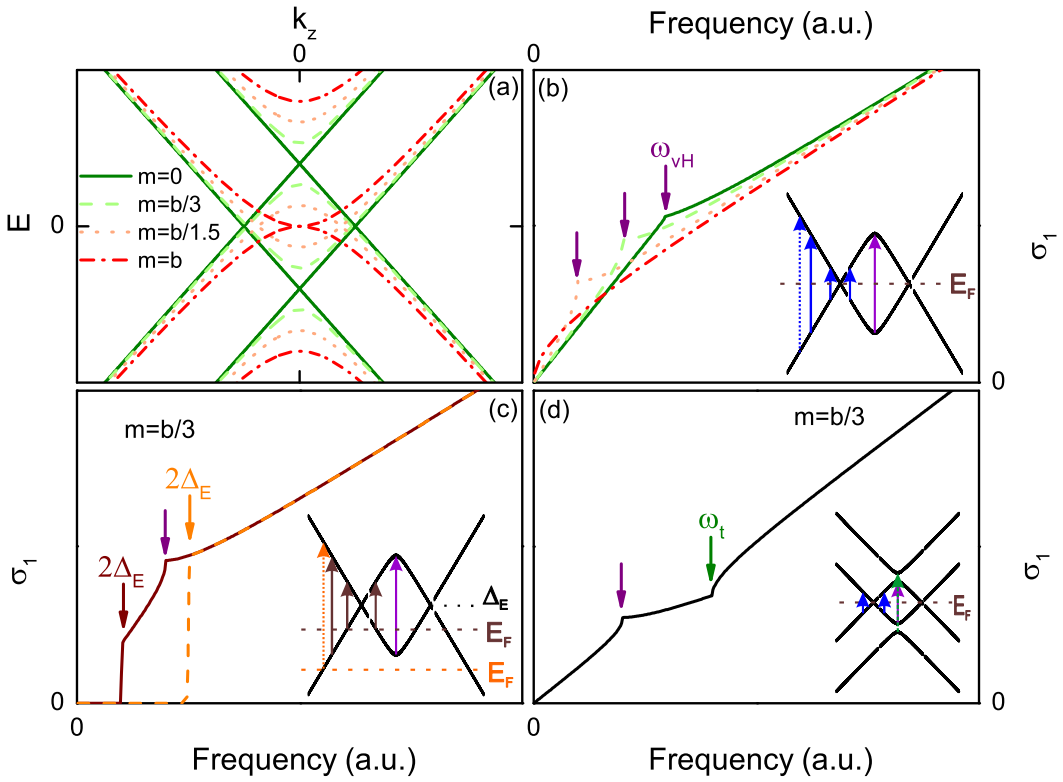

Figure 2.6.4: Frame (a) displays the bandstructure of a Weyl semimetal with four bands according to Eq. 2.6.5 for various values of m and b. The interband optical conductivity for the same m and b values and the Fermi energy at the nodes $\Delta_E = 0$ (b), and for two values of finite chemical potential $\Delta_E \neq 0$ (c). Only the two inner bands that exhibit a crossing ($s' = -$ in Eq. 2.6.5) are taken into account in frames (b) and (c). The interband conductivity for the full model with all four bands and $\Delta_E = 0$ is depicted in panel (d). The inserts display schematic bandstructures and transitions. The transitions at the van Hove singularities are marked with violet arrows, the onset of the transitions between the outer trivial bands with green arrows.

Ref. [74]. Note, that all pre-factors were set to 1, therefore the resulting spectra are in arbitrary units. The temperature T was kept constant close to zero. Increasing T simply leads to a smearing out of the features described in the following[9].
First, the 'outer bands' $s' = +$ are omitted, and only the $s' = -$ bands are taken into account, because those are the relevant bands exhibiting the Weyl nodes. Fig. 2.6.4 (b) displays the $\sigma_{1,\mathrm{IB}}(\omega)$ spectra for the same values of m/b as in panel (a) and the chemical potential at the nodes (or $\Delta_E = 0$). For $m < b$, the spectra consist of two

[9]Only the qualitative discussion is of interest here. The modeling of spectra in the course of the thesis will, however, be performed with the full quantitative expressions in proper units.

quasi linear regions. The part at lower energies, starting at the origin, corresponds to the transitions marked with blue solid arrows in the schematic bandstructure depicted as insert in the same panel. The frequency ω_{vH}, where the kink in the spectra occurs, corresponds to the apex of the bands, marked by the violet arrow (in all panels). Since the bands are flat at this point, a van Hove singularity arises in the density of states. For frequencies larger than ω_{vH}, the conductivity increases still linearly, however, much slower with a slope reduced by a factor of roughly 3.5 [74], and hence, does not extrapolate to zero. This frequency range corresponds to the transitions marked with a dashed blue arrow in the inset of Fig. 2.6.4 (b). For $b = m$ at the phase border between Weyl semimetal and gapped semimetal, $\sigma_{1,\mathrm{IB}}(\omega)$ sets in at $\omega = 0$ proportional to $\sqrt{\omega}$ in agreement with Fig. 2.6.1 (c), turns then, however, linear.

For finite chemical potential, the spectra exhibit a jump at $2\Delta_E$, in the same manner as in the single Dirac cone model discussed above in Sec. 2.6.1, as depicted for two values of Δ_E in Fig. 2.6.4 (c). Dependent on the position of the chemical potential, $2\Delta_E < \hbar\omega_{\mathrm{vH}}$ or $2\Delta_E > \hbar\omega_{\mathrm{vH}}$, the van Hove kink in the spectra is visible or not. Correspondingly those two cases are depicted in brown and orange, respectively, in panel (c).

Fig. 2.6.4 (d) eventually displays the interband optical conductivity $\sigma_{1,\mathrm{IB}}(\omega)$ for the full model, with all four bands, $0 < m < b$ and $\Delta_E = 0$. In addition to the van Hove peak at ω_{vH}, an onset of the transitions between the two trivial outer bands occurs at ω_t, marked with a green arrow.

2.7 Influence of magnetic field

Applying magnetic fields to (nonmagnetic) metals or semiconductors is known to lead to various effects that are reflected in the measurable physical quantities. The bending of the electron trajectories by the Lorentz force $F_{\mathrm{L}} = e\mathbf{v} \times \mathbf{B}$ can lead to a considerable magneto-resistance in very pure samples [81]. The formation of Landau levels leads to quantum-oscillation phenomena in physical quantities, as, for instance, magnetization or resistivity, i. e. to the de Haas-van Alphen and Shubnikov-de Haas effects, respectively [82].

The influence of the magnetic field on the electronic properties of a solid is also reflected in the optical spectra, and can be split into two major effects that are relevant in the course of this thesis (following the notation in Ref. [83]). Both are attributed to the splitting of the bands into sub-bands due to Landau quantization.

The inter Landau level transitions within the conduction band are responsible for the magneto plasma effect, while the transitions between magnetic sublevels of two different bands are referred to as interband effects in the following. Brief overviews are given, how those effects contribute to the optical response of Weyl semimetals, which were investigated with magneto-optical methods in this work.

2.7.1 Magneto plasma effects

In real materials possessing a free carrier density N, e.g. in doped semiconductors, in metals or in semimetals, the zero crossing of $\varepsilon_1(\omega)$ shown in Fig. 2.3.1 for the Drude model, can not be straightforwardly identified with the Drude plasma frequency $\omega_p^2 = 4\pi N e^2/m^*$, if interband transitions appear for frequencies below ω_p (and they definetly do). The zero crossing of $\varepsilon_1(\omega)$ in such cases occurs at the screened plasma frequency [51, 83]

$$\omega_{p,scr}^2 = \frac{4\pi N e^2}{m^* \varepsilon_\infty}, \tag{2.7.1}$$

which is renormalized by the high-frequency dielectric contributions ε_∞. For small scattering rates $\gamma \ll \omega_{p,scr}$, the reflectivity $R(\omega)$ is close to unity and exhibits the plasma edge at $\omega_{p,scr}$, where it sharply drops. In the following the optical response and its alteration by magnetic fields for frequencies at and below $\omega_{p,scr}$ will be discussed. Since the magneto-optical investigations in this work were only performed in Voigt geometry ($\vec{k} \perp \vec{H}$), only this case will be considered. Furthermore, we assume $\mu = 1$ as above, and therefore $H = B$.

In the absence of scattering ($\gamma = 0$), the free-carrier absorption in the Drude model is zero at finite frequencies, and the dielectric constant is real. For simplicity only this lossless case will be treated, which is valid for $\omega \gg \gamma$. In presence of a magnetic field B in Voigt geometry, two cases have to be distinguished. In case of the electric field of the light parallel to the external magnetic field $E \parallel B_0$ the motion of the electrons is unaltered. For $E \perp B_0$, however electrons perform a circular motion in a classical picture. The dielectric constant for those two cases read [84, 85],

$$\varepsilon_{1,\parallel}(\omega) = \varepsilon_\infty \left(1 - \frac{\omega_{p,scr}^2}{\omega^2}\right) \qquad (E \parallel B_0) \tag{2.7.2a}$$

$$\varepsilon_{1,\perp}(\omega) = \varepsilon_\infty \left(1 - \frac{\omega_{p,scr}^2(\omega_{p,scr}^2 - \omega^2)}{\omega^2(\omega_{p,scr}^2 - \omega^2 + \omega_c^2)}\right) \qquad (E \perp B_0) \tag{2.7.2b}$$

with the cyclotron frequency $\omega_c = eB/m^*$. The reflectivity $R(\omega)$, obtained from Eqns. 2.7.2 with Eqns. 2.1.5 and 2.1.7 with $k = 0$ since there are no absorptions, is displayed in Fig. 2.7.1 for $\omega_c = 0.5\omega_p$. The solid black $E \parallel B$ curve equals the case where $B = 0$ (see also Fig. 2.3.1 (c)). For $E \perp B$, a resonance appears at $\omega = \sqrt{\omega_p^2 + \omega_c^2}$ in Eq. 2.7.2b, manifested by the divergence of the dielectric function. In the reflectivity, this leads to the sharp increase to unity $R(\omega) = 1$ from lower to higher frequencies in the dashed red curve in Fig. 2.7.1. In the blue dotted curve, corresponding to an unpolarized measurement, all features are visible, however not as pronounced as in the $E \perp B$ case.

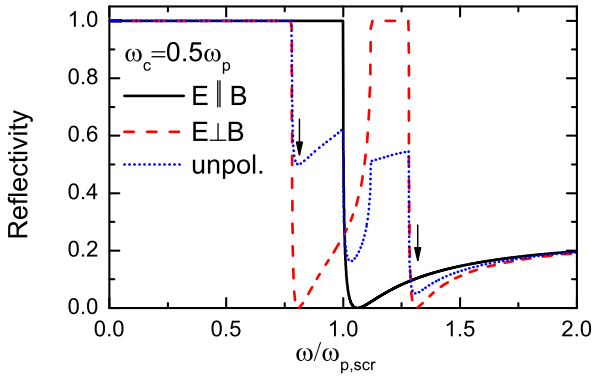

Figure 2.7.1: Splitting of the screened plasma frequency $\omega_{p,scr}$ in presence of a magnetic field B according to Eq. 2.7.2b (red dashed line) into two branches seperated by ω_c. The case of $B = 0$ corresponds to the case when $E \parallel B$ in Voigt geometry (black solid line). All features are also visible with unpolarized light (blue dotted line).

The important thing to note here are the two minima, marked by the black arrows in Fig. 2.7.1. They are the hallmarks of a plasma frequency splitting, since both appear at zero crossings of the $\varepsilon_{1,\perp}(\omega)$ function. These minima give indirect access to the effective mass of the carriers, since the splitting equals the cyclotron frequency ω_c in first order approximation [84, 85].

2.7.2 Interband effects

Now the alteration of the interband optical conductivity $\sigma_{1,\mathrm{IB}}(\omega)$ due to the formation of Landau levels will be discussed. The transitions between these magnetic sub-levels generally can be observed in the optical constants and give access to subtle details of the bandstructure [83].

For parabolic bands in a magnetic field, the Landau levels are equally spaced in energy. For massless particles, however, this is not the case. The energy eigenvalues of the Weyl Hamiltonian in presence of a magnetic field $\mathbf{B} = B\hat{z}$ are found to be of

the form [86–88]

$$\pm E_n = \pm\sqrt{\frac{2n}{l_B^2} + k_z^2} \qquad (n \geq 1) \tag{2.7.3a}$$

$$E_0 = -k_z, \tag{2.7.3b}$$

where $l_B^2 = c/eB$ is the magnetic length. Eqns. 2.7.3 describe the magnetic sublevel structure of a single Weyl node, dispersing along k_z. The $n = 0$ level is chiral and independent of magnetic field B. For the Weyl cone of opposite chirality the sign in Eq. 2.7.3b needs to be changed. In Fig. 2.7.2 (a) the Landau level structure is depicted. It is clear, that the transitions between these levels will be reflected in the optical response. To obtain an expression for the optical conductivity the Kubo formula needs to be fed with the Landau level basis wave functions and energy levels. This calculation is nicely performed in Ref. [86].

The real part of the interband optical conductivity $\sigma_{1,\mathrm{IB}}(\omega)$ in presence of a magnetic field is consequently computed utilizing the equation from Ref. [86], which is recited in appendix B of this work. Fig. 2.7.2 (b) displays the result for various positions of the chemical potential Δ_E. For zero chemical potential Δ_E, displayed as black solid lines in panel (a) and (b), the interband optical conductivity hosts a series of asymmetric peaks that ride on the linear background discussed in Sec. 2.6. The first peak of the series arises from the transition of the chiral $n = 0$ Landau level L_0 to the $n = 1$ level L_1 or L_{-1} to L_0, respectively, as indicated in Fig. 2.7.2 (b). The second peak comes from the $\mathrm{L}_{-1} \rightarrow \mathrm{L}_2$ and $\mathrm{L}_{-2} \rightarrow \mathrm{L}_1$ transitions, and so on. In contrast to conventional parabolic band semiconductors, where the selection rules differ for intraband and interband transitions, for massless quasiparticles one single selection rule is sufficient and transitions are allowed for Landau levels where $\Delta n = |n| - |n'| = \pm 1$ is fulfilled [89, 90]. The peaks occur at the frequencies $\omega l_B = \sqrt{2n+1} + \sqrt{2n}$, and are therefore proportional to $\sqrt{B}$, with the definition of l_B above [10]. This behavior is reminiscent of the predictions for graphene, where the peaks appear on a constant interband conductivity background [89, 91]. The $\sqrt{B}$-development of signatures in optical spectra that could be attributed to Landau level transitions, as well as the aforementioned characteristic frequency dependence on the Landau level index n were recently reported in various materials where massless quasiparticles are expected (i.e. graphene, topological insulators, 3D Dirac or

[10] For real units, the conversion $l_B^{-1} = 36.3 v_\mathrm{F} \sqrt{B} \times 10^{-9}\,\mathrm{eV}$ is given in Ref. [86].

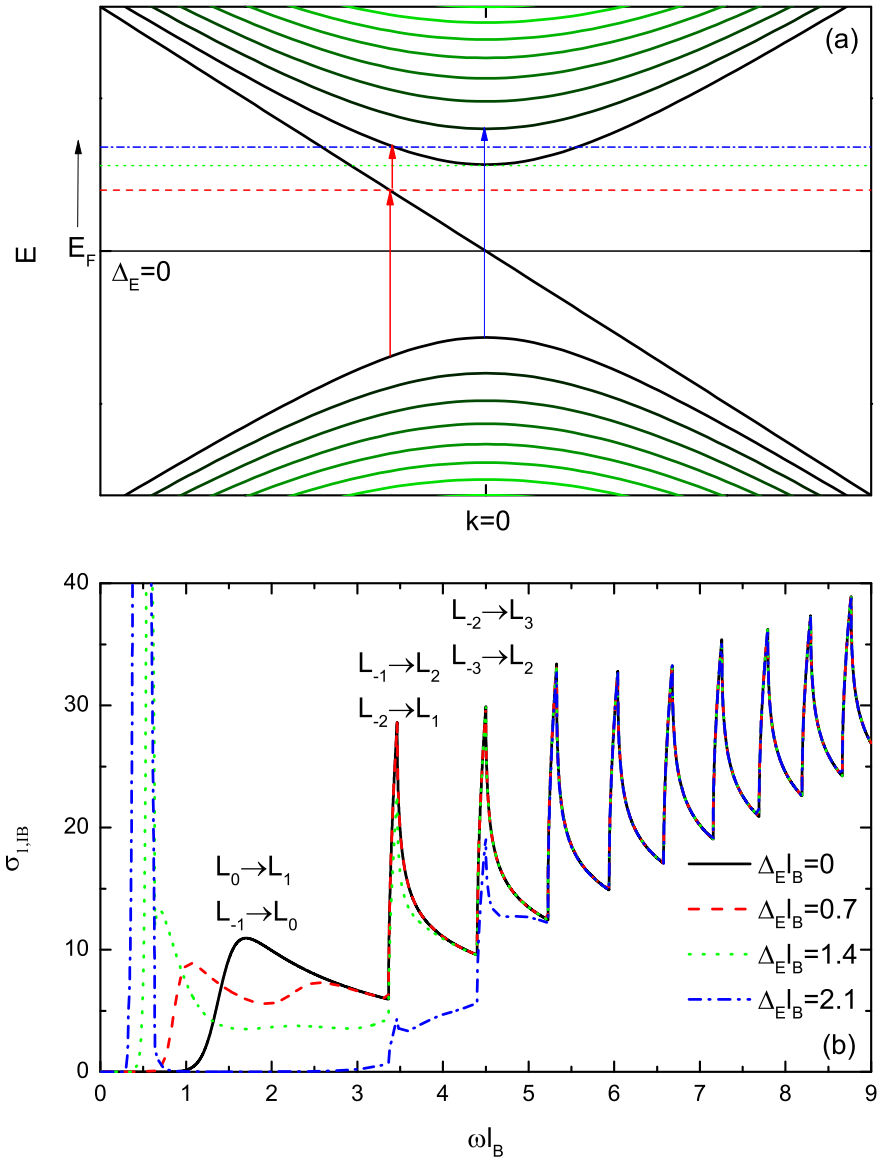

Figure 2.7.2: The Landau levels of a Weyl cone are depicted in panel (a). Horizontal lines schematically indicate various choices of the chemical potential utilized for the computation of $\sigma_{1,IB}(\omega)$ depicted in panel (b) in the same color code. The red vertical arrows in panel (a) emphasize the splitting of the $L_0 \to L_1$ and $L_{-1} \to L_0$ transitions for finite chemical potential Δ_E in the quantum limit. The transitions where L_0 is not involved always appear at $k = 0$ indicated with the blue arrow. The Landau level transitions are allowed for $\Delta n = \pm 1$. The spectra in panel (b) are computed utilizing Eq. B.0.2.

Kane systems) [69, 90, 92–96].
For finite values of the chemical potential, additional peaks appear in the interband optical conductivity $\sigma_{1,\mathrm{IB}}(\omega)$. These additional peaks exist for all values of the chemical potential and always involve the zeroth Landau level. For a chemical potential Δ_E the additional shoulders appear at $\omega l_B = \Delta_\mathrm{E} l_B + \sqrt{(\Delta_\mathrm{E} l_B)^2 \pm 2}$ [86]. Such case is depicted with the red dashed line in Fig. 2.7.2 (a) and (b), where the lowest Landau transition gets split into two. When the Fermi energy E_F approaches the $n = 1$ Landau level and starts to cut it, the lower energy Landau peaks start to disappear, and the spectral weight is transferred to a peak at low frequencies, while at higher frequencies the peak structure remains the same (green dotted and blue dashed-dotted lines in Fig. 2.7.2). This low energy peak comes from the transition between magnetic sub-levels within one band.

The chiral anomaly (or Adler-Bell-Jackiw anomaly), which was predicted and reported in Weyl semimetals [6, 24, 31, 97], is also supposed to leave a distinctive signature in the optical response with applied magnetic and electric fields parallel to each other [78]. During this work various attempts were made to observe the predicted hallmarks in the optical spectra of TaAs and NbP, which were, however, to date not successful. Therefore further discussions of the chiral anomaly in optical experiments will be omitted.

2.8 Optical models for superconductors

In FeSe, which is investigated in this work, a superconducting state is found at low temperatures (see Chap. 7). Therefore, the superconducting state and its optical properties shall be discussed in a nutshell in this section.

There are two characteristic phenomena that identify the superconducting state. The first hallmark to mention certainly is the vanishing of the electrical resistance below the critical temperature T_c, that was first observed in Hg by Heike Kamerleingh Onnes in 1911 [98]. The second peculiarity is the complete expulsion of magnetic fields and therefore the perfect diamagnetism of the superconducting state discovered by, and subsequently named after Meissner and Ochsenfeld in 1933 [99].
The microscopic understanding of superconductivity was reached by the development of the BCS theory in 1957 (after J. Bardeen, L.N. Cooper and J. R. Schrieffer) [100]. The key point of the BCS theory is the pairing between two electrons (fermions) to

Cooper pairs (bosons), that in turn condense into one single quantum ground state (Bose condensate). The pairing of the electrons is possible by an effective attractive interaction among them, mediated by phonons. Normally the pairing electrons possess opposing spins and momenta, and their condensation in the coherent ground state leads to the opening of a gap in the density of states (see Fig. 2.8.2).
The BCS theory is strikingly successful in predicting the behavior of a class of materials, namely the conventional superconductors. Many superconductors that are of current interest, as the cuprates discovered by J. Berdnorz and K. A. Müller [101], the superconducting heavy-fermion materials discovered by F. Steglich *et al.* [102], or the iron-based superconductors recently discovered by Kamihara *et al.* [103], are however out of the ordinary. They can be not accurately described by the BCS-theory, and, hence, are referred to as unconventional superconductors. In these, the pairing is likely not phonon mediated and the order parameter described below does not have to be isotropic.
Even though the expressions derived from the BCS theory for the optical conductivity are likely not the right tool to treat the iron based superconductors exactly [104], for this work they are sufficient to obtain the approximate energy scales [105].
In the BCS-theory the superconducting gap acts as a complex order parameter: $\Delta_{\mathrm{SC}}e^{\mathrm{i}\phi}$, where Δ_{SC} is the amplitude and ϕ is a phase. The magnitude of the superconducting gap Δ_{SC} at $T = 0$ is of the order of $k_B T_c$, where k_B is the Boltzmann constant [106]:

$$2\Delta_{\mathrm{SC}}(T = 0) \approx 3.53 k_B T_c. \tag{2.8.1}$$

For finite temperatures, the energy gap $\Delta_{\mathrm{SC}}(T)$ closes monotonically. For $T \ll T_c$ the changes of $\Delta_{\mathrm{SC}}(T)$ are small, in the vicinity of the critical temperature T_c, however the changes are rapid and the closing of the gap Δ_{SC} can be approximated by the expression [106]:

$$\frac{\Delta_{\mathrm{SC}}(T)}{\Delta_{\mathrm{SC}}(0)} \approx 1.74\sqrt{1 - \frac{T}{T_c}}, \tag{2.8.2}$$

which is the common behavior of mean-field order parameters. Eqns. 2.8.1 and 2.8.2 can also be utilized to describe the mean-field behavior of order parameters of other broken-symmetry ground states of metals [51].
A basic description of the electrodynamic properties can be derived from the approach of the brothers F. and H. London [107]. In this classical approximation of the superconducting state, the Drude lifetime, appearing in Eqns. 2.3.3, diverges

($\tau \to \infty$), however, any energy gap and quantum mechanical considerations are neglected and $T = 0$ is assumed. This yields:

$$\sigma_1(\omega) = \frac{\pi}{2}\frac{N_s e^2}{m}\delta(\omega = 0) = \frac{c^2}{8\lambda_{\mathrm{L}}^2}\delta(\omega = 0) \tag{2.8.3a}$$

$$\sigma_2(\omega) = \frac{N_s e^2}{m\omega} = \frac{c^2}{4\pi\lambda_{\mathrm{L}}^2\omega} \tag{2.8.3b}$$

Here, N_s now denotes the density of electrons in the superconducting Bose condensate, and

$$\lambda_{\mathrm{L}} = \sqrt{\frac{mc^2}{4\pi N_s e^2}} = \frac{c}{\omega_{p,s}} \tag{2.8.4}$$

is the London penetration depth, that can be related to the inverse of the 'superconducting plasma frequency' $\omega_{p,s}$ and to the square of the superfluid density, $\rho_s = \omega_{p,s}^2$. In this work, the quantity that is derived from optical experiments $\lambda(\omega) = \sqrt{\frac{c^2}{4\pi\sigma_2(\omega)\omega}}$ will be called penetration depth and only the $T = 0, \omega = 0$ value will be referred to as London penetration depth.

Eqns. 2.8.3 already contain valuable information on the optical response of the condensate. While the real part $\sigma_1(\omega)$ is zero at finite frequencies and infinite at $\omega = 0$, as a consequence of the vanishing DC resistivity, the $1/\omega$ divergence of the imaginary part $\sigma_2(\omega)$ directly reflects the response of the superfluid [106].

For a more accurate treatment of the optical properties of a superconductor, the Mattis-Bardeen formalism is necessary [51, 106, 108]. In their theory, Mattis and Bardeen not only included the energy gap Δ_{SC}, but also accounted for the coherence effects in the transitions between different states. These effects arise, because the transition probabilities in case of the superconducting ground state are modified compared to the probabilities in metals or semiconductors, as the transition possibilities for various combinations of electron pairs with opposing momenta and spins interfere.

The bulky expressions of the Mattis-Bardeen formalism can be parametrized to a relatively simple form [109], which also allows to take into account the scattering rate γ. Fig. 2.8.1 displays the optical constants $R(\omega)$, $\sigma_1(\omega)$ and $\varepsilon_1(\omega)$ of a superconductor for various temperatures. The scattering rate is set to be $\gamma = 8\Delta_{\mathrm{SC}}(0)$ (dirty limit). For $T = 0$, the reflectivity in panel (a) of Fig. 2.8.1 exhibits a sharp upturn and equals unity for frequencies $\omega \leq \Delta_{\mathrm{SC}}(0)/\hbar$. The absorption at $T = 0$

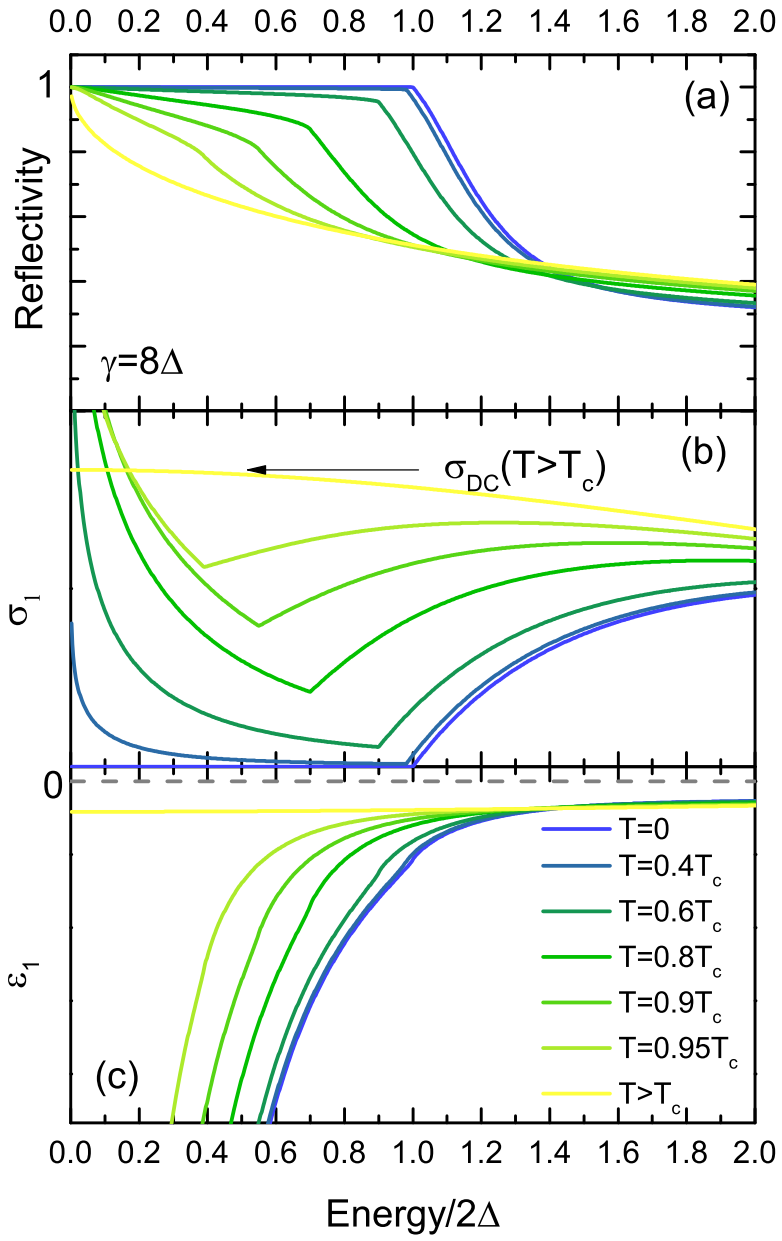

Figure 2.8.1: The development of the optical properties of the superconducting state for various temperatures between $T = 0$ and $T = T_c$ in the reflectivity $R(\omega)$ (a), the real part of the optical conductivity $\sigma_1(\omega)$ (b), and the real dielectric function $\varepsilon_1(\omega)$ (c). The scattering rate is set to $\gamma = 8\Delta/\hbar$ (T-independent). The gap Δ_{SC} at $T = 0$ or finite temperatures below T_c can be identified as the kink in the minimum of $\sigma_1(\omega)$ or in the reflectivity also as a kink subsequent to a steep increase towards unity as $\omega \to 0$. In $\varepsilon_1(\omega)$ the gap feature is weak, however, the $-1/\omega^2$ divergence enables access to the penetration depth and superfluid density via Eqns. 2.1.6 and 2.8.3b.

is zero until the photon energy exceeds $\hbar\omega \geq 2\Delta_{\mathrm{SC}}(0)$ and Cooper pairs can be broken, meaning $\sigma_1(\omega)$ is zero and starts to rise at $\omega = \Delta_{\mathrm{SC}}/\hbar$ as depicted in panel (b). In a single particle picture, this can be illustrated as in the lowest panel in Fig. 2.8.2, where the quasiparticles need to be excited across the full gap $2\Delta_{\mathrm{SC}}(0)$. The desity of states (DOS) is peaked at the gap edges for temperatures $T \leq T_c$ in this picture. Note, that he response of the Cooper pairs itself is a Dirac δ peak at $\omega = 0$ in $\sigma_1(\omega)$ in panel (b) of Fig. 2.8.1 and the Cooper pairs can not be illustrated in Fig. 2.8.2. The gap signature in $\varepsilon_1(\omega)$ is only a shallow kink, whereas the $-1/\omega^2$ divergence, expected from Eq. 2.8.3b, dominates the entire $\varepsilon_1(\omega)$ at these frequencies.

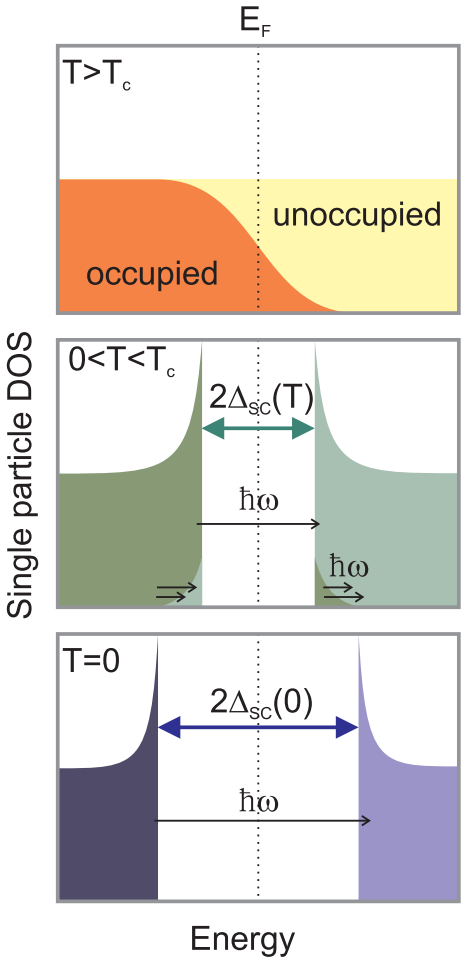

Figure 2.8.2: Schematic illustration of the superconducting state in a single particle picture. For $T > T_c$ the states are occupied up to the Fermi energy E_F and a few carriers are thermally excited according to the Fermi-Dirac-distribution function (upper panel). For finite temperatures below T_c a gap develops around E_F and the single particle density of states is peaked at the gap edges. The possible transitions are either across the gap $2\Delta_{SC}(T)$ or within the upper and lower branches of the single particle DOS, where thermal activation of the states makes optical transitions with arbitrary small energies possible (middle panel). At $T = 0$ the gap $2\Delta_{SC}(0)$ is fully opened, the single particle DOS diverges at the gap edges, and the only remaining possible transitions are across the gap (lower panel).

For finite temperatures $0 < T < T_c$, also the states above the the gap $\Delta_{\mathrm{SC}}(T)$ are occupied by thermally activated quasiparticles, as illustrated in the middle panel of Fig. 2.8.2. Furthermore, the gap closes monotonically towards T_c, as stated above.

The response of the optical constants can be separated into three parts, that are best described in the optical conductivity $\sigma_1(\omega)$. The first contribution arises from the Cooper pairs, that still give an infinite response at $\omega = 0$. The second contribution appears at very low frequencies and stems from the thermal quasiparticles that can be excited by arbitrary small photon energies. This gives rise to the narrow peak at low energies in $\sigma_1(\omega)$. The third contribution are the transitions across the gap $\Delta_{\mathrm{SC}}(T)$. The gap $\Delta_{\mathrm{SC}}(T)$ can now be identified as the minimum in $\sigma_1(\omega)$ spectra. In $R(\omega)$, the finite temperatures smear out the sharp jump to unity, while in $\varepsilon_1(\omega)$ the $-1/\omega^2$ response gets shifted to lower frequencies in the same manner as $2\Delta_{\mathrm{SC}}(T)$ is getting smaller.
For temperatures $T > T_c$, the response of a normal metal is restored in the optical constants in Fig. 2.8.1, and any gap is vanished in Fig. 2.8.2.

Note, that in the clean limit when the scattering rate is smaller than the gap $\gamma \ll 2\Delta_{\mathrm{SC}}$, the hallmarks of any superconducting gap can often not be resolved in the optical spectra [110–112].

In Fig. 2.8.1 (b) it appears, as if some spectral weight is lost in the superconducting state as compared to the normal state, challenging the f-sum rule in Eq. 2.2.2. This 'lost' spectral weight corresponds to the carriers, that have condensed into the ground state, and therefore do not contribute to the response at finite frequency anymore. This means, the spectral weight is transferred to the Dirac δ peak at $\omega = 0$ as schematically illustrated in Fig. 2.8.3.

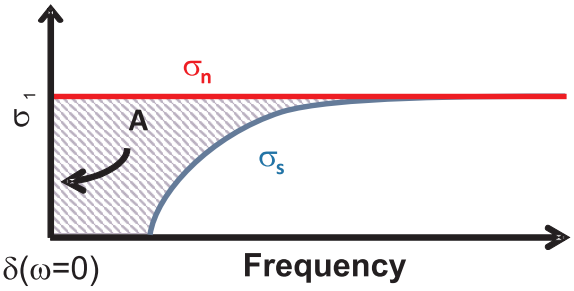

Figure 2.8.3: Schematic illustration of the FGT sum rule, that relates the area A between the superconducting spectrum σ_s and the normal conducting spectrum at T_c σ_n to the superfluid density ρ_s, which is responsible for the Dirac δ peak at $\omega = 0$.

This fact is utilized in the so called Farrel-Glover-Tinkham (FGT) sum rule that relates the area A between normal conducting spectrum $\sigma_{1,n}$ and the superconducting spectrum $\sigma_{1,s}$ to the superfluid density ρ_s and therefore to the penetration depth, since $\lambda = c/\sqrt{\rho_s}$ [51, 106]. In this sense, the FGT sum rule equals the f sum rule

for the particular case of a superconductor in the superconducting state, and can be expressed as:

$$8A = 8\int_{0+}^{\infty} [\sigma_{1,n} - \sigma_{1,s}]\, d\omega = \rho_s \tag{2.8.5}$$

3. Experimental Techniques

To obtain the frequency dependent optical response functions of solids, nowadays one can pick from a large variety of experimental approaches [51, 57]. The choice of the technique strongly depends on the energy scales where interesting effects are expected to be seen in the investigated material. In correlated electron materials, high temperature superconductors, and also in narrow gap semiconductors or semimetals the infrared frequency range ($\approx 300\,\mathrm{GHz} - 750\,\mathrm{THz}$ corresponding to photon energies of approximately $1\,\mathrm{meV} - 2\,\mathrm{eV}$) contains manifold information on lattice properties, carrier dynamics and on the condensate in case of superconductors [113–115]. In this range of photon energies there are three main types of spectrometers that are widely applied: Fourier transform spectrometers, grating spectrometers and ellipsometers. The latter two spectrometer types are in particular very powerful at higher infrared frequencies (IR), in the visible (VIS) and ultra-violet (UV) frequency ranges, but they have difficulties to reach the deeper infrared region. However, since exactly this range is highly desired for the investigations performed during this thesis, the applied technique is the Fourier transform infrared spectroscopy (FTIR), which has significant advantages at low frequencies.

At this point it is expedient to split up the relatively crude definition of 'infrared frequency range' according to the ranges that were measured with different settings and at different setups as presented in Table 3.0.1.

Name/Abbreviation	$\tilde{\nu}(\mathrm{cm}^{-1})$	$\nu(10^{12}\,\mathrm{Hz})$	$\lambda(\mu\mathrm{m})$
far-infrared/FIR	10–1000	0.3–30	1000–10
mid-infrared/MIR	700–8000	21–240	14–1.2
near-infrared/NIR	2000–12000	60–360	5–0.8
visible/VIS	9000–25000	270–750	1.1–0.4

Table 3.0.1: Definitions of the frequency ranges from far-infrared to visible

In this section the experimental technique as well as the setups will be discussed. In

Sec. 3.1 a brief introduction into the main principles of FTIR-spectroscopy will be given. Secs. 3.2 and 3.3 introduce the experimental techniques for measurements in the far-infrared (FIR) and at higher frequencies (MIR, NIR, VIS), respectively. The main focus of this chapter will be the magneto-optical setup (Sec. 3.4), which was designed, assembled and characterized in the framework of this thesis. Hence, for this setup a detailed discussion of the design and a complete characterization concerning stability and performance will be presented. For the other setups references to the theses, where correspondent characterizations are disclosed, will be given. In Sec. 3.5 further techniques applied in this work will be addressed briefly.

3.1 Fourier transform infrared spectroscopy

There is a large number of dedicated literature presenting detailed concepts for spectroscopy at infrared frequencies (e.g. Refs. [116, 117]). Furthermore, brief introductions to various spectroscopic principles can be found in every textbook on optical or solid state spectroscopy (e.g. Refs. [51, 57]). For this thesis, only the fundamental concept of FTIR spectroscopy will be reviewed in the following.
The centerpiece of a FTIR-spectrometer is a Michelson type interferometer, schematically depicted in Fig. 3.1.1. The light of a source S, carrying spectral information in the form $S(\nu)$ (meaning the power of the light at the frequency ν) gets separated into two beams by a beam splitter BMS. Both beams are reflected at a mirror, M1 and M2, respectively. After recombination of the two beams at the beam splitter the interfering light hits the detector D. The intensity of the interfering light is in general dependent on the difference of the optical path δ between the two beams. One of the mirrors, in case of Fig. 3.1.1 M2, is dynamically moving. The information entering the detector is consequently now $I(\delta)$, the intensity as a function of path difference δ, and is called interferogram. This process can be viewed as a mechanical Fourier transform and the spectral information can be regained by numerically back transforming the signal recorded by the detector.

Fig. 3.1.2 displays examples for the signals $I(\delta)$ recorded by the detector. In case of a monochromatic source as in panel (a), the interferogram is simply a $(\cos)^2$ function which transforms into a single Dirac-δ-peak at the frequency of the emitted light, seen in panel (d), upon applying fast Fourier transform (FFT). For a source emitting more frequencies, $I(\delta)$ is a pattern with a maximum at the position of equal optical paths in both arms of the interferometer $\delta = 0$, as demonstrated for three discrete

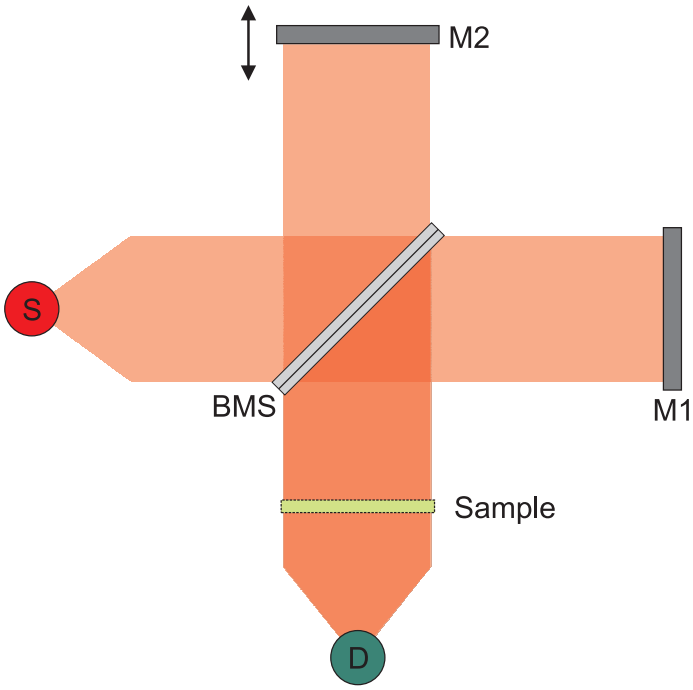

Figure 3.1.1: Schematic representation of a Michelson-type interferometer as employed in FTIR spectrometers. Light from the source S gets separated by a beam splitter BMS into two beams. One beam gets reflected at a fixed mirror M1, while the other hits the moving mirror M2. The light recombines at the BMS and hits the detector D after being reflected at, or passing through, the sample (or the reference, see text).

frequencies with a finite line width in Fig. 3.1.2 (b). Consequently the FFT yields the three Lorentz shaped peaks shown in panel (e). The finite line width of the frequencies is the cause for the exponentially decaying envelope of the interferogram pattern in Fig. 3.1.2 (b).

Finally Fig. 3.1.2 (c) illustrates the interferogram of a continuous black body radiator as it is used in FTIR spectrometers. The main maximum of $I(\delta)$ is located at $\delta = 0$ and decays rapidly to larger mirror displacements. It is important to note, that the interferogram is not a straight line for large δ but still exhibits a small oscillating pattern from the interfering light, which is not visible on the scale of Fig. 3.1.2 (c). This small deviations from a straight line, extending theoretically to an infinite optical path difference between the two interferometer arms, carries most of the spectral information. The regions for large mirror displacements in the interferogram get in particular important for measurements where a high spectral resolution $\Delta\nu$ is desired, since $\Delta\nu$ is inversely proportional to the maximal mirror displacement $\Delta\nu \propto 1/\delta_{\max}$. The corresponding spectrum after FFT, depicted in panel (f) of Fig. 3.1.2, is a typical spectrum recorded in the MIR with a Globar light source, a KBr beam splitter and a photovoltaic detector (see Sec. 3.3).

This power spectrum displayed in Fig. 3.1.2 (f) shows a pronounced frequency dependence which is set by the type of source, the beam splitter and other optical elements, like windows etc., utilized in the measurement setup, as well as the sensitivity of the

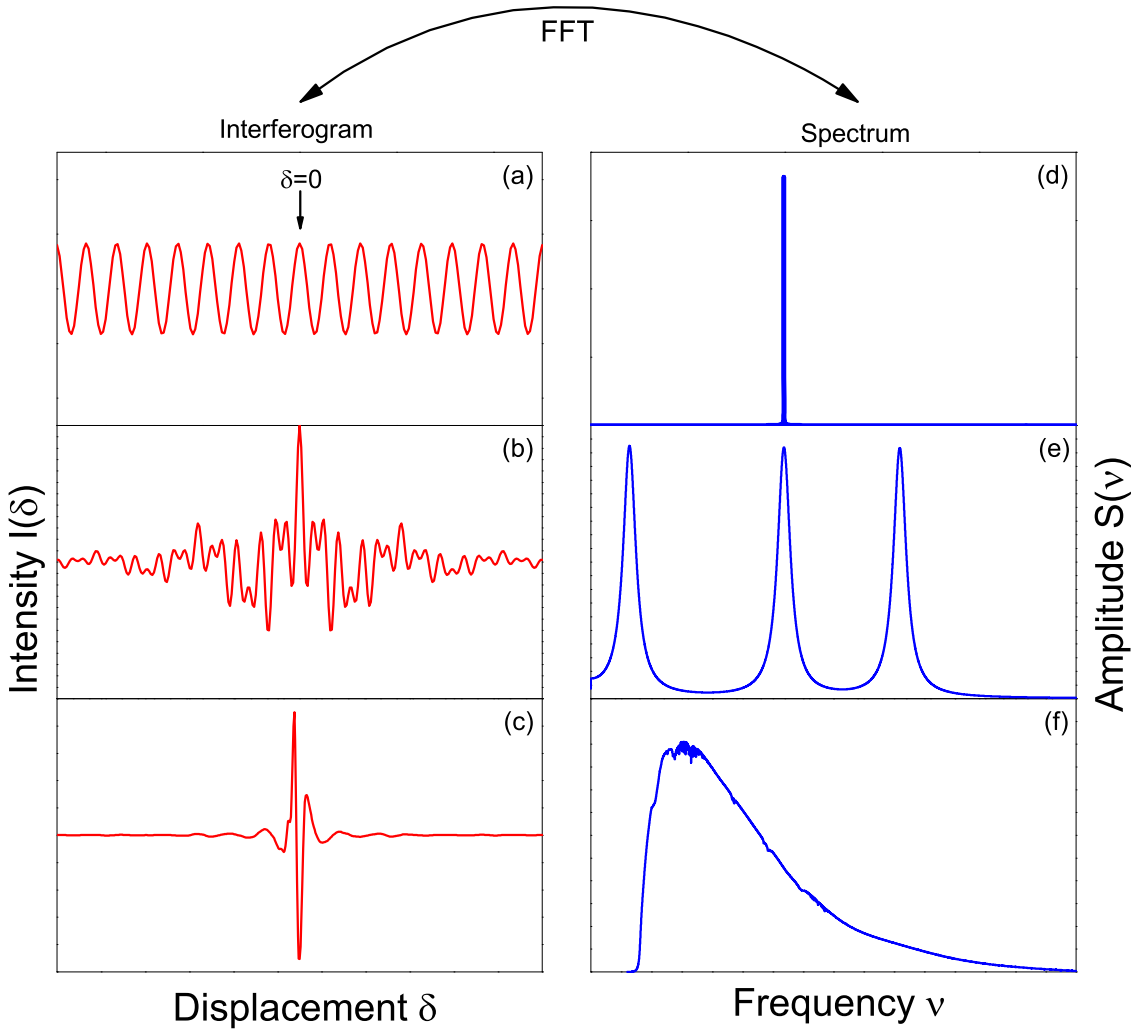

Figure 3.1.2: Interferograms $I(\delta)$ of a perfectly monochromatic source (a) and a source emitting three frequencies with finite line widths (b). The fast Fourier transform of the interferogram $I(\delta)$ yields the power spectra $S(\nu)$ of the two aforementioned hypothetical sources displayed in (d) and (f), respectively. Panel (c) depicts a real interferogram as recorded in the MIR with a globar source, a KBr beam splitter and a photovoltaic detector (see Sec. 3.3). The resulting power spectrum after FFT is plotted in panel (f). All axes are in arbitrary units.

detector in use. This circumstance makes it necessary to conduct reference measurements in order to obtain final transmittance or reflectance spectra of a sample. The standard procedure is as follows: First, a spectrum is recorded with a sample placed in the beam between interferometer and detector (as sketched in Fig. 3.1.1), where the signal entering the detector got either transmitted through, or reflected at, the sample. The resulting spectrum $S_{\text{sample}}(\nu)$ is obtained by FFT. Subsequently, the measurement is repeated without sample to record the reference $S_{\text{reference}}(\nu)$. In case of a transmission measurement this means, that the light only travels through free space, where it passed the sample before. For a reflection measurement, the light is reflected on a mirror that possesses a flat, frequency independent reflectivity close to unity in the frequency range of interest. The final frequency dependent transmittance $T(\nu)$ or reflectance $R(\nu)$ is then obtained by normalizing the sample spectrum to the reference spectrum $R(\nu), T(\nu) = \frac{S_{\text{sample}}(\nu)}{S_{\text{reference}}(\nu)}$.
To get $R(\nu)$ and $T(\nu)$ quantitatively correct in a real measurement, it is important to make sure, that the light collected by the detector is commensurate for both, the sample and the reference measurement runs. This is done with ease by the use of an aperture in transmission measurements. In this work, only reflectivity measurements were conducted. The methods that were applied to obtain the absolute reflectance spectra will be discussed in the two following sections.

3.2 Far-infrared technique

3.2.1 The spectrometer

All optical measurements in the FIR were performed with a Bruker IFS 113v spectrometer. Fig. 3.2.1 displays a schematic sketch of the spectrometer with the relevant beam path highlighted. During a measurement the whole system is pumped to a pressure of $p \approx 7\,\text{mbar}$ to avoid absorptions from air molecules. In the source chamber ① one of three light sources can be selected by a switchable mirror. Three sources are available: A glowing SiC bar (Globar), a mercury arc lamp (Hg-lamp), and a tungsten wire bulb. For FIR measurements only the former two are suitable. The light subsequently enters the Michelson interferometer, which is arranged in a peculiar geometry in this spectrometer. This so-called Genzel arrangement [118] holds some advantages against the conventional rectangular arrangement of the Michelson interferometer shown in Fig. 3.1.1. First of all, the light is focused on the beam splitter illustrated at ② in Fig. 3.2.1. This allows the use of small beam split-

ters arranged on a wheel, which enables changing the beam splitter *in situ* without venting the spectrometer. Several Mylar beam splitters, with thicknesses depending on the measured frequency range, were applied in the FIR measurements (see Tab. 3.2.1). The second peculiarity of the Genzel geometry is the fact, that, after passing the beam splitter, the two branches of the light get reflected on the same scanning element, which has mirrors on the front and back, illustrated at ③. Thus, while for one branch the optical path is shortened, for the other branch the path is elongated. Therefore, this geometry provides a twofold optical path difference for the same mirror displacement as compared to the conventional Michelson interferometer, and hence, a twofold higher resolution. The position of the scanner is determined from the zero crossings of the interference fringes of a He-Ne laser, that passes a small separate Michelson interferometer, which utilizes the same scanning mechanics (also illustrated in Fig. 3.2.1 at ③).

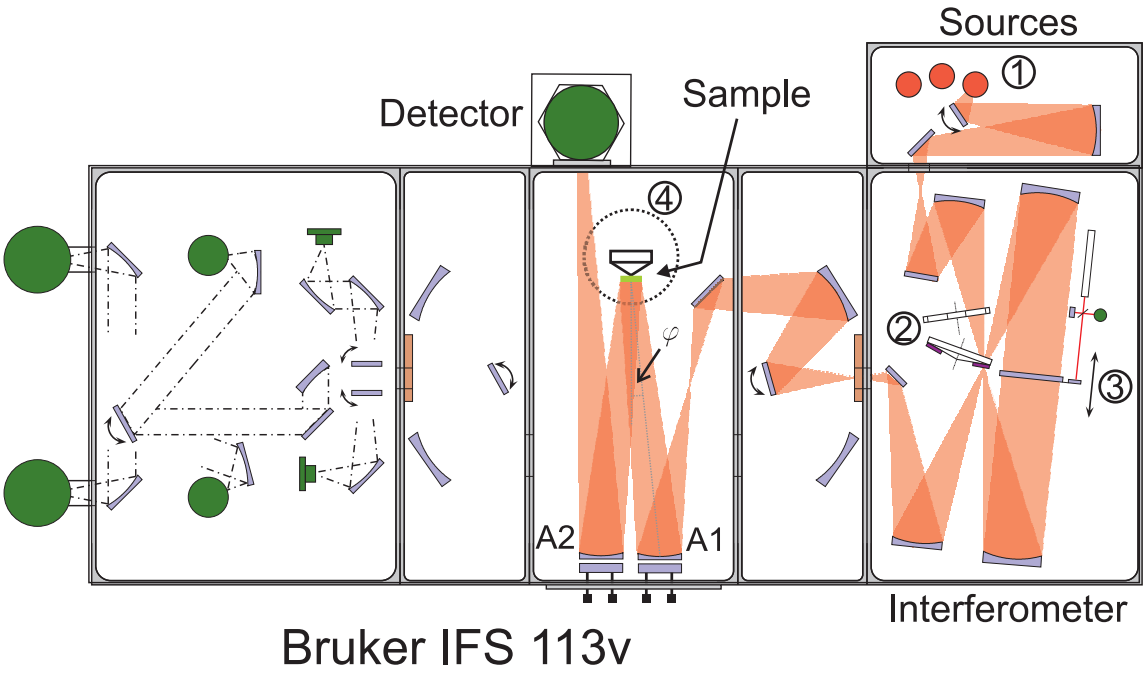

Figure 3.2.1: The Bruker IFS 113v spectrometer. The light from a source ① is focused via a couple of optical elements on the beam splitter ②. The two branches of the light get reflected on the front and back side of the same scanning mirror ③. This arrangement of a Michelson interferometer is called Genzel geometry (see text). The recombined light is then guided to, and focused on a sample, sitting in a cryostat ④. The incident angle is $\varphi \leq 8°$. *Adapted from [119].*

After recombination at the beam splitter, the light is guided to the sample compartment. Here, it is focused by the *in situ* adjustable mirror A1 on the sample,

which sits on a cone inside a continuous flow cryostat ④. Thereafter the light reflected from the sample is focused by the second *in situ* adjustable mirror A2 on the detector. In this work, various silicon based bolometers containing different low pass filters and operating at different temperatures were utilized as summarized in Tab. 3.2.1. It is important to note, that the angle of incidence of the light to the surface normal of the sample is $\varphi \leq 8°$. For such a small angle the reflectivity can be approximated as the response at normal incidence , and hence, the application of Kramers-Kronig relations (see Sec. 2.2) to the obtained reflectivity data is justified [51].

Name	$\tilde{\nu}$ (cm^{-1})	BMS	Detector	Source	Window
FIR	70–1000	Mylar/Ge 6 μm	Si bolometer @ 4.2 K	Globar	PP
F^2IR	20–300	Mylar 23 μm	Si bolometer @ 1.3 K	Hg-lamp	PP
F^3IR	10–60	Mylar 50 μm	Si bolometer @ 1.3 K	Hg-lamp	PP

Table 3.2.1: Frequency ranges and the corresponding experimental parameters in FIR measurements performed at the Bruker IFS 113v during this work. The Mylar/Ge 6 μm contains a thin Germanium coating. PP denotes polypropylene and Si is the chemical symbol for silicon.

3.2.2 The cryostat

The cryostat for zero field FIR measurements (④ in Fig. 3.2.1) was implemented in the lab as a supplementary project in this work. The basic component is a CryoVac Spectro A continuous flow cryostat operating at temperatures between 300 K and 3 K. The customized cryostat, housing, window flanges, sample holder etc. were all built by CryoVac.

The cryostat is attached to a linear translator, and can be moved vertically, driven by a stepping motor. The sample holder provides three spots to mount a sample or a mirror, which is important for the measurement procedure, as described in Sec. 3.2.3. There is an additional feed through in the housing for a gold evaporation unit, meaning simply two contacts, connected by a tungsten spiral, which is equipped with gold wire pieces (see Fig. 3.2.2). The ability to vertically move the whole cryostat allows each spot on the sample holder to be placed either in front of the window or the gold evaporation unit and, beyond that, the compensation of thermal shrinking-effects.

An extensive characterization of the cryostat and the whole measurement system,

performed by J. Merz and A. Baumgartner, was supervised during this work. Hence for detailed descriptions of the cryostat and the characterization the reader is referred to Refs. [120, 121] at this point.

3.2.3 The measurement

To accurately measure the absolute reflectance of small, mm-sized, opaque samples at low infrared frequencies one has to overcome the following obstacles:

- Low frequency means large wavelength[1], therefore, microscope based techniques as described in Sec. 3.3 are not an appropriate option, because of diffraction problems.
- Thermal radiation sources only provide a weak intensity at these frequencies, thus the collection of as much light reflected by the sample as possible is desired.
- To obtain the absolute reflectivity one also has to measure a reference as already stated in Sec. 3.1. The use of an aperture in front of the sample and a mirror would grant the comparability of sample and reference measurements, because the light had hit the same area each time. However, for such an approach the plane parallel adjustment of sample and mirror is crucial, which is, depending on the sample geometry, often rather difficult.
- Samples often have imperfect and structured surfaces leading to scattering and diffraction. As a result artifacts appear in the final spectra.

The *in situ* gold coating of the sample elegantly overcomes the aforementioned issues [122]. The measurement scheme is depicted in Fig. 3.2.2. The light spot of the incoming radiation IR is chosen larger than sample and reference mirror. The sample S as well as the mirror M in column ① are mounted on a cone. Accordingly, only the light hitting the sample or mirror is reflected back, while other portions get deflected. Advantageously, this setting maximizes the signal and minimizes diffraction. The measuring procedure is as follows: Sample S and mirror M both are measured at all desired temperatures as depicted in column ① and ② of Fig. 3.2.2. Subsequently, the sample is coated by a gold layer (column ③). This has to be done at room temperature by applying a large current to the tungsten helix, equipped with ringlets of gold wire, in order to evaporate the gold. After waiting a sufficient time to

[1] $\tilde{\nu} = 20\,\mathrm{cm}^{-1} \equiv \lambda = 0.5\,\mathrm{mm}$

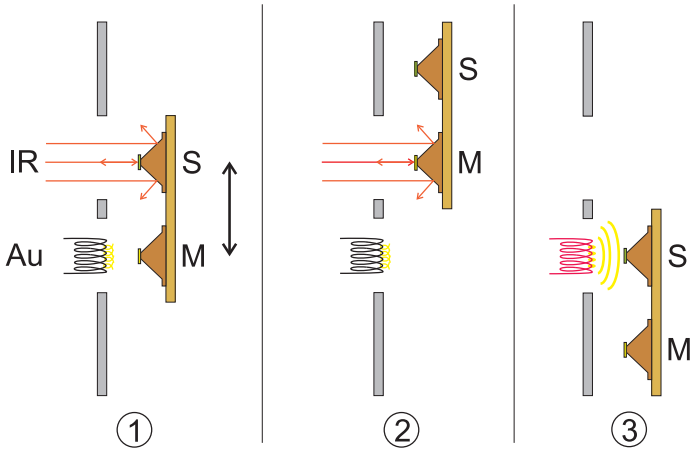

Figure 3.2.2: Illustration of the gold evaporation measurement principle. First the sample S and mirror M are measured at all desired temperatures (①,②). The mounting on the cone guarantees, that only IR light reflected on S and M is captured. Subsequently, the sample is gold-coated by the gold evaporation unit Au ③. Afterward the measurement of S and M is repeated at all temperatures.

get a thick enough gold layer[2], the measurement of the henceforth gold coated sample and the reference mirror is repeated at all previously measured temperatures. It has to be noted, that the vacuum inside the cryostat housing should be $p = 10^{-5}$ mbar of magnitude, in order to get a high quality gold coverage of the sample[3].

In principle, the sample is used as its own reference. Consequently there are no worries about size or angle mismatch between sample and reference, and most of the scattering effects from the surface structure should cancel out [122]. The final reflectivity spectra are calculated as:

$$R = \frac{\frac{S}{M}}{\frac{\widetilde{S}_{\mathrm{Au}}}{\widetilde{M}}} = \frac{S \cdot M \cdot \Delta}{S_{\mathrm{Au}} \cdot \Delta \cdot M} = \frac{S}{S_{\mathrm{Au}}} \tag{3.2.1}$$

In Eq. 3.2.1 S and M represent the sample and reference mirror spectra, respectively. $\widetilde{S}_{\mathrm{Au}}$ and $\widetilde{M}$ are the spectra recorded after gold evaporation on the gold coated sample and the mirror. The tilde denotes, that the whole experimental setting could have underwent a drift in signal, caused by fluctuations in source intensity or detector sensitivity, since between the two measurement runs before and after gold evapo-

[2]Thick enough means a multiple of the skin depth of gold, see Sec. 3.4.4.

[3]Further gold evaporation parameters used in this work are: current $I \approx 1.7$ A; evaporation time $t \approx 70$ s; common resistance of the gold evaporation unit measured on the leads at the power supply $R \approx 1.2\,\Omega$ ($R \approx 0.7\,\Omega$ measured directly at the leads of the gold evaporation unit). The reference mirrors, utilized in this work, were mostly gold coated glass substrates. However, also aluminum or silver mirrors are fine. Even polished stainless steel can be used, since the signal of reference mirror will cancel out when calculating the final reflectivity spectra with Eq. 3.2.1. See also Refs. [120, 121].

ration a long time possibly has passed. Those drifts are commonly reflected by a multiplicative factor Δ. Hence, this factor and the mirror spectra cancel out, and the absolute reflectivity of the sample is obtained.

3.3 Setup for mid-infrared, near-infrared and visible

3.3.1 The spectrometer

The optical measurements at higher infrared frequencies presented in this thesis, meaning MIR, NIR and VIS, were conducted at a Bruker HYPERION infrared microscope, attached to a Bruker VERTEX 80v FTIR spectrometer. Fig. 3.3.1 schematically illustrates the 80v spectrometer and highlights the relevant beam path. As in the 113v (Sec. 3.2.1) the centerpiece is the interferometer. Contrary to the 113v, the 80v hosts a Michelson interferometer with indeed tilted, but still conventional geometry. This allows only lower resolutions as in the 113v, though there are other advantages, e.g. the actively aligning optics and the highly precise scanner, enabling measurements up to UV frequencies.

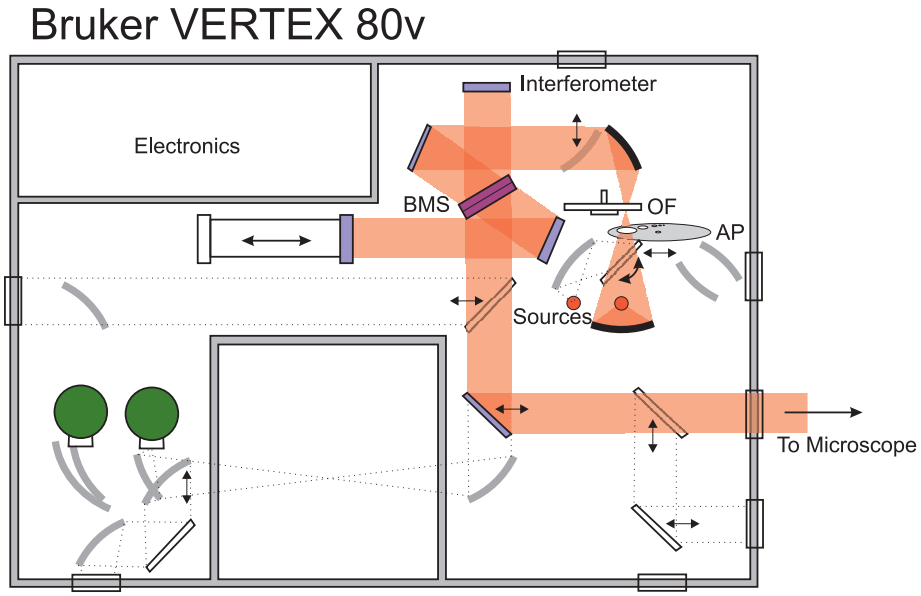

Figure 3.3.1: The Bruker Vertex 80v Adapted from [123].

As internal sources, a Globar as well as a tungsten source are installed. From the sources the radiation is guided through an aperture AP and an optional optical filter

wheel OF to the interferometer. The beam is then led through a window out of the spectrometer compartment. Here it enters the HYPERION IR microscope and gets strongly focused on the sample. The achievable spot size of the light on the sample ranges from 20 μm to 250 μm. It has to be noted, that unlike the spectrometer, the microscope is not under vacuum. To prevent atmospheric absorptions it is, however, continuously flushed with nitrogen gas. For different frequency ranges, particular experimental parameters were used, which are summarized in Tab. 3.3.1.

Name	$\tilde{\nu}$ (cm^{-1})	BMS	Detector	Source	Window
MIR	700–8000	KBr	MCT @ 77 K	Globar	KBr
NIR	2000–12000	CaF_2	InSb @ 77 K	Tungsten	KBr
VIS	9000–25000	CaF_2	Si-diode @ 300 K	Tungsten	KBr/Quartz

Table 3.3.1: Frequency ranges and the corresponding experimental parameters in measurements at MIR, NIR and VIS frequencies conducted at the 80v during this work. MCT denotes mercury cadmium telluride, which is the detector material. KBr, CaF_2, InSb and Si are the chemical prescriptions for potassium bromide, calcium fluoride, indium antimonide and silicon, respectively. For the detectors also the operating temperatures are stated.

3.3.2 The cryostat

For the measurements at the IR microscope the Konti Micro, a contiouos flow cryostat by CryoVac, was utilized. The accessible temperature range reaches from 300 K to 10 K at the sample position. The sample holders mounted to the cryostat were designed by S. Kaiser [124] and A. Baumgartner [121], respectively. The general idea of the sample holders is, to provide two stages that can separately be tilted, to be able to align each, the sample as well as the reference mirror independently (see Sec. 3.3.3). For a more detailed description and characterization of the setup combining FTIR spectrometer and IR microscope, the reader is referred to Refs. [121, 124].

3.3.3 The measurement

Compared to the measurement principle in the FIR as described in Sec. 3.2.3, the approach in the microscope is much less complicated. As already stated above the light is strongly focused. This is accomplished by a Schwarzschild objective in the HYPERION [125], schematically illustrated in Fig. 3.3.2. The spot size is chosen

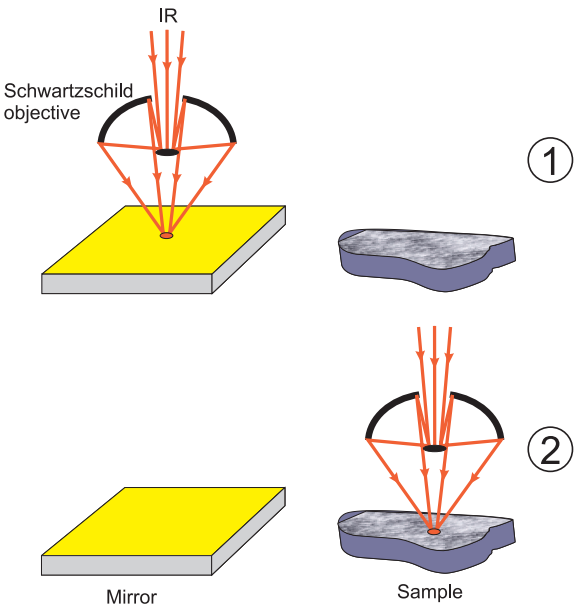

Figure 3.3.2: Schematic illustration of the measurement principle in MIR, NIR and VIS. The IR light is strongly focused by the Schwarzschild objective of the HYPERION on the sample or the mirror, respectively [125]. The spectra of mirror ① and sample ② are recorded with the same spot size. The ratio of sample to mirror spectrum straightforwardly yields the final reflectivity of the sample.

such, that it covers a flat area free from distinctly visible defects on the sample, and as large as possible. Aligning sample and mirror plane parallel is most crucial for reliable absolute values of reflectance spectra in the microscope, hence much care was taken regarding this issue in this work. The reflectivity is recorded with the same spot size on mirror (step ① in Fig. 3.3.2) and sample (step ② in Fig. 3.3.2). The final reflectivity of the sample is then straightforwardly calculated as,

$$R = \frac{S}{M} \tag{3.3.1}$$

where S denotes the sample spectrum and M the mirror spectrum.

3.4 Magneto-optical setup

One main issue of this work was to design, construct, assemble and characterize a setup for infrared optical measurements in high magnetic fields. The outcome is a combination of an Oxford Instruments 7 T Spectromag (SM4000) with the Bruker IFS 113v. In Fig. 3.4.1 two opposing bird's eye views of the magnet and the relevant attached parts are displayed. Some of the components used, e.g. the transmission optics, could be recycled from a previously existing magneto-optical setup, which was discharged because of a lack of accuracy, particularly in reflection measurements. The design, eventually realized, adapts the gold evaporation technique described in Sec. 3.2.3 for reflectivity measurements. This requires the use of an external cryostat that is in high vacuum. A similar approach for a magneto-optical FTIR setup, de-

scribed in Ref. [126], is realized in the lab of Dimitri Basov in San Diego[4], and was a valuable source of inspiration for the design presented here.

The aim was to construct the setup as versatile as possible and leave room for possible future modifications. In the following Secs. 3.4.1-3.4.3 the relevant details will be presented. In Sec. 3.4.4 the characterization regarding reproducibility and stability, as well as common values of various parameters are given. It should be pointed out, that all parts manufactured for the magneto-optical installation, are made from 'non-magnetic' metals, i.e. brass, aluminum, stainless steel or copper, to avoid possible complications from strong forces caused by stray fields of the superconducting magnet.

3.4.1 The magnet

The magnet installed in the magneto-optical setup is an Oxford Instruments Spectromag 4000-7T manufactured in the year 1993. It belongs to the family of superconducting split coil magnets. Compared to the other Spectromag systems available, which can even reach higher fields up to 11 T, the SM4000-7T has a big advantage for the intended use, since the bottom bot, depicted in Fig. 3.4.2 ①, possesses nearly square dimensions. This symmetry enables a straightforward design of the setup with the ability to turn the magnet from Faraday to Voigt geometry[5] without the necessity to change the optical elements.
The window elements are accordingly the same for all four sides of the bottom pot of the recipient. While Fig. 3.4.2 ① displays the pot with the mounted window elements and various attached accessory parts, ② depicts one window element itself. The front part B is mounted on the outside of the recipient housing, while the back part A counters from the inside. Vacuum tightness is accomplished by an o-ring seal on the backside of part B.

On the outer parts of the window elements (B in Fig. 3.4.2), various accessory parts can be mounted, dependent on the desired magnet geometry (Faraday or Voigt) and frequency range to measure. The adapter from the window to a DN63 CF[6] flange in ③ is utilized as joint for the cryostat. At the DN40 KF adapter displayed in ④ the whole system is pumped to a high vacuum with a combination of turbo molecular

[4]Basov Infrared Laboratory, Department of Physics, University of California, San Diego
[5]Faraday geometry: external field parallel to $\vec{k}$ of light $\vec{B} \parallel \vec{k}$; Voigt geometry: $\vec{B} \perp \vec{k}$
[6]DN63 = nominal width, CF = Conflat flange, KF = Klein flange

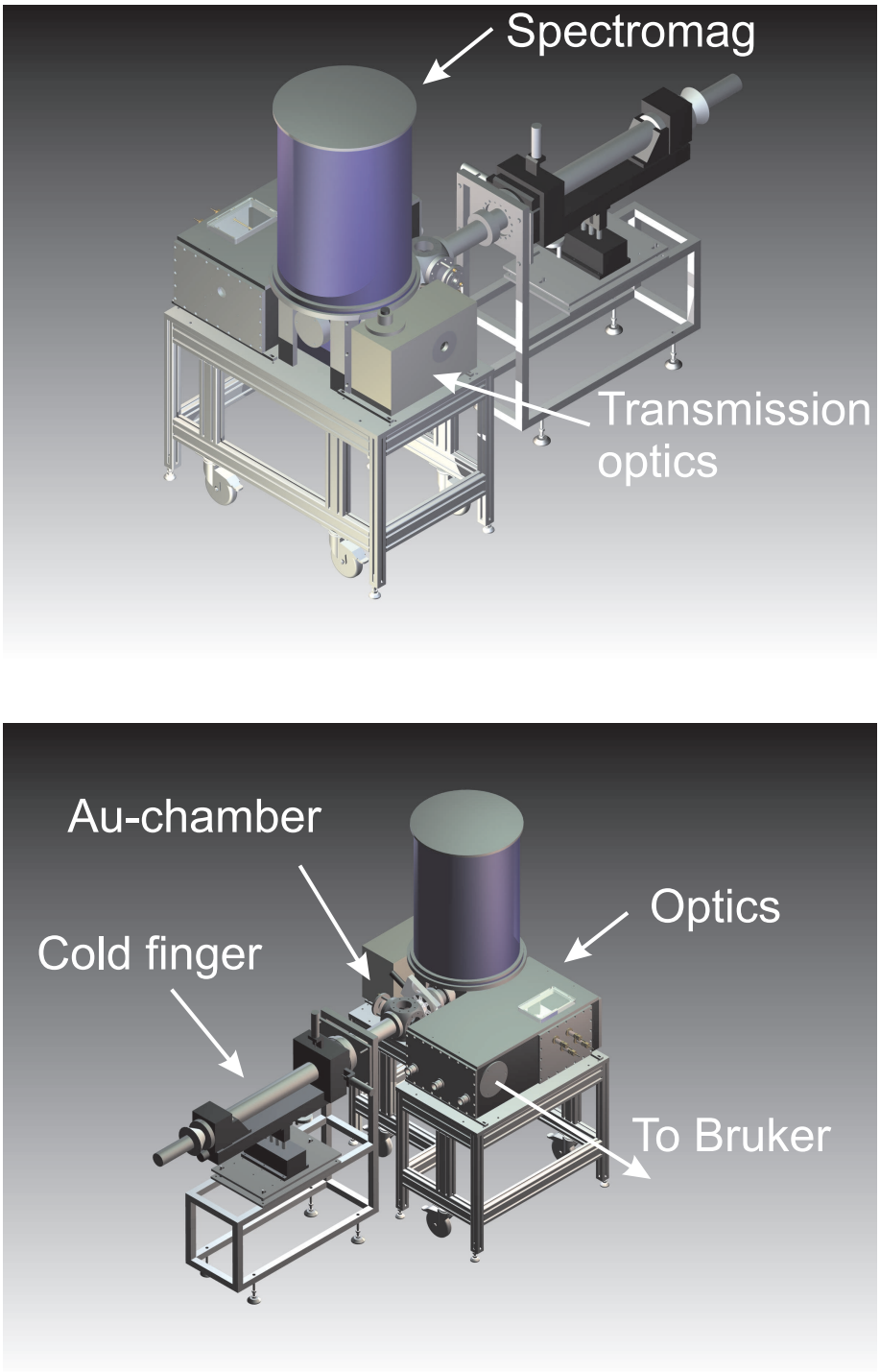

Figure 3.4.1: Two opposing bird's eye views of the magneto-optical setup developed in this work. The pictures are rendered from the original construction file. Individual components are marked in the images.

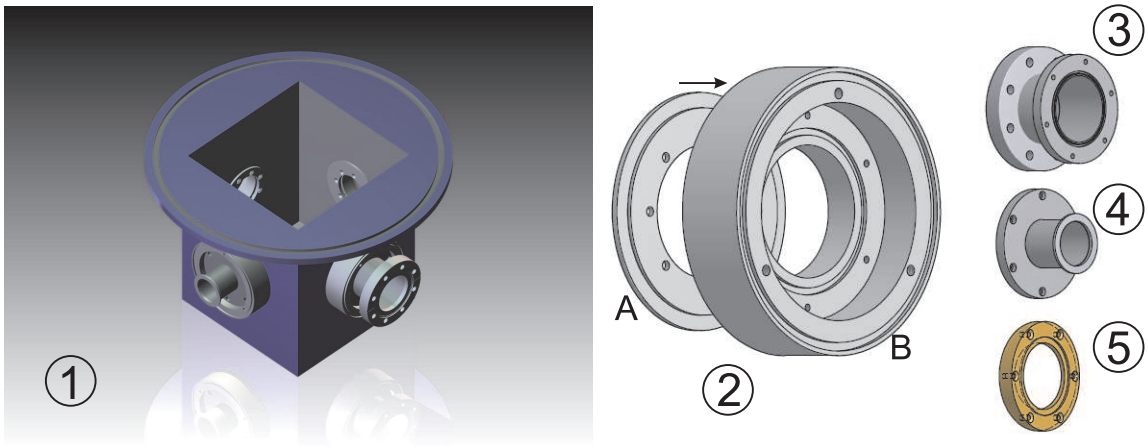

Figure 3.4.2: The bottom pot of the SM4000 with attached window elements and accessory is displayed in ①. The window element consists of a part A that is on the inside of the pot and counters the screws holding part B on the outside of the pot. ③, ④ and ⑤ depict the DN63 CF adapter, the DN40 KF adapter and an example for a tilted window frame, respectively.

pump and rotary pump, as indicated schematically in Fig. 3.4.6. In ⑤ an example of a window frame is displayed. Various tilted and non tilted frames are available for FIR and MIR, NIR. In the FIR a 270 μm thick PP foil is utilized. The comparably thick foil is necessary, since the window diameter is rather large. For MIR and higher frequencies a tilted KBr window is available. It consists of a 5 mm thick crystal with a diameter of 70 mm glued to a window frame with an epoxy resin[7]. The tilting of the crystal window, and also of the PP window, avoids that a parasitic signal reflected on the window surface enters the detector.

Apart from the custom build windows, yet another modification of the SM4000 is established. In the standard configuration all Spectromags are equipped with a variable temperature insert (VTI), that offers space for a sample stick, that can be inserted from the top of the whole magnet vessel. Since the installation described here takes advantage of a horizontally inserted cold finger cryostat, the VTI had to be dismantled. The capillary that connects the helium bath of the Spectromag with the VTI for the purpose of cooling in a conventional SM4000 cryostat was detached, and blocked with a brass cap and an indium sealing inside the recipient.

Removing the VTI bears the aditional advantage, that the light focused on a sample only has to pass one window, namely the outer cryostat window, which increases the yield of signal from the sample, since each passed window absorbs a portion of the

[7]Emerson & Cuming ECCOBOND 286

light.

For the operation of the Spectromag an Oxford Instruments Mercury IPS power supply is set up for the magneto-optical installation, as indicated in Fig. 3.4.6 . It has to be noted, that the 'common' switch heater of the SM4000 is broken, hence the 'spare' heater has to be utilized to run the field (see Ref. [127]).

3.4.2 The optics

The optics for measurements in the magneto-optical setup was completely new designed and is depicted in Fig. 3.4.3. To avoid any influence of magnetic stray fields from the cryo-magnet on possibly magnetic or moving parts of the spectrometer, the whole installation is located more than 1 m away from the IFS 113v. A connector pipe between the optical box and the spectrometer grants the propagation of the IR radiation in vacuum all the way to the magnet. The beam catcher stage that parallelizes the beam and reflects it to the optical box, as well as the connector pipe could be recycled from the previously installed magneto-optical setup. This is also true for the mirrors M5, M6, M7 and the transmission box in Fig. 3.4.3, which are used for transmission measurements.
For transmission, the parallel beam arriving from the spectrometer, is simply deflected on mirror M5, which focuses on the sample, as indicated with dashed lines in Fig. 3.4.3. Subsequently after passing the sample the light is focused on the detector via M6 and M7.
On the reflection mirror stage, the beam possesses a focal point, which is advantageous for two reasons:

- The image quality is rather poor after the light traveled the long path through the connector pipe, which can be corrected by focussing the light.
- An additional aperture or a polarizer can be placed in the optical box. This is in particular necessary, if one needs a well defined polarization state. After the spot inside the spectrometer, where a polarizer can be placed, the light undergoes many reflections, which could smear out the polarization. By placing an additional polarizer right in front of the detector, also measurements with crossed polarizers are possible.

After the focal point, the light is deflected, focused on the sample by M3 and, subsequent to the reflection at the sample, focused on the detector by M4. The incident

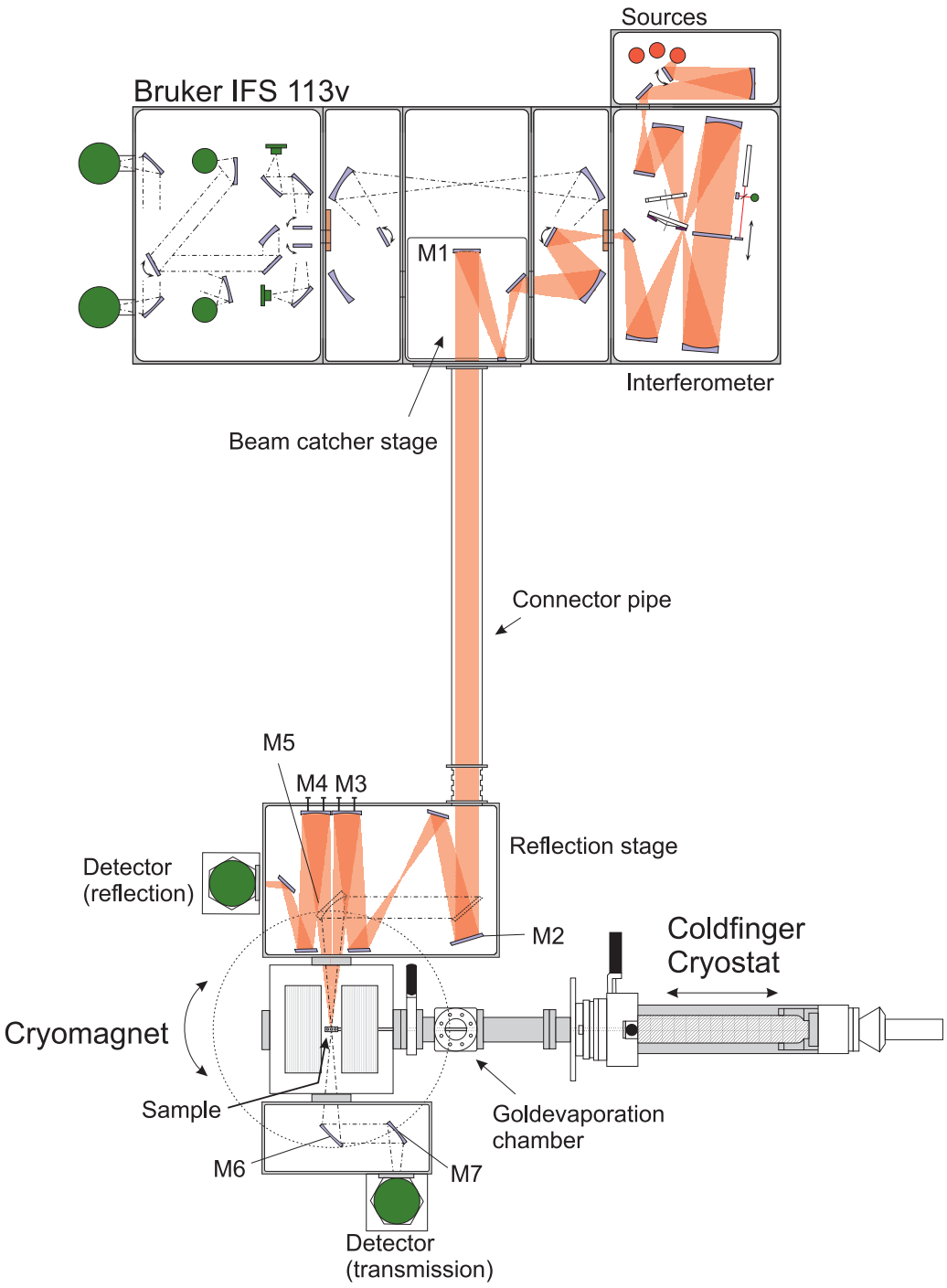

Figure 3.4.3: Schematic representation of the beam path in the magneto-optical setup. The course of the beam in reflection mode is illustrated in orange, while the transmission path is indicated with dashed lines. The incident angel of the light to the sample normal is $\phi \approx 6°$. The relevant focusing mirrors, dubbed M1-M7 are specified in Tab. 3.4.1. Further substantial parts are named in the image. Bruker schematics adapted from [119].

angle of the light to the sample normal is $\phi \approx 6°$. Therefore, the obtained data can be viewed as normal incidence reflectance. Both M3 and M4 are assembled on custom designed mirror mounts that can be adjusted in vacuum via the handles depicted in Fig. 3.4.4 ①. All other mirror mounts of the reflection stage are purchased from Radiant Dyes Laser Accessories GmbH. The mirrors of the reflection stage are made from highly polished massive aluminum purchased from Kugler GmbH. The relevant focal lengths and specifications of the mirrors M1-M7 are listed in Tab. 3.4.1

Name	Type	Focal length (mm)	Diameter (mm)
M1	spherical	R500	70
M2	parabolic 17°	409	75
M3, M4	parabolic on axis	204.5	75
M5	parabolic 45°	250	80
M6	parabolic 45°	250	50
M7	parabolic 45°	180	50

Table 3.4.1: Focussing mirrors that come to use in the magneto-optical installation. The R in the focal length of the spherical mirror M1 stands for the radius of the sphere.

The optical box itself is designed in a modular concept, to permit potential future modifications. The core, made of cast aluminum, is manufactured by the Albert Braach GmbH. On this frame various cover plates can be assembled, as illustrated in Fig. 3.4.4. At ① the cover with the wobble sticks for *in situ* adjustment of mirror M3 and M4 is attached. At ② a cover containing three DN25 KF flanges, one connecting to the transmission box via a flexible hose, is installed. The detector can be mounted to the cover at ③. All the cover plates are sealed with o-rings. The top of the box can be closed with an aluminum plate possessing an acrylic glass window to be able to see the joints between M3/M4 and the wobble sticks.

3.4.3 The cold finger

The cold finger cryostat and linear translator are from the HVK-ST series provided by VAb Vakuum-Anlagenbau GmbH, and were previously used in a different work [128]. The mounting of the cold finger and linear translator on a bench were performed prior to this work by a student assistant[8].
For accurate positioning of the cryostat, the linear translator was modified and

[8]Stefan Wolf

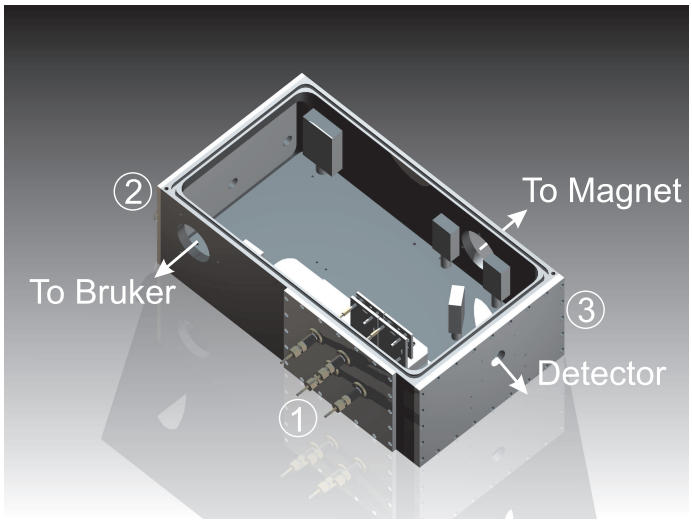

Figure 3.4.4: Representation of the optical box with it's modular concept. At ① a cover with four handles for mirror alignment is mounted. The covers at ② and ③ provide space for vacuum feed through and detector, respectively.

equipped with a VRDM stepping motor from Berger Lahr[9] that is recycled from a discharged setup described in Ref. [129]. The motor is powered by TLC 411 power supply, which can be controlled with the TwinLine control tool on the lab PC. With this arrangement highly accurate horizontal positioning within $\pm 50\,\mu$m or even better is possible[10]. Furthermore the cryostat can be turned 360°. Since the turning motion is carried out manually, a laser pointer reflected on a small mirror on the outside of turning feed through can be utilized for highly accurate reproducibility.
The Cryostat housing is equipped with a chamber for the gold coating of the sample, indicated in Figs. 3.4.1 and 3.4.3. The basic operating principle is the same as described in Sec. 3.2.3. In detail, however, it is necessary to move the gold evaporation unit, which is mounted on rods, towards the sample for the evaporation process. Afterward it needs to be pulled out again, before actuating a linear movement of the cryostat, else cryostat and gold evaporation unit will collide. This chamber also provides access to the sample holder. Therefore, by separating the cryostat from the magnet vacuum (by valve V6, see Fig. 3.4.6), an easy sample exchange is possible without the necessity to warm up and vent the whole magnet.
Fig. 3.4.5 displays the two available sample holders for reflection and transmission measurements in the magneto-optical installation. The reflection sample holder offers space for two cones[11], one for a sample, the other for a reference mirror. The transmission sample holder can be equipped with various frames, each containing three aperture holes. The sample holders can be mounted directly to the cold head

[9] at present a part of Schneider Electric
[10] Note: 500 steps of the motor correspond to approximately 0.1 mm of cryostat movement
[11] identical to those utilized in the zero field cryostat described in Sec. 3.2.3

of the cryostat. To guarantee good thermal conduction both holders are made from (untreated) copper.

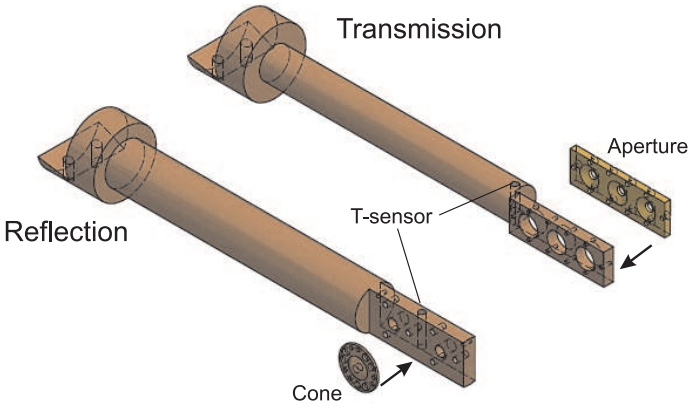

Figure 3.4.5: Illustration of the reflection and transmission sample holders for the cold finger cryostat. The location, where the temperature sensor S2 is inserted in each case is indicated in the image.

Two temperature sensors permit the readout of the cryostat and sample temperature. Both sensors are of the Cernox type, to avoid large influence of the magnetic field on the temperature read. The sensor S1, located at the cold head of the cryostat, is only utilized for stabilizing the temperature. The temperature of the sample is read by a sensor S2 [12], that is mounted at the sample holder as indicated in Fig. 3.4.5. Tab. 3.4.2 summarizes the specifications of the two sensors. A 30 Ω heater close to the cold head enables proportional-integral-derivative (PID) controlled temperature stabilization with a Lakeshore temperature controller.

Sensor	Location	Type	Curve
S1	cold head	Cernox 1050, SD package	CX-1050-SD-X67661
S2	sample holder	Cernox 1050, AA package	CX-1050-AA-X75450

Table 3.4.2: Specifications and locations of the temperature sensors inside the cold finger cryostat. Note, that owing to the unfavorable packaging of S1, the accuracy of the temperature reading of this sensor at low temperatures is poor. Therefore this sensor should only be used for stabilizing purposes. The sample temperature is read with high accuracy by S2 (see Sec. 3.4.4).

3.4.4 Setup operation and characterization

Magnet operation and common parameters

In this section, the performance and common parameters that are to be expected in normal operation of the magneto-optical installation are specified. Since the magnet

[12] Both sensors were calibrated by student assistant Katja Parkkinen.

was modified (VTI removal, new windows; see Sec. 3.4.1) it is of interest to verify the vacuum tightness of the magnet recipient with attached cold finger cryostat. The whole system is pumped to a high vacuum (HV) by the magnet HV pump stage displayed in Fig. 3.4.6. This pump stage is connected via a long DN40 KF flexible hose to one of the window elements at the bottom of the magnet. The long tube is necessary, to guarantee a sufficient distance of the fast spinning turbo pump from the magnet, since eddy currents from magnetic stray fields could else cause severe damage to the pump. The pressure of the system is monitored at the top of the magnet at S1 in Fig. 3.4.6 by a full range gauge. This gauge can be detached from the vacuum via the valve V1, for routinely necessary gauge cleaning. To pump the system, valves V1, V5 and V6 need to be opened, while V7 needs to be closed. Usually pressures of the order of $p \approx 3 \times 10^{-5}$ mbar are achieved upon pumping the system for 3 days starting at ambient conditions, which is sufficient to fill cryogenic liquids in the magnet [127]. Note, that valve V5 should be closed after filling the magnet with liquid He, to avoid a back flow of residual gas from the pump to the magnet, since the cryo pumping effect is stronger than the turbo pump[13].

For a magnet cool down, the He tank of the cryomagnet needs to be pumped and flushed with He gas several times prior to filling liquid helium (L-He). For this purpose a rotary pump (magnet - He pump in Fig. 3.4.6) is attached at valve V4 and a He cylinder or the exhaust from a L-He vessel is connected to V2. During this process the He recovery line valve V3 needs to be closed. The pressure of the system was not affected by this procedure at any time, proving, that the indium sealing of the He capillary, discussed in Sec. 3.4.1, is tight.
The cold finger cryostat can be detached from the magnet vacuuum by valve V6 to exchange samples or restore the gold evaporation unit. To re-establish the connection to the magnet vacuum, the cold finger needs to be evacuated first to a sufficient low pressure ($p \leq 1 \times 10^{-4}$ mbar), before opening V6 again[14]. Pumping the cold finger cryostat separately can be accomplished with another HV pumping station attached to V7 in Fig. 3.4.6. The pressure can then be read by a second full range gauge at S2. Note, that the pumping system at V7 is venting automatically after switch off, hence the valve V7 should be closed before.
Fig. 3.4.6 furthermore displays the rotary pump, that is utilized to pump He from

[13] see pressure of the system at 4.2 K in Tab. 3.4.3

[14] This is in particular important when the magnet contains cryogenic liquids, since the magnet vacuum is then at $p \approx 1 \times 10^{-7}$ mbar and opening V6 with the cold finger at ambient pressure would cause huge L-He and L-N_2 boil-off.

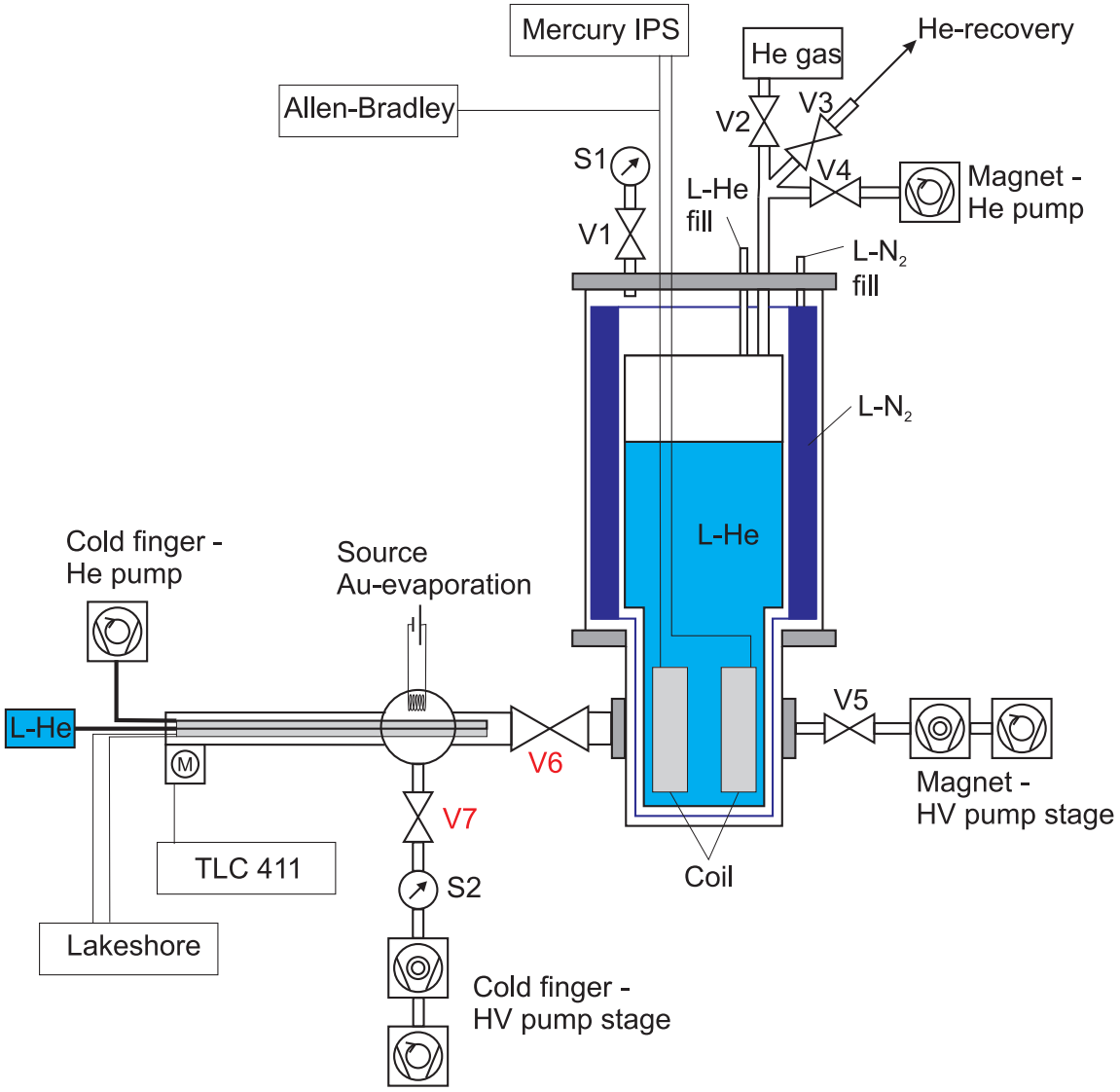

Figure 3.4.6: Schematic representation of the magneto-optical installation showing all valves, pressure gauges and pumps attached. All connected electrical devices are indicated. Special care should be taken when operating valves V6 and V7.

a L-He vessel trough the cold finger cryostat (cold finger - He pump). The lowest temperatures that were achieved at the sensor S1 were $T \approx 5\,\mathrm{K}$ for the reflection holder and $T \approx 6\,\mathrm{K}$ for the transmission holder. Note, that the lowest possible temperatures at the sample holders require the best possible thermal coupling between cold head and sample holder and can only be reached when the cold finger is moved inside the magnet which is filled with L-He.

All relevant electrical connections are also displayed in Fig. 3.4.6. The electrical parts and their purpose are listed below.

- Mercury IPS: power supply for the SM4000 and He level monitor
- Allen Bradley: resistor on top of the coil for cool down monitoring
- TLC 411: power supply for the stepping motor
- Lakeshore: temperature controller for the cold finger cryostat
- Source Au evaporation: current source for the gold evaporation unit

Common parameters expected during a cool down of the magnet are summarized in Tab. 3.4.3.

Temperature (K)	system pressure (mbar)	Allen Bradley (Ω)
300	$\approx 3 \times 10^{-5}$	≈ 151.5
77	$\approx 6 \times 10^{-6}$	≈ 176
4.2	$\approx 1 \times 10^{-7}$	≈ 1016

Table 3.4.3: Common values of pressures and Allen Bradley resistances in the magnet at various temperatures.

In this work the magnet was mainly used in the F^2IR, FIR and MIR, and nice data was obtained between roughly $40\,cm^{-1}$ and $3500\,cm^{-1}$. Towards higher frequencies, the 113v spectrometer was not stable enough to provide reliable data.
To perform measurements in the MIR, the MCT detector, usually located inside the 113v, needs to be assembled outside of the optical box with a special adapter, at the same spot like the bolometers. A KBr window is available for this frequency range.

Reproducibility and error bars

Having characterized the parameters of the magnetic field related apparatus, it is of most vital interest to estimate the accuracy of the whole installation in a real reflection measurement. To do so, several test measurements were conducted. First the reproducibility of the movements of the cold finger cryostat shall be assessed. For this purpose, a measurement was conducted in the FIR at 300 K to exclude thermal shrinking effects. An Al coated glass substrate acted as sample. The stability is best exposed by dividing the spectra recorded under different circumstances by an initial spectrum. Fig. 3.4.7 summarizes the results of this characterization measurement. Panel (a) displays an initial 1-line, meaning two spectra recorded in succession divided by each other, while panel (b) reveals the stability of the setup, when no

movements were carried out and only some time has passed ($\approx 10\,\mathrm{min}$). In panel (c) the cold finger cryostat was moved to different positions, before returning to the sample position and recording the spectrum. In panel (d) the cryostat was moved horizontally and additionally turned. A laser pointer was utilized to reproduce the initial position in the turning motion[15]. From Fig. 3.4.7 it is clear, that the error arising from the cryostat movements can be estimated as $\leq \pm 0.3\%$.
Note, that the presented characterization data is measured with a Mylar/Ge $6\,\mu$m beam splitter and the Globar light source. Measurements at lower frequencies, utilizing a pumped bolometer and corresponding optical settings (see Tab. 3.2.1), as well as at higher frequencies utilizing a MCT detector and KBr beam splitter revealed, that the accuracy stated above holds roughly from $40\,\mathrm{cm}^{-1}$ to $2500\,\mathrm{cm}^{-1}$. At even higher frequencies measurements are in principle possible with the magneto-optical setup. The limiting factor here turned out to be the stability of the 113v spectrometer.

To evaluate the error, when additionally a magnetic field is applied, another test measurement was performed, again at 300 K in the FIR. Two differently sized gold mirrors acted as sample and reference mirror, respectively. The spectra of the sample and the mirror were measured at different fields and the reflectivity was subsequently calculated according to Eq. 3.3.1. In Fig. 3.4.8 (a), (b), (c) the reflectivity recorded at 0 T, 3 T and 7 T normalized to an initial reflectivity recorded at 0 T are displayed. These panels reveal, that the error remains roughly the same as above without applied magnetic field. In the panels (d), (e) and (f), in principle the same normalized spectra are displayed, but this time the reference mirror was left out of the calculation, meaning sample spectra at field are directly divided by the initial sample spectrum. Those panels reveal first of all a slight magnetic field dependence of the bolometer signal. Furthermore strong oscillations occur in the 7 T normalized spectrum in panel (f). Those oscillations are however independent of magnetic field. They were also observed in spectra where no field was applied, but a long time passed between the individual measurements that were divided by each other[16]. The periodicity ($\approx 13\,\mathrm{cm}^{-1}$) of the oscillations is known from spectra recorded in other cryostats possessing the same $270\,\mu$m PP foil as windows. Hence they can be ascribed to interference effects in the window material that do not cancel out completely un-

[15] Dependent on the side of the magnet where the cold finger cryostat is attached, the turning motion is not needed for a reflection measurement with the gold coating technique. To exclude this possible source of error, for the magneto-optical measurements on NbP and TaAs, conducted in this work, the cold finger was attached such, that no turning motion of the cryostat was needed to coat the samples with gold.

[16] Choosing a smaller aperture helps to reduce these oscillation patterns in the spectra.

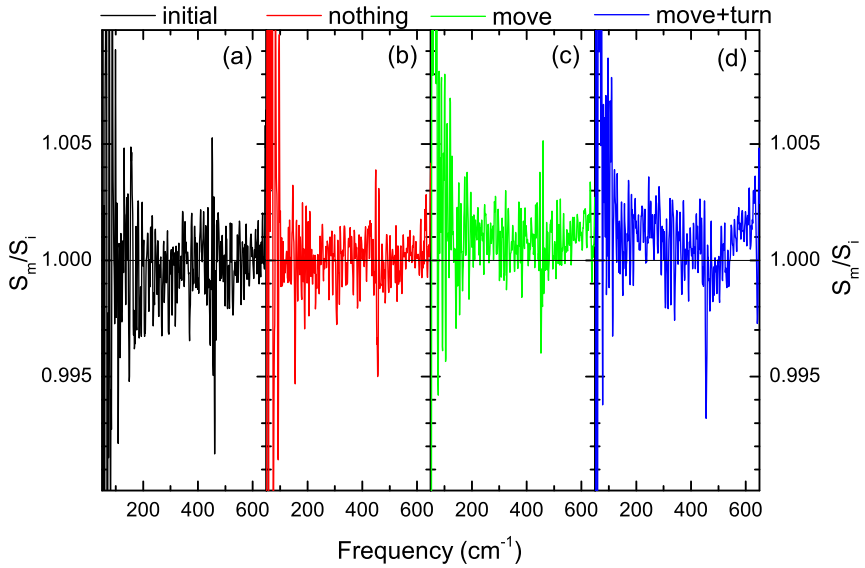

Figure 3.4.7: Reproducibility of the spectra after cold finger movements in the magneto-optical installation. Panel (a) displays an initial 1-line, meaning two divided spectra S_i recorded directly after each other. The other panels display spectra S_m, after (b) nothing was done, (c) linear translation of the cryostat, and (d) linear translation and turning of the cryostat divided by the initial spectra S_i.

der some circumstances (time definitely plays a crucial role). However, panels (a)-(c) proof, that applying careful referencing enables measurements with a satisfying accuracy and an error of $\leq \pm 0.3\%$.
Again, also with magnetic fields applied, the reproducibility and error bars in the F^{2}IR and in the MIR for frequencies below 2500 cm^{-1} are comparable to those presented above in the FIR.

Gold evaporation parameters

Having knowledge of the error, it is important to figure out parameters that result in sufficiently thick gold coatings in the evaporation process. Sufficiently thick means, the thickness should significantly exceed the skin depth of gold in the FIR. The classical skin depth δ_0 of a metal can be calculated as [51],

$$\delta_0 = \sqrt{\frac{c^2}{2\pi\omega\mu_1\sigma_1}}, \tag{3.4.1}$$

where c denotes the speed of light, ω the angular frequency of the light, μ_1 the per-

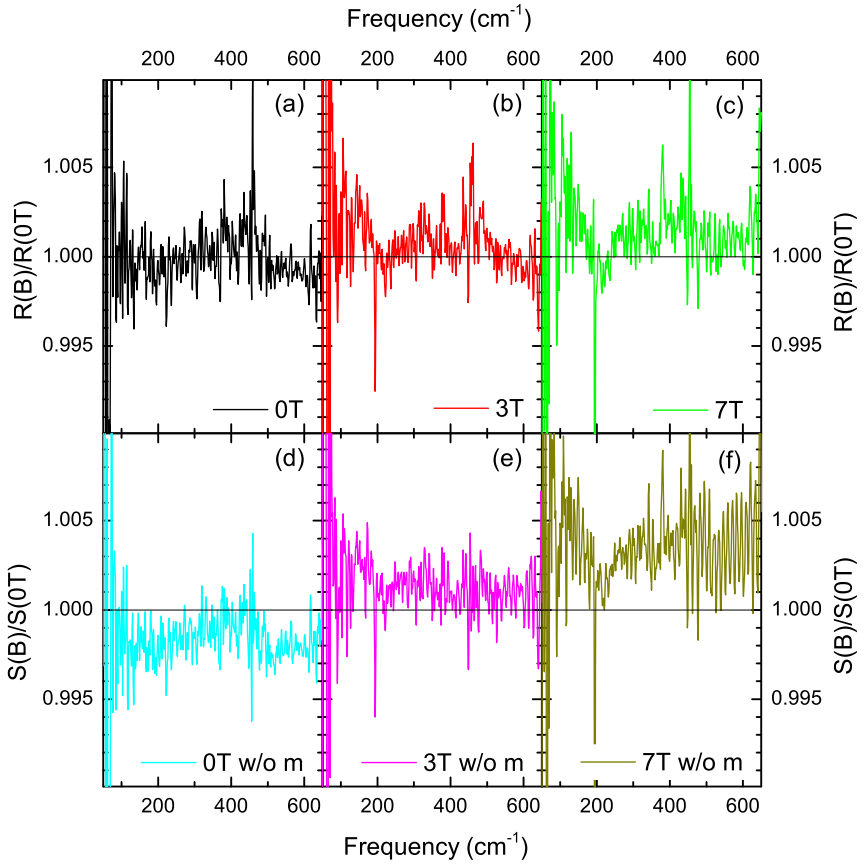

Figure 3.4.8: Reproducibility of the spectra in the magneto-optical setup with applied magnetic fields. Panels (a),(b) and (c) display the reflectivity at different fields calculated according to Eq. 3.3.1 divided by an initial 0 T reflectivity. In panels (d),(e) and (f) the sample spectra are directly normalized to the initial sample spectrum.

meability and σ_1 the conductivity. Straightforwardly, the permeability of gold can be assumed to be unity: $\mu_1 = 1$. The lowest frequency we can achieve is roughly $20\,\mathrm{cm}^{-1}$ and the resistivity of gold at room temperature is $\rho = \frac{1}{\sigma_1} = 2.35\,\mu\Omega\mathrm{cm}$ [130]. Inserting these values into Eq. 3.4.1 we find $\delta_0 \approx 100\,\mathrm{nm}$.

Fig. 3.4.9 displays the thickness of two gold layers determined with a Dektak profiler[17]. The gold layers were evaporated in the magneto-optical installation with different parameters on glass substrates. For the thickness determination the Au-layer from one half of the substrate was removed with sticky tape. The Dektak

[17]The Dektak measurements were performed in the clean room facilities of the 4. Physikalisches Institut (PI4), Universität Stuttgart with technical assistance of Monika Ulb from the PI4.

profiler utilizes a thin tip that is moved over the surface to record the height profile. The parameters utilized for panels (a) and (b) of Fig. 3.4.9 are summarized in Tab. 3.4.4.

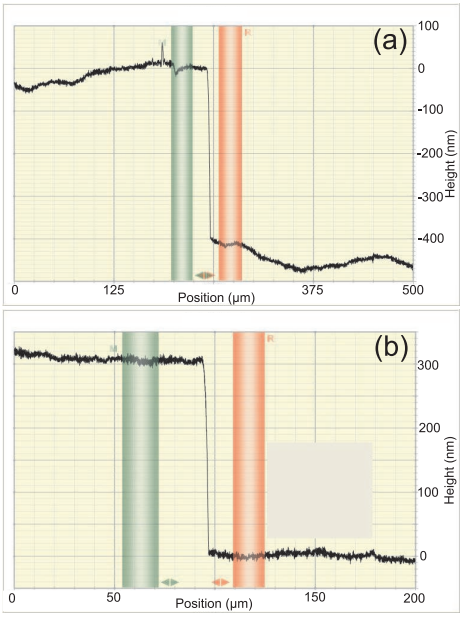

Figure 3.4.9: Gold layer thicknesses obtained in the magneto-optical setup with different parameters given in Tab. 3.4.4 determined with a Dektak profiler. Both gold layers are adequate for measurements in the FIR.

Panel in Fig. 3.4.9	(a)	(b)
No. of Au ringlets	6	5
No. of W wire convolutions	13	11
$R_{\text{Au-unit}}/R_{\text{power-supply}}(\Omega)$	0.8 / 1.2	0.6 / 1.1
Evaporation time t(s) @ Current I(A)	60 @ 1.7	60 @ 1.7

Table 3.4.4: Parameters used for the gold coatings displayed in Fig. 3.4.9. $R_{\text{Au-unit}}$ and $R_{\text{power-supply}}$ refer to the resistance measured directly at the gold evaporation unit leads and at the leads at the power supply, respectively.

The gold layers are roughly 400 nm thick with the parameters utilized in panel (a) and 300 nm for the parameters in panel (b). Comparing these values with the skin depth δ_0 of gold calculated above shows, that both sets of parameters lead to thicknesses of the Au-layers that are sufficient for measurements down to lowest possible frequencies. Note, that the applied parameters are comparable to those that have been proven to be suitable for the zero field gold evaporation cryostat described in Sec. 3.2.3 [120].

Comparison zero-field setup, magneto-optics

At last, reflectivity measurements were conducted at zero field in the magneto-optical setup and compared with the spectra obtained in the 0-field cryostat. Fig. 3.4.10 (a) depicts the FIR reflectivity of the Weyl semimetal NbP at $T = 10\,\mathrm{K}$ recorded in the magneto-optical setup (blue) and the 0-field cryostat (red). Both curves coincide fairly well. This indicates, that apart from the lower signal-to-noise ratio in the magneto-optical installation, the spectral quality is comparable for both setups. Panel (b) of Fig. 3.4.10 displays the reflectivity at $T = 8\,\mathrm{K}$ normalized to the reflectivity at the critical temperature $T_c = 20\,\mathrm{K}$ $R(8\,\mathrm{K})/R(T_c)$ of the iron pnictide superconductor $Ba_{0.6}Eu_{0.4}(Fe_{0.9}Co_{0.1})_2As_2$ in the same manner. Again those relative reflectivity spectra exhibit a good agreement and show the opening of the superconducting gap below $150\,\mathrm{cm}^{-1}$.

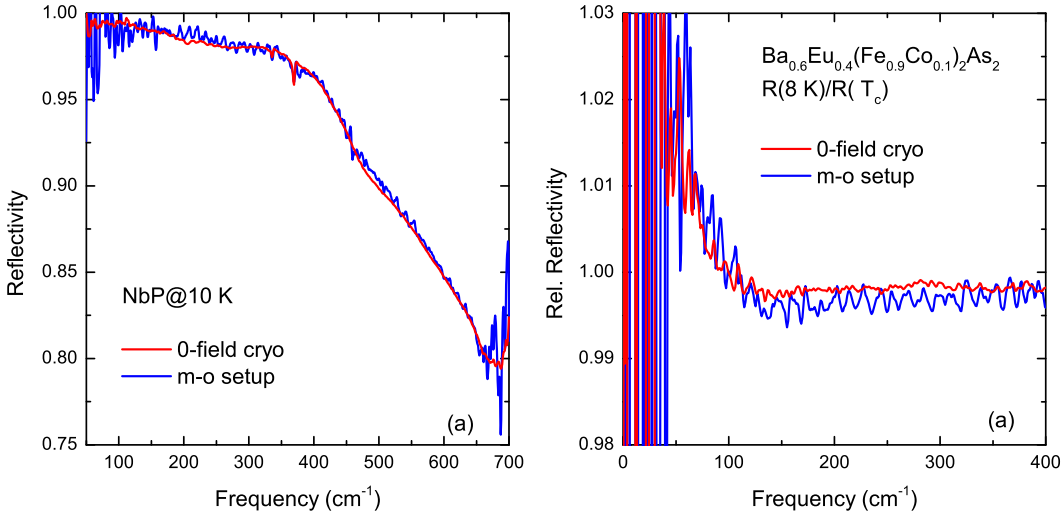

Figure 3.4.10: A comparison of the absolute reflectivity of NbP obtained in the magneto-optical setup (blue) and in the 0-field gold evaporation cryostat (red) is displayed in panel (a). The quality of the spectral information gained is comparable apart from a lower signal-to-noise ratio in the magneto-optical installation. Panel (b) depicts the relative reflectivity of $Ba_{0.6}Eu_{0.4}(Fe_{0.9}Co_{0.1})_2As_2$ with the same color code. Both spectra exhibit a superconducting gap of the same magnitude.

3.5 Further techniques applied

In the framework of this thesis some samples were also characterized by magnetization and resistivity measurements. The magnetization measurements were conducted with a Quantum Design MPMS 7 T magnetometer. The MPMS is a commercial machine, hence the reader is referred to Ref. [131] for a detailed description.
The temperature dependent resistivity data were obtained in standard 4-contact measurements in a home built setup (briefly described in Ref. [121]).

3.6 Data treatment and errors

In the course of this thesis, most of the presented data are not smoothed. This is in particular the case for all zero-field optical data, the transport data as well as the magnetization data. The relative reflectivity spectra measured in the novel magneto-optical setup up to 7 T are moderately smoothed with the adjacent averaging over 20 data points, which is sufficient to remove the noise without perturbing the magnetic field induced changes in the spectra. The relative reflectivity spectra measured in the high field magnet laboratory in Nijmegen require a little bit more radical smoothing due to a larger noise level. Hence, these spectra are smoothed with an adjacent averaging over 30 data points.
In the analysis of the relative reflectivity spectra, the frequency positions of the features are read out by eye. Hence, depending on the width of these signatures in the spectra the error at low fields up to 7 T is estimated to be roughly $\pm 10\,\mathrm{cm}^{-1}$, while in the high field measurements the errors are larger due to broader features and an increased noise level, and can be stated to be roughly $\pm 30\,\mathrm{cm}^{-1}$ (see Secs. 5.2.3, 6.2.3).
The fitting accuracy of phonon peak positions is limited by the choice of the spectral resolution of $1\,\mathrm{cm}^{-1}$ (see Secs. 4.2.2, 7.2.2).
The fits applied to the zero field optical spectra should be considered as models describing the data in the picture of Dirac and Weyl semimetals in Secs. 4.2.2, 5.2.2 and 6.2.2. In Sec. 7.2.2 an established model in the field of iron based superconductors is applied. Cross-correlations of the model parameters were not investigated in this work.

4. The Dirac semimetal Cd_3As_2

In this chapter, the optical properties of the Dirac semimetal Cd_3As_2 are discussed. Sec. 4.1 will give a brief introduction to the material properties. In Sec. 4.2 the analysis of transport and optical data is presented. Conclusions will be drawn in Sec. 4.3, and the findings will be summarized.
Parts of the data and analysis presented in this chapter are published in Ref. [68].

4.1 The material

Cd_3As_2 is well known for decades as a non-cubic II-V semiconductor. The interest in this compound in the last century was mainly triggered by the observation of a high electron mobility [132, 133], a small bandgap [133–135] and a large magneto resistance [134, 136]. The exact bandstructure of Cd_3As_2 was, and still is, a matter of lively discussion [95, 137, 138]. Possible applications of Cd_3As_2 and related alloys as infrared lasers or ultrafast broadband photodetectors were discussed [139–142].

Very recently, Cd_3As_2 regained broad interest, encouraged by the prediction that the bandstructure hosts a pair of 3D Dirac points in the bulk, protected by symmetry [22]. The existence of the Dirac points in Cd_3As_2 was in the meantime well confirmed by ARPES, magneto-transport, scanning tunneling spectroscopy, as well as refined bandstructure calculations [7, 8, 33, 36, 48, 143–145].

Below 475 °C, Cd_3As_2 has a tetragonal centrosymmetric crystal structure with the space group $I4_1/acd$ (No. 142). The unit cell depicted in Fig. 4.1.1 (a) counts 32 formula units and has the lattice constants $a = 12.633\,\text{Å}$ and $c = 25.427\,\text{Å}$ [145]. The structure can be viewed as Cd cubes, stacked in a corkscrew along the c-axis. Two edges on one face of these cubes are vacant, which leads to a distortion. The As ion is located in the centers of these cubes.
The bandstructure calculated in Ref. [145] utilizing this centrosymmetric crystal

structure is depicted in Fig. 4.1.1 (b). Along Γ-Z, a bandcrossing stabilized by the tetragonal symmetry occurs. Because of the preserved inversion and time reversal symmetries, there is no spin splitting and all bands are twofold degenerate. This degeneracy was lifted in earlier bandstructure calculations utilizing a non-centrosymmetric crystal structure for Cd_3As_2 ($I4_1cd$) [22]. The overall appearance of the electronic structure is, however, rather similar for both structures [22, 145].
The electronic dispersion around the Dirac points is illustrated in Fig. 4.1.1 (c) [7, 33, 144]. Valence and conduction branches are depicted in red and blue, respectively. The dispersions along k_x and k_y are rather similar, while along k_z the Fermi velocities are lower [8]. The exact amount of anisotropy was found to depend on the position of the Fermi energy [33]. The Lifshitz transition points (the apices between the Dirac nodes) are located at Γ. The "Lifshitz gap" between these points is yet not reliably determined [144].
Generally, the Dirac points are not at the Fermi energy E_F. Depending on the doping, the Dirac bands will form small electron or hole pockets, as illustrated in Fig. 4.1.1 (d) with the positions of E_F in blue and red, respectively. The corresponding Fermi surfaces are small ellipsoids along the Γ-Z line as illustrated in Fig. 4.1.1 (e) [7, 33, 48]. Typically, Cd_3As_2 is electron doped because of As vacancies [144].

4.2 Cd_3As_2: Results and Discussion

In the following the results obtained on high quality single crystals of Cd_3As_2 in the course of this work are presented. The samples were provided by Dr. Alex Nateprov, from the IAP Moldova[1]. Transport data were contributed by Anja Löhle from PI1[2]. The optical measurements were conducted by the author.

4.2.1 Transport properties

The investigated samples were synthesized and annealed for decades at room temperature as described in Ref. [147]. With this treatment, usually a low carrier density of $N = 6 \times 10^{17}\,\mathrm{cm}^{-3}$ (T independent) and high mobility of $\mu = 8 \times 10^4\,\mathrm{cm}^2\,\mathrm{V}^{-1}\,\mathrm{s}^{-1}$ (at $T = 12\,\mathrm{K}$) is achieved [147]. The sample is n-doped, meaning the charge carriers are electron like.
The temperature dependent resistivity $\rho(T)$ of Cd_3As_2 was measured in the isotropic (001) plane in a standard four-contact geometry. The resulting $\rho(T)$ is depicted in

[1] Institute of Applied Physics, Chisinău, Moldova.
[2] 1. Physikalisches Institut - Universität Stuttgart

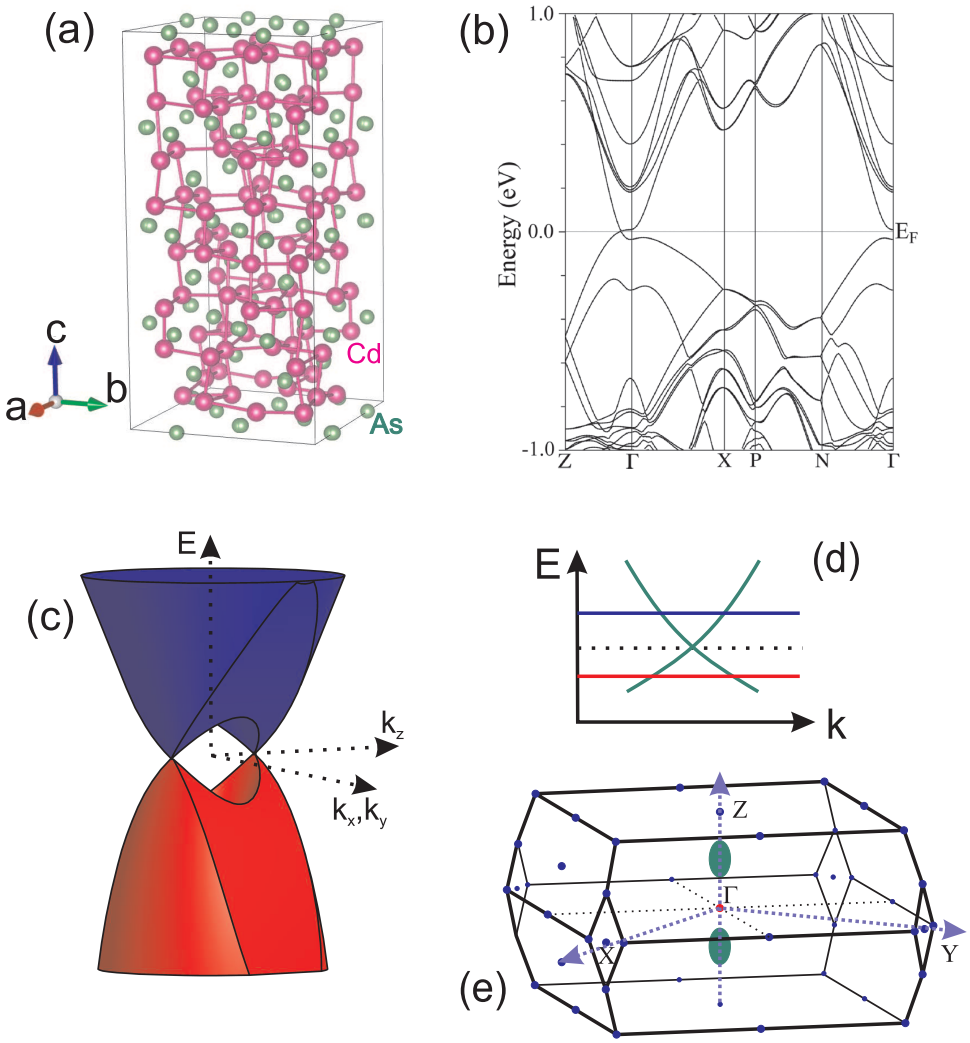

Figure 4.1.1: The unit cell of Cd_3As_2 drawn with VESTA [146] utilizing the crystallographic data from Ref. [145] (a). The bandstructure (b) hosts a band crossing along Γ-Z. A schematic illustration of the dispersion around the Dirac points is depicted in panel (c) [7, 33, 144]. The position of the Fermi energy E_F (d) for electron doping (blue) and hole doping (red). The resulting electron or hole Fermi surface ellipsoids are located on the Γ-Z line in the Brillouin zone (green) (e) [7, 33, 48]. Panel (b) reprinted from Ref. [145] with permission. Copyright (2014) American Chemical Society.

Fig. 4.2.1 (a). The resistivity is overall metallic and for $T \geq 100\,\mathrm{K}$ it increases linearly in temperature, emphasized by the orange line in panel (a). In metals, such behavior is indicative for a predominant electron-phonon scattering mechanism. The inset reveals a residual resistivity of $\rho_0 \approx 0.27\,\mathrm{m\Omega\,cm}$. With this, the investigated sample has a residual resistivity ratio of $RRR = \rho(300\,\mathrm{K})/\rho_0 = 5.5$. Panel (b) of Fig. 4.2.1 displays $\Delta\rho = \rho(T) - \rho_0$ on a double logarithmic scale. The orange line in this panel reveals that $\Delta\rho \propto T^{1.6}$ for $T \lesssim 100\,\mathrm{K}$. This behavior is far off the expectations for simple metals ($\propto T^5$) or a Fermi liquid ($\propto T^2$). The slopes of $\rho(T)$ at low temperatures, the RRR, and the mobility were found to vary dramatically even for crystals of the same boule in Ref. [148]. The record residual resistivity ratio $RRR = 4100$ and mobility $\mu \approx 9 \times 10^6\,\mathrm{cm\,V^{-2}\,s^{-1}}$ are reported there. However, comparing our transport results to a crystal with similar mobility (sample A4 in Ref. [148]), and taking into account the differences in carrier concentrations, the overall appearance is similar, even though a different crystal growth technique is applied in Ref. [148].

4.2.2 Optical experiments

The temperature dependent optical response of Cd_3As_2 was obtained in the (001) plane for frequencies $\omega = 40 - 25\,000\,\mathrm{cm^{-1}}$. The light was polarized along the [100] and [010] directions. The (001) surface was polished prior to optical measurements. For extrapolation at high frequencies, reflectivity data between $3\,\mathrm{eV} \approx 25\,000\,\mathrm{cm^{-1}}$ and $12\,\mathrm{eV} \approx 100\,000\,\mathrm{cm^{-1}}$ from Refs. [135, 149] were utilized, additionally to the method described in Sec. 2.2.

Panel (a) of Fig. 4.2.2 displays the reflectivity spectra at $T = 10\,\mathrm{K}$ with light polarized along [100] and [010], respectively. The spectra are identical, confirming that the response of the isotropic (001) plane is probed. Since the response is independent of the polarization, henceforth all presented spectra will be averages of both measured polarizations.
The temperature dependent reflectivity is depicted in Fig. 4.2.2 (b). Above $2000\,\mathrm{cm^{-1}}$, the spectra are T-independent. Below $2000\,\mathrm{cm^{-1}}$, only weak changes are observed. A number of sharp dips in $R(\omega)$ in the FIR arise from a series of optical phonons. At $\omega \approx 400\,\mathrm{cm^{-1}}$, a steep downturn of the reflectivity marks the screened plasma frequency $\omega_{p,scr}$. After passing a minimum, the reflectivity remains roughly constant over a wide frequency range, $\omega = 2000 - 8000\,\mathrm{cm^{-1}}$. The highest diplayed frequencies above $10\,000\,\mathrm{cm^{-1}}$ are dominated by a broad peak. Note the good agreement of the

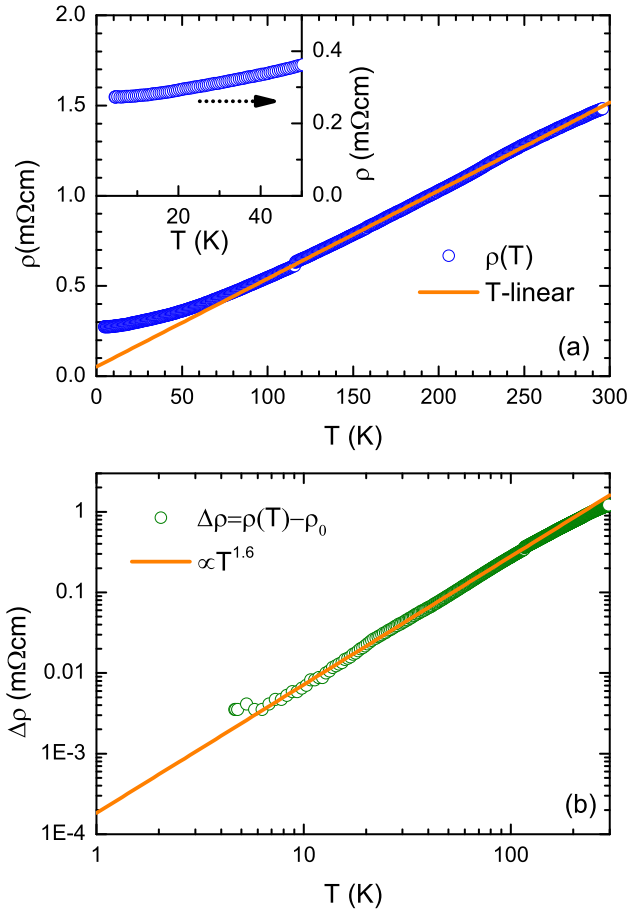

Figure 4.2.1: The temperature dependent resistivity $\rho(T)$ of Cd_3As_2 is displayed as blue circles in panel (a). The orange line emphasizes the T-linear behavior for $T \geq 100\,\mathrm{K}$. The inset reveals a residual resistivity of $\rho_0 \approx 0.27\,\mathrm{m\Omega\,cm}$. Panel (b) depicts $\Delta\rho = \rho(T) - \rho_0$ on a double logarithmic scale. The orange line in this panel reveals the power law $\propto T^{1.6}$ below 100 K. Note, that the tiny step in the data in panel (a) around 120 K is an artifact from the measurement.

reflectivity data presented in Fig. 4.2.2 with previous [149–151] and recent [80, 95] reports.

The optical conductivity $\sigma_1(\omega)$ in Fig. 4.2.2 (c) can be separated into three parts. The low energy region in the FIR is dominated by a Drude-like response superimposed with a series of phonons. Between $200\,\mathrm{cm^{-1}}$ and $1500\,\mathrm{cm^{-1}}$, temperature dependent structures dominate. With decreasing temperature, the conductivity around $1300\,\mathrm{cm^{-1}}$ gets strongly suppressed and vanishes completely in a narrow frequency region, which was previously interpreted as an optical gap [133]. The third region appears linear in the double logarithmic plotting style of Fig. 4.2.2 (c), corresponding to a powerlaw increase of the optical conductivity, $\sigma_1(\omega) \propto \omega^{1.6}$, emphasized by the dashed gray line. This region is dominated by the interband transitions between the peculiar shaped Dirac bands in Cd_3As_2, as will be discussed later. The step, preceding the powerlaw increase of $\sigma_1(\omega)$, marks the onset of these interband transitions at $2\Delta_E \approx 1700\,\mathrm{cm^{-1}}$.

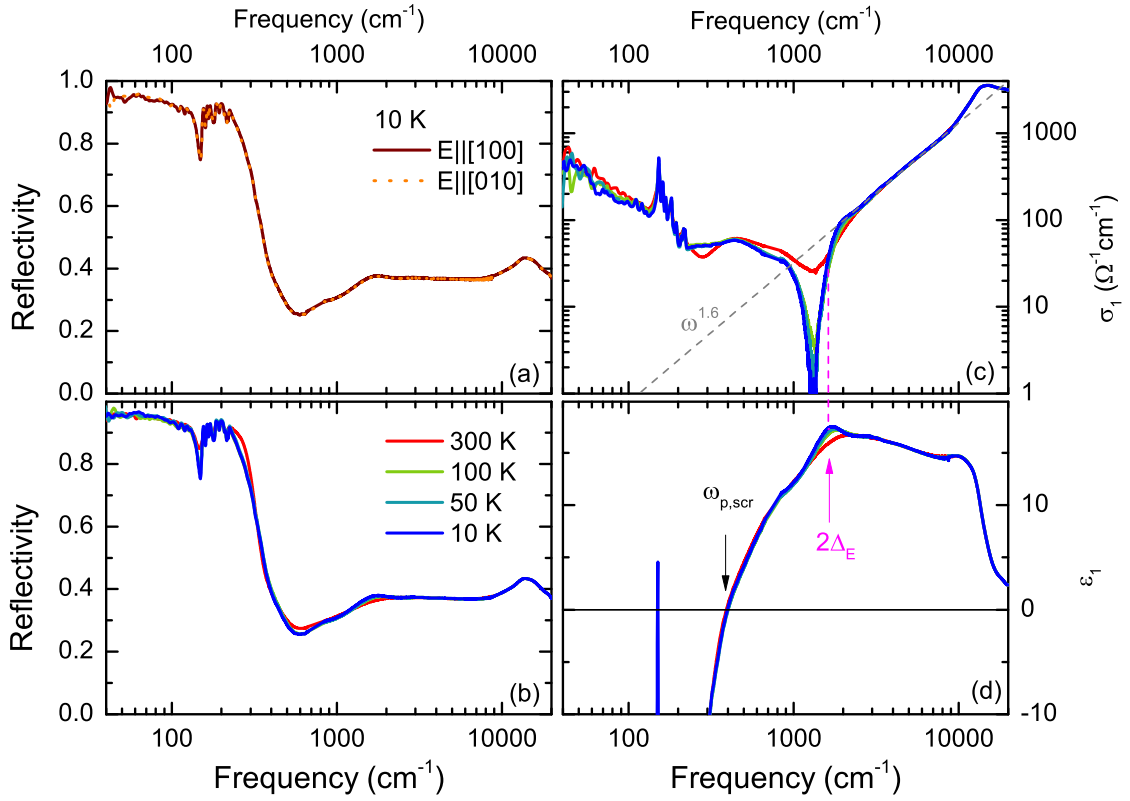

Figure 4.2.2: Optical response functions of Cd_3As_2 over a wide frequency range on a logarithmic scale. The reflectivity at 10 K for light polarized along [100] and [010] in panel (a) confirms the isotropic nature of the (001) plane. The temperature dependence of $R(\omega)$ (b) reveals a relatively sharp plasma edge and a wide range of temperature independent roughly constant reflectivity. This range of constant $R(\omega)$ turns up as an increase $\propto \omega^{1.6}$ of $\sigma_1(\omega)$ (c) after Kramers-Kronig. The onset of this interband conductivity crops up in $\varepsilon_1(\omega)$ (d) as a peak at $2\Delta_E$. The screened plasma frequency $\omega_{p,scr}$ is found at the zero crossing of $\varepsilon_1(\omega)$.

The dielectric function $\varepsilon_1(\omega)$ depicted in Fig. 4.2.2 (d) is peaked at $2\Delta_\mathrm{E}$ in agreement with the theoretical considerations in Sec. 2.6. At low frequencies, $\varepsilon_1(\omega)$ takes large negative values because free charge carriers are present in the system. In the apex at $2\Delta_\mathrm{E}$, the dielectric function takes a value of $\varepsilon_1 \approx 17$. The zero crossing marks the screened plasma frequency, $\omega_{p,scr} = 400\,\mathrm{cm}^{-1}$.
In the following, a closer look will be taken, first, on the powerlaw interband part, second, on the intraband conductivity and the lattice vibrations, and third, on the intermediate region where most of the temperature dependent dynamics are observed in the spectra.

Before diving deeper into the analysis, one important remark regarding the Kramers-Kronig transform and extrapolation needs to be made. As it was pointed out above, for the high frequency extrapolation reflectivity data obtained with synchrotron radiation from Refs. [135, 149] is utilized. The data in these references includes the peak at $\omega \approx 15\,000\,\mathrm{cm}^{-1}$, that is also observed in Fig. 4.2.2 (a,b) validating the data in the present work. However, an additional strong peak at $\omega \approx 30\,000\,\mathrm{cm}^{-1}$ observed in Refs. [135, 149] is important to be included in the extrapolation. The powerlaw observed in $\sigma_1(\omega)$ is altered for different extrapolations and reduces down to $\omega^{1.4}$, if only a free electron decay $\propto \omega^{-4}$ is utilized beyond the measured range (see appendix C).

Interband conductivity

Eq. 2.6.1 states, that the exponent of the interband optical conductivity for crossing bands equals $\frac{d-2}{z}$ with the dimensionality of the crossing point d and the exponent of the band dispersion z. Utilizing Eq. 2.6.1 with the observed powerlaw ($\omega^{1.6}$) and the 3-dimensional nature of Cd_3As_2 straightforwardly yields, that the dispersion for energies larger than Δ_E is sublinear, i.e., $\epsilon(\mathbf{k}) \propto |k|^{0.6}$. The exponent of sublinear dispersion needs to be considered as a mean value. Optical experiments average over all k-directions, and a possible asymmetry of conduction and valence branches of the Dirac bands is not included in Eq. 2.6.1. Both, anisotropic cones and an asymmetry of conduction and valence bands are evident in Cd_3As_2 [7, 8, 144].

Fig. 4.2.3 (a) depicts the optical conductivity for 300 K and 10 K on a linear frequency scale. The gray dashed line represents the powerlaw $\omega^{1.6}$. The green line is a linear approximation, which describes the spectra quite well between $3000\,\mathrm{cm}^{-1}$ and $5000\,\mathrm{cm}^{-1}$. Utilizing Eq. 2.6.2 and the number of nondegenerate cones $N_\mathrm{W} = 4$, the slope of this line corresponds to a Fermi velocity $v_\mathrm{F} \approx 2 \times 10^5\,\mathrm{m\,s}^{-1}$. Note that the green line has a positive intersect with the frequency axis. In Sec. 2.6 and Eq. 2.6.3, such an intersect was discussed to arise from a massless gap driven by self-energy effects. For Cd_3As_2, the scenario of cones narrowing towards the Dirac nodes provides, however, a much more realistic explanation.
Narrowing cones with sub-linear dispersion imply an energy dependent Fermi velocity, and Eq. 2.6.2 yields,

$$v_\mathrm{F}(\omega) = \frac{e^2 N_\mathrm{W}}{24\hbar^2}\left(\frac{\delta\sigma_1}{\delta\omega}\right)^{-1}. \tag{4.2.1}$$

The frequency dependence of v_F for 10 K is displayed in Fig. 4.2.3 (d). The Fermi velocity increases linearly towards lower frequencies for $\omega \approx 8000 - 3000\,\mathrm{cm}^{-1}$, emphasized by the thin black line. Thereby, the gain is $1.03 \times 10^5\,\mathrm{m\,s^{-1}\,eV^{-1}}$ towards lower ω (slope $-12.8\,\mathrm{m\,s^{-1}\,cm}$ on the scales of panel (d)). At $3000\,\mathrm{cm}^{-1}$, a kink occurs and for lower frequencies the Fermi velocity grows much faster. The kink coincides with the energy of the "Lifshitz gap" E_L, as will be discussed in the next paragraph. The hump in v_F close to the kink is therefore likely related to the transitions around E_L. The dashed red line represents a linear fit of the steep increase of v_F below $3000\,\mathrm{cm}^{-1}$. The slope of this fit is $-190\,\mathrm{m\,s^{-1}\,cm}$ on the scales of panel (d) which corresponds to an increase of $1.5 \times 10^6\,\mathrm{m\,s^{-1}\,eV^{-1}}$ towards lower energies.

The zero frequency limit of this fit yields $v_F(\omega = 0) = 7.6 \times 10^5\,\mathrm{m\,s^{-1}}$. This can be understood as the Fermi velocity of the Dirac bands near the nodes (assuming that the bands do not change slope below Δ_E), and is in excellent agreement with the values from other reports [7, 8, 48, 95, 144, 148, 152].

Panels (b) and (c) of Fig. 4.2.3 depict enlarged views of $\varepsilon_1(\omega)$ and $\sigma_1(\omega)$, respectively, around the onset of the Dirac interband transitions. Panel (b) reveals, that the cusp in $\varepsilon_1(\omega)$ attributed to the onset of the Dirac interband transitions has a sizable temperature dependence and shifts to lower frequencies with lowering T, as shown by the black arrow. In other words, the Dirac interband transitions start at lower energies, when the temperature is lowered. Indeed, the temperature dependence of the chemical potential, is expected to be of relevance in Dirac and Weyl semimetals. Theory predicts, that the chemical potential shifts down with increasing the temperature proportionally to T^2 [75]. The temperature dependence of Δ_E, extracted from $\varepsilon_1(\omega)$ is depicted in Fig. 4.2.3 (e) and clearly deviates from this expectation. The dashed black line represents a linear fit, revealing $\Delta_E(T = 0) = 104\,\mathrm{meV}$ and a rise in temperature with a slope of $0.115\,\mathrm{meV\,K^{-1}}$.

A T-linear development of the absorption edge in Cd_3As_2 was previously reported, however, with a negative slope [153, 154]. The interpretation of the temperature dependence in these works is discussed to arise from the T-dependence of a direct gap in the Kane model [155], which is widely suggested for Cd_3As_2 [95, 153, 156, 157]. The origin of the unexpected increase of Δ_E observed in this work is yet unresolved and calls for further investigations.

For relativistic particles, the effective mass m^* and the Fermi energy are proportional to each other, $E_F = m^* v_F^2$ [95]. From the values above ($\Delta_E = E_F = 104\,\mathrm{meV}$, $v_F(\omega = 0) = 7.6 \times 10^5\,\mathrm{m\,s^{-1}}$) the effective mass is estimated as $m^* \approx 0.03\,m_e$.

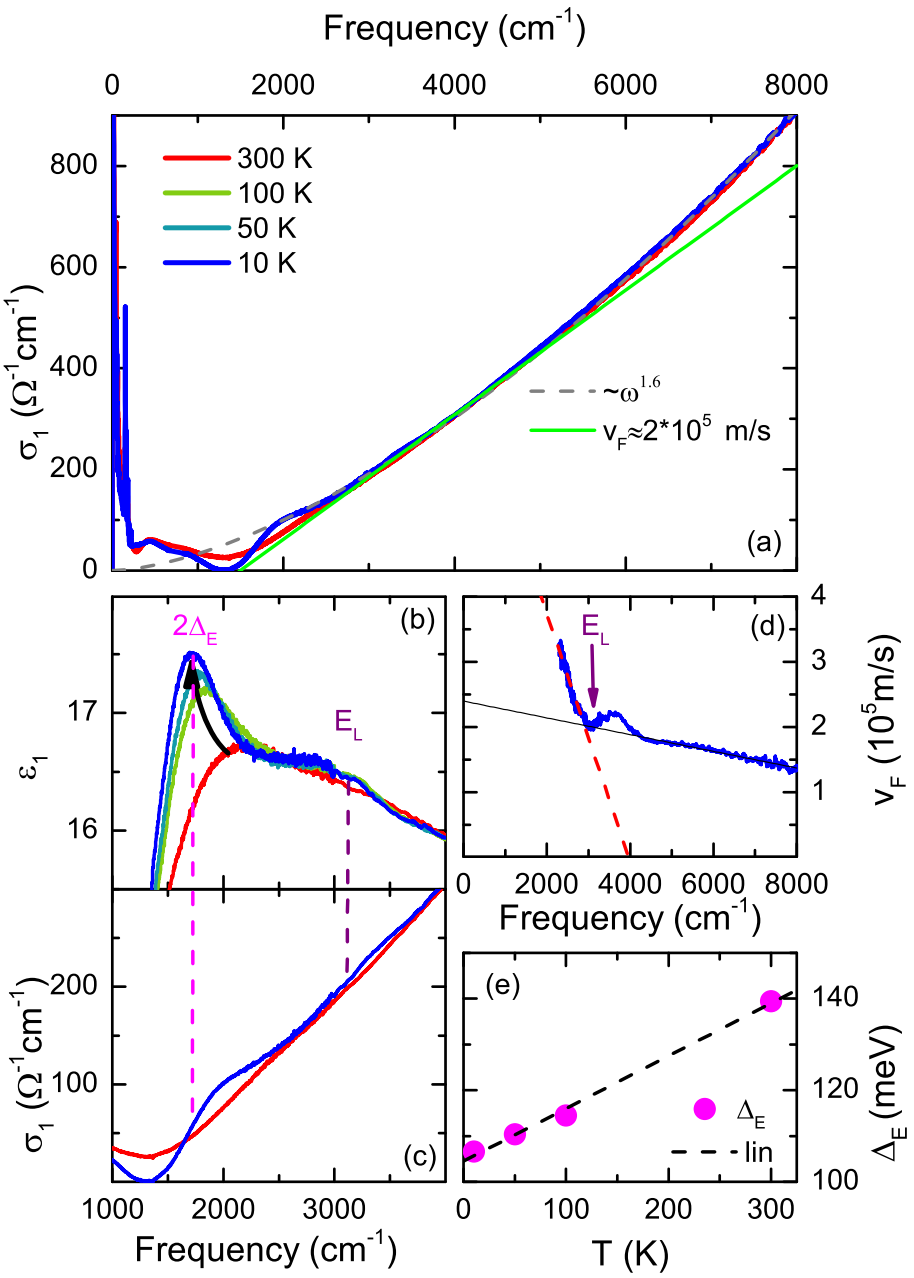

Figure 4.2.3: Even though the interband optical conductivity (a) of Cd_3As_2 follows a powerlaw $\propto \omega^{1.6}$ (dashed gray), it can be approximated linearly (green). The slope corresponds to a Fermi velocity of $v_F \approx 2 \times 10^5\,\mathrm{m\,s^{-1}}$. The frequency dependent Fermi velocity (see text) reveals two linear regimes (d) and approaches $v_F \approx 7.6 \times 10^5\,\mathrm{m\,s^{-1}}$ at the nodes (assuming, the slope remains the same down to $\omega = 0$). The kink in $v_F(\omega)$ appears at the Lifshitz transition energy E_L which is also found as a hump in $\varepsilon_1(\omega)$ (b). The onset of the interband transitions between the Dirac bands at $2\Delta_E$ is temperature dependent (b,e) and Δ_E increases linear in temperature. Panel (c) depicts $\sigma_1(\omega)$ and the features corresponding to E_L and $2\Delta_E$.

In the dielectric function $\varepsilon_1(\omega)$ in Fig. 4.2.3 (b) at $E_L \approx 3000\,\mathrm{cm}^{-1}$, a second hump is resolved at low temperatures. In the optical conductivity, at these frequencies a weak anomaly can be identified. These features can be assigned to the van Hove singularity in the density of states arising from the Lifshitz transition point between the two Dirac nodes. Consequently, the energy between the two Lifshitz transition points (the "Lifshitz gap") is approximately 370 meV. Note the recent report of a similar feature at the same energy in the reflectivity of Cd_3As_2 [80].

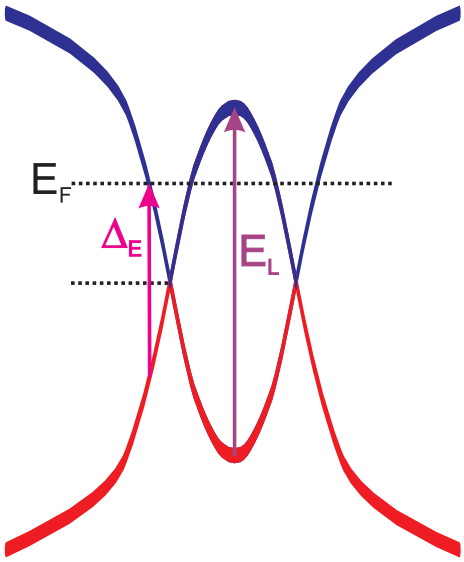

Figure 4.2.4: Schematic bandstructure of the Dirac bands as obtained from the optical data. The bands narrow towards the Dirac nodes and exhibit a kink at an energy around E_L. The onset of the Dirac interband transitions is marked with a pink arrow, while the transitions at the Lifshitz transition points are depicted in purple.

The findings above allow to draw a schematic bandstructure around the Dirac points as depicted in Fig. 4.2.4. The blue branch represents the conduction band and the red the valence band. The onset of the Dirac interband transitions is marked with a pink arrow. The transition at the Lifshitz point marked with a purple arrow is responsible for the second hump in $\varepsilon_1(\omega)$, as discussed above. At energies around the Lifshitz points the bands are bent and continue to flatter towards higher energies, but are still sub-linear in k.

Intraband conductivity and lattice vibrations

The intraband conductivity of Cd_3As_2 can be nicely fit with a single Drude term, as depicted in Fig. 4.2.5 (a). The low frequency limit of the Drude terms $\sigma_{\mathrm{Drude}}(\omega \to 0)$ was roughly anchored at the σ_{DC} values for all measured temperatures. The phonon contributions are accounted for by a series of Lorentz-type oscillators. The inverse of zero frequency limit of the Drude conductivity $1/\sigma_{\mathrm{Drude}}(\omega \to 0)$ is depicted in Fig. 4.2.5 (b) together with the DC-resistivity ρ_{DC} and the Drude scattering rate γ.

The temperature dependence of γ reveals the same shape as ρ_{DC}. Therefore, the metallic decrease of $\rho(T)$ in Cd_3As_2 is solely driven by the decreasing scattering rate (while N/m is constant; cf. Eq. 2.3.4).

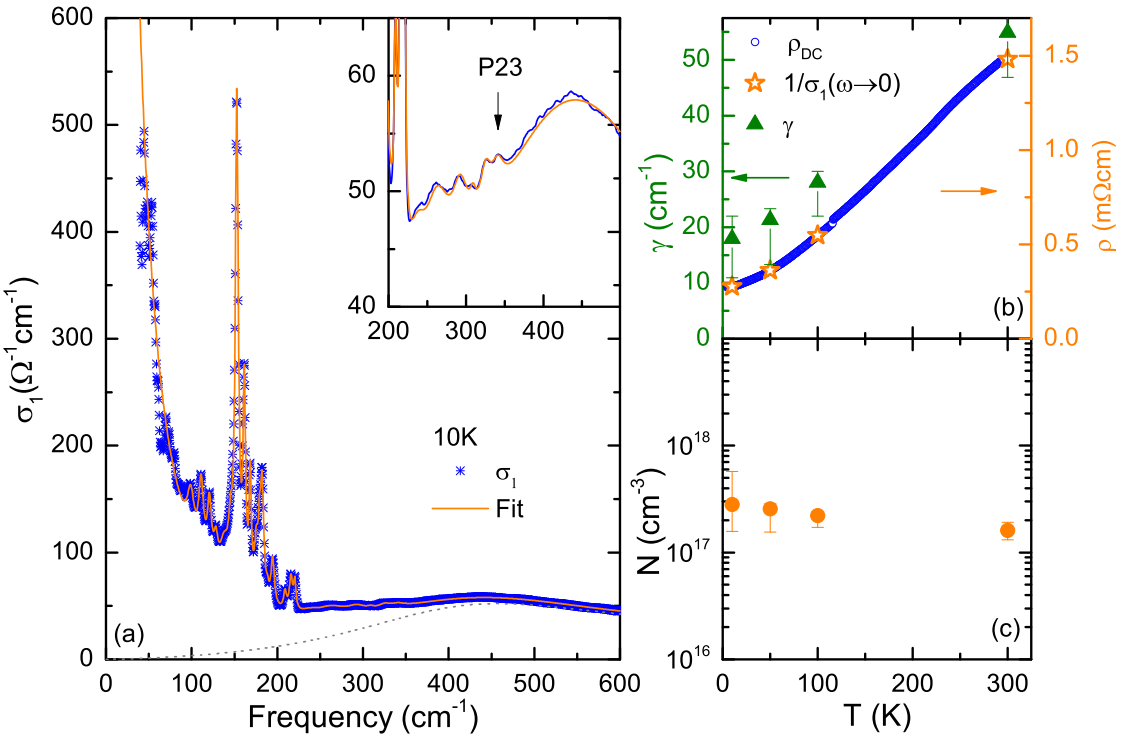

Figure 4.2.5: The intraband optical conductivity of Cd_3As_2 can nicely be fit with a single Drude term (a). Additionally 23 Lorentz terms are included to account for phonons. The inset of panel (a) depicts an enlarged view of $\sigma_1(\omega)$ and reveals the highest phonon frequency P23 around 350 cm^{-1}. The temperature dependence of the scattering rate γ of the Drude term (b) follows the DC-resistivity. The carrier density N calculated from ω_p of the Drude term with an effective carrier mass of $m^* = 0.0065(^{+0.004}_{-0.001})\, m_e$ is roughly constant in temperature and of the order $N \approx 2 - 3 \times 10^{17}$ cm^{-3}.

From the low temperature mobility suggested for the investigated sample ($\mu = 8 \times 10^4\,\mathrm{cm^2\,V^{-1}\,s^{-1}}$) and the relation of mobility to the scattering time $\mu = \frac{e\tau}{m^*}$ (where $\tau = 1/2\pi c\gamma$) [158], the effective mass of the carriers can be estimated. Inserting the value for the scattering time at 10 K obtained from the fit yields a very low mass $m^* = 0.0065(^{+0.004}_{-0.001})\, m_e$, lower by a factor of $3 - 5$ than the cyclotron mass obtained in magneto-transport and magneto-optical studies [48, 95, 152], and the value obtained above from the interband conductivity. To test the self-consistency of this

result, the plasma frequency of the Drude terms and m^* can be utilized to calculate the carrier density as $N = \frac{\omega_p^2 m^*}{4\pi e^2}$. The result is depicted in Fig. 4.2.5 (c). The carrier density is roughly constant in temperature and of the order of $2 - 3 \times 10^{17}\,\mathrm{cm}^{-3}$, which agrees well with the low carrier density suggested for the investigated sample ($N = 6 \times 10^{17}\,\mathrm{cm}^{-3}$).
Lattice vibrational features are found in the spectra up to approx. $350\,\mathrm{cm}^{-1}$ revealed by the enlarged view of $\sigma_1(\omega)$ in the inset of Fig. 4.2.5 (a). This agrees well with a previous infrared optical study on the phonons in the (112)-plane of Cd_3As_2 [151]. The feature with the highest frequency that safely can be interpreted as a phonon is marked as P23 in the inset of Fig. 4.2.5 (a). The broad peak at $450\,\mathrm{cm}^{-1}$ in $\sigma_1(\omega)$ (gray dotted line) will be discussed in the next paragraph. The fit parameters of the 23 phonons found in the low temperature spectra are summarized in Tab. 4.2.1.
For the proposed centrosymmetric structure with the space group $I4_1/acd$ (No. 142) [145], Cd_3As_2 hosts $14A_{2u}$ and $30E_u$ infrared active modes [159]. Even though the present work reports the largest number of phonons so far [150, 151], not all E_u modes (which should be visible when probing the in-plane infrared response) are observed. This possibly arises from weak dipolar moments in the Cd_3As_2 structure [151], or some modes may have very similar frequencies and, hence, are hard to resolve.

Intermediate region

In the range from $200\,\mathrm{cm}^{-1}$ to $2500\,\mathrm{cm}^{-1}$, between the Drude dominated frequencies and the interband response, some temperature dependent structures appear in the spectra. In a simple picture, where only the Dirac bands are at the Fermi level and the chemical potential is finite (see Fig. 4.2.4), aside from the free carriers and the interband response there should be no further structures. Hence the understanding of these spectral features is not straightforward.
Fig. 4.2.6 (a) depicts the optical conductivity $\sigma_1(\omega)$ below $2500\,\mathrm{cm}^{-1}$ for $T = 300\,\mathrm{K}$ and 10 K. The spectral weight, which is lost at low temperatures around $1500\,\mathrm{cm}^{-1}$, appears to be transferred to lower as well as to higher energies, indicated with the dotted black arrows. Note the unconventional temperature dependence in the frequency range below $450\,\mathrm{cm}^{-1}$ (emphasized by the light blue circle). All attempts to satisfactorily fit this temperature dependence failed. The fit of the 10 K spectrum in Fig. 4.2.6 contains additionally to the Drude response and the phonons discussed above, a Lorentz term (L) at $445\,\mathrm{cm}^{-1}$, an asymmetric Fano resonance term (F) at

Phonon	$\omega_0(\mathrm{cm}^{-1})$	$\gamma(\mathrm{cm}^{-1})$	$\Omega = \omega_p^2(10^4\,\mathrm{cm}^{-2})$
P1	98.9	9.6	2.29
P2	111.0	6.7	3.16
P3	120.8	5.8	1.92
P4	128.3	5.6	0.99
P5	137.9	12.4	2.71
P6	145.5	6.1	1.79
P7	152.7	4.2	11.4
P8	161.4	3.5	4.15
P9	168.3	3.1	2.37
P10	175.6	5.5	1.77
P11	179.2	3.0	0.76
P12	182.2	4.7	3.26
P13	188.5	3.1	0.26
P14	194.6	4.8	1.95
P15	209.0	4.1	0.83
P16	215.9	4.5	0.88
P17	220.5	3.2	0.87
P18	237.6	27.6	3.24
P19	263.2	43.1	4.87
P20	292.7	26.8	5.60
P21	309.0	9.8	0.45
P22	325.3	17.9	6.68
P23	340.9	20.6	1.90

Table 4.2.1: Center frequencies ω_0, dampings γ and the oscillator strengths $\Omega = \omega_p^2$ (at $T = 10\,\mathrm{K}$) of the Lorentz terms utilized in the fits of the optical conductivity $\sigma_1(\omega)$ of Cd_3As_2 to model the phonons P1-P23.

$1085\,\mathrm{cm}^{-1}$ with negative coupling $q \approx -1$[3] and a Dirac interband term (D-IB) according to Eq. 2.6.3 with $N_\mathrm{W} = 4$, $v_\mathrm{F} = 3.7 \times 10^5\,\mathrm{m\,s}^{-1}$, $\Delta_\mathrm{E} = 825\,\mathrm{cm}^{-1} = 102\,\mathrm{meV}$. The single contributions to the optical conductivity at 10 K are depicted in Fig. 4.2.6

[3]The asymmetric Fano line shape occurs when a discrete state couples to a continuum of excitations at the same energy [160]. The optical conductivity of such a resonance minus the background can be described as [161]: $\Delta\sigma_1(\omega) = \frac{\omega_p^2}{4\pi\Gamma}\frac{q^2+2qz-1}{q^2(1+z^2)}$ with $z = 2(\omega-\omega_0)/\Gamma$. Here, Γ is the linewidth, ω_0 is the center frequency and ω_p is the plasma frequency of the resonance. q denotes a dimensionless coupling parameter. For $q \to \infty$ the Lorentz shape is recovered.

(f). Note, that the observation of Fano shaped modes was recently also reported in other Dirac and Weyl materials as, TaAs [162] and Graphene [161, 163].

The attempt to apply the same model to the 300 K spectrum works well for a wide frequency range as revealed by panel (d) in the same figure. The fit depicted in this panel contains the same terms as before. The coupling of the Fano term decreased slightly to $q \approx -1.5$ and the damping of the Dirac interband onset increased as did Δ_{E}. In the range of the Lorentz term, where the anomalous temperature dependence is observed (emphasized by the light blue circle), the fit does not describe the spectra well. Even though all the phonons contributing in that range (P17-P23) are set to zero oscillator strength, the fit overestimates the real conductivity.

To get further insight into the temperature dynamics in the intermediate spectral range, the Drude and phonon contributions (dashed gray lines in Fig. 4.2.6 (b,d)) are subtracted from the optical conductivity $\sigma_1(\omega)$ at $T = 300\,\mathrm{K}$ and 10 K. The resulting spectra are depicted in Fig. 4.2.6 (c). From these spectra the spectral weight $SW = \int_0^\infty \sigma_1(\omega)\mathrm{d}\omega$ is calculated. The normalized spectral weight $SW(10\,\mathrm{K})/SW(300\,\mathrm{K})$ displayed in Fig. 4.2.6 (e), then reveals the redistribution, without perturbations from the Drude dynamics. From panel (e), it is evident, that a portion of charges (or dipoles) get more mobile upon cooling, while another portion gets more localized. At $2500\,\mathrm{cm}^{-1}$ the spectral weight is conserved, meaning all the dynamics happen below this energy scale. It is hard to imagine, that the spectral weight of the same electronic system is redistributed to lower *and* higher energies. In other words, to understand the temperature dependent structures in the intermediate spectral range, two subsystems need to be considered.
It is yet unresolved, which electronic excitations or transitions are responsible for the features just discussed. A first candidate are the transitions between the trivial bands found along N-Γ (see Fig 4.1.1 (b)). Even though the direct gap between these bands in the bandstructure calculations of Ref. [145] appears slightly too high $\approx 100\,\mathrm{meV} \approx 800\,\mathrm{cm}^{-1}$, aside from the Dirac bands, they are the only ones that are found in a reasonable energy distance to E_{F}.
Second, in the Kane model, extensively discussed for the bandstructure in Cd_3As_2 [95, 138, 144, 153, 156, 157], a heavy hole band illustrated as brown line in Fig. 4.2.7 has two band touching points with the conduction band. The transitions from this hole band to the conduction band (black arrow) would be candidates for the observed structures in the optical conductivity between intraband and interband frequency

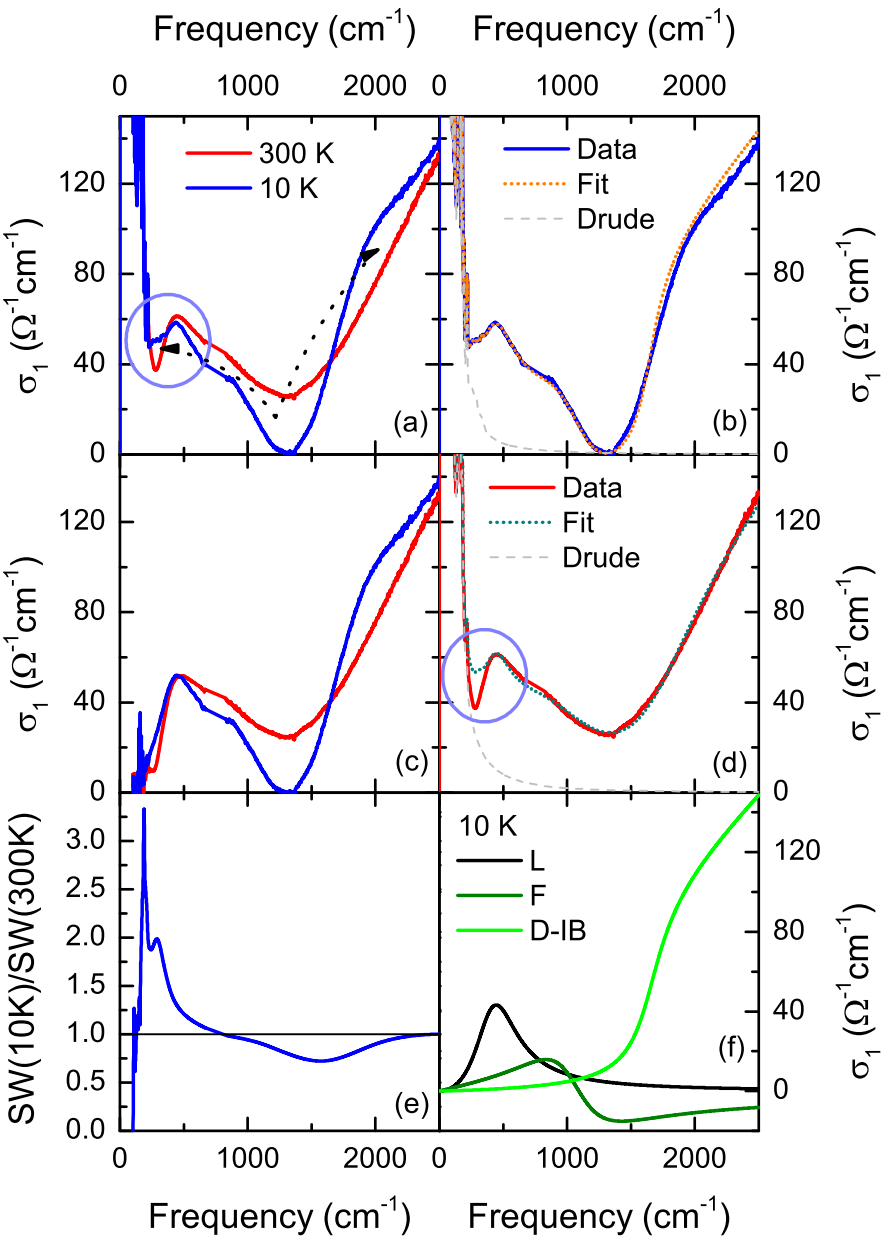

Figure 4.2.6: In the intermediate frequency range, $\sigma_1(\omega)$ exhibits an anomalous temperature dependence (see light blue circle) and unconventional spectral weight transfer (a,e). While the 10 K spectrum up to 2500 cm^{-1} can nicely be fit with a Lorentz term (L), a Fano resonance (F) and a Dirac interband term (D-IB) additional to the interband Drude and the phonons (gray dashed line) (b,f), this approach fails to capture the anomalous temperature dependence below 450 cm^{-1} (d). The normalized spectral weight in frame (e) is calculated from the Drude subtracted spectra (c).

ranges. Then the 'interband' conductivity corresponds to the transitions from the red valence to the blue conduction band. The question is, where in this situation the second hump in $\varepsilon_1(\omega)$ at E_L stems from.
Hence, the exact model suitable to describe the bandstructure of Cd_3As_2 remains puzzling. The origin of the anomalous temperature dependence and spectral weight redistribution, as well as the details of the mechanism responsible for the appearance of a Fano shaped resonance are also unresolved to date and further investigations are necessary to clarify these issues.

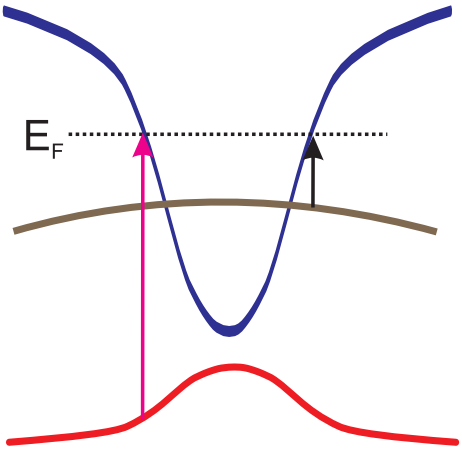

Figure 4.2.7: Schematic bandstructure for Cd_3As_2 in the Kane model with an additional heavy hole band (brown) crossing the conduction band. The transitions indicated with black arrows are possible candidates for the structures observed in $\sigma_1(\omega)$ at intermediate frequencies, while the transitions marked in pink are responsible for the interband part of $\sigma_1(\omega)$.

4.3 Conclusions

In conclusion, the interband optical conductivity of Cd_3As_2 reveals Dirac bands with a sub-linear dispersion. We find evidence that the "Lifshitz gap" is approx. 370 meV. The intraband conductivity can be well described with a single Drude term. The temperature dependence of the Drude parameters indicates scattering rate dominated transport characteristics. The effective mass m^* of the carriers is deduced from the inter- and intraband optical conductivities (see Tab. 4.3.1). To fit the intraband part satisfactorily, 23 Lorentz terms are introduced to account for lattice vibrational features.
In the intermediate frequency range, where neither the Drude nor the interband transitions between the Dirac bands contribute significantly to the optical conductivity $\sigma_1(\omega)$, the spectra reveal an anomalous temperature dependence and spectral weight transfer. The analysis evidences, that two subsystems contribute to the conductivity in this frequency range. The exact mechanisms remain, however, puzzling to date.

Tab. 4.3.1 summarizes values of the characteristic quantities extracted in this work and compares them with values found in literature.

RRR	N ($10^{17}\,\frac{1}{\mathrm{cm}^3}$)	v_F ($10^5\,\frac{\mathrm{m}}{\mathrm{s}}$)	Δ_E (meV)	m^* (m_e)	Ref.
5.5	≈ 3	7.6 (@nodes)	106 (@10 K)	0.03 (IB) 0.0065 (ω_p)	this, O, T
- -	1 8	9.3 9.3	100 200	0.02 0.04	[95], MO, O
-	52	15 ($k_{x,y}$) 1 (k_z)	200	-	[33], ARPES
781	91	9.3	232	-	[148], MT
5.5	53	11	-	0.044	[48], MT
-	1.3	-	96	-	[80], O
-	17	10	286	0.05	[152], MT
-	10	15	-	0.023	[164], MT
-	25	8.8	192	0.044	[36], MT
-	-	7.6	150	-	[7], ARPES
-	-	13 ($k_{x,y,l}$) 3.3 ($k_{z,l}$) 7.6 ($k_{x,y,u}$) 2.3 ($k_{z,u}$)	-	-	[8], ARPES

Table 4.3.1: Summary of the characteristic quantities of Cd_3As_2 found in this work and extracted from references. The abbreviation (M)T, O, MO, and ARPES stand for (magneto)-transport, optics, magneto optics, and angle resolved photoemission spectroscopy and point out, which technique was used to determine the values. The (IB) and (ω_p) denote the values extracted from the interband conductivity and Drude plasma frequency, respectively. The $k_{x,y,z}$ denote the momentum direction where the Fermi velocities are determined, and the indices l and u refer to the lower (valence) and upper (conduction) cones.

5. The Weyl semimetal NbP

In this chapter, first, the material NbP will be introduced in Sec. 5.1 and the state of research will be reviewed. Second, in Sec. 5.2 the experimental results will be presented. Finally, in Sec. 5.3 the findings will be concluded and discussed in the context of published theoretical and experimental investigations.

5.1 The material

NbP belongs to a class of binary compounds which comprises, next to TaAs, TaP and NbAs. All of these compounds share the same crystal structure, but feature subtle differences in terms of fermiology, due to varying amounts of spin-orbit coupling. In this sense, NbP and TaAs mark the corner stones of this novel material class, since those two exhibit the least and largest amount of spin-orbit coupling, respectively, as Nb and P are rather light elements compared to Ta and As. The spin-orbit coupling plays an important role for the appearance of Weyl nodes in NbP (as well as the other materials of this class) and will be further illuminated in this section. First, however, the crystal structure of NbP will be discussed.

NbP crystallizes in a body centered tetragonal symmetry with the space group $I4_1md$ (No. 109), the lattice parameters are $a = 3.3324\,\text{Å}$ and $c = 11.3705\,\text{Å}$ [165]. The unit cell is illustrated in Fig. 5.1.1 (a). It is important to note, that the structure is lacking an inversion center. The corresponding bulk Brillouin zone hosts two mirror planes marked blue and yellow in Fig. 5.1.1 (b).

The interplay of the broken inversion symmetry with the spin-orbit coupling generally can lead to the splitting of the Bloch bands almost everywhere in the Brillouin zone due to the lifting of the spin degeneracy [166].

This effect is observed in various calculations, comparing the bandstructure without and with inclusion of the spin-orbit coupling in this family of non-centrosymmetric mono pnictides [28, 167, 168]. In the following a review of the relevant results for NbP, following these references will be presented.

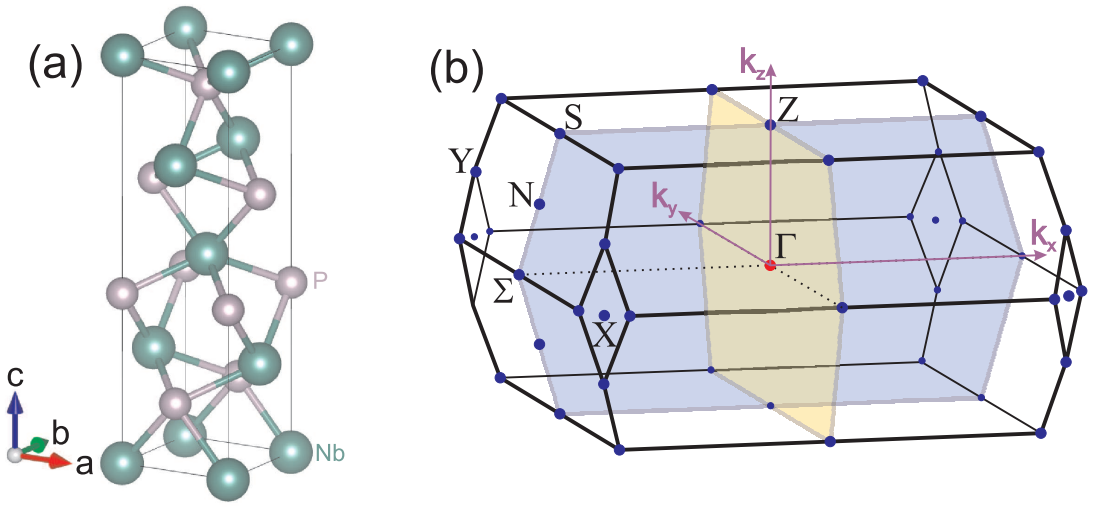

Figure 5.1.1: The unit cell of NbP drawn with VESTA [146] according to crystallographic data from Ref. [165] (a). The niobium atoms are depicted as large green spheres, while phosphorus has accordingly a smaller diameter and is depicted in gray. Note the lack of an inversion center in the unit cell. Panel (b) depicts the corresponding bulk Brillouin zone with the high symmetry points labeled [28]. Blue and yellow shaded planes represent the mirror planes $k_x = 0$ and $k_y = 0$.

In the absence of spin-orbit coupling it is found, that the valence and conduction bands cross, and form closed nodal rings bound to the mirror planes $k_x = 0$ and $k_y = 0$ as illustrated in Fig. 5.1.2 (a) and (c). The rings depicted in panel (c) are in the $k_x = 0$ plane, while the rings in the $k_y = 0$ plane can be found by performing a C_4 rotation. Away from the high symmetry lines, no accidental band crossings are found.
With the inclusion of the spin-orbit coupling (SOC), in the generalized gradient approximation (GGA) calculations, the band crossings disappear, and valence and conduction band become fully gapped along the high symmetry lines (Fig. 5.1.2 (b)). The nodal rings are consequently also gapped almost everywhere, but three pairs of Weyl nodes per loop remain, illustrated as red dots in Fig. 5.1.2 (c). In total two species of Weyl points, inequivalent by symmetry, are found away from the Fermi energy E_F, and away from the high symmetry planes.

The Fermi surfaces that are formed by the trivial hole (red) and electron (blue) pockets are depicted in Fig. 5.1.2 (d). In their shape altogether the Fermi surfaces are reminiscent of the nodal loops that appear, when spin-orbit coupling is absent.

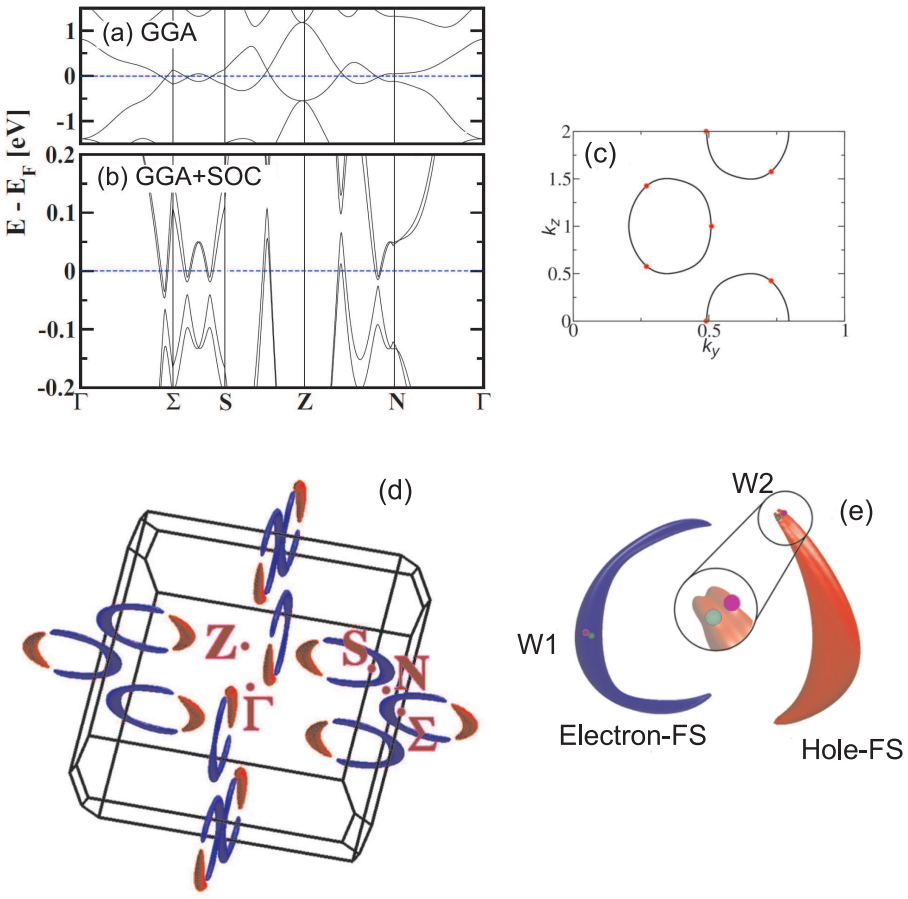

Figure 5.1.2: Bandstructure and Fermi surfaces of NbP from generalized gradient approximation calculations (GGA) with and without spin-orbit coupling (SOC) according to Refs. [28, 167, 168]. Panels (a) and (b) emphasize the drastic effect of the spin-orbit coupling on the bandstructure. The nodal rings get gapped and three pairs of Weyl nodes emerge per loop, illustrated by the red solid circles in panel (c), when spin-orbit coupling is included. The Fermi surfaces of the hole and electron pockets are depicted in panel (d) in red and blue, respectively. The Weyl nodes W1 are enclosed in the electron Fermi surfaces, while the W2 nodes sit in the hole Fermi surfaces [49]. Panels (a), (b), (d) are adapted with permission from Ref. [167]; copyright (2015) by the American Physical Society. Panel (c) is adapted with permission from Ref. [168]; copyright (2015) by the American Physical Society. Panel (e) is adapted with permission from [49]; copyright (2016) by the American Physical Society.

The trivial hole pockets form flat banana shaped surfaces and the electrons flat half circles. The interplay of the missing inversion center and the spin-orbit coupling leads to the doubling of the Fermi surfaces, meaning each Fermi surface in Fig. 5.1.2 (d) encloses another one that is concentric, which is not seen in the figure. Note, that since the Weyl points are not at E_{F}, they will also form small Fermi surfaces. The Weyl points are characterized by a chirality of ± 1. Mirror images of Weyl nodes possess opposite chirality, while those related by rotational or time reversal symmetry have the same chirality. The two species of Weyl cones are commonly referred to as W1 and W2. The W1 Weyl points are found within the electron-like Fermi surfaces and the W2 nodes are enclosed in the hole-like Fermi surface, as depicted as solid circles in Fig. 5.1.2 (e) [49]. The green and purple color denote the different chirality of the Weyl nodes.

In total, 24 Weyl points are found in the Brillouin zone (meaning 12 pairs of nodes with opposing chirality). The W1 Weyl points belonging to cones of opposing chirality are located in the $k_z = 0$ plane separated by the $\Sigma - \Gamma$ line close to the Σ point. By the fourfold rotational symmetry it is clear, that there exist 8 W1 nodes in the Brillouin zone, as illustrated in Fig. 5.1.3 (a) and (b). The W2 points are located at a general $\vec{k}$ point off the $k_z = 0$ plane, and in total 16 nodes are found. In the top view, on the (001) pane in Fig. 5.1.3 (b) it is illustrated, that the k-splitting between the mirror pairs of the Weyl nodes is larger for W2 than for W1 which is generally the case in this family of non-centrosymmetric transition metal mono-pnictides [168, 169]. With increasing amount of spin-orbit coupling, the k-splitting increases for both species of Weyl nodes, meaning in TaAs the nodes are separated further than in NbP [47, 169].
It is evident from quantum oscillations studies, ARPES and theoretical calculations, that the W1 nodes possesses lower energy than the W2 nodes, which is true for all compounds of this family [28, 49, 167, 168, 170]. In particular in NbP it was found, that the W2 nodes possess a small positive energy distance $\Delta_{E,\mathrm{W2}}$ to the Fermi energy E_{F}. For the W1 nodes, $\Delta_{E,\mathrm{W1}}$ is much larger and negative, meaning they are located below E_{F} [49, 171]. The dispersions around W1 and W2 are schematically illustrated in Fig. 5.1.3 (c).

As it was pointed out in Sec. 1, Weyl fermions should exhibit exceptional topological surface states, namely the Fermi arcs, connecting Weyl nodes of opposite chirality in the bulk via the crystal surface. In NbP the topological surface states were in

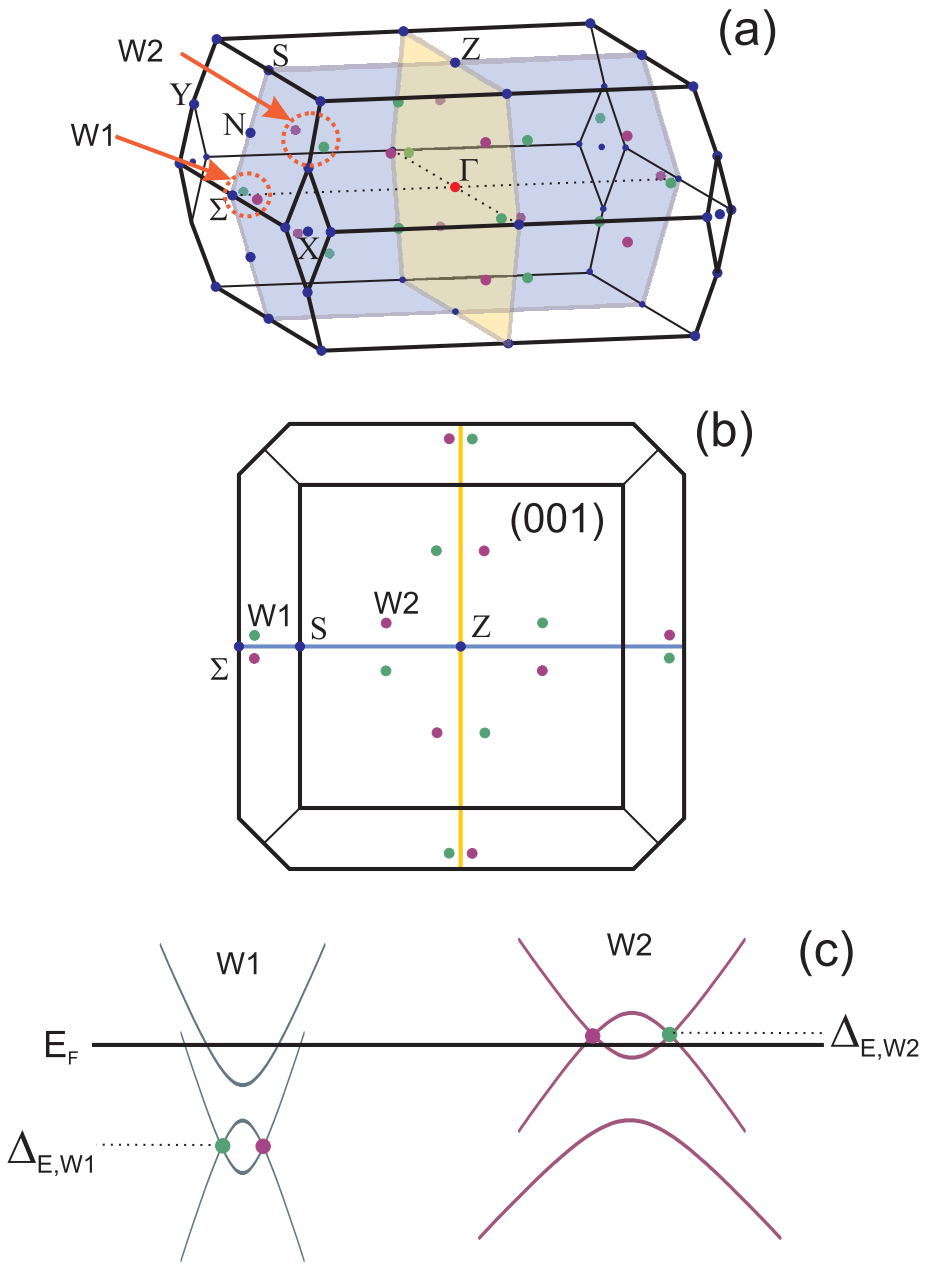

Figure 5.1.3: Schematic representation of the locations of the 24 Weyl nodes in the Brillouin zone (a) [28, 170]. The green and purple solid circles denote the Weyl nodes of opposite chirality. The W1 nodes are located in the k_z plane close to the Σ point, while the W2 nodes are found at a general k point. The top view on the Brillouin zone emphasizes the different distances in k of W1 and W2 nodes which are related by mirror symmetry (b) [28]. Panel (c) schematically illustrates the locations of W1 and W2 nodes with respect to the Fermi energy E_F [49].

detail discussed in *ab initio* calculations and observed in ARPES measurements [47, 169, 171, 172]. The second remarkable prediction of a non-conserved chiral charge in presence of parallel magnetic and electric fields, the chiral anomaly, was very recently reported in Ga-doped NbP [173]. The Ga doping is thereby necessary, to shift the Fermi energy E_F closer to the Weyl nodes, in order to assure a well defined chirality [49, 174].

Many Dirac and Weyl semimetals exhibit extremely high mobilities (e.g. Cd_3As_2 [148], Na_3Bi [175]) which is ascribed to large Fermi velocities v_F of the massless particles and a suppressed back scattering probability. For the extremely high mobility in NbP, possibly also the almost perfect electron-hole compensation plays an important role [170, 176], which is also discussed to be responsible for the linear non-saturating magneto-resistance and high mobility in the type II Weyl semimetal candidate WTe_2 [177].

5.2 NbP: Results and Discussion

In the following the results that were obtained on high quality single crystals of NbP in this work will be presented. The samples were provided by Dr. Ralph Hübner, of the FMQ at the University of Stuttgart[1]. Transport and magneto-transport data were contributed by Anja Löhle from PI1[2]. The optical and magneto-optical measurements were performed by the author, except from the zero field measurements in the MIR and NIR, which were conducted by Weiwu Li from the PI1.

5.2.1 Transport properties

T-dependent resistivity

First, the temperature dependent resistivity $\rho(T)$ in the isotropic (001) plane of NbP will be discussed. The transport measurements were conducted in four-contact geometry on a sample of the same batch as the sample utilized for the optical and magneto-optical measurements. Fig. 5.2.1 (a) displays $\rho(T)$ from room temperature down to liquid helium temperatures. A clear metallic behavior is observed. For $T \geq 150\,\mathrm{K}$ the resistivity increases linear in temperature, emphasized by the orange solid

[1] Institut für Funktionelle Materie und Quantentechnologien - Universität Stuttgart
[2] 1. Physikalisches Institut - Universität Stuttgart

line. This behavior is commonly expected for metals above the Debye temperature, and indicative for predominant electron-phonon scattering. The inset of Fig. 5.2.1 (a) enlarges the low temperature region of the resistivity $\rho(T)$ and reveals a residual resistivity of the order $\rho_0 \approx 0.55\,\mu\Omega$cm, which is of the same order as in other reports [170, 176, 178]. The residual resistivity ratio $RRR = [\rho(300\,\mathrm{K})/\rho_0] \approx 40$ of our sample reaches only half of the best reported values [170, 176, 178]. This indicates a larger impurity concentration in the sample investigated in this work. Interestingly, the extremely high carrier mobility was found to be rather independent of the RRR in NbP and persists even in samples with lower residual resistivity ratio [178].

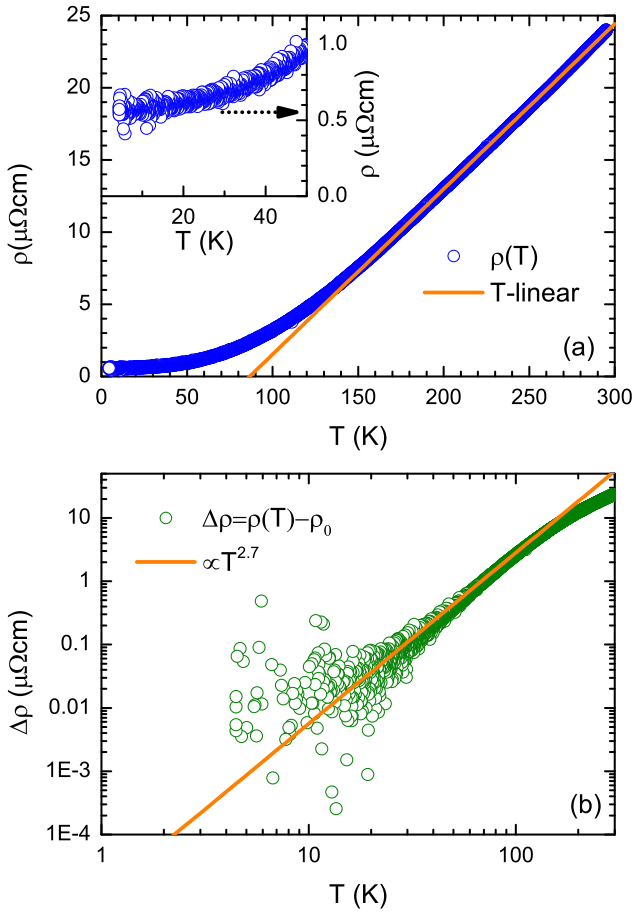

Figure 5.2.1: The temperature dependent resistivity $\rho(T)$ of NbP is displayed as blue circles in panel (a). The orange line emphasizes the T-linear behavior above $T \geq 150\,\mathrm{K}$. The insert reveals a very low residual resistivity of $\rho_0 \approx 0.55\,\mu\Omega$cm. Panel (b) depicts $\Delta\rho = \rho(T) - \rho_0$ on a double logarithmic scale. The orange line in this panel reveals the power law $\propto T^{2.7}$ below 150 K, which is indicative for the importance of electron-electron interactions and the temperature dependence of the chemical potential in NbP.

Fig. 5.2.1 (b) displays $\Delta\rho = \rho(T) - \rho_0$ on a double logarithmic scale. The orange solid line in this plot reveals a power law behavior of this reduced resistivity $\Delta\rho \propto T^{2.7}$ for $T \lesssim 150\,\mathrm{K}$ in good agreement with the findings in Ref. [178]. A predominant electron-phonon scattering in metals yields a resistivity $\propto T^5$ at low temperatures. Hence, there have to be limiting mechanisms. One aspect are the electron-electron

interactions that are expected to play a non negligible role for 3D Weyl particles [70]. As it is well known, in case of an interacting electron liquid (Fermi liquid) the resistivity follows a T^2 behavior at low temperatures.
If correlations are important, the mass m of the carriers is renormalized ($m \rightarrow m^*$). The effective mass m^*, is in general temperature dependent ($m^*(T)$), as widely observed in heavy fermion compounds (e.g. $CeAl_3$ [179]).
In semimetals the chemical potential (or Fermi energy E_F), is temperature dependent in general [75], and in NbP in particular [167]. This means, that additionally to the temperature dependent relaxation time $\tau(T)$ and the temperature dependent effective mass $m^*(T)$ the carrier density N, cannot be assumed to be constant but enters as another temperature dependent factor in[3]

$$\rho(T) = \frac{m^*(T)}{N(T)\tau(T)e^2}. \tag{5.2.1}$$

Therefore, the interpretation of the temperature dependence of the resistivity $\rho(T)$ in NbP is highly non-trivial.

T-dependent resistivity in magnetic fields

To gain a deeper insight into the properties of the carriers in NbP, magneto-transport measurements were performed. Fig. 5.2.2 (a) displays the temperature dependence of the in plane resistivity $\rho_{xx}(T)$ at various magnetic fields applied along the c-direction ($B \perp (001)$, see inset). The resistivity was measured in the (001) plane. Already fields as small as $B = 0.1\,\mathrm{T}$ induce drastic changes in the resistivity $\rho(T)$. In magnetic fields, NbP exhibits semiconducting behavior below an onset temperature T^* that can be defined as the temperature, where the resistivity changes slope from positive to negative. The onset temperature T^* grows monotonous, and exceeds the measured temperature range at fields larger than $B = 4\,\mathrm{T}$, and the resistivity behaves like that of a semiconductor for higher fields. Note, that for the fields $B \geq 2\,\mathrm{T}$ at low temperatures a second decrease in the resistivity is observed in our measurements, which, however, is not consistent with the reports in Refs. [170, 176]. Similar anomalies were observed for other compounds in this family of materials and other high mobility compounds [6, 174, 180, 181]. These anomalies are likely arising from current jetting effects [32, 174, 181]. Therefore the data in Fig. 5.2.2 (a) for $B \geq 2\,\mathrm{T}$ is cut to avoid misleading impressions. Furthermore, cutting out the high field data

[3] with Eq. 2.3.4 and $\rho = 1/\sigma_{DC}$

does not perturb the further analysis of the resistance in magnetic fields.
The crossover from metallic to semiconducting behavior with increasing magnetic fields appears to be common in these non-centrosymmetric mono pnictides and is reported for all compounds of the family [6, 170, 174, 176, 180]. The development from metallic to an insulating characteristic of the resistivity with increasing magnetic fields is not unique to the Weyl semimetals, but was observed recently in various large magneto-resistance and high mobility compounds [177, 181–186].
A first naive approach to elucidate the nature of this 'metal to insulator transition' is, to analyze the thermal-activation-like behavior in the semiconducting regime of the $\rho_{xx}(T)$ curves, to extract the relevant energy scale. For semiconductors, the gap energy E_g can usually be estimated, since the resistivity follows an Arrhenius type temperature dependence [187]

$$\rho_{xx}(T) = \rho_0 e^{\frac{E_g}{k_B T}}, \tag{5.2.2}$$

where ρ_0 is a multiplicative factor, and k_B denotes the Boltzmann constant. Note, that the E_g in Eq. 5.2.2 is related to the band gap energy E_{bg} via $E_{bg} = 2E_g$. Applying the natural logarithm to Eq. 5.2.2 enables direct access to the gap energy E_g. Therefore, Fig. 5.2.2 (b) displays $\ln \rho_{xx}$ versus the inverse temperature T^{-1}, where the thermal activated behavior according to Eq. 5.2.2 should appear linear. Indeed for magnetic fields $B \neq 0$, Fig. 5.2.2 (b) reveals quasi linear sections, emphasized by the red dotted lines. From the derivative $d \ln \rho_{xx}/dT^{-1}$ in Fig. 5.2.2 (c) it is clear, that the linearity is not well defined, since the curves do not exhibit constant values over broader temperature ranges. The poor linearity could be ascribed to several bands with different gaps that have to be taken into account. However, there is yet no final conclusion in the community concerning the magnetic field induced gap-like behavior depicted in Fig. 5.2.2 (b), and the overall unconventional magneto-transport properties discussed in the next paragraph. The maximum slope in $\ln \rho_{xx}(T^{-1})$ (Fig. 5.2.2 (b)) and equivalently the peak heights in Fig. 5.2.2 (c) can be interpreted as a maximum gap value. The magnetic field dependence of this maximum gap, determined from the steepest slope of the curves in Fig. 5.2.2 (b), is depicted in Fig. 5.2.2 (d). The red line represents a $\sqrt{B}$ fit of E_g and is reminiscent of the behavior expected for the magnetic Landau levels in the Weyl bands (see Sec. 2.7.2).

Aside from the development of E_g with the magnetic field B, Fig. 5.2.2 (c) also reveals the development of the transition temperature T^* that shows up as zero crossings in $d \ln \rho_{xx}/dT^{-1}$. For the $B \geq 4\,\mathrm{T}$ curves an estimation of T^* can be made by extrap-

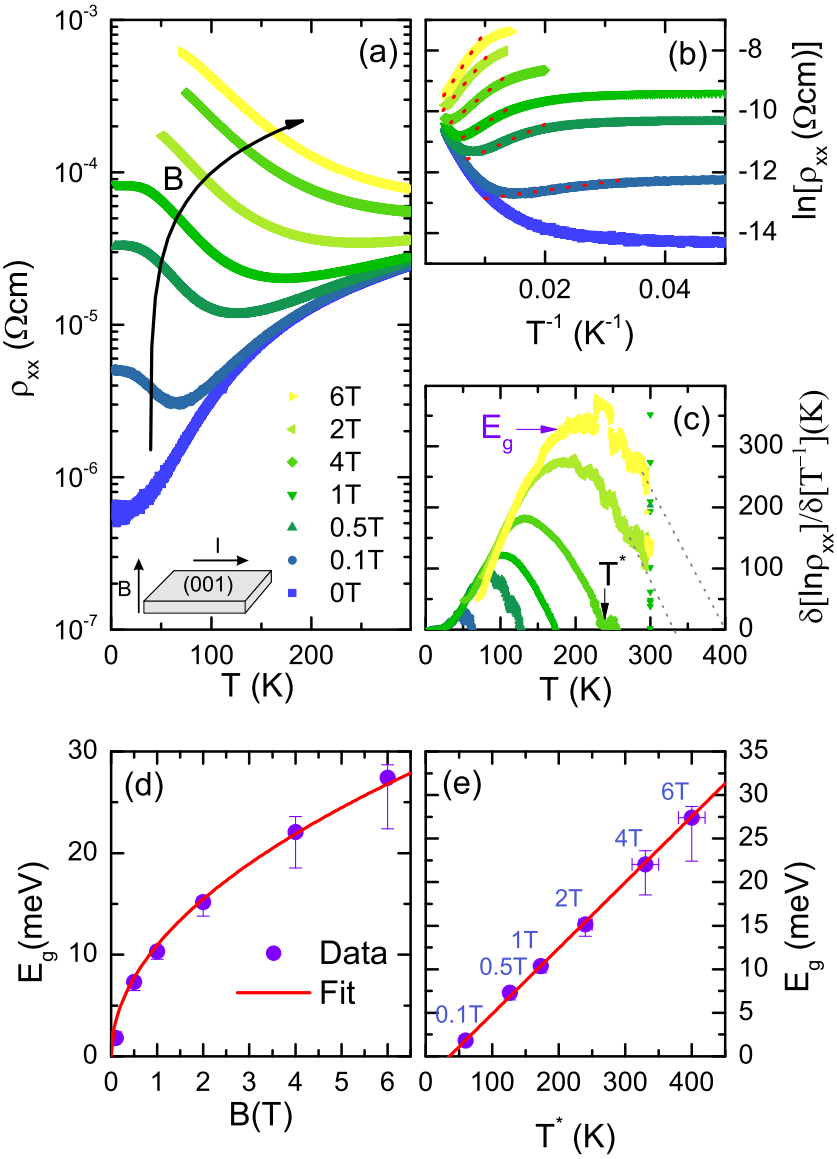

Figure 5.2.2: The temperature dependent in-plane resistivity $\rho_{xx}(T)$ exhibits a transition from metallic to insulating behavior in magnetic fields applied along the c-axis (a). The onset temperature T^*, defined as the minimum, is increasing monotonous in field B. The Arrhenius plot in panel (b) reveals the thermal activated characteristic as quasi linear regions of the displayed curves emphasized by dashed red lines. From the derivative $d \ln \rho_{xx}/dT^{-1}$ in panel (c) the maximum gap E_g is obtained. E_g exhibits a $\sqrt{B}$ dependence (d), reminiscent of the Landau level behavior in Weyl cones. The temperatures T^*, corresponding to the zero crossing in panel (c), and the height of the maxima, corresponding to E_g, share a linear relation displayed in panel (e). Violet solid circles in (d) and (e) correspond to data points, red lines to fits (see text).

olating the curves linearly as indicated by the dashed black lines in Fig. 5.2.2 (c). From Fig. 5.2.2 (e), the transition temperature T^* and the gap E_g can be related linearly. The fit (red line) reveals, that the gap value does not extrapolate to zero for $T = 0$. Nonetheless, the slope of the fit yields $E_g = 1.1 k_B T^*$. The linear scaling of T^* and E_g implies, that T^* evolves also with $\sqrt{B}$ and either quantity defines the relevant energy scale.

Note, that in highly oriented pyrolitic graphite the magnetic field induced insulating behavior was ascribed to an excitonic insulator phase that gaps the quasiparticle spectrum and creates a site-centered charge density wave [188]. Even though in the proposed model the characteristic $\sqrt{B}$ dependence of the gap as well as of the transition temperature occurs, it has to be dismissed in the present case of NbP, since the chiral Weyl cones can not be gapped unless two cones of opposing chirality are translated to the same position in the reciprocal space (see Sec. 1).

Hall effect and transverse magneto-conductivity

A far more common approach to analyze the magneto-transport properties, found in literature, is the fitting of the field dependent diagonal and off-diagonal elements of the Hall resistivity tensor $\rho_{xx}(B)$ and $\rho_{xy}(B)$ with a single, or multi band model. Hence, following the lines of many other works (e.g. [170, 176, 178]), the data in this work is also analyzed in this regard. Note, that the discussion above, about a magnetic field induced gap, and the analysis in the following, in a picture of free carriers, are contradicting each other, and yet none of them is fully satisfying.
The transverse magneto-resistance $MR = [\rho_{xx}(B) - \rho_{xx}(B = 0)] / \rho_{xx}(B = 0)$ is displayed in Fig. 5.2.3 (a) and (b) for $T \leq 150\,\mathrm{K}$ and $T \geq 200\,\mathrm{K}$, respectively. The investigated sample exhibits an extremely high magneto-resistance at $T = 4.5\,\mathrm{K}$ and $B = 6.5\,\mathrm{T}$ of $MR = 1.4 \times 10^3$. This compares well with other reported values in NbP at similar fields and temperatures [170, 176, 178]. Note, that sample to sample variations reflecting the differences in the RRR are, however, evident in these references. Though the MR is extremely large in NbP, the record is held by WTe_2 [189], which exhibits a MR of 3.1×10^4 at $B = 10\,\mathrm{T}$ and low temperatures for highest RRR samples [190], but still, also values of the MR are reported, that are an order of magnitude lower [191]. Fig. 5.2.3 (a) also reveals pronounced Shubnikov-de Haas (SdH) oscillations in the 4.5 K and 10 K curves. This agrees with the finding, that the MR is sensitive to the RRR, but the SdH oscillation amplitude is barely af-

fected in NbP [178]. Surprisingly, the magneto-resistance of the investigated sample at $T = 300\,\mathrm{K}$ and $B = 6.5\,\mathrm{T}$ of $MR = 3$ (see Fig. 5.2.3 (b)) is even exceeding the reported values of the samples with the highest RRR [170, 176].

In most of the compounds exhibiting extremely large, transverse magneto-resistance, as for instance WTe_2 [177], $NbSb_2$ [185] or $TaAs_2$ and $NbAs_2$ [181], the MR increases quadratically with the magnetic field. The MR in NbP (as well as in the other compounds of the family [176, 192]) develops quasi linear in field as seen in Fig. 5.2.3 (a) and discussed in Refs. [170, 176, 178]. Commonly for metals, however, a quadratic saturating magneto-resistance is expected. The linear non-saturating behavior of the MR in NbP was suggested to arise from mobility fluctuations [176, 192, 193]. This effect is also discussed to be the origin for the linear magneto-resistance in the Dirac semimetal Cd_3As_2 [164].

The Hall resistivity $\rho_{xy}(B)$ displayed in Fig. 5.2.3 (c) reveals a change from positive to negative slope, indicating a change from hole dominated to electron like transport towards low temperatures. The temperature where this change in transport characteristic happens can best be determined from the temperature dependent Hall coefficient $R_H = \rho_{xy}(B)/B$, which is depicted for $B = 6.5\,\mathrm{T}$ in Fig. 5.2.3 (d). The zero crossing of R_H at $T \approx 125\,\mathrm{K}$ marks the crossover from hole to electron dominated transport, in excellent agreement with other experimental reports, as well as theoretical calculations [167, 170, 176, 178]. Therefore at least two carrier species need to be considered.
According to Kohler's rule, the magneto-resistance in case of two contributing carrier types is

$$MR = m\left(\frac{B}{\rho_0}\right)^{\beta}, \tag{5.2.3}$$

where m and β depend on the material and $\rho_0 = \rho_{xx}(B = 0)$, if both carrier types have the same scattering rate $1/\tau$ [158]. Fig. 5.2.3 (e) clearly demonstrates, that Kohler's rule is not satisfied in NbP. A change of the power β with temperature is observed, as exemplified by the linear fits to the 300 K and 4.5 K. Furthermore, a drastic change in slope is occurring at low fields. The deviation of the MR from Kohler's rule is evidence, that the two types of carriers are affected differently by different scattering mechanisms [158]. Therefore, a single carrier treatment is not appropriate, and a two-band-model needs to be applied for the further analysis of the magneto-transport data.

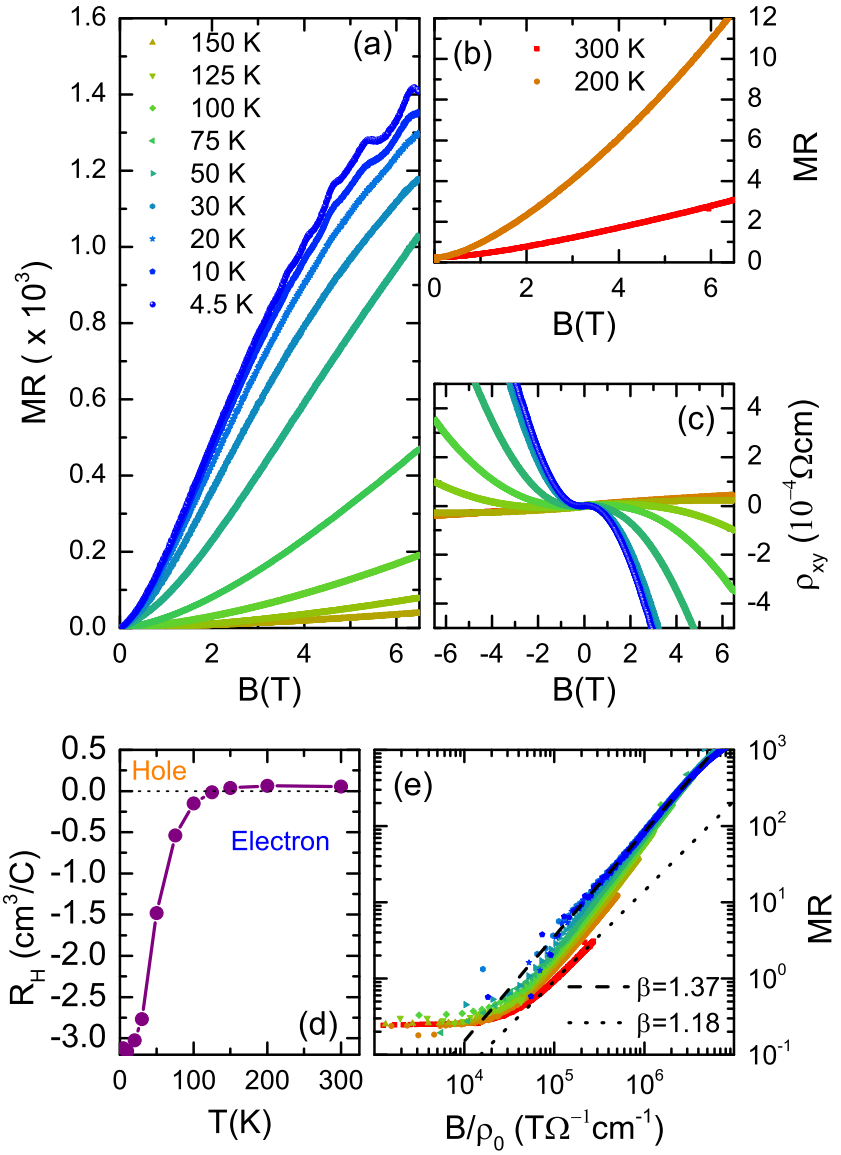

Figure 5.2.3: The magneto-resistance $MR = [\rho_{xx}(B) - \rho_{xx}(B=0)]/\rho_{xx}(B=0)$ *in NbP adopts an extremely large value at* $T = 4.5\,\mathrm{K}$ *and* $B = 6.5\,\mathrm{T}$ *of* $MR = 1.4 \times 10^3$ *(a). At room temperature, the resistivity at highest measured field still increases by a factor of* 3 *(b). The Hall resistivity* $\rho_{xy}(B)$ *(c) and the Hall coefficient (extracted at* $6.5\,\mathrm{T}$*)* R_H *(d) reveal a change from hole to electron like transport below approx.* $125\,\mathrm{K}$*. Kohler's rule states that* $MR = m\left(\frac{B}{\rho_0}\right)^{\beta}$ *if there is only one scattering rate* $1/\tau$*. The violation of this rule (e) indicates, that a two band model is required for the further analysis of* $\rho_{xx}(B)$ *and* $\rho_{xy}(B)$

The entries of the Hall conductivity tensor

$$\widehat{\sigma} = \begin{pmatrix} \sigma_{xx} & \sigma_{xy} \\ \sigma_{yx} & \sigma_{xx} \end{pmatrix} \tag{5.2.4}$$

relate to the measured transverse magneto resistivity $\rho_{xx}(B)$ and Hall resistivity $\rho_{xy}(B)$ as,

$$\sigma_{xx}(B) = \frac{\rho_{xx}(B)}{\rho_{xy}(B)^2 + \rho_{xx}(B)^2} \tag{5.2.5a}$$

$$\sigma_{yx}(B) = -\sigma_{xy}(B) = \frac{\rho_{xy}(B)}{\rho_{xy}(B)^2 + \rho_{xx}(B)^2}. \tag{5.2.5b}$$

The diagonal and off-diagonal elements $\sigma_{xx}(B)$ and $\sigma_{xy}(B)$ of the field dependent Hall conductivity tensor in a two carrier model are represented as (see e.g. [6, 158, 176, 181, 194, 195]):

$$\sigma_{xx}(B) = \frac{N_e \mu_e e}{1 + (\mu_e B)^2} + \frac{N_h \mu_h e}{1 + (\mu_h B)^2} \tag{5.2.6a}$$

$$\sigma_{yx}(B) = eB \left[N_h \mu_h^2 \frac{1}{1 + (\mu_h B)^2} - N_e \mu_e^2 \frac{1}{1 + (\mu_e B)^2} \right]. \tag{5.2.6b}$$

The indices e and h stand for the electron and hole like carriers, while N and μ denote the respective carrier concentrations and mobilities.

Fig. 5.2.4 (a) and (c) display the fits of the conductivity with Eqns. 5.2.6 for selected temperatures. For high temperatures decent fits (lines) to the data (symbols) are obtained. At low temperatures, however the low-field data point density appears to be too coarse to really judge the fit quality. In the inset of Fig. 5.2.4 (c), the measured $\sigma_{xx}(B = 0)$, as well as the total conductivity calculated from the fit parameters as, $\sigma_{xx} = e\left[\mu_e N_e + \mu_h N_h\right]$, are displayed. Large discrepancies are observed at low temperatures for the values obtained by the fits of $\sigma_{yx}(B)$ (solid blue circles), while those from the fits to $\sigma_{xx}(B)$ (open red circles) give a rather consistent picture. The deviations of the total conductivity from the measured $\sigma_{xx}(B = 0)$ are not surprising considering the insufficient data resolution at low temperatures.
The four free parameters in Eqns. 5.2.6, further hamper the acquisition of reliable absolute values from the fits, and hence the following discussions are to be taken

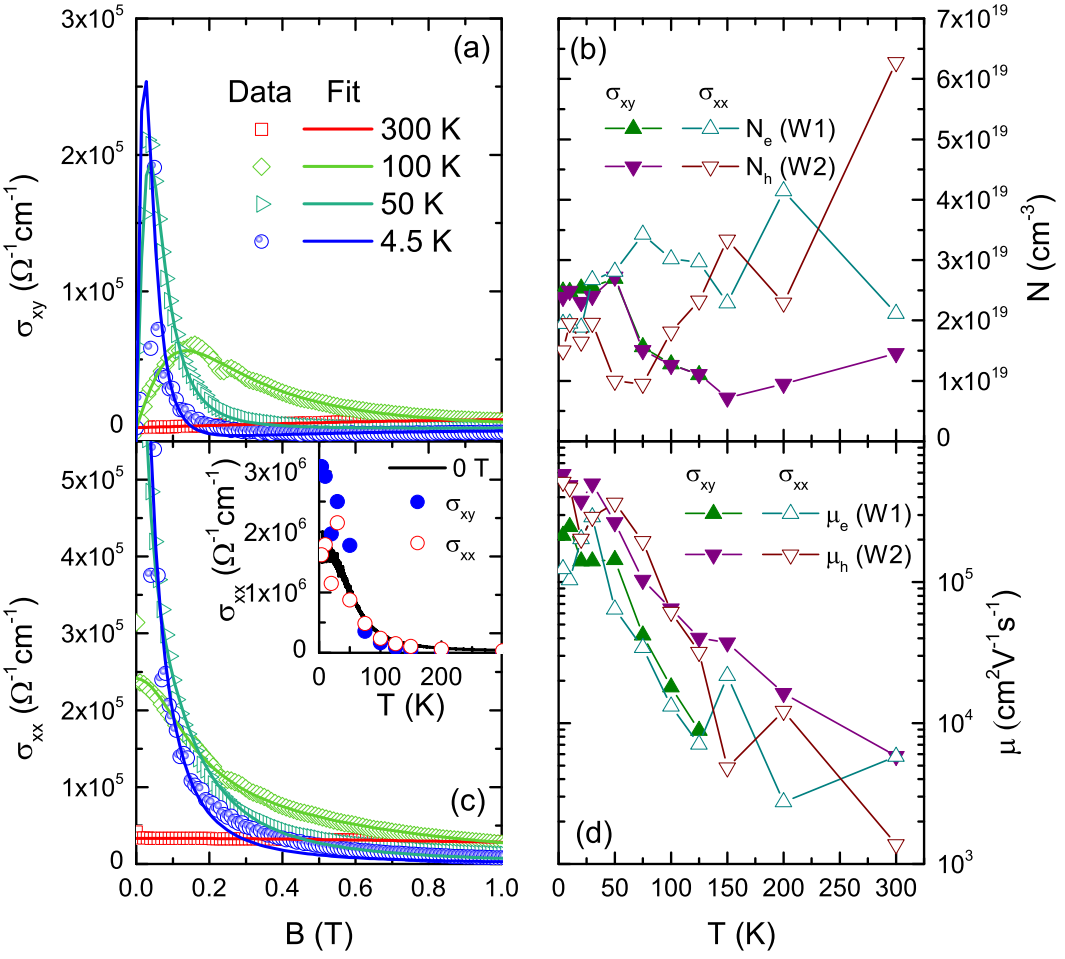

Figure 5.2.4: The fits to the $\sigma_{yx}(B)$ and $\sigma_{xx}(B)$ are presented in the panels (a) and (c), respectively. The inset of panel (c) displays the $\sigma_{xx}(T)$ at $B = 0\,\mathrm{T}$ together with the values calculated from the fit parameters via $\sigma_{xx} = e\,[\mu_e N_e + \mu_h N_h]$, to evaluate the self consistency of the fits. The carrier densities N_e and N_h are weakly temperature dependent and of the order of $2 \times 10^{19}\,\mathrm{cm}^{-3}$ (b). The mobilities μ_e and μ_h exhibit a strong temperature dependence and increase by two orders of magnitude over the measured temperature range. The hole mobility is on average higher than the electron mobility and takes values as high as $\mu_h \approx 5 \times 10^5\,\mathrm{cm}^2\,\mathrm{V}^{-1}\,\mathrm{s}^{-1}$.

with a grain of salt. Nonetheless, the fits allow determination of the approximate magnitude and the temperature developments of carrier densities and mobilities of the electrons and holes. Note, that the fits were applied over the whole field range. Fig. 5.2.4 (b) depicts the carrier densities obtained from the fits of $\sigma_{xy}(B)$ as filled symbols. The densities obtained by the fits of $\sigma_{xx}(B)$ are represented as open symbols. The electron densities N_e, are depicted as triangles pointing upwards and the hole densities N_h as triangles pointing downwards. Since it is evident, that the trivial bands play a negligible role in the DC transport, the carrier densities and mobilities can straightforwardly be assigned to the W1 cones in case of the electrons and to the W2 cones in case of the holes. Both carrier densities are in the order of $N_e \approx N_h \approx 2 \times 10^{19}\,\mathrm{cm}^{-3}$ and show no pronounced temperature dependence within the rather large uncertainties. Note that from the two band model of $\sigma_{xy}(B)$ no information about the electrons can be obtained above 125 K in the hole dominated transport regime.

The mobilities μ_e and μ_h, displayed in Fig. 5.2.4 (d) in the same style as the carrier densities reveal a drastic increase with decreasing temperatures for both carrier species. The hole mobility μ_h is roughly a factor of 2 to 5 larger than the electron motility μ_e and exhibits very high values of $\mu_h \approx 5 \times 10^5\,\mathrm{cm}^2\,\mathrm{V}^{-1}\,\mathrm{s}^{-1}$.

The mobility is related to the transport relaxation time τ via $\tau = \frac{m^*}{e}\mu$, where m^* is the effective carrier mass. Here, the cyclotron mass $m_c = 0.02\,m_e$ found in the magneto-optical measurements presented in Sec. 5.2.3, can be utilized for an estimation. With the Fermi velocity $v_\mathrm{F} = 3.0 \times 10^5\,\mathrm{m\,s}^{-1}$ found above for W2 the transport mean free path of the carriers $l_f = v_\mathrm{F}\tau$ can be obtained. The calculation yields $l_{f,h} = 1.7\,\mu$m for the carriers of the W2 cone at $T = 4.5$ K. This value is large compared to the mean free path, commonly found in metals (e.g. 9 nm in Nb [196]), however, still an order of magnitude smaller than in Cd_3As_2 [148]. The high mobility and large mean free path in the Dirac and Weyl semimetals are discussed to possibly arise from a mechanism that prevents back scattering of the carriers from impurities [148, 178].

5.2.2 Optical experiments

In this section the temperature dependent optical data of NbP without magnetic field will be discussed. The optical response was acquired on the as grown (001) surface of the crystal for frequencies $\omega = 40 - 25\,000\,\mathrm{cm}^{-1}$. Fig. 5.2.5 displays the reflectivity $R(\omega)$, the real part of the optical conductivity $\sigma_1(\omega)$ and the real part of

the dielectric function $\varepsilon_1(\omega)$ in the panels (a), (b) and (c), respectively. For clarity only the spectra of three temperatures, namely $T = 300, 150, 10\,\mathrm{K}$, are displayed in the main panels. Note the logarithmic frequency axes in all panels, as well as the logarithmic conductivity axis in frame (b). The reflectivity at high frequencies is only weakly temperature dependent. In the MIR and FIR below $3000\,\mathrm{cm}^{-1}$, moderate dynamics is observed. Two sharp features at $335\,\mathrm{cm}^{-1}$ and $369\,\mathrm{cm}^{-1}$ can be resolved. These sharp modes are better seen in real part of the optical conductivity $\sigma_1(\omega)$ in Fig. 5.2.5 (b) and are accentuated with black arrows. The peak positions are almost temperature independent, as revealed by the enlarged view in the inset of panel (b). The dotted black lines act as guide to the reader's eye. Both modes can be assigned to optical phonons mainly involving in-plane displacements of the P-atoms in the lattice [197, 198].
The metallic nature of NbP discussed in Sec. 5.2.1 manifests in a very high reflectivity at low frequencies as well as a peak at $\omega = 0$ in $\sigma_1(\omega)$ narrowing with decreasing temperature. The dielectric function $\varepsilon_1(\omega)$ correspondingly exhibits large negative values at low frequencies. The reflectivity exhibits a steep downturn at $\omega \approx 450\,\mathrm{cm}^{-1}$, reminiscent of plasma edge. In the same frequency range, the dielectric function $\varepsilon_1(\omega)$ in Fig. 5.2.5 (c) experiences a zero crossing. Hence, the screened plasma frequency can be estimated as $\omega_{p,scr} \approx 700 - 800\,\mathrm{cm}^{-1}$. Looking closely at the steep downturn of the reflectivity in frame (a), a shoulder-like structure can be identified at low temperatures.

The optical conductivity reveals a gap-like feature where the shoulder appears in the reflectivity, followed by a step towards higher frequencies. The permittivity $\varepsilon_1(\omega)$ also exhibits a kink-like structure (marked by a black arrow), which can be interpreted as a peak in the spectrum, that is superposed with the rapid decrease from the free carriers. The step in $\sigma_1(\omega)$, the peak in $\varepsilon_1(\omega)$, as well as the shoulder in the reflectivity all appear at the same frequency (emphasized by the vertical grey dotted line), and are hallmarks of the onset of interband transitions within a Weyl cone in case of finite chemical potential $\Delta_E \neq 0$ (see Sec. 2.6).
From the step towards higher frequencies a quasi linear increase of $\sigma_1(\omega)$ is found between $1000\,\mathrm{cm}^{-1}$ and $2200\,\mathrm{cm}^{-1}$ for all temperatures. This ω-linear increase is emphasized by the dashed black line in Fig. 5.2.6, where $\sigma_1(\omega)$ is depicted on a linear scale. This supports the interpretation of the step in $\sigma_1(\omega)$ as onset of Weyl cone interband transitions.
The ω-linear part does not extrapolate to zero, indicating, that the simple model of a single Weyl cone (Sec. 2.6.1) is not sufficient. Since it is yet unclear which cone(s)

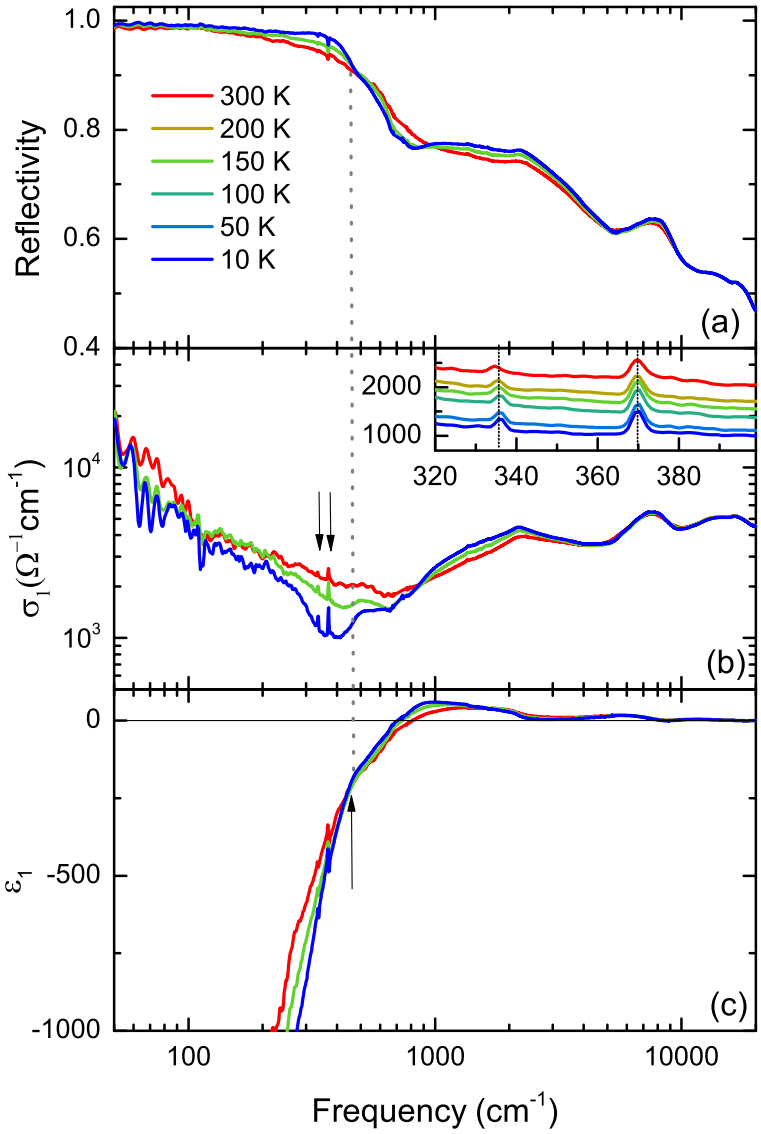

Figure 5.2.5: The temperature dependent reflectivity $R(\omega)$ (a), optical conductivity $\sigma_1(\omega)$ (b), and dielectric function $\varepsilon_1(\omega)$ (c) for selected temperatures. The inset of frame (b) highlights the temperature independence of the two phonons marked in the main frame with black arrows at 335 cm^{-1} and 369 cm^{-1}. The kink in the dielectric function (marked with an arrow in panel (c)), comes along with a step in the optical conductivity and a shoulder in the reflectivity. These features are reminiscent of the onset of the Weyl cone interband transitions with finite chemical potential (see Sec. 2.6).

contribute in the linear conductivity region, N_W is unknown and it is not appropriate to obtain a Fermi velocity from the slope of $\sigma_1(\omega)$ with Eq. 2.6.3.
To get quantitative information, the spectra are fit with the four-band model presented in Sec. 2.6, which is, due to the spin orbit split bands in NbP, the most appropriate of the available models. This model predicts distinct features in the optical response related to certain transitions within the Weyl bands. Consequently, prior to modeling, locating these subtle details of the spectra is crucial.
Before coming to that, one more comment: the optical response at higher frequencies is dominated by structures that straightforwardly can be assigned to interband transitions between lower valence and higher conduction bands. In the following, the analysis of these high energy features will be omitted.

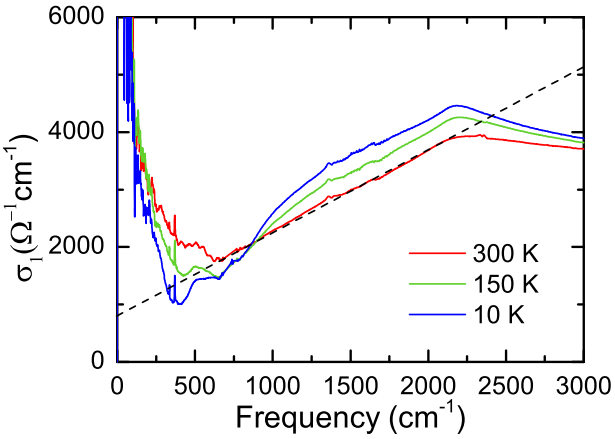

Figure 5.2.6: The optical conductivity displayed on linear scale reveals an ω-linear increase for all temperatures between approx. $1000\,\mathrm{cm}^{-1}$ and $2200\,\mathrm{cm}^{-1}$. The dashed black line acts as guide to the readers eye. Note, that the linear conductivity does not extrapolate to $\omega = 0$.

A close look on the spectra reveals various faint features. The first two are found in the FIR and will be referred to as ω_1 and ω_2. They are highlighted with pink and purple arrows in Fig. 5.2.7 (a) and (b), which display enlarged views of the reflectivity $R(\omega)$ and optical conductivity $\sigma_1(\omega)$ in the FIR range. The spectra for different temperatures are shifted for clarity. These two humps are subtle, however, they are well within the FIR spectral range. There, the relative measurement accuracy is high, and hence these structures can assumed to be real, unlike the kink at $100\,\mathrm{cm}^{-1}$ that simply arises from the merging of FIR and F^2IR spectral ranges.
It is surprising that the feature at ω_2 appears to get broader with decreasing temperature, which is especially evident in the conductivity spectra in panel (b).
Another, more prominent detail is the step in the optical conductivity, already discussed above as an obvious onset of Weyl interband transitions, marked with an violet arrow and labeled ω_3 in Fig. 5.2.7 (c). The sharp kink, after the step preceding the linear increase of the optical conductivity, is labeled with ω_4 and marked with a

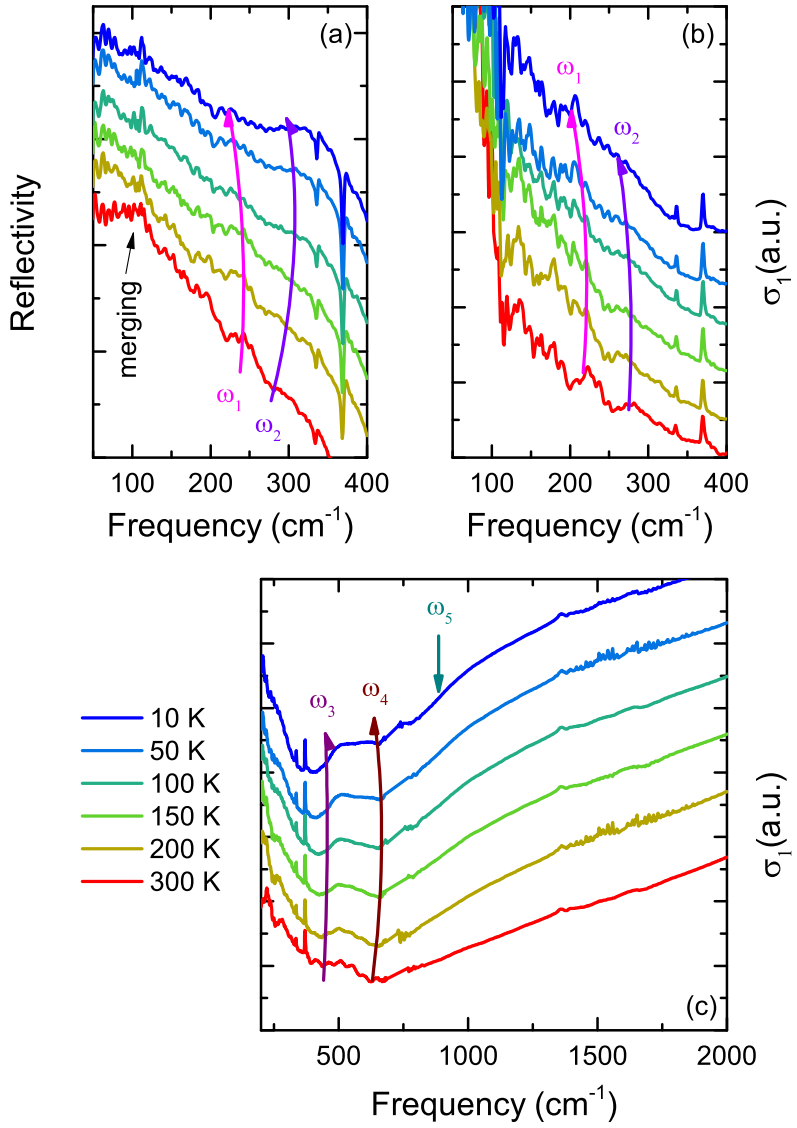

Figure 5.2.7: The subtle features at ω_1 and ω_2 in NbP can be traced in the reflectivity $R(\omega)$ (a) and the optical conductivity $\sigma_1(\omega)$ (b). These two features appear well within the FIR measurement range, where the relative accuracy is high. The feature at $100\,\mathrm{cm}^{-1}$, arises from the merging of FIR and F^2IR. More pronounced features at higher frequencies are marked in the optical conductivity $\sigma_1(\omega)$ in panel (c) and labeled ω_3, ω_4 and ω_5. The spectra in all panels are vertically offset for clarity.

brown arrow.
One more aspect of the spectra needs to be highlighted, although it is only clearly resolved at low temperatures. In Fig. 5.2.7 (c) the green arrow labeled ω_5 marks an inflection point in the low temperature spectra, that can be attributed to details of the bandstructure in NbP.

Having identified all the spectral details, the four-band model introduced in Sec. 2.6 can be applied to fit the interband optical conductivity. Two separate terms are introduced to account for the W1 and W2 interband transitions. The free carrier response can be accounted for by Drude terms (see Sec. 2.3). The magneto-transport data discussed in Sec. 5.2.1 indicates two carrier species with high mobilities. Hence, two Drude terms with low scattering rates γ are utilized to model their response[4]. In the fitting process, a third Drude term with much larger γ and low conductivity σ_{DC} needs to be introduced to fit the optical conductivity $\sigma_1(\omega)$ satisfactorily. This term can straightforwardly be assigned to carriers of the trivial pockets.
Note, that only the real part of the optical conductivity $\sigma_1(\omega)$ could be fit by the analytical expressions given in Ref. [74], since there is yet no expression for the imaginary part $\sigma_2(\omega)$ available. The high frequency interband transitions and spectral features for $\omega \geq 2500\,\mathrm{cm}^{-1}$ were ignored in the fitting process.

Fig. 5.2.8 (a) and (b) display the optical conductivity of NbP at 300 K and 10 K as red and blue stars, respectively. The corresponding fits are depicted as solid black and gray lines. Both fit curves contain the three Drude terms, for the W1 carriers (D-W1), the W2 carriers (D-W2) and the carriers of the trivial pockets, that are mostly hole like (D-TH) [170]. Two terms (W1-IB and W2-IB) are included to model the Weyl interband response.
The sum of conductivities in the zero frequency limit $\sigma_1(\omega \to 0)$ of the Drude terms was anchored at the measured DC-condudctivity, as depicted in Fig. 5.2.8 (c). In this panel, the small red open circles represent the measured DC-conductivity σ_{DC} and the purple solid circles the sum of the Drude conductivities at zero frequency in the fit. The highly mobile Weyl carriers posses a scattering rate γ in the order of $10\,\mathrm{cm}^{-1}$, which places most of their Drude spectral weight outside the measured frequency range. Thus, the constraint of the Drude terms by the DC-conductivity is necessary to guarantee consistency of optical and transport data, and reduce the

[4]The response of the two high mobility carrier species can be also approximated by a single Drude term.

free parameters of the Drude terms.
Fig. 5.2.8 (d) displays the temperature dependence of the scattering rates of the three carrier types (same color scheme as in panels (a) and (b)). All scattering rates reduce with lowering the temperature, as expected for a metal. The carriers with the lowest scattering rate can be assigned to the hole-like W2 carriers, and the other species with low scattering rate to the electron-like W1 carriers.
The scattering rate γ relates to the carrier mobility μ via

$$\gamma = \frac{e}{m^*\mu}. \tag{5.2.7}$$

Utilizing the cyclotron mass of $m_c = 0.02\,m_e$ as m^*, (see Sec. 5.2.3) and inserting the mobilities of the W1 and W2 carriers deduced in the magneto-transport at 10 K (see Sec. 5.2.1), yields scattering rates $\gamma_{\mathrm{W1}} \approx 18\,\mathrm{cm}^{-1}$ and $\gamma_{\mathrm{W2}} \approx 6\,\mathrm{cm}^{-1}$. The scattering rates γ of W1 and W2 at low temperatures deduced from optics, depicted in Fig. 5.2.8 (d), are of the same order, which demonstrates the excellent consistency of the presented analyses.

Fig. 5.2.8 (e) displays the total carrier density N_{tot} calculated from the Drude terms as

$$N_{tot} = \frac{m^*\omega_{p,tot}^2}{4\pi e^2}, \tag{5.2.8}$$

with the total plasma frequency $\omega_{p,tot} = \sqrt{\omega_{p,\mathrm{W1}}^2 + \omega_{p,\mathrm{W2}}^2 + \omega_{p,\mathrm{TH}}^2}$ and the effective carrier mass m^* approximated with $m_c = 0.02\,m_e$ as before. The total carrier densities $N_{tot} = N_e + N_h$ obtained from $\sigma_{xx}(B)$ and $\sigma_{xy}(B)$ in Sec. 5.2.1 are depicted as open and solid triangles, respectively, while the values obtained from $\sigma_1(\omega)$ are represented as purple solid circles. All carrier densities are of the same order ($\approx 5 \times 10^{19}\,\mathrm{cm}^{-3}$), further proving the trustworthiness of the analyses.

Regarding the interband part, all spectral features labeled with ω_i ($i = 1 - 5$) discussed above are captured qualitatively in the fit. The fits to spectra below 300 K contain an additional Lorentz oscillator (L) at $\approx 200\,\mathrm{cm}^{-1}$, which is indicated in light gray in panel (b). There are two possible explanations for this feature. Either it arises from a low energetic interband transition between trivial bands in the complicated bandstructure of NbP, which is overdamped at room temperature, and hence not visible in the 300 K spectrum. Or, since it appears in the close vicinity to ω_2, it might also be related to the van Hove singularity of the W2 bandstructure. The

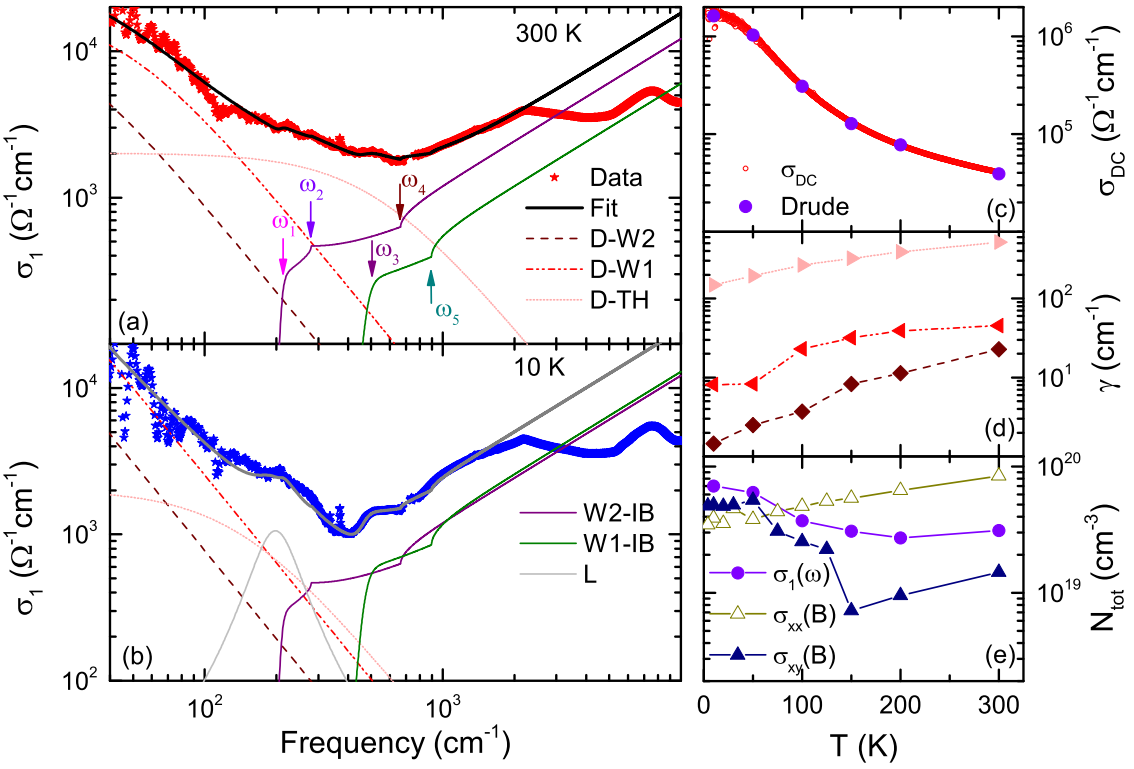

Figure 5.2.8: The fit (black solid line) to the optical conductivity $\sigma_1(\omega)$ at 300 K (red stars) consists of three Drude terms D-W2, D-W1 and D-TH to account for the free carrier response of the W2 cone, the W1 cone and the trivial bands, respectively. The Weyl interband transitions are modeled with two terms W2-IB and W1-IB utilizing the four-band model presented in Ref. [74]. The fit (gray solid line) to the optical conductivity $\sigma_1(\omega)$ at 10 K (blue stars) contains an additional Lorentz term L (light gray) (as do all other spectra at tempertures below 300 K). Panel (c) demonstrates the consistency of the fit in the $\omega \to 0$ limit with the σ_{DC} data. The scattering rate γ of the trivial carriers is at least an order of magnitude larger compared to the Weyl carriers (d). The total carrier density N_{tot} obtained in the optical analysis is in good agreement with the densities deduced from magneto-transport data in Sec. 5.2.1, which is another evidence for a decent self-consistency of the presented analyses.

model presented in Ref. [74] does not allow to introduce different mass parameters m for the four different bands. Hence, if one of the 'inner' bands is more flat than the other, possibly the corresponding spectral feature is stronger.
The deviations of the fit from the linear portion of $\sigma_1(\omega)$ at low temperatures, clearly seen in Fig. 5.2.8 (b), can be understood in a similar fashion. The model does not allow to introduce different Fermi velocities v_F, for the single bands. Since the deviations appear at frequencies, just above the onset of the interband transitions between the 'outer' bands of W1, corresponding to ω_5, this would mean, that these 'outer' bands possess actually a larger v_F than set in the fit parameters for all four bands.

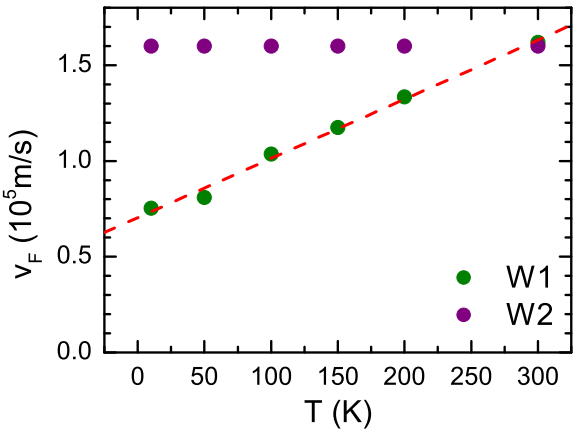

Figure 5.2.9: For a satisfactory fit of $\sigma_1(\omega)$, the Fermi velocity v_F of the W1 term (green solid circles) needs to possess a temperature dependence, while for the W2 term it is constant (violet solid circles). The dashed red line is a linear fit and reveals a linear decrease of $v_{F,W1}$ with $310\,\mathrm{m\,s^{-1}\,K^{-1}}$.

Another peculiarity of the interband response is, that the W1 term needs a temperature dependent Fermi velocity v_F to obtain satisfactory fits. In Fig. 5.2.9, the temperature dependence of the Fermi velocities are displayed. Clearly $v_{\mathrm{F,W1}}$ decreases towards lower temperatures, while $v_{\mathrm{F,W2}}$ is constant. The red dashed line in this plot represents a linear fit that reveals a decrease of $v_{\mathrm{F,W1}}$ with a slope of $310\,\mathrm{m\,s^{-1}\,K^{-1}}$. The observation of a linearly decreasing Fermi velocity is intriguing, however yet not understood. Note, that a similar temperature dependent Fermi velocity was reported very recently in $YbMnBi_2$ [199], where this observation is discussed to arise from a combination of temperature dependent chemical potential, bandstructure and self energy effects. However, in case of NbP, possibly also a temperature dependent trivial interband transition, that contributes at the same frequencies as the W1 interband response could be the origin such behavior in the fit parameters.
Irrespective of the temperature dependence of the W1 Fermi velocity, the extracted values of $v_{\mathrm{F,W2}} = 1.6 \times 10^5\,\mathrm{m\,s^{-1}}$ and $v_{\mathrm{F,W1}}$ of the same order $\approx 10^5\,\mathrm{m\,s^{-1}}$, are in excellent agreement with the value extracted from the magneto-transport data in

Sec. 5.2.1 as well with the values reported in Refs. [167, 168, 170, 178]. For a meaningful comparison, the momentum averaging nature of optical experiments needs to be remembered.

The Weyl fit parameters m, b and Δ_{E} remain constant in temperature and are summarized in Tab. 5.2.1. The knowledge of v_{F}, m, b and Δ_{E} for the Weyl cones, enables to plot a quantitative bandstructure around the Weyl nodes according to Eq. 2.6.5. Since optics is a momentum averaging probe, the resulting bands are 'effective' dispersions averaged over k_x, k_y and k_z. Furthermore, as already discussed above, the four-band model of Ref. [74] does not account for possible asymmetries. The energy scales are, however, adequate. Fig. 5.2.10 displays the resulting effective dispersions $\epsilon_{eff,\mathrm{W1}}$ and $\epsilon_{eff,\mathrm{W2}}$ around the W1 and W1 Weyl nodes, respectively. The W1 dispersion is thereby plotted with the Fermi velocity at 150 K. The transitions between the bands, responsible for the subtle details of the optical conductivity, are illustrated with arrows and labels ω_i $(i = 1 - 5)$ in the same colors as in Figs. 5.2.7 and 5.2.8.

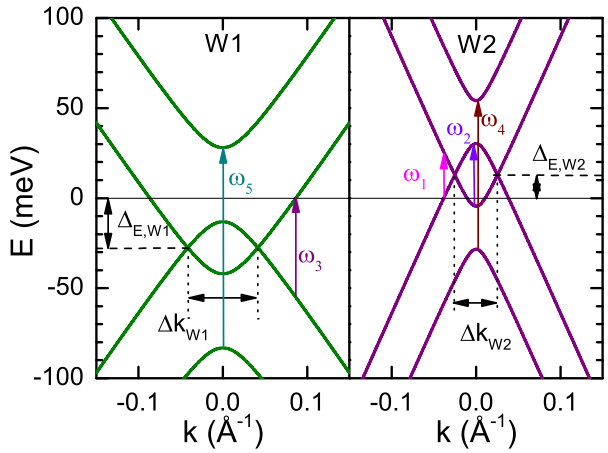

Figure 5.2.10: The effective dispersions $\epsilon_{eff,W1}$ and $\epsilon_{eff,W2}$ around the W1 and W2 Weyl nodes according to Eq. 2.6.5. The transitions between the bands responsible for the subtle details in the spectra are marked with arrows and labeled ω_i $(i = 1 - 5)$.

A remarkable finding in Fig. 5.2.10 is the fact that, the k-splitting of the W1 nodes of opposing chirality ($\Delta k \approx 0.08\,\text{Å}^{-1}$) is larger than the k-splitting of the W2 nodes ($\Delta k \approx 0.05\,\text{Å}^{-1}$). However, the extraction of the k-splitting from the momentum averaged optical data has to be treated very cautiously. Nevertheless, the approximate value of the k-splittings in Fig. 5.2.10 are in good agreement with the findings in an ARPES study [47].

Cone	m(meV)	b(meV)	Δ_{E}(meV)	$v_{\mathrm{F}}(10^5\,\mathrm{m\,s^{-1}})$
W1	20.6	35.0	27.6	1.0 (@ 150 K)
W2	11.9	29.3	12.9	1.6

Table 5.2.1: The parameters of the Weyl interband terms utilized to fit $\sigma_1(\omega)$ as depicted in Fig. 5.2.8. The displayed Fermi velocity v_F of the W1 cone corresponds to the fit at 150 K.

5.2.3 Results: Magneto-Optics

Low field measurements

This section is dedicated to the analysis of the optical properties of NbP in high magnetic fields. The spectra up to $B = 7\,\mathrm{T}$ were measured in the setup described in Sec. 3.4 for frequencies $\omega \approx 80 - 2000\,\mathrm{cm^{-1}}$. The field range was extended up to $B = 30\,\mathrm{T}$ in the HFML in Nijmegen[5] in the FIR $\omega \approx 30 - 900\,\mathrm{cm^{-1}}$. All magneto-optical measurements were conducted in Voigt geometry with field applied in the (001) plane of the crystal and the optical response of the selfsame was measured with unpolarized light. While in the measurements in the setup built in this work absolute spectra were obtained with the gold evaporation technique, in the HFML only relative reflectivity spectra could be gathered.

First, the spectra in fields up to $B = 7\,\mathrm{T}$ will be discussed. Fig. 5.2.11 (a) depicts the reflectivity measured in the magneto-optical setup at fields of $B = 0\,\mathrm{T}$ and $B = 7\,\mathrm{T}$ and a temperature of $T = 7\,\mathrm{K}$ as thick blue and orange lines. For comparison, also the spectrum measured in the zero field gold evaporation cryostat at $T = 10\,\mathrm{K}$ is displayed as a thin black line. Some small, field induced changes are clearly visible already in the absolute reflectivity. The most pronounced feature occurs around the plasma edge and the changes are accentuated with the violet arrows. The shifting of the reflectivity to lower and higher frequencies in magnetic fields at these frequencies can straightforwardly be assigned to the magnetic field induced splitting of the screened plasma frequency $\omega_{p,scr}$ discussed in Sec. 2.7.1. In the relative reflectivity $R(7\,\mathrm{T})/R(0\,\mathrm{T})$ in Fig. 5.2.11 (c), this magneto plasma effect turns up as two minima, separated by a maximum, indicated again by violet arrows. The dashed violet lines act as guide to the reader's eye. In panel (c) the relative spectra of two independent measurement runs (M1 and M2) are displayed, to emphasize the reproducibility of the features discussed in the following, and to set them apart from noise.

[5]High Field Magnet Laboratory, Nijmegen, The Netherlands

Frame (b) of Fig. 5.2.11 depicts the optical conductivity $\sigma_1(\omega)$ in the same style as in frame (a). For the Kramers-Kronig transformation, the 10 K zero field spectrum is utilized to extrapolate the spectra measured in the magneto-optical setup. A series of asymmetric peaks appears in field in agreement with the expectations for Weyl Landau level transitions (see Sec. 2.7.2). To prevent confusion, the phonon already discussed in Sec. 5.2.2 is marked with a black arrow.
The peaks that can unambiguously be resolved in the optical conductivity $\sigma_1(\omega)$ are marked with arrows pointing downwards and labeled λ_i ($i = 3, 4, 5$) in panel (b). The dotted lines reveal, that the peaks in $\sigma_1(\omega)$ correspond to minima prior to maxima, or better, the positive slopes in the relative reflectivity in panel (c). Knowing this, further features can be determined in $R(7\,\mathrm{T})/R(0\,\mathrm{T})$, which is the quantity that is most sensitive to field induced changes. These features, found in $R(7\,\mathrm{T})/R(0\,\mathrm{T})$, are marked with arrows pointing upwards and labeled λ_i ($i = 1, 2, 7$) in panel (c). The dotted lines reveal, that also these features belong to peaks in $\sigma_1(\omega)$ which are perturbed by noise in case of $\lambda_{1,2}$ and fall in the range of a maximum arising from the magneto plasma effect in case of λ_7. Further support for the interpretation of these features is obtained by considering the complete field dependence in the next paragraphs.

To trace down the field dependence of the signatures that can *a priori* be assumed to arise from Landau level transitions, as well as the development of the plasma edge splitting, the relative reflectivity spectra $R(B)/R(0\,\mathrm{T})$ for fields up to $B = 7\,\mathrm{T}$ are displayed in Fig. 5.2.12 (a). For clarity the spectra are stacked along the y-axis. This figure reveals a rich structure of field induced changes to the reflectivity for all measured fields. The development of the features labeled with λ_i in Fig. 5.2.11, is indicated by the symbols displayed in the background of the spectra. One additional signature of a Landau level transition is found between λ_5 and λ_7 at fields $B \leq 6\,\mathrm{T}$, which is masked by the large spectral changes arising from the plasma frequency splitting. In Fig. 5.2.12 (a) this feature is labeled with λ_6. All marked details labeled with λ_i ($i = 1 - 7$) exhibit a shift to higher frequencies with increasing fields. The exact field dependence of this characteristic behavior will be discussed later.
First, light will be shed on the splitting of the plasma edge in field. The violet stars in Fig. 5.2.12 (a) mark the approximate positions of the minima that can be assigned to the splitting of $\omega_{p,scr}$. Especially the minimum at higher frequencies is perturbed by some field dependent processes. At 1 T, for instance, it appears as if a broad hump is overlaying the minimum. Furthermore, a weak hump shifting through the minimum

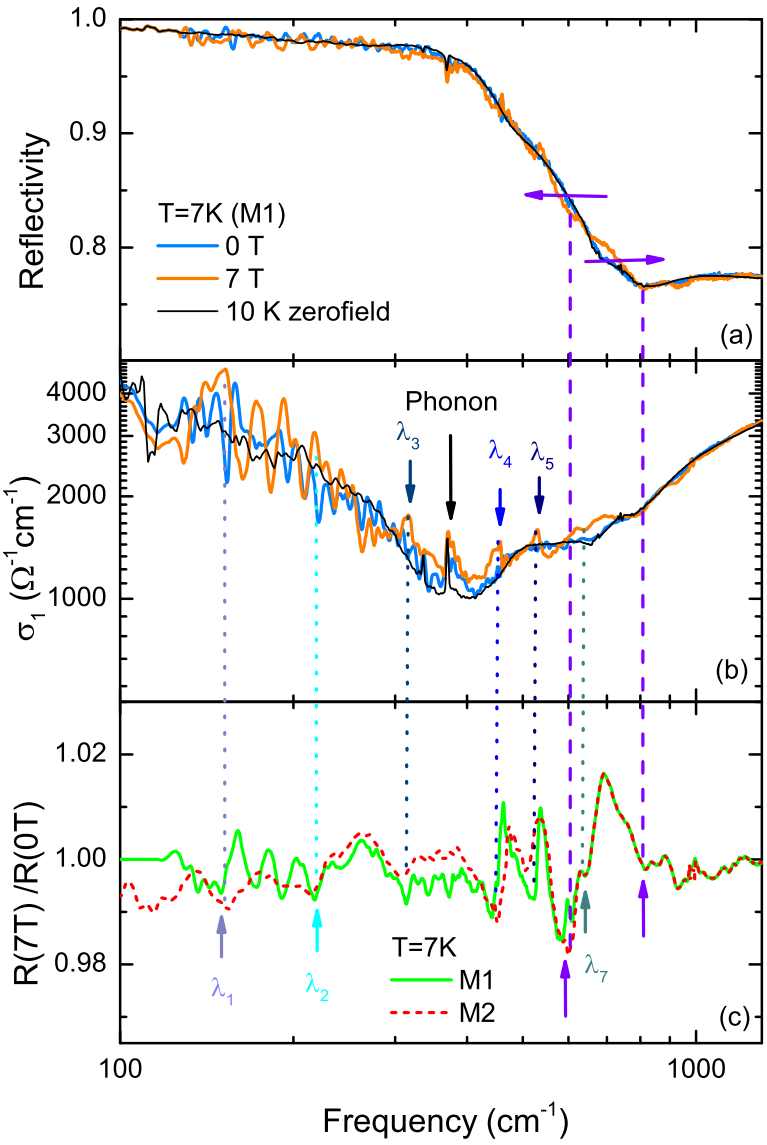

Figure 5.2.11: The absolute reflectivity $R(\omega)$ (a) and optical conductivity $\sigma_1(\omega)$ (b) of NbP measured in the magneto-optical setup at $B = 0\,\mathrm{T}$ and $B = 7\,\mathrm{T}$. The spectra obtained in the zero field cryostat are additionally displayed as thin black lines. A clear splitting of the plasma frequency $\omega_{p,scr}$ is observed in the reflectivity (purple arrows) which turns up as two dips in the relative reflectivity $R(7\,\mathrm{T})/R(0\,\mathrm{T})$ (c). Multiple features that can be attributed to inter Landau level transitions are labeled with λ_i ($i = 1-7$) in frame (b) and (c). The relative reflectivities of two independent measurements M1 and M2 reveal large reproducibility of these features (c).

is resolved for $B \geq 5\,\mathrm{T}$. The frequency distance of these minima corresponds to the cyclotron frequency ω_c as discussed in Sec. 2.7.1. The field dependence of the cyclotron energy $E_c = \hbar\omega_c$ is displayed in Fig. 5.2.12 (b) as violet stars. Additionally displayed, as green solid circles in this panel, is the field dependence of the 'gap energy' E_g that was extracted from the resistance measurements in magnetic fields in Sec. 5.2.1. Both quantities display stunning agreement. This indicates, that the development of the 'gap energy' in the magneto transport data is likely related to the localization of carriers on Landau orbits. Moreover this demonstrates excellent self-consistency of the data sets and their analysis. The cyclotron energy E_c (or energy distance between two adjacent Landau levels in a Weyl cone) follows [86, 95, 200]

$$E_c = E_{n+1} - E_n = v_\mathrm{F}\sqrt{2e\hbar B}\left(\sqrt{|n+1|} - \sqrt{|n|}\right), \tag{5.2.9}$$

The red line is the fit of the cyclotron energy E_c where $n = 0$ is assumed. This yields a Fermi velocity of $v_\mathrm{F} = 3.1 \times 10^5\,\mathrm{m\,s^{-1}}$ as a lower limit (because of the choice of $n = 0$).

The observation of the $\sqrt{B}$-dependence of E_c challenges the statement, that the cyclotron frequency of massless particles also scales linear with the magnetic field just like for conventional massive particles of parabolic bands [69, 201, 202]. This putative objection is easily resolved considering the fact, that the expectation of a B-linear ω_c only holds in the semi-classical limit. In other words, NbP is in the quantum limit already at very low fields. Note, that E_c in Fig. 5.2.12 (b) could also be approximated linear, however the resulting positive intercept with the y-axis would be unphysical.
Nevertheless, approximating the cyclotron frequency at each field with the linear relation $\omega_c = eB/m_c$ leads to a field dependent cyclotron mass m_c ranging from $0.01\,m_e$ at 1 T to $0.025\,m_e$ at 7 T. In average the effective cyclotron mass $m_c = 0.02\,m_e$, utilized in the sections above, is obtained as a rough estimate.

Another intriguing aspect of the spectra in Fig. 5.2.12 (a) is found between $800\,\mathrm{cm^{-1}}$ and $900\,\mathrm{cm^{-1}}$. The hump in this frequency range is not moving in field, similar to the maximum separating the two minima arising from the plasma frequency splitting. Therefore as an interpretation of this feature a second split of the plasma frequency could be discussed, which would confirm the dispersive nature of the Landau levels of the Weyl cones and the consequential existence of a distribution of resonance fre-

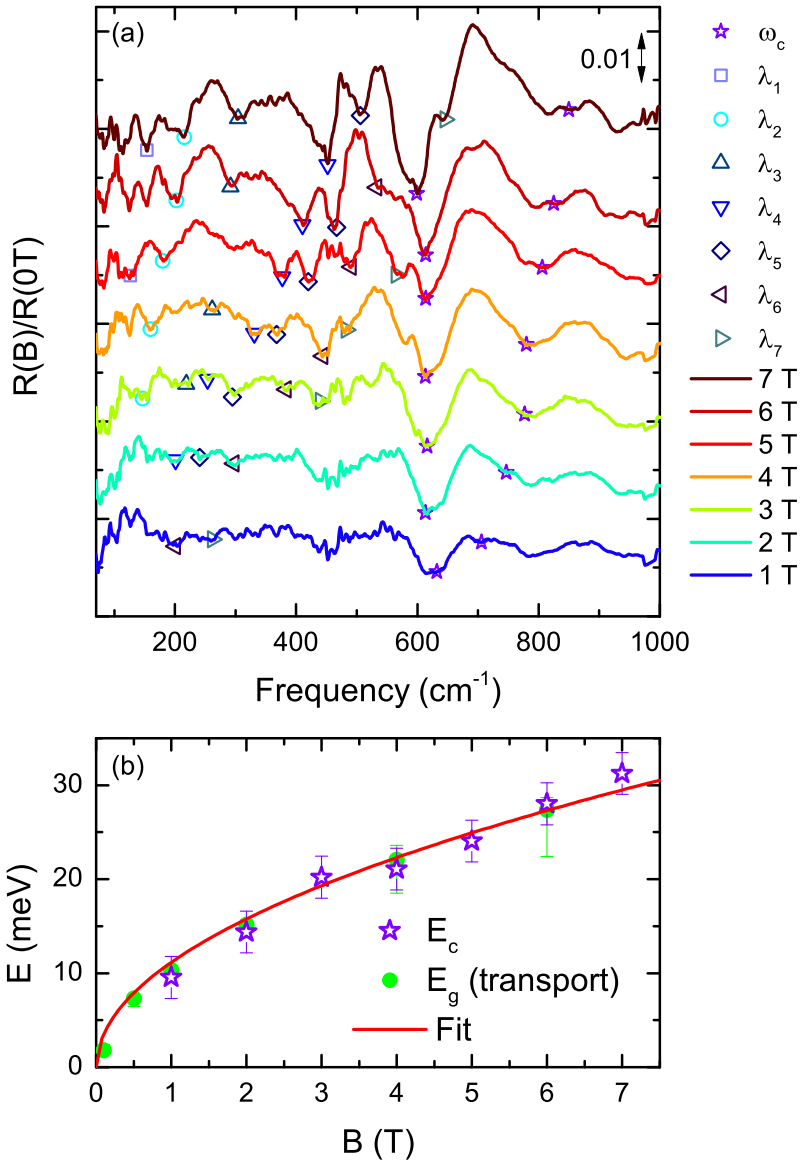

Figure 5.2.12: The relative reflectivities $R(B)/R(0\,\mathrm{T})$ for fields from $B = 1\,\mathrm{T}$ to $B = 7\,\mathrm{T}$ in $1\,\mathrm{T}$ steps (a) obtained in the magneto-optical setup. For clarity, the spectra are stacked vertically. The field dependence of the features labeled with λ_i can be traced nicely, as indicated by the open symbols. The splitting of the plasma frequency is marked with violet open stars, and the correspondent cyclotron energy E_c is displayed in panel (c). An excellent agreement of E_c and E_g (found in magneto-transport, Sec.5.2.1) is obtained.

quencies [83]. However, the minima accompanying this hump do not appear to split further in field, rather the opposite is the case. Hence, at this point the interpretation of this feature remains unclear and further investigations are needed to clarify its origin.
Note, that the frequencies exceeding the displayed range in Fig. 5.2.12 (a), which were also measured in magnetic fields, did not reveal any significant changes and are consequently not shown. Furthermore, it has to be mentioned, that the determination of the features depicted in Fig. 5.2.12 (a) was crosschecked with the appearance of peaks in the absolute optical conductivity in field $\sigma_1(B)$ as well as with peaks in the relative optical conductivity $\sigma_1(B)/\sigma_1(0\,\mathrm{T})$, to achieve the best possible confidence in the trustworthiness of the features.

High field measurements

To further trace the developments of the spectral features in magnetic field, the measurements up to 30 T are displayed in Fig. 5.2.13 (a) in a stacked manner. Three of the dips, namely λ_1, λ_2 and λ_3 are found in the displayed frequency range, and hence, can also be traced for the higher magnetic fields. The noise in the high field measurements is larger, but also the features get more pronounced with increasing the field. The transitions labeled with higher indices $i = 4, 5, 6, 7$ can not be resolved. Anyway, these are expected to move out of the frequency window at moderate fields already. The black arrow emphasizes the lower frequency dip, that belongs to the plasma frequency splitting. At $B = 12\,\mathrm{T}$ this dip has vanished due to a maximum that moves in the same frequency range. The development of this plasma edge splitting at low fields nicely confirmes the observation in Fig. 5.2.12 (a).
In the $B = 20\,\mathrm{T}$ spectrum a new dip λ_8 appears at a frequency below λ_1. Also this feature develops in field, and hence, can be assumed to arise from another inter Landau level transition. A useful way to figure out the transitions responsible for the optical signatures λ_i is, to examine the ratios between their frequencies. The frequencies of $\lambda_1 : \lambda_3 : \lambda_4 : \lambda_5 : \lambda_6 : \lambda_7$ relate like $1 : 2.2 : 3.1 : 3.3 : 4.0 : 4.4$. These ratios compare reasonably well with the ratios expected for the signature frequencies of inter Landau level transitions for Weyl cones discussed in Sec. 2.7.2 which would be: $1 : 1 + \sqrt{2}(\approx 2.4) : \sqrt{2} + \sqrt{3}(\approx 3.1) : \sqrt{3} + \sqrt{4}(\approx 3.7) : \sqrt{4} + \sqrt{5}(\approx 4.2) : \sqrt{5} + \sqrt{6}(\approx 4.7)$.
The features at λ_8 and λ_2 fall out of this scheme. However, these two themselves

relate as $\lambda_8 : \lambda_2 \equiv 1 : 2.3$[6].
The frequencies labeled with the λ_i can accordingly be assigned to the interband Landau level transitions $L_{-n} \rightarrow L_{n+1}$ and $L_{-(n+1)} \rightarrow L_n$ as indicated in Fig. 5.2.12 (b) and summarized in Tab. 5.2.2. Fitting the field dependence of the transitions in Fig. 5.2.12 (b) with the equations introduced in Sec. 2.7.2 or Eq. 5.2.9, respectively, yields average Fermi velocities of $v_{\mathrm{F,W2}} = 1.78 \times 10^5\,\mathrm{m\,s^{-1}}$ and $v_{\mathrm{F,W1}} = 1.25 \times 10^5\,\mathrm{m\,s^{-1}}$. These values excellently agree with the values obtained from the fits to the optical conductivity $\sigma_1(\omega)$ at zero field. The values of the single fits are displayed in Tab. 5.2.2, and exhibit only a small scattering around the averages just stated.

The assignment of the transitions to the cones W1 and W2 in Tab. 5.2.2 is obvious by comparison of the values of the Fermi velocities v_F obtained from the fits, with those gathered from the zero field spectra. Furthermore, the fact, that the W1 node is further away from the Fermi energy, and therefore, only enters the quantum limit at fields as high as $B = 20\,\mathrm{T}$, while for W2 cone already clearly the case at $B = 5\,\mathrm{T}$, supports the assignment of the transitions as stated in Tab. 5.2.2.
Note, that the λ_3 frequency can be interpreted as the $L_{-1} \rightarrow L_2$ ($L_{-2} \rightarrow L_1$) transition of the W2 cone or as $L_{-2} \rightarrow L_3$ ($L_{-3} \rightarrow L_2$) transition of the W1 cone, since both approximately coincide for the Fermi velocities $v_{\mathrm{F,W1}}$ and $v_{\mathrm{F,W2}}$ stated above. The other transitions can, however, be assigned unambiguously.

Label	Cone	Transition	$v_\mathrm{F}(10^5\,\mathrm{m\,s^{-1}})$
λ_1	W2	$L_0 \rightarrow L_1$; $L_{-1} \rightarrow L_0$	1.86
λ_3	W2	$L_{-1} \rightarrow L_2$; $L_{-2} \rightarrow L_1$	1.69
λ_4	W2	$L_{-2} \rightarrow L_3$; $L_{-3} \rightarrow L_2$	1.85
λ_5	W2	$L_{-3} \rightarrow L_4$; $L_{-4} \rightarrow L_3$	1.70
λ_6	W2	$L_{-4} \rightarrow L_5$; $L_{-5} \rightarrow L_4$	1.75
λ_7	W2	$L_{-5} \rightarrow L_6$; $L_{-6} \rightarrow L_5$	1.80
λ_8	W1	$L_0 \rightarrow L_1$; $L_{-1} \rightarrow L_0$	1.21
λ_2	W1	$L_{-1} \rightarrow L_2$; $L_{-2} \rightarrow L_1$	1.29

Table 5.2.2: Assignment of the features labeled with λ_i to the inter Landau level transitions $L_{-n} \rightarrow L_{n+1}$; $L_{-(n+1)} \rightarrow L_n$ of the W1 and W2 Weyl cones. The Fermi velocities v_F are obtained by fitting the field dependence of the features.

[6]Note, that the stated experimental ratios are averaged over the ratios at all fields where the corresponding transitions are visible.

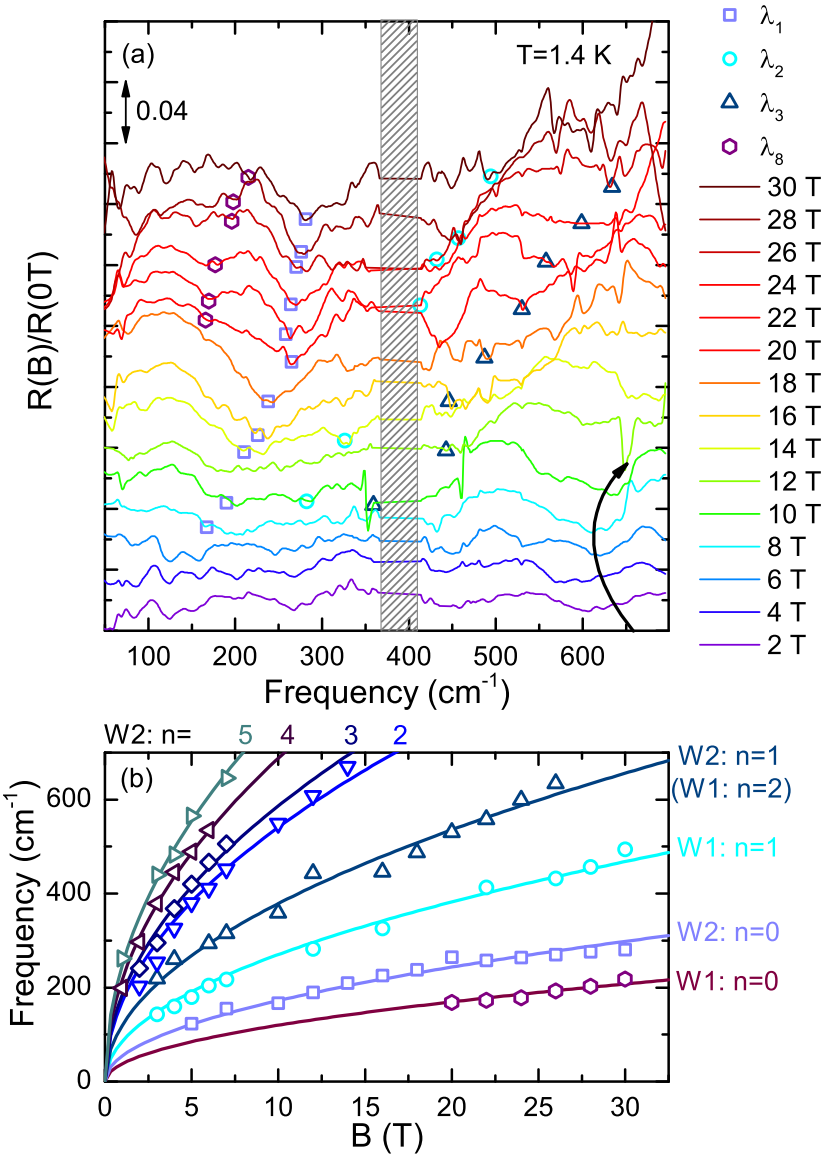

Figure 5.2.13: The relative reflectivities $R(B)/R(0\,\mathrm{T})$ at $T \approx 1.4\,\mathrm{K}$ for fields from $B = 2\,\mathrm{T}$ to $B = 30\,\mathrm{T}$ in $2\,\mathrm{T}$ increments (a) obtained in the HFML in Nijmegen. For clarity, the spectra are stacked vertically. The field dependence of the features labeled with λ_1, λ_2 and λ_3 is traced as indicated by the corresponding open symbols. At $B = 20\,\mathrm{T}$ an additional feature appears labeled λ_8. The black arrow emphasizes the lower frequency branch of the plasma frequency splitting. The frequencies of the features labeled λ_i are plotted versus magnetic field B in panel (b). The solid lines correspond to fits yielding Fermi velocities v_F as summarized in Tab. 5.2.2. In the gray shaded area excessive noise arising from a signal minimum of the utilized beam splitter was cut out.

Fig. 5.2.14 displays a contour plot of the relative reflectivity spectra. The color code therein represents the relative change with field. Additionally, expected positions of the inter Landau level transitions for the W2 and W1 cones, computed with the average Fermi velocities $v_{\mathrm{F,W1}}$ and $v_{\mathrm{F,W2}}$ are displayed. The $n = 1$ transition of the W1 cones is represented as black solid line, while the transitions of the W2 cones are drawn in white. All lines nicely follow the structures evolving in the contour plot with increasing the magnetic field.

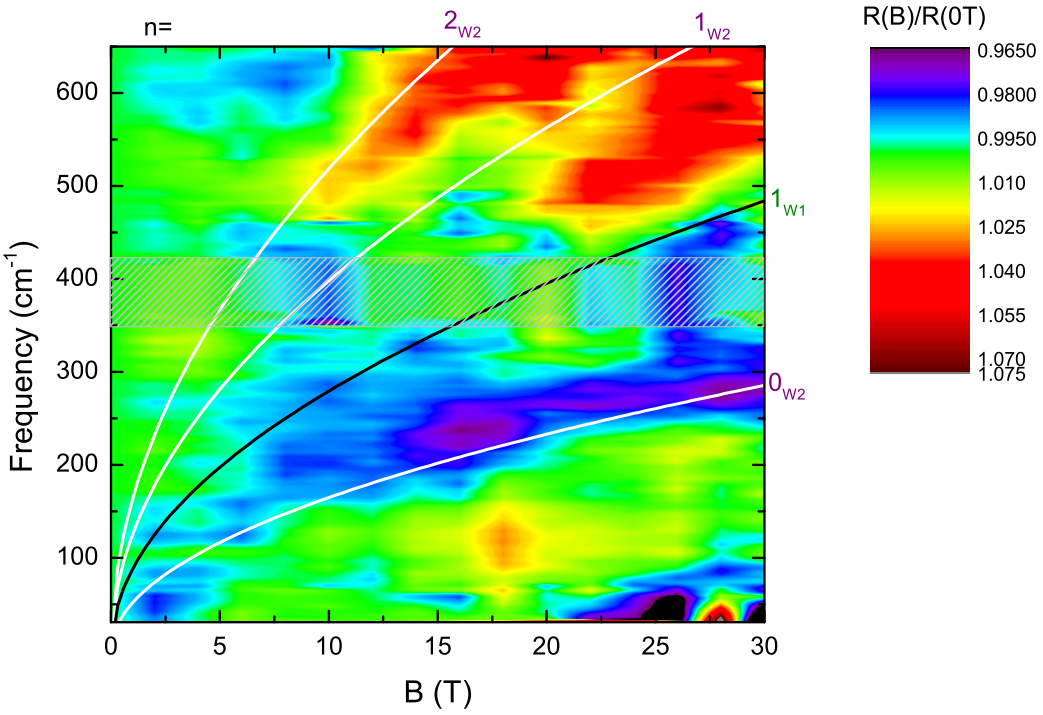

Figure 5.2.14: The relative reflectivity $R(B)/R(0\,\mathrm{T})$ as a contour plot, where the color represents the amplitude of relative change. The solid lines represent the theoretical field and frequency dependencies of inter Landau level transitions for the W1 and W2 cones computed utilizing the average Fermi velocities stated in the text. The solid lines nicely follow the $\sqrt{B}$- dependence of the colored contours. In the gray shaded area excessive noise arising from a signal minimum of the utilized beam splitter was cut out.

Landau level dispersion

Concerning the appearance of the peaks arising from the inter Landau level transitions it is noticeable, that especially for the W1 cone, these appear below the onset of the linear conductivity in zero field. In Sec. 2.7.2 it was discussed, that the peaks in the optical conductivity arising from Landau level transitions sit on the linear interband background of the Weyl cones. Hence, the appearance of Landau level transitions at frequencies below the onset of the Weyl interband transitions is not trivial. In NbP this observation arises from the interplay of the Landau level structure with the chemical potential. In Sec. 5.2.2 it was deduced from the zero field spectra, that the bandstructure around the Weyl points in NbP can be approximated with Eq. 2.6.5, as displayed in Fig. 5.2.10. For such a bandstructure, the Landau level spectrum is described by [203]

$$\epsilon_{s,s'}(\mathbf{k},\mathbf{B},\mathbf{n}) = s\sqrt{2e\hbar v_{\mathrm{F}}^2 B + m^2 + b^2 + (v_{\mathrm{F}}\hbar\mathbf{k})^2 + 2bs'\sqrt{(v_{\mathrm{F}}\hbar k_z)^2 + m^2}};(n>0) \tag{5.2.10a}$$

$$\epsilon_{s'}(\mathbf{k}) = -b - s'\sqrt{(v_{\mathrm{F}}\hbar k_z)^2 + m^2};(n=0), \tag{5.2.10b}$$

if Zeeman terms are neglected. Note, that Eq. 5.2.10b also contains the characteristic $\sqrt{B}$ dependence of the Landau levels.

Utilizing the parameters for m and b obtained from the zero field optical data and stated in Tab. 5.2.1, as well as the average Fermi velocities $v_{\mathrm{F,W2}} = 1.78 \times 10^5\,\mathrm{m\,s^{-1}}$ and $v_{\mathrm{F,W1}} = 1.25 \times 10^5\,\mathrm{m\,s^{-1}}$, the Landau level dispersion is plotted in Fig. 5.2.15 for levels L_n with $n = 0 - 6$. The Landau levels of W1 in panel (a) are displayed for $B = 20\,\mathrm{T}$, where the data in Fig. 5.2.13 indicates, that this cone enters the quantum limit. To capture this experimental observation, the absolute value of the chemical potential needs to be reduced from the value found in the zero field spectra to $|\Delta_E| = 20\,\mathrm{meV}$. Then the transition $L_0 \rightarrow L_1$ marked with the brown arrow agrees well with the appearance of the dip in the spectra (see Fig. 5.2.13). It is clear, that also transitions with lower energies from L_0 to L_1 are possible as indicated with the dotted brown arrows (the same is true for slightly larger energies). The appearance of the dip at the frequency of the solid brown arrow can be attributed to the fact, that the L_1 level gets flat there, and therefore a van Hove singularity should appear in the density of states. The lower/higher energy transitions should provide a broadening of the mode observed in the spectra, in agreement with the experimental data in Fig. 5.2.13, where all features extend over more than $100\,\mathrm{cm^{-1}}$ at $B = 20\,\mathrm{T}$.

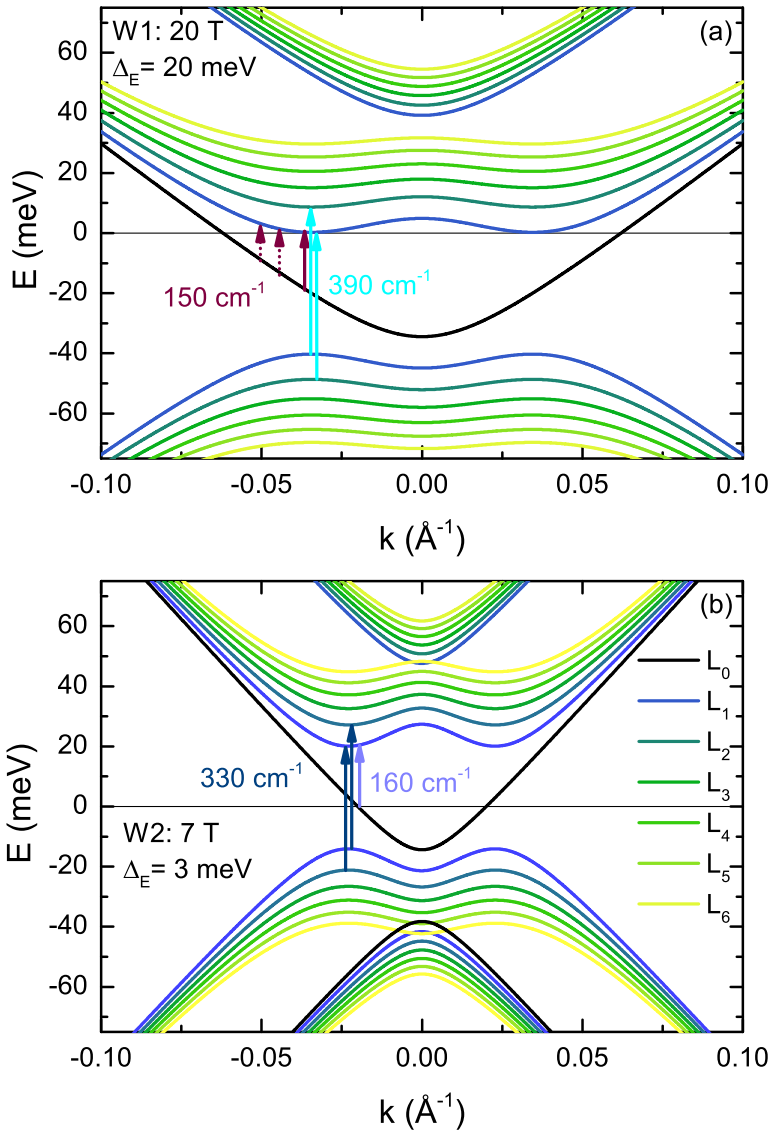

Figure 5.2.15: Landau level structure of NbP, assuming a 4-band model as in Sec. 5.2.2 of the W1 (a) and W2 (b) cones. The plots are generated with Eq. 5.2.10b [203], utilizing the parameters b and m found in the zero field measurements summarized in Tab. 5.2.1, and the average Fermi velocities found in the magneto-optical experiments stated in the text. The absolute values of the chemical potentials Δ_E of both cones need to be reduced as compared to the zero field values to merge the transitions involving the L_0 level in the quantum limit. The energies of the transitions are in good agreement with the experimentally observed frequencies.

Note, that also the transitions $L_{-1} \rightarrow L_2$ and $L_{-2} \rightarrow L_1$ marked with the cyan arrows in Fig. 5.2.15 (a) agree quantitatively with the experimental frequency of these transitions.
In the same manner, the Landau levels of W2 are displayed in Fig. 5.2.15 (b) at $B = 7\,\mathrm{T}$, where this cone is also in the quantum limit. Again the chemical potential is adjusted to merge the $L_0 \rightarrow L_1$ transition, an this yields $|\Delta_E| = 3\,\mathrm{meV}$. All observed transitions of the W2 cone at 7 T (see Figs. 5.2.12, 5.2.13) agree well with the characteristic energy distances in Fig. 5.2.15 (b). The transitions from L_0 to L_1 and between the levels with $n = \pm 1, \pm 2$ are indicated with light purple and dark blue arrows, respectively.
Note that the $L_{-1} \rightarrow L_0$ transition in the W1 cone according to Fig. 5.2.15 roughly coincides in energy with the $L_{-1} \rightarrow L_2$ and $L_{-2} \rightarrow L_1$ transitions and hence, is not observed separately in the spectra. In the W2 cone, since the chemical potential is so small the $L_{-1} \rightarrow L_0$ transition possibly contributes to a broadening of the mode in the spectra.

In magnetic fields, the chemical potential needs to be adjusted to lower absolute values for both cones. This behavior is also discussed for Cd_3As_2, TaP and for Weyl semimetals in general, and it was found, that in the quantum limit $\Delta_E \propto B^{-1}$ [95, 204, 205].

5.3 Conclusions

The data presented in this chapter leaves no doubt, that the transport, as well as the optical response up to the MIR is dominated by relativistic massless carriers. The analyses of the magneto-transport, optical and magneto-optical data yield a stunning agreement, and by this strongly support the picture drawn here on NbP.
The analysis of the zero field data allows to illuminate the subtle details of the Weyl bands. With the $\sqrt{B}$-behavior of the inter Landau level transitions linearity of these bands in NbP is proven. Furthermore, the combination of the knowledge from zero-field and B-field data allows to elucidate the magnetic sub-level structure. Tab. 5.3.1 summarizes the quantities characterizing the Weyl cones. For comparison, published values are also stated. The findings of this work are in excellent agreement with the predictions of theory, as well as the other published experimental works.

RRR	N_{tot} ($10^{19}\,\frac{1}{\mathrm{cm}^3}$)	μ ($10^5\,\frac{\mathrm{cm}^2}{\mathrm{Vs}}$)	v_F ($10^5\,\frac{\mathrm{m}}{\mathrm{s}}$)	Δ_E (meV)	m_c (m_e)	Ref.
40	≈ 5	≈ 5	3	10.2	-	this, MT
40	≈ 7	≈ 2	W1: 1.0 (@150 K) W2: 1.6	W1: 27.6 W2: 12.9	-	this, O
40	-	-	W1: 1.2 W2: 1.7 3.1 (ω_c)	-	0.02	this, MO
115	0.18	50	4.8	-	0.076	[170], MT
95	0.2	100	1.8	W2: 15	W1: 0.1 W2: 0.06	[178], MT
-	-	W1: 0.076 W2: 0.26	-	W1: 42.2 W2: 3.7	W1: 0.086 W2: 0.048	[206], dHvA
-	≈ 2.5	-	-	W1: 57 W2: 5	0.05	[49], dHvA, BS
-	≈ 1.3	-	3.7	-	-	[167], BS
-	≈ 1.5	-	W1: $v_x = 3.7$ $v_y = 1.5$ $v_z = 0.0$ W2: $v_x = 2.1$ $v_y = 2.1$ $v_z = 3.8$	W1: 53.4 W2: 25.9	W1: 0.086 W2: 0.048;	[168], BS

Table 5.3.1: Summary of the characteristic quantities of NbP found in this work and extracted from references. All mobilities μ and total carrier densities N_{tot} are for low temperatures. The abbreviation MT, O, MO, dHvA and BS stand for magneto-transport, optics, magneto-optics, de Haas-van Alphen and bandstructure calculations, respectively and point out, which technique was used to determine the values. The ω_c indicates the value of v_F obtained from the plasma frequency splitting.

6. The Weyl semimetal TaAs

This chapter is dedicated to the Weyl semimetal TaAs, a sister compound of NbP (see Chap. 5). First, the material will be intoduced in Sec. 6.1, then the experimental results will be discussed in Sec. 6.2. In Sec. 6.3, summaries of the experimental findings and concluding remarks are given.

6.1 The material

TaAs belongs to the same family of non-centrosymmetric transition metal monopnictides like NbP. Compared to NbP, TaAs exhibits much larger spin orbit coupling. This has considerable consequences for the band structure and Fermi surfaces.
TaAs crystallizes in a tetragonal structure with the space group $I4_1md$ (No. 109). The lattice parameters are $a = 3.438\,48\,\text{Å}$ and $c = 11.641\,\text{Å}$, respectively [28]. The structure is displayed in Fig. 6.1.1 (a). Band structure calculations without the inclusion of spin orbit coupling reveal a clear band inversion and several band crossings near the Fermi level. These band crossings lead to the nodal rings discussed in Sec. 5.1 [28, 29, 168].
The band structure is drastically changed when spin orbit coupling is included. Fig. 6.1.1 (b) displays the band structure of TaAs along the high symmetry lines with spin orbit coupling included [28]. All band crossings are gapped. The gap between the bands 2 and 3 in Fig. 6.1.1 (b) is, however, very small ($\approx 3\,\text{meV}$) as revealed in the inset [28].
Just like NbP, TaAs hosts 12 pairs of Weyl nodes. The W1 nodes are located in the $k_z = 0$ plane and the W2 are found at more general k-points (see Fig. 5.1.3). The k-splitting of the Weyl nodes in TaAs is larger as compared to NbP, as a direct consequence of the larger spin orbit coupling [47, 169]. Fig. 6.1.1 (c) and (d) depict the Fermi surfaces arising from the trivial hole pocket in red (band 2 in panel (b)) and the W2 pockets in blue, which can be electron like or hole like depending on the position of the chemical potential [31]. Recent studies also revealed banana shaped

electron like Fermi surfaces enclosing the W1 nodes [31, 50]. The W1 nodes are lower in energy than the W2 nodes, just like in NbP. The exact energy distance of the nodes from the Fermi energy E_F was found to vary noticeably from sample to sample [31].

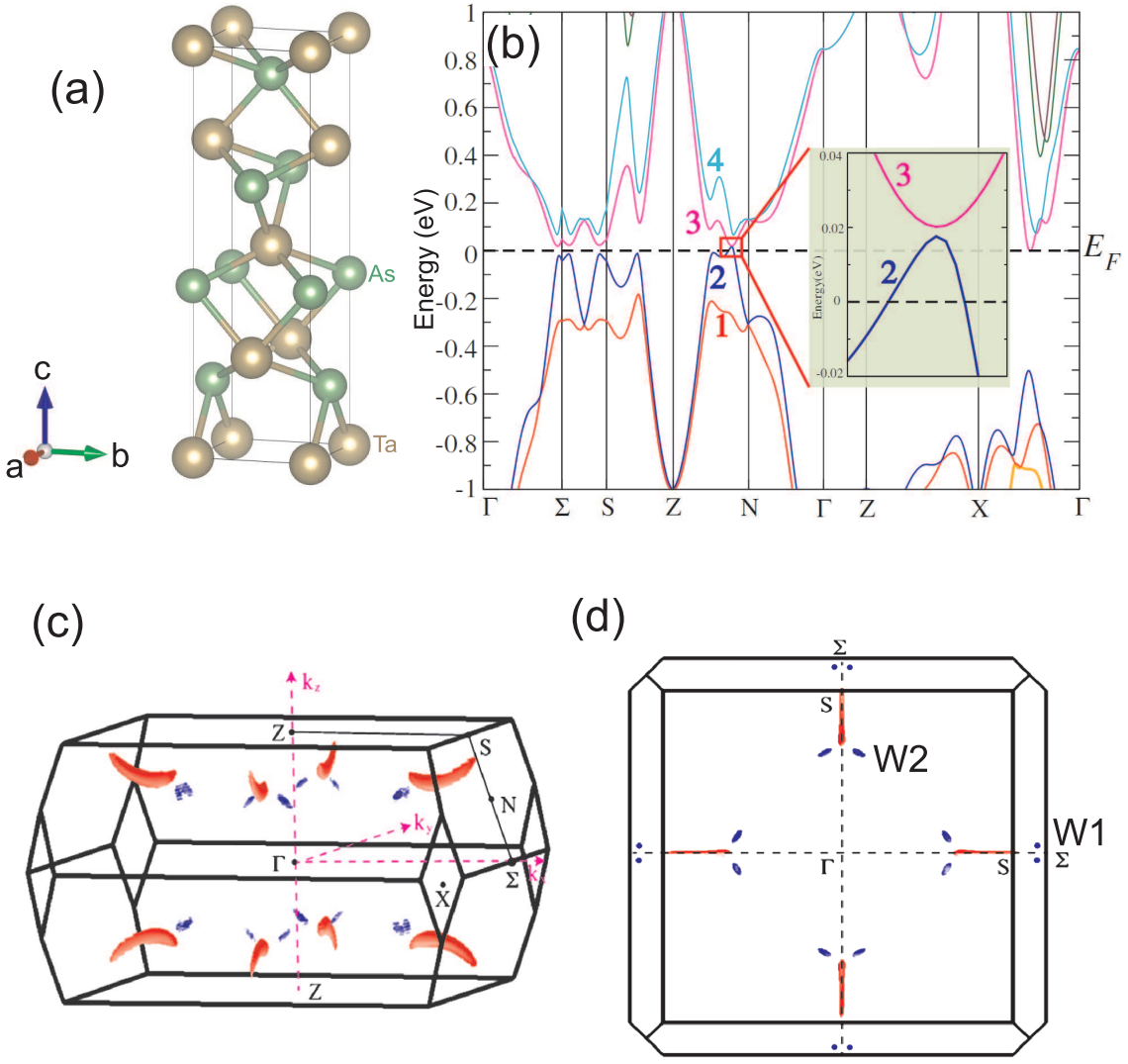

Figure 6.1.1: The unit cell of TaAs (a) is the same as the one of NbP, however, with different lattice parameters. The band structure (b) is gapped almost everywhere around the Fermi energy E_F. There is only one small hole pocket from band 2. Therefore the Fermi surface (c, d) consists of banana shaped trivial hole like sheets. The W1 and W2 nodes are enclosed by small Fermi surfaces, due to non zero chemical potential. (a) drawn with VESTA [146] with crystallographic data from Ref. [28]. (b) reprinted from [28] licensed under CC BY 3.0. (c, d) modified from [6] licensed under CC BY 3.0.

6.2 TaAs: Results and Discussion

The results presented in the following were obtained on high quality single crystals of TaAs. The samples were provided by the group of Prof. Dr. C. Felser of the MPI-CPfS[1]. All optical and magneto-optical measurements were performed by the author in Stuttgart and Nijmegen. The transport data was contributed by Anja Löhle from the PI1.

6.2.1 Transport properties

The temperature dependent resistivity $\rho(T)$ of TaAs was measured in the (001) plane in a standard four contact geometry. The resulting $\rho(T)$ is depicted in Fig. 6.2.1 (a). For $T \geq 170\,\mathrm{K}$, the resistivity increases linear in temperature, emphasized by the orange line. This indicates the prominence of electron-phonon scattering processes in this temperature regime. The inset of Fig. 6.2.1 (a) displays an enlarged view of $\rho(T)$ at low temperatures. The dotted black arrow marks the residual resistivity $\rho_0 \approx 7\,\mu\Omega\mathrm{cm}$. This value is an order of magnitude larger compared to the ρ_0 of NbP. The carrier densitiy of TaAs is expected to be at least a factor of 10 lower than of NbP [168]. Accordingly, ρ_0 can be expected to be larger in TaAs, if the scattering processes are assumed to be comparable.
The residual resistivity ratio of the investigated sample is $RRR \approx 16$ and falls well in the spread of other reported values [50, 207].
Frame (b) of Fig. 6.2.1 depicts $\Delta\rho = \rho(T) - \rho_0$ on a double logarithmic scale. The orange line in this panel reveals that $\Delta\rho \propto T^{4.2}$ for $T \lesssim 30\,\mathrm{K}$. This finding places the temperature dependence of the resistivity in TaAs close to the behavior expected for simple metals, in contrast to NbP. The lower carrier density in TaAs likely reduces the importance of Coulomb interactions that are predicted to play a role in Weyl and Dirac semimetals [70].
Unfortunately an elaborate analysis of the transport characteristics in the investigated TaAs sample is not possible, since no magneto-transport data is available. Published data indicates similar behavior as presented in Sec. 5.2.1 for NbP. The temperature dependent resistivity $\rho(T)$ in magnetic fields was found to also exhibit a crossover from metallic to semiconducting behavior [6]. The analysis of the Hall data reveals two carrier species, electrons and holes. The electrons possess a higher mobility of the order $\mu_e \approx 10^5\,\mathrm{cm^2\,V^{-1}\,s^{-1}}$ at low temperatures, while the holes are less mobile $\mu_h \approx 10^4\,\mathrm{cm^2\,V^{-1}\,s^{-1}}$ [6, 31]. Note, that this is the opposite in NbP, where

[1]Max Planck Institute for chemical physics of solids, Dresden.

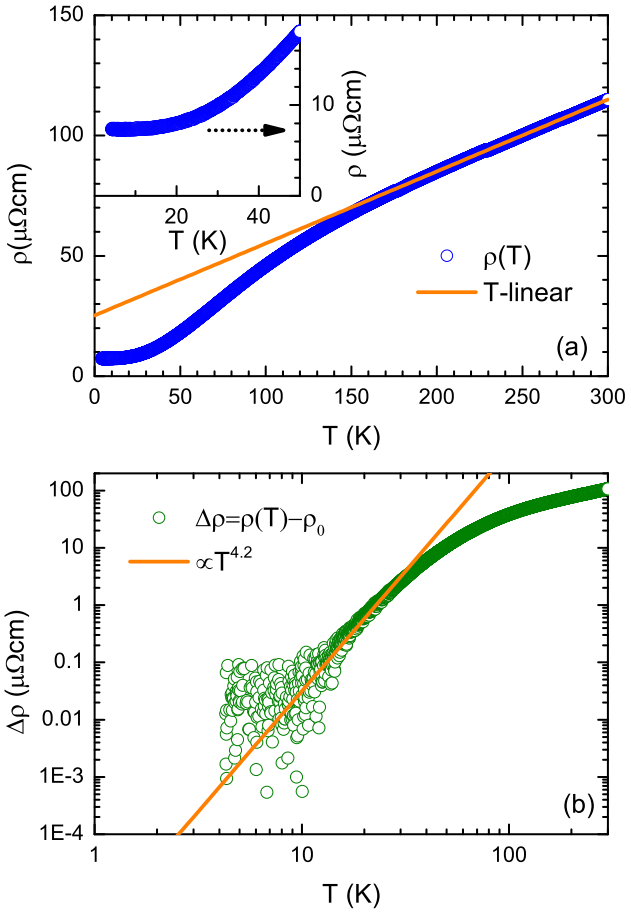

Figure 6.2.1: The temperature dependent resistivity $\rho(T)$ of TaAs is displayed as blue circles in panel (a). The orange line emphasizes the T-linear behavior above $T \geq 170\,\mathrm{K}$. The insert reveals a residual resistivity of $\rho_0 \approx 7\,\mu\Omega\mathrm{cm}$, an order of magnitude larger than in NbP (see Sec. 5.2.1). Panel (b) depicts $\Delta\rho = \rho(T) - \rho_0$ on a double logarithmic scale. The orange line in this panel reveals the power law $\propto T^{4.2}$ below $T \approx 30\,\mathrm{K}$, which places the resistivity of TaAs (unlike NbP) close to the expected T^5 behavior of a simple metal.

the electrons are less mobile. Carrier densities in the order of $N \approx 10^{17} - 10^{19}\,\mathrm{cm}^{-3}$ are reported [6, 31, 50].

The transverse magneto resistance in TaAs, with current applied perpendicular to the magnetic field $I \perp B$, increases linear in field and takes values of $MR = 0.8 \times 10^3$ at $T = 1.8\,\mathrm{K}$ and $B = 10\,\mathrm{T}$ [6]. The longitudinal magneto resistance in TaAs, with the current and field applied parallel $I \parallel B$, becomes negative. This behavior is ascribed to the chiral anomaly [6, 31], but could also arise from current jetting effects [32].

6.2.2 Optical experiments

The temperature dependent reflectivity of TaAs was measured in the isotropic (001) plane for frequencies $\omega = 20 - 25\,000\,\mathrm{cm}^{-1}$. The surface for the optical experiments was polished prior to measurements. The resulting reflectivity spectra $R(\omega)$ are displayed in Fig. 6.2.2 (a) over a wide frequency range for $T = 300, 150, 10\,\mathrm{K}$.

For frequencies above $800\,\mathrm{cm}^{-1}$, $R(\omega)$ is basically temperature independent. Below $800\,\mathrm{cm}^{-1}$ the temperature dependence is weak and only below $300\,\mathrm{cm}^{-1}$ pronounced changes are observed.

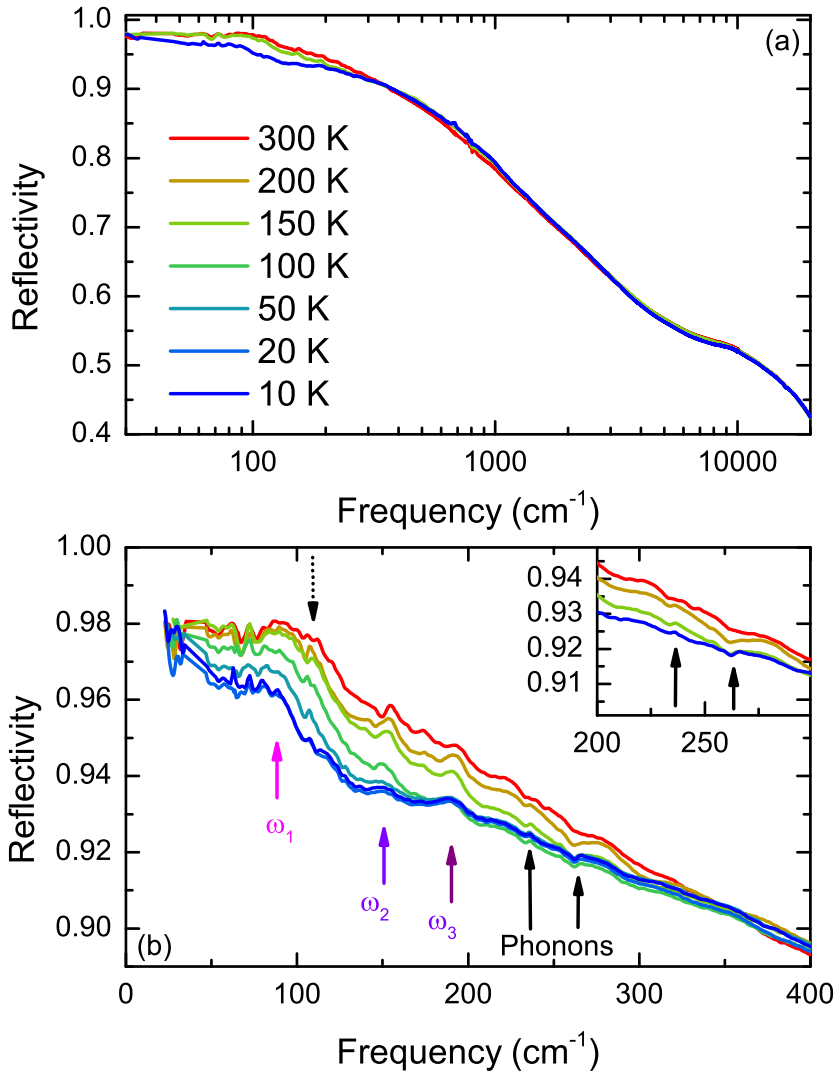

Figure 6.2.2: The reflectivity $R(\omega)$ of TaAs for $T = 300, 150, 10\,\mathrm{K}$ on a logarithmic frequency scale (a). An enlarged view of the FIR range is displayed in (b) on a linear scale. The black arrows mark the faint features that can be assigned to phonons, better seen in the magnified view in the inset of panel (b). The features marked with colored arrows and labeled ω_i $(i = 1, 2, 3)$ are related to the Weyl interband transitions and will be discussed later.

In Fig. 6.2.2 (b) an enlarged view on the FIR range is depicted. Two phonons are

marked with black arrows at 233 cm^{-1} and 263 cm^{-1} in this panel and the inset. They can be assigned to in plane vibrations of As-atoms, just like the two phonons observed in NbP (see Sec. 5.2.2) [197, 198]. The vibrational frequencies are lower than in NbP due to the higher atomic mass of As. In TaAs these phonons only leave a very weak signature in the spectra, as compared to the strong features in NbP. The reason is likely, that the TaAs (001) surface was polished, while that of NbP was not.
Possibly a third infrared active phonon is resolved at 106 cm^{-1}, marked by the downwards pointing black dotted arrow in Fig. 6.2.2 (b). The reported vibrational frequency of this phonon in Raman experiments is slightly higher [197, 198], and below 100 cm^{-1} the noise level in the spectra starts to increase towards lower frequencies. Hence, the interpretation of this feature as a phonon is speculative, even though it appears in the spectra of all temperatures at the same position.
In panel (b) of Fig. 6.2.2 three additional features are marked. ω_1 marks a sharp kink in the reflectivity. ω_2 and ω_3 mark two humps, that can not be assigned to lattice vibrations. These features correspond to distinctive signatures of transitions between the Weyl bands in the four-band model (see Sec. 2.6), as will be discussed later.

Further insight into the electrodynamic properties of TaAs is gained by examining the optical conductivity $\sigma_1(\omega)$ and the dielectric function $\varepsilon_1(\omega)$ depicted in Fig. 6.2.3. The optical conductivity $\sigma_1(\omega)$ in frame (a) reveals two pronounced humps around ω_1 and ω_3. The hump around ω_3 thereby consists of two smaller peaks, that correspond to the features labeled with ω_2 and ω_3 in the reflectivity in Fig 6.2.2 (b). Towards higher frequencies the optical conductivity $\sigma_1(\omega)$ increases linear in frequency between 3500 cm^{-1} and 8000 cm^{-1}. This linearity is emphasized by the black dashed line in Fig. 6.2.3 (c), which displays $\sigma_1(\omega)$ on a linear scale. Two further characteristic features are marked in panel (c). At ω_4 and ω_5 the spectra experience a slight kink. Note also the broad bulge in the spectra between ω_4 and ω_5, which arises from a trivial interband transition, as discussed later.

The dielectric function $\varepsilon_1(\omega)$ exhibits two peaks at low temperatures at the frequencies marked with ω_1 and ω_3 in Fig. 6.2.3 (b). These peaks overlay with the strong decrease of $\varepsilon_1(\omega)$ to large negative values at low frequencies arising from the free charge carriers. It was discussed in Sec. 2.6 that the onset of Weyl interband transitions is marked by peaks in the dielectric function $\varepsilon_1(\omega)$. Identifying the two features

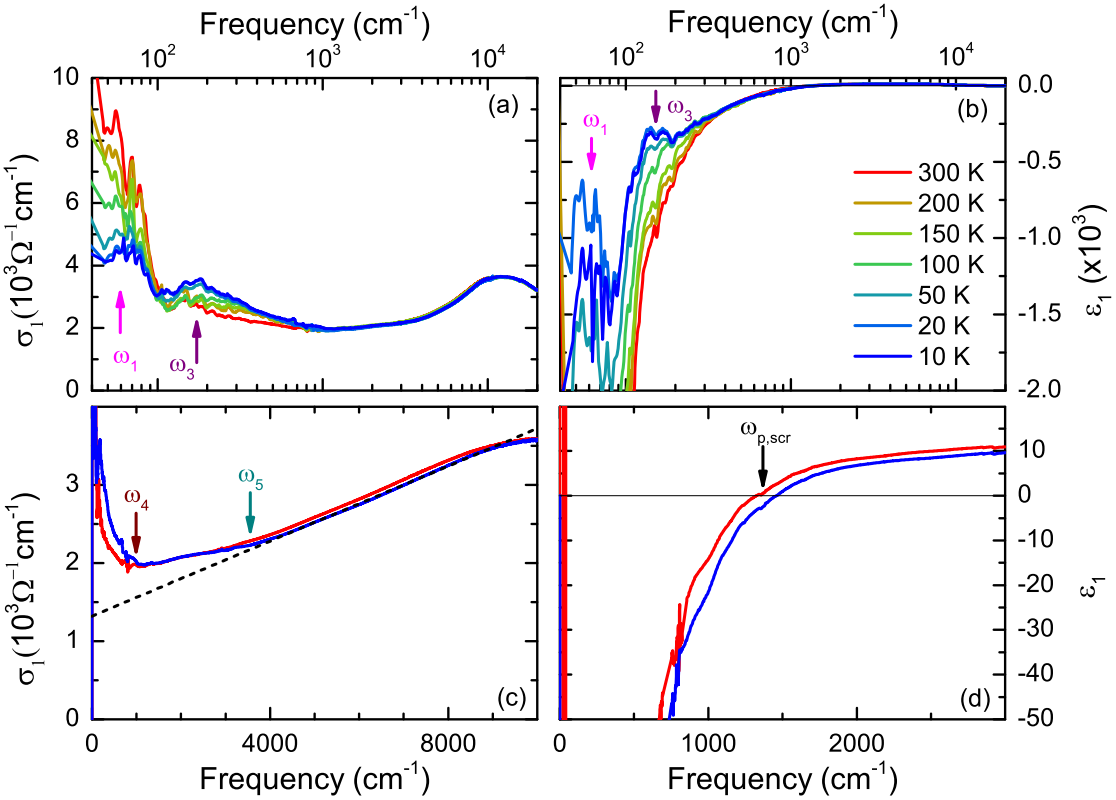

Figure 6.2.3: In the optical conductivity $\sigma_1(\omega)$ (a) and the dielectric function $\varepsilon_1(\omega)$ (b) on logarithmic frequency scale the onsets of the Weyl interband transitions are marked with ω_1 and ω_3. The linear frequency scale in panel (c) reveals a linear increase of $\sigma_1(\omega)$ between 3500 cm^{-1} and 8000 cm^{-1}. Two kinks in the optical conductivity are labeled with ω_4 and ω_5 in frame (c). The screened plasma frequency $\omega_{p,scr} \approx 1400\,\mathrm{cm}^{-1}$ is marked in panel (d) at the zero crossing of $\varepsilon_1(\omega)$.

in Fig. 6.2.3 (b) with the onsets of transitions within the W2 and W1 cones yields $\Delta_{E,W2} \approx 30\,\mathrm{cm}^{-1} \equiv 4\,\mathrm{meV}$ and $\Delta_{E,W2} \approx 70\,\mathrm{cm}^{-1} \equiv 9\,\mathrm{meV}$.
It can safely be assumed, that the W1 nodes are located below the Fermi energy E_F. Therefore the W2 nodes are likely located 4 meV above E_F in the investigated sample, because the energy distance between W1 and W2 nodes is around $13 - 14\,\mathrm{meV}$ [5, 31].
The zero crossing of the dielectric function at the screened plasma frequency, is marked in Fig. 6.2.3 (d). From this $\omega_{p,scr} \approx 1400\,\mathrm{cm}^{-1}$ is found.

For a quantitative analysis the optical conductivity is fit in a similar fashion as it was done in Sec. 5.2.2 for NbP. A narrow Drude term accounts for the highly mobile

carriers of the Weyl cones, while another, much broader, Drude term arises from the trivial hole band. The interband response of the Weyl cones is modeled utilizing two terms of the 4-band model reported in [74]. Additionally, for a satisfactory fit, four Lorentz terms need to be introduced.

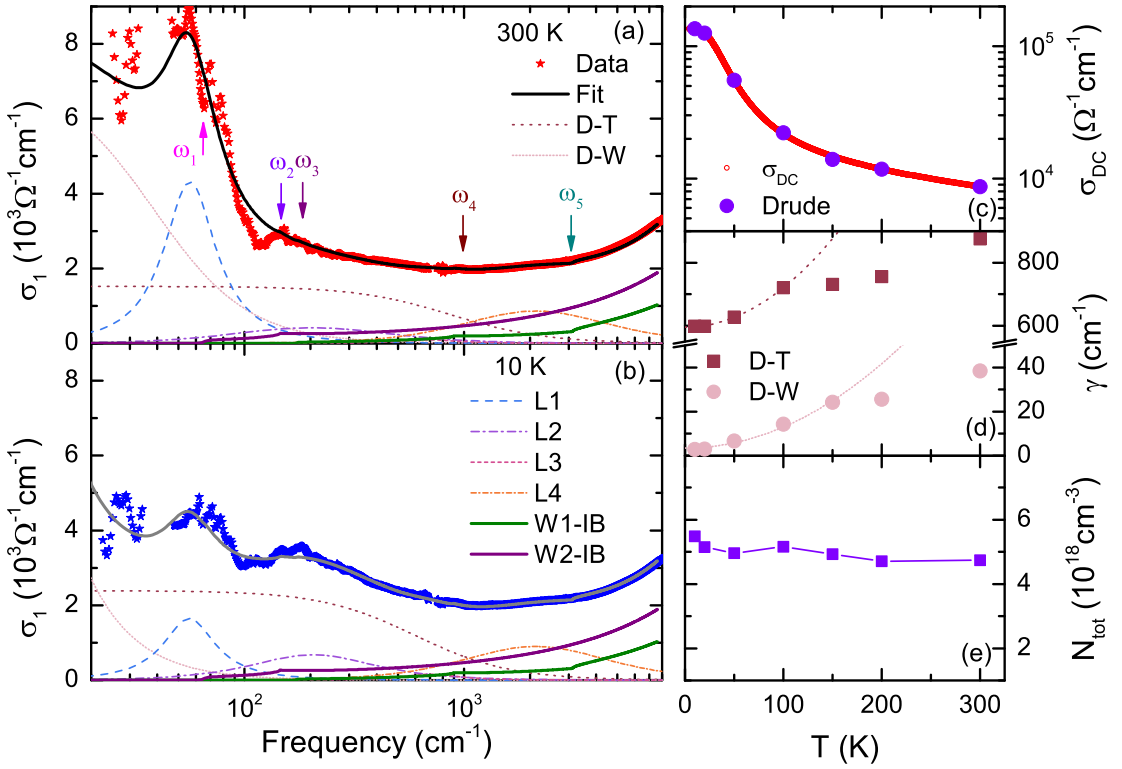

Figure 6.2.4: The fit of the optical conductivity $\sigma_1(\omega)$ (a, b) contains two Drude components; D-T for the trivial hole carriers and D-W for the highly mobile Weyl carriers. Three Lorentz terms L2 - L4 are introduced to account for trivial interband transitions. The origin of L1 is yet not clear (see text). The interband response of the Weyl cones is modeled by two terms after the four-band model in Ref. [74]. The anchoring of the low frequency limit of the fit $\sigma_1(\omega \to 0)$ at the measured DC-conductivity σ_{DC} guarantees self-consistency of the two independently obtained data sets (c). The scattering rates of both Drude components follow a T^2 behavior at low temperatures (dashed lines in panel (d)). The total carrier density $N_{tot} \approx 5 \times 10^{18}\,\mathrm{cm}^{-3}$ is roughly temperature independent (e).

The resulting fits are displayed in Fig. 6.2.4 for the conductivity spectra at 300 K (a) and at 10 K (b). For all temperatures the spectra are described well by the fits. The narrow Drude term D-W, which describes the highly mobile Weyl carriers, has most of it's spectral weight below the accessible measurement range. Therefore

the zero frequency conductivity $\sigma_1(\omega \to 0)$ of the fit is anchored at the measured DC-conductivity σ_{DC}. This assures the consistency of these two sets of data as depicted in Fig. 6.2.4 (c). The scattering rate of the broad Drude term D-T, describing the carriers of the trivial hole pocket is at least an order of magnitude higher than that of D-W. This was also observed in NbP. The scattering rates γ of both Drude components follow a T^2 behavior at low temperatures up to $T = 100 - 150\,\mathrm{K}$. The dashed lines in Fig. 6.2.4 (d) are fits of the scattering rates with $\gamma(T) = \gamma_0 + A \cdot T^2$. The zero temperature limit γ_0 is $595\,\mathrm{cm}^{-1}$ for D-T and $3.5\,\mathrm{cm}^{-1}$ for D-W, and the prefactors are $A \approx 0.01$ and $A \approx 0.001$, respectively. Note, that a scattering rate $\gamma \propto T^2$ was also reported in another optical study on TaAs [67], and is in agreement with theoretical predictions for Weyl semimetals [77]. The kinks in the temperature dependence of the scattering rates in Fig. 6.2.4 (d) around $T = 100 - 150\,\mathrm{K}$ coincide with the temperatures where a kink in the temperature dependence of the electron and hole mobilities μ_e and μ_h were reported [31]. These anomalies are possibly related to the change of sign of the Hall coefficient, meaning with the change from hole type to electron type conduction from high to low temperatures [6].
To estimate the total carrier density N_{tot}, the total plasma frequency is calculated as $\omega_{p,tot} = \sqrt{\omega^2_{p,\mathrm{D\text{-}W}} + \omega^2_{p,\mathrm{D\text{-}T}} + \omega^2_{p,\mathrm{L1}}}$. Here, the carriers contributing to the lowest lying Lorentz term are included, since the spectral weight of L1 is basically solely in the range of the Drude terms. The contribution of L1 to the total plasma frequency is, however, minor. With the effective carrier mass found in the magneto-optical experiments $m^* = 0.004\,m_e$ (see Sec. 6.2.3) the total carrier density $N_{tot} = \frac{m^* \omega^2_{p,tot}}{4\pi e^2}$ is calculated and displayed in Fig. 6.2.4 (e). The carrier density is roughly constant in temperature and in the range of $N_{tot} \approx 5 \times 10^{18}\,\mathrm{cm}^{-3}$, and therefore an order of magnitude lower than in NbP.

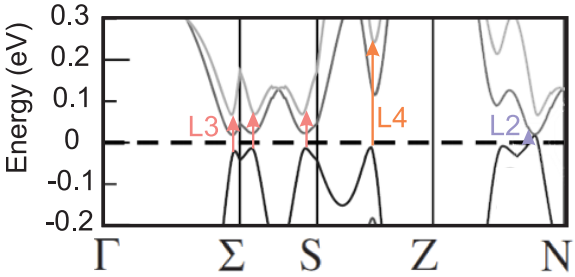

Figure 6.2.5: Enlarged detail of the band-structure of TaAs. The transitions related to the Lorentz terms L2, L3 and L4 are marked with colored arrows. Modified from [28] licensed under CC BY 3.0

The origin of the Lorentz terms L2, L3 and L4 can be found, looking at the band-structure introduced in Sec. 6.1. The center frequencies ω_0 of these terms correspond to energies $E_0 = \hbar\omega_0$, that match transitions across the Fermi energy E_{F}. Fig. 6.2.5

depicts an enlarged detail of the bandstructure of TaAs (See also Fig. 6.1.1 (b)). The transitions, related to the terms L2, L3 and L4 are marked with colored arrows in the figure. For L1 no suitable transitions are found in Fig. 6.2.5. Possibly the cause for this Lorentz term is found in the Weyl bands, since its center frequency roughly coincides with the onset of the W2 interband transitions. Tab. 6.2.1 summarizes the parameters of the Lorentz terms.

Lorentz term	$\omega_0(\mathrm{cm}^{-1})$	$E_0(\mathrm{meV})$
L1	56	7
L2	200	25
L3	700	87
L4	2120	262

Table 6.2.1: Center frequencies ω_0 and energies E_0 of the Lorentz terms utilized in the fits of the optical conductivity $\sigma_1(\omega)$ of TaAs.

Now the interband response of the Weyl cones remains to be discussed. The onsets of the Weyl interband transitions were found in the dielectric function $\varepsilon_1(\omega)$, and correspond to the features that were marked with ω_1 and ω_3. The other prominent signatures of transitions in the Weyl bands are displayed and labeled in Fig. 6.2.6. Note, that for a satisfactory fit, the 'outer' bands of the W2 cone are missing. Therefore, the parameters m and b of this term are not unique, and only the difference $m - b$ is well defined. The fit parameters of the 4-band Weyl terms are summarized in Tab. 6.2.2. Unlike in NbP, all fit parameters of the Weyl interband response are temperature independent. The Fermi velocities v_F are found to be larger in TaAs as in NbP.

The separation in k of the nodes in Fig 6.2.6 is smaller than in NbP, in contradiction with the theoretical calculations and reports from ARPES [47, 168]. As already discussed in Sec. 5.2.2, the momentum averaging nature of the optical experiment prevents a reliable determination of Δk by modeling the data with the effective four-band model.

Cone	m(meV)	b(meV)	Δ_E(meV)	$v_\mathrm{F}(10^5\,\mathrm{m\,s}^{-1})$
W1	69	124	10.7	7.2
W2	148	157	4	4.8

Table 6.2.2: The parameters utilized to fit the Weyl interband response of TaAs with the 4-band model of Ref. [74].

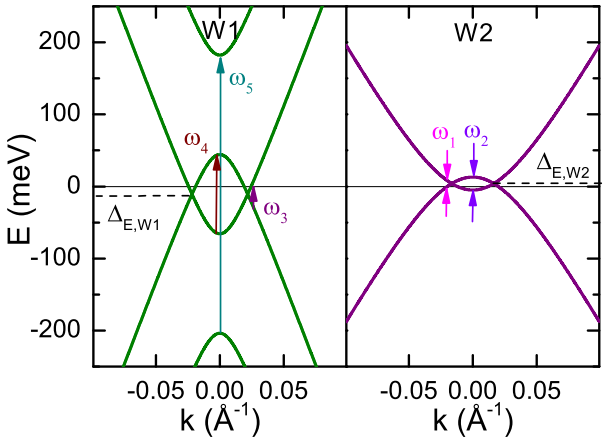

Figure 6.2.6: The effective dispersions $\epsilon_{eff,W1}$ and $\epsilon_{eff,W2}$ around the W1 and W1 Weyl nodes according to Eq. 2.6.5. The transitions between the bands responsible for the features at ω_i ($i = 1-5$) are marked with arrows.

6.2.3 Results: Magneto-Optics

The magneto-optical measurements on TaAs up to $B = 7\,\mathrm{T}$ were performed in Stuttgart for frequencies $\omega \approx 20-2000\,\mathrm{cm}^{-1}$. The sample temperature was $T = 7\,\mathrm{K}$. Further measurements were performed at $T = 1.4\,\mathrm{K}$ up to $B = 30\,\mathrm{T}$ in the HFML in Nijmegen. All magneto-optical measurements were performed in Voigt geometry with unpolarized light and the field applied in the (001) plane. The measurements in Stuttgart were conducted with the gold evaporation technique. In Nijmegen only relative spectra were recorded.

First, the low field data up to $B = 7\,\mathrm{T}$ will be discussed. In the same style as it was presented for NbP (Sec. 5.2.3), Fig. 6.2.7 (a) displays the absolute reflectivity $R(\omega)$ measured at $T = 7\,\mathrm{K}$ in the magneto-optical setup as blue line at $0\,\mathrm{T}$ and as orange line at $7\,\mathrm{T}$. Note that only the FIR range is displayed. The thin black line corresponds to the $10\,\mathrm{K}$ spectrum recorded in the zero field gold evaporation cryostat. The data obtained in the two different setups agree well, and the main features discussed above in the zero field spectra are also found in the measurement at $0\,\mathrm{T}$ inside the magnet. While in NbP a large variety of field induced changes were observed, in TaAs only below $200\,\mathrm{cm}^{-1}$ a dramatic change of the reflectivity is apparent.

The magnetic field induced changes in the reflectivity lead to an enormous peak in the conductivity displayed in Fig. 6.2.7 (b). In the apex this peak reaches a conductivity twice as large as the zero field value. The suppression of conductivity left and right of the large peak assures that the f-sum rule (Eq. 2.2.2) holds. In the relative reflectivity in Fig. 6.2.7 (c), the maximum in the conductivity corresponds to the middle of the positive slope. This first dramatic feature is labeled with λ_1. The field

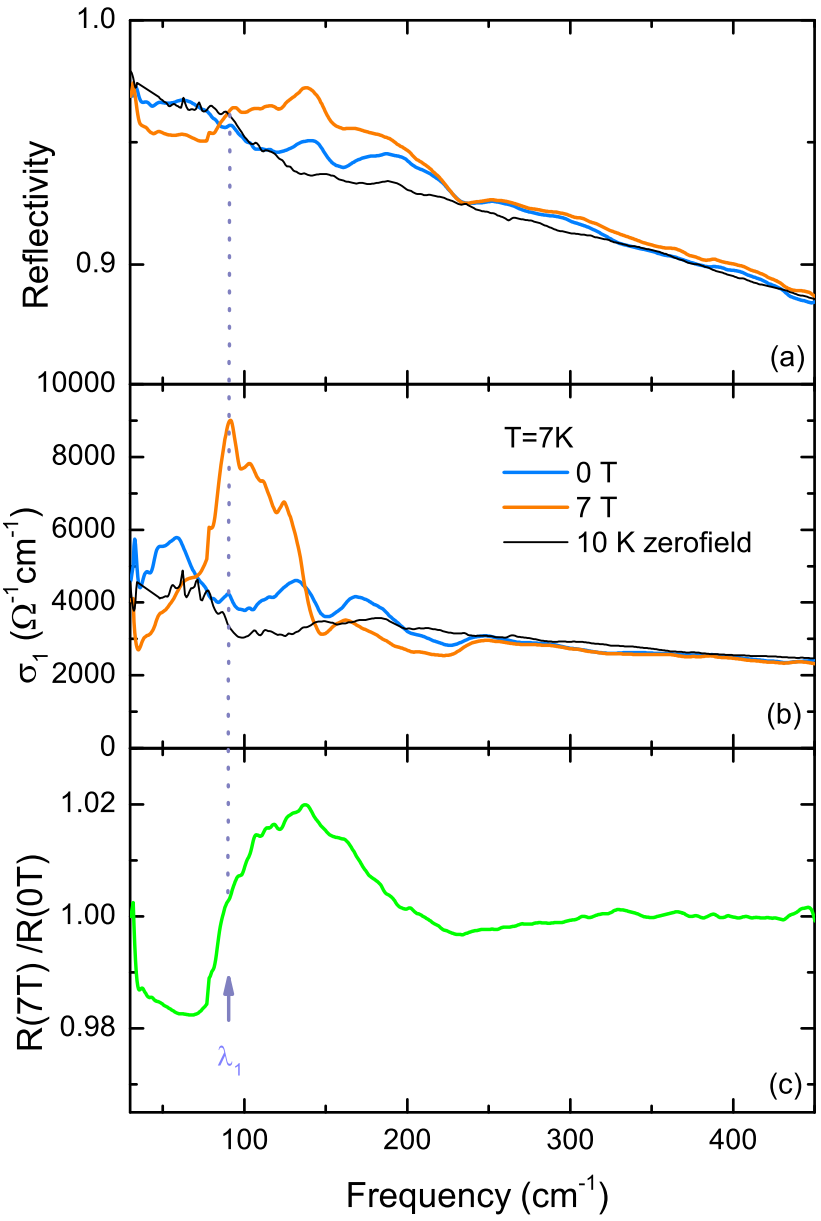

Figure 6.2.7: The absolute reflectivity $R(\omega)$ (a) and optical conductivity $\sigma_1(\omega)$ (b) of TaAs measured in the magneto-optical setup at $B = 0\,\mathrm{T}$ and $B = 7\,\mathrm{T}$. The spectra obtained in the zero field cryostat are additionally displayed as thin black lines. Below $200\,\mathrm{cm}^{-1}$ the B field induces drastic changes in the reflectivity which manifest themselves as a pronounced asymmetric peak in the optical conductivtiy $\sigma_1(\omega)$ (b). In the relative reflectivity $R(7\,\mathrm{T})/R(0\,\mathrm{T})$ (c) the peak position corresponds to the steep positive slope, emphasized by the dotted line labeled with λ_1.

dependence of λ_1 (and other features) will be discussed later.

In NbP, the most pronounced changes in the low field spectra were found to arise from the plasma frequency splitting. The large feature at λ_1 found for TaAs in the FIR is however far-off the screened plasma frequency $\omega_{p,scr} \approx 1400\,\mathrm{cm}^{-1}$ determined from the zero field optical measurements. Fig. 6.2.8 (a) displays the relative reflectivity spectra $R(B)/R(0\,\mathrm{T})$ in 1 T steps for frequencies around $\omega_{p,scr}$. The spectra are stacked for clarity.

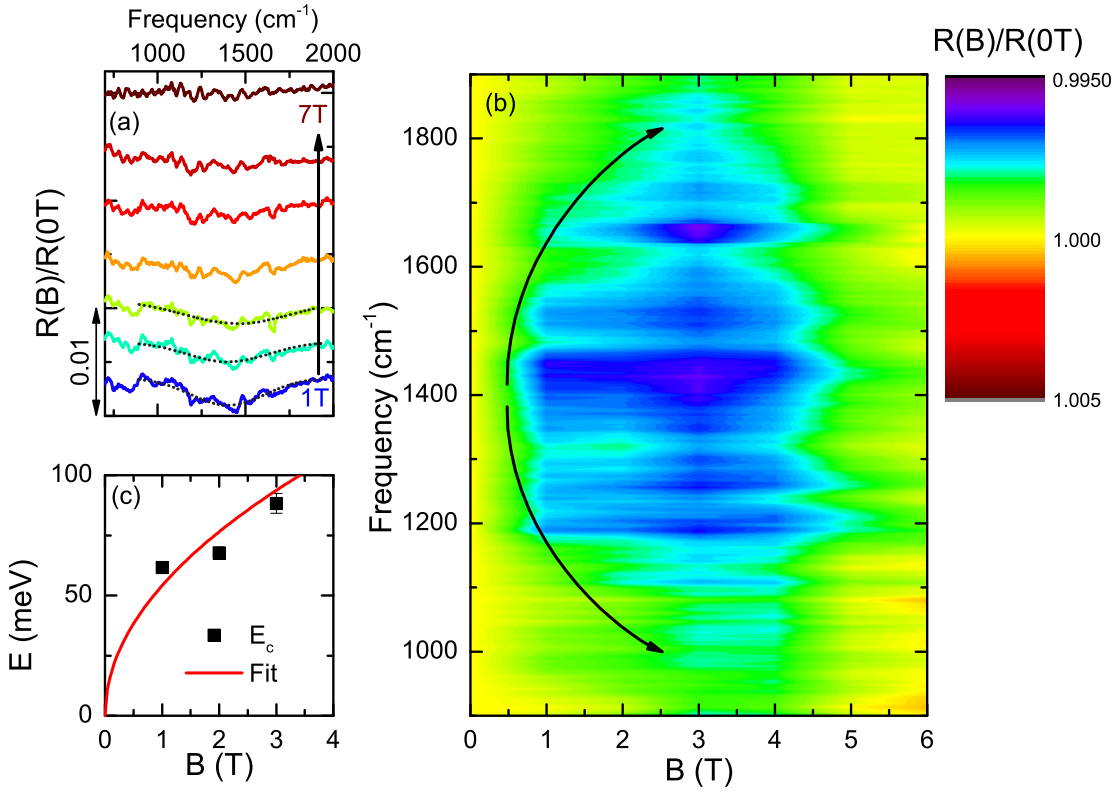

Figure 6.2.8: In the frequency range of the screened plasma frequency $\omega_{p,scr} \approx 1400\,\mathrm{cm}^{-1}$ slight changes appear in magnetic fields (a). The relative reflectivity spectra $R(B)/R(0\,\mathrm{T})$ in panel (a) are displayed in steps of 1 T, vertically shifted for clarity. Dotted black lines are Gauss fits. The width of the blue structure in the contour plot (b) clearly broadens up to 3 T (black arrows). The field dependence of the cyclotron energy E_c extracted as described in the text is displayed in (c) as solid squares. The fit (red line) yields $v_F = 1.5 \times 10^6\,\mathrm{m\,s}^{-1}$.

Indeed some faint field induced changes are observed around $1400\,\mathrm{cm}^{-1}$. Fig. 6.2.8 (b) depicts a contour plot of the relative reflectivity. This panel reveals spectral changes broadening with increasing field more clearly. For $B \geq 4\,\mathrm{T}$ the spectral changes diss-

apear. It can be assumed, that the width of the spectral changes correspond roughly to the magnetic field induced plasma frequency splitting. With this assumption, the splitting is approximated by fitting Gauss curves to the relative spectra in Fig. 6.2.8 (a), which are depicted as dotted black lines. The full width at half maximum of the Gauss fits is utilized as an estimate of the cyclotron frequency ω_c (see Sec. 2.7.1). Fig. 6.2.8 (c) depicts the cyclotron energy $E_c = \hbar\omega_c$ versus the magnetic field. In the same fashion as in NbP, E_c is best fit with Eq. 5.2.9, since any linear fit would result in an unphysical finite cyclotron energy at $B = 0\,\mathrm{T}$. The $\sqrt{B}$ dependence of E_c is a direct consequence of the linear dispersing bands and furthermore it indicates, that TaAs is in the quantum limit already at $B \approx 1\,\mathrm{T}$. The fit depicted as a red line in frame (c) yields a very large Fermi velocity of $v_\mathrm{F} = 1.5 \times 10^6\,\mathrm{m\,s^{-1}}$. For the average cyclotron mass, calculated the same way as for NbP in Sec. 5.2.3, $m_c \approx 0.004\,m_e$ is obtained.

To trace down the magnetic field dependence of the feature labeled with λ_1, Fig. 6.2.9 (a) displays the relative reflectivity $R(B)/R(0\,\mathrm{T})$ for $B = 1 - 7\,\mathrm{T}$ in $1\,\mathrm{T}$ steps. The spectra are offset vertically for clarity. In addition to the extremely strong feature λ_1, a series of signatures from Landau level transitions are found towards higher frequencies. All dips are marked with colored symbols which are labeled with λ_i ($i = 1 - 5$). The field dependence of the λ_i is depicted in Fig. 6.2.9 (b). To elucidate the Landau level transitions, responsible for the features found in the spectra, the frequency ratios are calculated. It is found that $\lambda_1 : \lambda_2 : \lambda_3 : \lambda_4$ relate roughly as $1 : 2.6 : 3.4 : 3.8$. The transitions between Landau levels from linear bands are found at the signature frequencies dependent on $\sqrt{n} + \sqrt{n+1}$ with the Landau level index n. Hence, it is evident, that the λ_i ($i = 1 - 4$) can be assigned to the transitions $L_{-n} \rightarrow L_{n+1}$ and $L_{-(n+1)} \rightarrow L_n$ as summarized in Tab. 6.2.3. From the fits of the field dependence of the Landau level transitions, displayed in Fig. 6.2.9 (b) as solid lines, the Fermi velocities are obtained (see Tab. 6.2.3).

The feature at λ_5 falls out of the scheme of the signature frequencies. Hence, this feature is assigned to a Landau level transition of a different cone.
The comparison of the Fermi velocities obtained from the field dependence of Landau level transitions with the Fermi velocities deduced from the fit of the zero-field optical conductivity suggests, that λ_{1-4} can be assigned to W2 and λ_5 to W1.
In average, the values of Tab. 6.2.3 yield $v_{\mathrm{F,W1}} = 6.68 \times 10^5\,\mathrm{m\,s^{-1}}$ and $v_{\mathrm{F,W2}} = 1.34 \times 10^5\,\mathrm{m\,s^{-1}}$. The consistency of $v_{\mathrm{F,W1}}$ with the value from the zero field op-

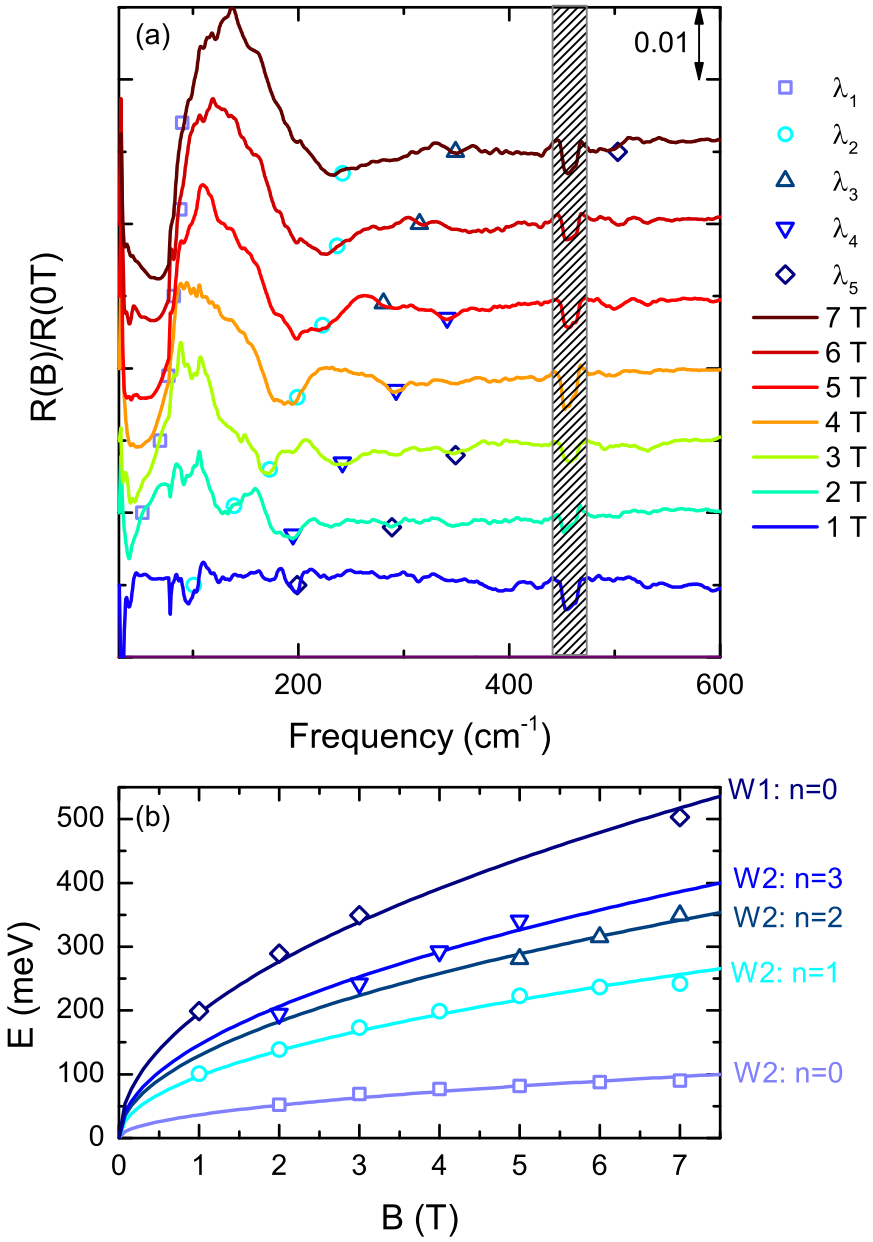

Figure 6.2.9: The relative reflectivities $R(B)/R(0\,\mathrm{T})$ of TaAs for fields from $B = 1\,\mathrm{T}$ to $B = 7\,\mathrm{T}$ in $1\,\mathrm{T}$ steps in the FIR range (a). For clarity, the spectra are stacked vertically. The field dependence of the features labeled with λ_i can be traced nicely, as indicated by the open symbols. The frequencies of the features labeled with λ_i are plotted versus magnetic field B in panel (b). The solid lines correspond to fits yielding Fermi velocities v_F as summarized in Tab. 6.2.3. In the gray shaded area the spectra are perturbed by a feature from the beam splitter.

Label	Cone	Transition	$v_F(10^5\,\mathrm{m\,s^{-1}})$
λ_1	W2	$L_0 \to L_1$; $L_{-1} \to L_0$	1.25
λ_2	W2	$L_{-1} \to L_2$; $L_{-2} \to L_1$	1.37
λ_3	W2	$L_{-2} \to L_3$; $L_{-3} \to L_2$	1.40
λ_4	W2	$L_{-3} \to L_4$; $L_{-4} \to L_3$	1.33
λ_5	W1	$L_0 \to L_1$; $L_{-1} \to L_0$	6.68

Table 6.2.3: Assignment of the features labeled with λ_i to the inter Landau level transitions $L_{-n} \to L_{n+1}$; $L_{-(n+1)} \to L_n$ of the W1 and W2 Weyl cones. The Fermi velocities v_F are obtained by fitting the field dependence of the features.

tical conductivity is remarkable, while for $v_{F,W2}$ there is a discrepancy, since the zero field data yield a Fermi velocity larger by a factor of 3.5.

The broad peak between λ_1 and λ_2 in the relative reflectivity Fig. 6.2.9 (a) continues to broaden for higher fields up to 30 T, very well seen in the contour plot in Fig. 6.2.10. The white lines mark the theoretical development of the $L_0 \to L_1$ ($L_{-1} \to L_0$) and $L_{-1} \to L_2$ ($L_{-2} \to L_1$) transitions, computed for the W2 Fermi velocity $v_{F,W2} = 1.34 \times 10^5\,\mathrm{m\,s^{-1}}$. The line for the $L_{-1} \to L_2$ (n=1) nicely follows the structure in the contour plot. The same is true for the line representing the $L_0 \to L_1$ (n=0) transition, however only up to approximately 8 T, indicated with the black dotted vertical line. For higher fields, the red structure appears to broaden, and starts to expand to lower frequencies. Such behavior is very unusual.

To explore the unconventional field dependence of the structure related to the n=0 transition in Fig. 6.2.10, the optical conductivity $\sigma_1(\omega)$ of the high field measurements is calculated. To obtain $\sigma_1(\omega)$ from the relative reflectivity of the high field measurements, the absolute reflectivity at zero field is multiplied by the relative reflectivity at finite field. The Kramers-Kronig of the resulting spectrum yields the absolute optical conductivity at finite field.

The relative optical conductivity $\sigma_1(B)/\sigma_1(0\,\mathrm{T})$ for selected fields is displayed in Fig. 6.2.11 (a). The spectra are vertically shifted. The peak, arising from the $L_0 \to L_1$ ($L_{-1} \to L_0$) transition of the W2 cone is located around $100\,\mathrm{cm^{-1}}$ at 6 T. Towards higher fields, this peak first broadens and then splits into four sub-peaks, clearly resolved at 26 T. The splitting is emphasized by the black and gray arrows in Fig. 6.2.11 (a) and the sub-peaks are enumerated $1-4$.

The underlying mechanism, responsible for the anomalous behavior towards high magnetic fields is likely the Zeeman splitting of Landau levels. A similar four fold splitting was reported in a magneto-optical study of the semimetal $ZrTe_5$, which

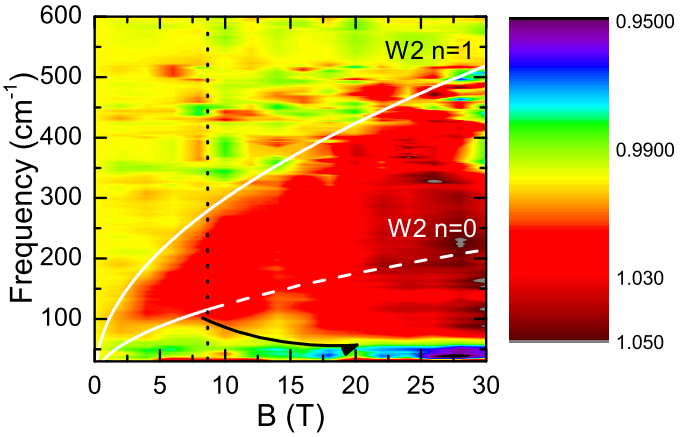

Figure 6.2.10: The two white lines correspond to the theoretical development of the $L_0 \rightarrow L_1$ ($L_{-1} \rightarrow L_0$) and $L_{-1} \rightarrow L_2$ ($L_{-2} \rightarrow L_1$) transitions of the W2 cone nicely follow the structures in the contour plot of the relative reflectivity $R(B)/R(0\,\mathrm{T})$ up to 8 T. For higher fields this is only true for the $L_{-1} \rightarrow L_2$ ($L_{-2} \rightarrow L_1$) transition. For fields beyond the black dotted vertical line, an anomalous development of the structures to lower frequencies with increasing field is observed, emphasized by the black arrow.

hosts massive Dirac particles. There, the splitting was also discussed in the Zeeman context [93].

Adding a Zeeman term to the Weyl Hamiltonian is known to shift the Weyl nodes in k-space [2, 17, 93, 208]. Landau levels with Landau level index $n \neq 0$ from cones of opposing chirality become shifted in k in opposite directions. The $n = 0$ Landau levels are lowered (or lifted) in energy in the same direction [93]. In the effective 4-band model widely utilized in this work to approximate the low energy physics of NbP and TaAs, a Zeeman term can be included by replacing the parameter b in Eq. 5.2.10b with $b \pm \overline{g}\mu_B B$ [203]. Here, $\overline{g}$ denotes an average g-factor for the conduction and valence band and μ_B is the Bohr magneton. The scenario is schematically depicted for one Weyl cone in Fig. 6.2.11 (c). The black solid line is the $n = 0$ Landau level of the cone. The purple lines are the $n = \pm 1$ Landau levels that are shifted to the left by the Zeeman term, while the green lines belong to the cone of opposing chirality and hence shifted to the right (emphasized by the arrows of corresponding color). The observation of four peaks is well explained by the finite chemical potential in the investigated sample, and the transitions between the $n = 0$ Landau level and the $n = \pm 1$ levels, indicated in Fig. 6.2.11 (c). The transitions 1 and 2 in this picture will produce stronger peaks since they occur between levels of the same chirality. The transitions 3 and 4 are only allowed, if the Landau levels are not purely of one spin species. In this case the intensity of these transitions are expected to be strongly

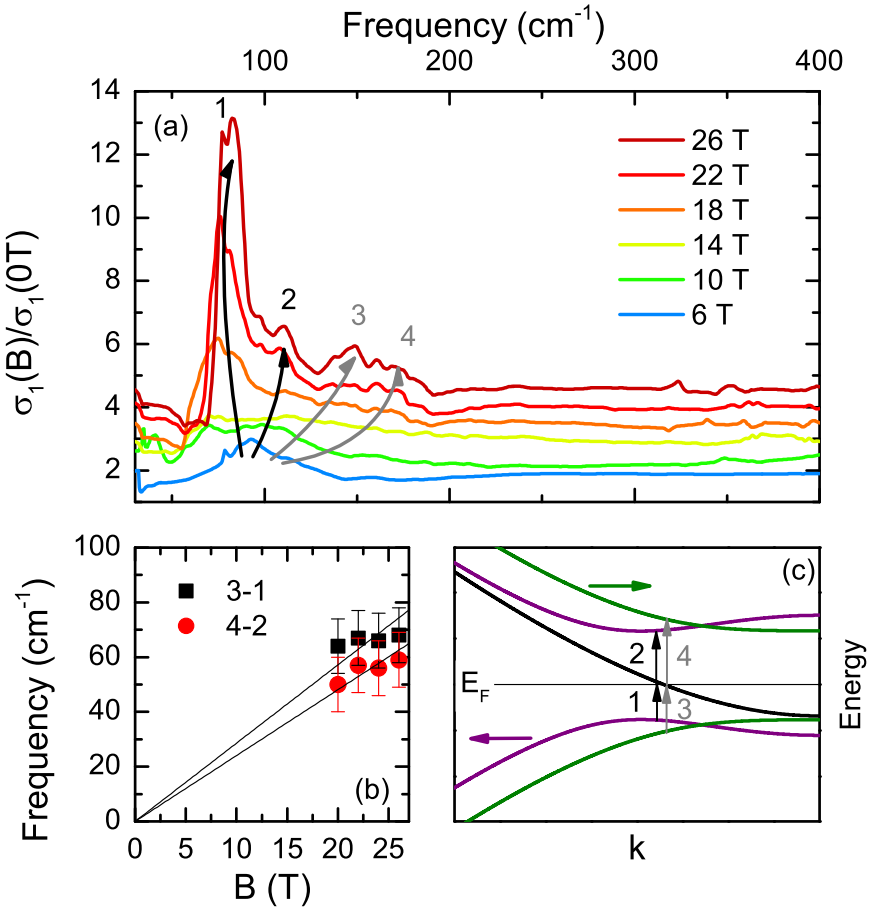

Figure 6.2.11: The relative optical conductivity $\sigma_1(B)/\sigma_1(0\,\mathrm{T})$ exhibits a clear fourfold splitting of the lowest peak (a) numbered with $1-4$. This can be understood considering a Zeeman term, which shifts the Landau levels with $n \neq 0$ of opposite chirality in opposite k directions, schematically depicted in panel (c). The green and purple arrow emphasize the direction of the k shift. The transitions responsible for the four peaks are indicated in panel (c). Identifying the frequency distance of the peaks with the Zeeman energy $E_Z = \overline{g}\mu_B B$ allows a rough estimation of the g-factor (b).

suppressed [93], which is in good agreement with the experimental facts in Fig. 6.2.11 (a). Therefore, the chirality of the Weyl cones in our sample is likely not well defined. Identifying the energy splitting of the Landau levels with the Zeeman energy $E_Z = \overline{g}\mu_B B$ allows to extract an effective g-factor $\overline{g}$ from the energy distances between 1 and 3 or 2 and 4. The frequency differences versus the magnetic field are displayed in Fig. 6.2.11 (b). The solid lines are fits according to the Zeeman energy with $\overline{g} \approx 6$ for $3-1$ and $\overline{g} \approx 5$ for $4-2$, respectively. The extracted g factors compare well to the values found in the sister compound TaP ($\approx 2-7$) [209].

The above analysis of the Zeeman splitting is clearly only a superficial approximation. For a more detailed treatment the low energy Hamiltonian of TaAs with additional Zeeman term needs to be solved and the optical conductivity needs to be computed. Certainly theoretical input is needed regarding this issue.

6.3 Conclusions

In conclusion, the presented transport, optical and magneto-optical study of TaAs gives deep insight into the electrodynamics and bandstructure of this compound. The low energy zerofield optical conductivity can be described with two Drude components representing the Weyl and trivial carriers, respectively. Additionally, three Lorentz oscillators account for trivial interband transitions, while the interband response between the Weyl bands can be approximated by an effective four-band model for each speciecs of Weyl cones. A fourth Lorentz oscillator of unknown origin is needed at very low frequencies for a satisfactory fit.
The magneto-optical response reveals a series of Landau level transitions developing with $\sqrt{B}$. This is a direct hallmark Landau levels evolving from linear bands. At very high fields an anomalous splitting of the lowest peak likely arises from a Zeeman splitting of the Landau levels in TaAs.
Tab. 6.3.1 summarizes the relevant quantities extracted from the fits in this work. For comparison, values found in literature are also presented.

Compared to NbP (see Chap. 5), TaAs exhibits larger Fermi velocities for the Weyl carriers. Additionally, the Weyl nodes are closer to the Fermi energy. Especially the low chemical potential makes TaAs a promising candidate for observing the chiral anomaly in optical experiments [174].
The finding of the Zeeman splitting of Landau levels in TaAs requires, however, that the chirality is not well defined, which in turn would prevent the observation of the chiral anomaly. The fact that a Zeeman splitting is found in TaAs, but not in NbP is intriguing itself. Possibly, the stronger spin-orbit coupling in TaAs leads to a mixing of spin up and spin down components, and therefore prevents a well defined chirality. The question arises then, why the chiral anomaly was clearly observed in magneto-transport experiments on TaAs [6, 31]. Further investigations and theoretical input are certainly needed to clarify this issue.

RRR	N_{tot} ($10^{18}\ \frac{1}{\mathrm{cm}^3}$)	v_F ($10^5\ \frac{\mathrm{m}}{\mathrm{s}}$)	Δ_E (meV)	m_c (m_e)	$\overline{g}$	Ref.
16	≈ 5	W1: 7.1 W2: 4.8	W1:-10.7 W2:+4.0	-	-	this, O
16	-	W1: 6.7 W2: 1.3 12 (ω_c)	-	0.004	5-6	this, MO
10	35	W1: 2.96 TH: 7.55	W1:-20 W2:-8	0.01-0.1	-	[50], MT, dHvA, BS
-	≈ 2	1.16	W1:-11.5 W2:+1.5	0.15	-	[31], MT, BS
-	≈ 0.6	W1: $v_x = 2.5$ $v_y = 1.2$ $v_z = 0.2$ W2: $v_x = 2.4$ $v_y = 3.5$ $v_z = 34.3$	W1: -22.1 W2: -8.9	-	-	[168], BS
					2-6.7 (TaP)	[209], MT

Table 6.3.1: Summary of the characteristic quantities of TaAs found in this work and extracted from references. The abbreviation MT, O, MO, dHvA and BS stand for magneto-transport, optics, magneto-optics, de Haas-van Alphen and bandstructure calculations, respectively and point out, which technique was used to determine the values. The ω_c behind the Fermi velocity in column three refers to the value obtained by the plasma frequency splitting.

7. The iron based superconductor FeSe

In this chapter the optical properties of the iron based superconductor FeSe will be presented. In the framework of this thesis, special attention will be payed to the Dirac like dispersion, evident in this material, and to its signatures in the optical response. This chapter is slightly off the topic of the previous chapters, since *a posteriori* it is clear, that the Dirac physics in FeSe is rather 2D than 3D.
First, some general introductory remarks concerning the material and the contemporary research will be made in Sec. 7.1. Then, the results of the transport and optical experiments will be discussed in Sec. 7.2, and conclusions will be drawn in Sec. 7.3.

7.1 The material

The discovery of the iron based superconductors in 2008 by Kamihara *et al.* [103], triggered enormous research efforts, resulting in thousands of publications within a few years (see e.g. Refs. [210–214] for reviews). Among the iron based superconductors, FeSe has the simplest crystal structure. However, not only because of its simplicity FeSe is of special interest, but also, because a very high superconducting transition temperature $T_c \approx 100\,\mathrm{K}$ was reported recently, on FeSe films of only one unit cell thickness [215]. Additionally, FeSe is very susceptible to pressure, and a superconducting transition temperature of $T_c \approx 37\,\mathrm{K}$ can be achieved by pressurizing bulk crystals [216].
Aside from the high T_c, the evidence for non-trivial topological aspects related to the superconducting state, as well as the suggested proximity to the BCS-BEC crossover (Bardeen Cooper Schrieffer - Bose Einstein Condensate) of FeSe and related compounds are of special interest in the contemporary research on these systems [217–219]. The evidences for Dirac like dispersing bands in FeSe are of special interest in the framework of this thesis [9, 10, 40, 220, 221].

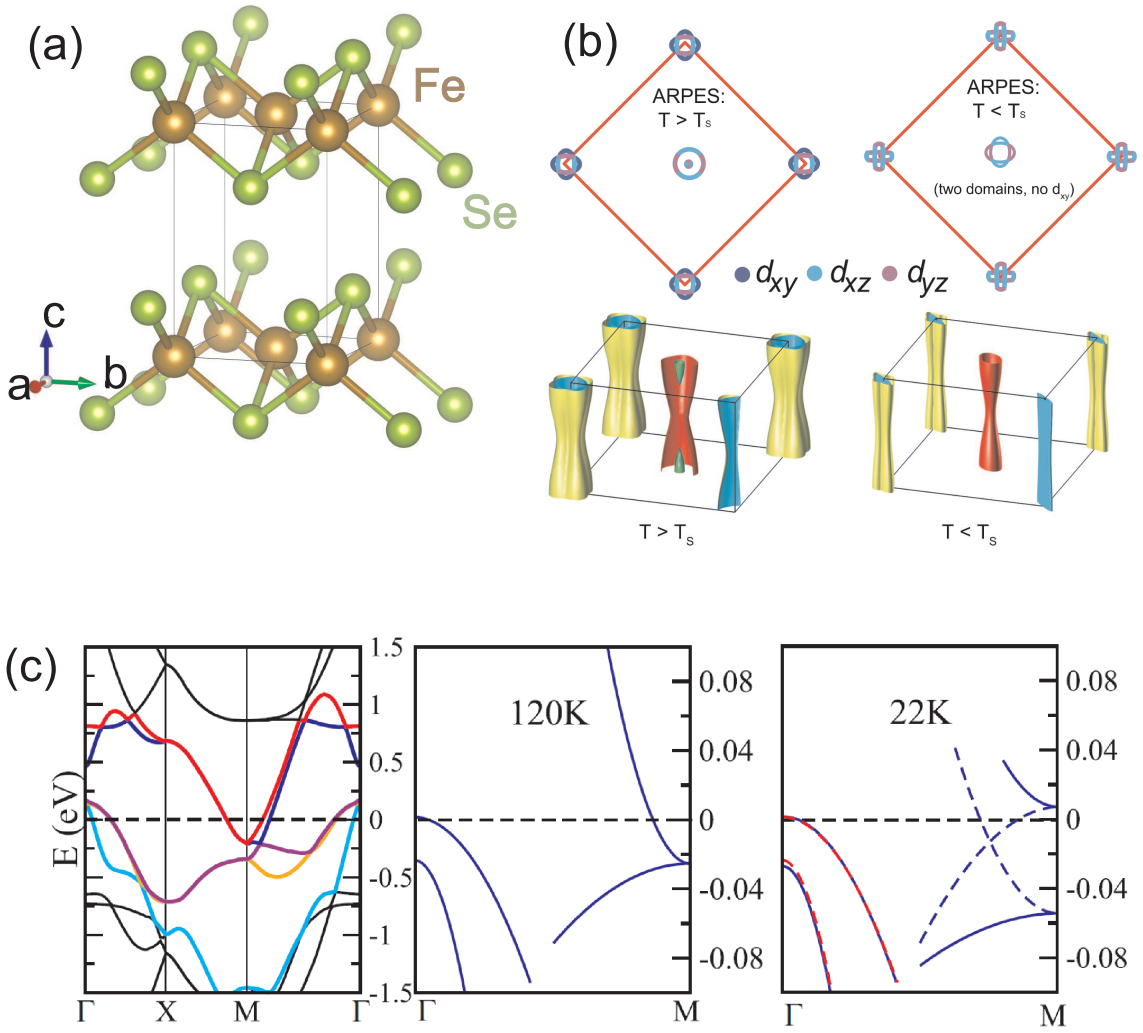

Figure 7.1.1: The room temperature unit cell of β-FeSe drawn with VESTA [146] utilizing the crystallographic data from Ref. [222] (a). The structural transition which lowers the symmetry of FeSe from tetragonal to orthorhombic has considerable impact on the bandstructure and Fermi surfaces (b,c). Panel (b) depicts the Fermi surface obtained with ARPES above (left) and below (right) T_s. Left panel of (c): bandstructure of FeSe calculated with LDA (local density approximation) methods. Middle and right panel of (c): the ARPES result above (middle) and below (right) the structural transition. The bands at the M-point experience a drastic splitting at T_s which leads to Dirac like band crossings (right panel (c)). Panel (b) reprinted from Ref. [223] with permission. Copyright (2015) by the American Physical Society. Panel (c) reprinted from Ref. [220] with permission. Copyright (2016) by the American Physical Society.

FeSe can crystallize in various phases of different symmetries [222]. The β phase with the tetragonal P4/nmm (No. 129) crystal structure at room temperature depicted in Fig. 7.1.1 is the one, that is hosting the superconducting and topological properties stated above. Recent advances in the crystal growth technique made high quality crystals of this β-FeSe available [224]. The β phase FeSe will henceforth simply be referred to as FeSe, since only crystals of this structure were investigated in this work. The lattice parameters of the tetragonal unit cell are $a = 3.77\,\text{Å}$ and $c = 5.52\,\text{Å}$ [222]. At $T \approx 90\,\text{K}$ FeSe undergoes a structural transition that lowers the symmetry to orthorhombic (space group Cmma) [224]. The low temperature orthorhombic state is often refered to as 'nematic', since the electronic in plane anisotropy by far exceeds the structural distortion [223]. Unlike other iron based superconductors, where the structural transitions are accompanied by a spin density wave ordering of the Fe moments [225], in FeSe no magnetic order is observed [226, 227]. However, the strong spin fluctuations [228], as well as the appearance of magnetic ordering under pressure [229–231] indicate, that FeSe still is close to a magnetic instability [232].

The structural transition has a substantial impact on the bandstructure and Fermi surface of FeSe. The unusually large discrepancies between the bandstructure, calculated with local density approximation methods (Fig. 7.1.1 (c) left panel), and the band dispersion determined with ARPES, especially around the M-point (Fig. 7.1.1 (c) middle panel), are still puzzling [220]. Note that the band touching point of the quadratic bands above the structural transition temperature T_s in the ARPES result, depicted in the middle panel, is $\approx 25\,\text{meV}$ from E_F at the M-point, while in the calculated bandstructure in the left panel the corresponding energy scale is $\approx 250\,\text{meV}$. Below T_s when the C_4 rotational symmetry is broken, the bands at the M-point get drastically split and Dirac point like crossings appear slightly below E_F, as depicted in Fig. 7.1.1 (c) right panel. The crossing points are slightly gapped by spin orbit coupling [220].
Also the hole bands at the Γ-point are affected at the structural transition, however, the effects are less pronounced compared to the massive splitting at the M-point [223, 233].
Above the structural transition, the Fermi surface consists of a shallow hole pocket at the Brillouin zone center and one or two even smaller electron pockets at the zone corners, as depicted in Fig. 7.1.1 (b) [218, 223]. Below the structural transition the hole and electron pockets form elongated ellipses. In the case of a crystal with twin domains, two ellipses appear rotated 90° to each other (see Fig. 7.1.1 (b) right panel).

The elongated Fermi surfaces cause the strong electronic anisotropy of the nematic state.
The low temperature Fermi surfaces of FeSe are found to be rather two dimensional. Very recent angular dependent magneto resistance data indicate, that the Dirac like dispersion discussed above is likely also of 2D nature [234].

7.2 FeSe: Results and Discussion

In the following, the results obtained on stoichiometric high quality single crystals of FeSe will be presented. The samples were provided by Dr. Thomas Wolf of the IFP at the KIT[1]. The resistivity measurements were contributed by MSc Baharak Heydari of the PI1. The optical and magnetization measurements were performed by the author, except from the NIR and VIS measurements, which were conducted by MSc Stephan Ludwig of the PI1.

7.2.1 Transport properties

First the temperature dependent resistivity $\rho(T)$ measured with the standard four probe technique in the (001) plane of FeSe will be discussed. Fig. 7.2.1 (a) depicts $\rho(T)$ over the whole measured temperature range. The overall appearance of the resistivity is metallic. The full temperature range view already allows to identify two anomalies. Between 100 K and 50 K a small kink in $\rho(T)$ marks the structural transition, and below 10 K the resistivity exhibits a steep drop to zero when FeSe enters the superconducting state. The inset of panel (a) displays an enlarged view of $\rho(T)$ around the superconducting transition temperature T_c. The very narrow superconducting transition in the resistivity reflects the high quality of the samples and the transition temperature is found to be $T_c = 8\,\mathrm{K}$. The transition temperature of the structural transition $T_s = 86\,\mathrm{K}$ can be determined from the pronounced minimum in the temperature derivative $\delta\rho/\delta T$ depicted in Fig. 7.2.1 (b) and marked with a violet arrow. The pronounced minimum at $T^* = 20\,\mathrm{K}$ marked with a black arrow was previously interpreted as the temperature scale, where superconducting fluctuations start to enhance the normal state conductivity. These fluctuations appear at temperatures that are more then twice of the transition temperature T_c. The unusual strong superconducting fluctuations in FeSe were interpreted as an indicator for preformed Cooper pairs and a pseudogap [218]. The analysis of the optical

[1]Institut für Festkörperphysik, Karlsruher Institut für Technologie, Karlsruhe, Germany

data presented in this chapter indicates, that additional to strong superconducting fluctuations, the emergence of a Dirac like carrier species with high mobility leads to an enhancement of the conductivity below T_s.

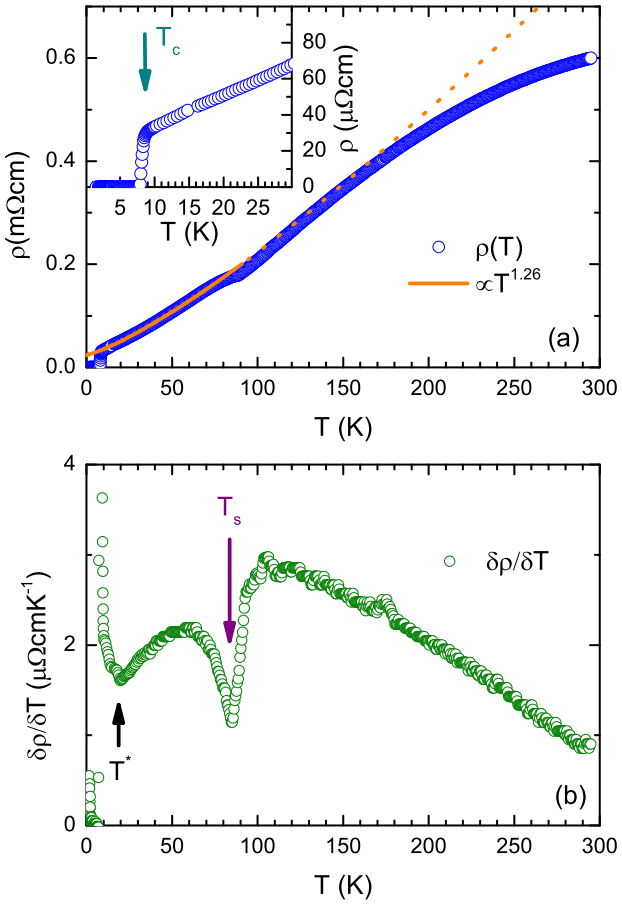

Figure 7.2.1: The temperature dependence of the resistivity $\rho(T)$ (blue circles in (a)) can be nicely fit with a temperature power law $T^{1.26}$ for $T_c < T < T_s$ (orange line). The superconducting transition at $T_c = 8\,\mathrm{K}$ is well resolved in the enlarged view in the inset of frame (a). The structural transition at $T_s = 86\,\mathrm{K}$ can be identified in the derivative $\delta\rho/\delta T$ (b). The minimum marked with $T^* = 20\,\mathrm{K}$ in panel (b) was previously assigned to the energy scale of strong superconducting fluctuations [218].

The preformed Cooper pair scenario and pseudogap phase are usually evolving out of a non Fermi liquid state, characterized by a T-linear $\rho(T)$. For $T_c < T < T_s$, the resistivity can be nicely fit with $\rho(T) = \rho_0 + AT^n$ with the extrapolation of the normal state resistivity to zero temperature ρ_0, a fit parameter A and the power of the temperature n. The fit is depicted as orange line in panel (a) and yields $\rho_0 = 24\,\mu\Omega\mathrm{cm}$, $A = 6.1 \times 10^7\,\Omega\,\mathrm{cm\,K^{-n}}$ and the power $n = 1.26$ in good agreement with Ref. [218]. The deviation from the Fermi liquid theory exponent $n = 2$ is indicating, that FeSe is fairly close to a non Fermi liquid state.
The residual resistivity ratio of the investigated samples is $RRR = \rho(300K)/\rho(T \gtrsim T_c) \approx 20$. For a more elaborate analysis of the resistivity of the investigated FeSe

samples and its evolution with pressure see Ref. [235].

For further characterization of the samples, measurements of the static magnetic susceptibility χ_{DC} were performed. In Fig. 7.2.2, the molar susceptibility measured with an applied field of $B = 1\,\mathrm{mT}$ is depicted for temperatures around T_c. The zero field cooled (ZFC) measurement exhibits a sharp decrease at $T_c = 8\,\mathrm{K}$ and a strong diamagnetic signal for temparatures $T < T_c$. The sharp transition and strong diamagnetic signal is further confirming the excellent quality of the samples. The field cooled (FC) curve exhibits only a weak diamagnetic signal, due to the trapped flux inside the sample, since FeSe is a type II superconductor.

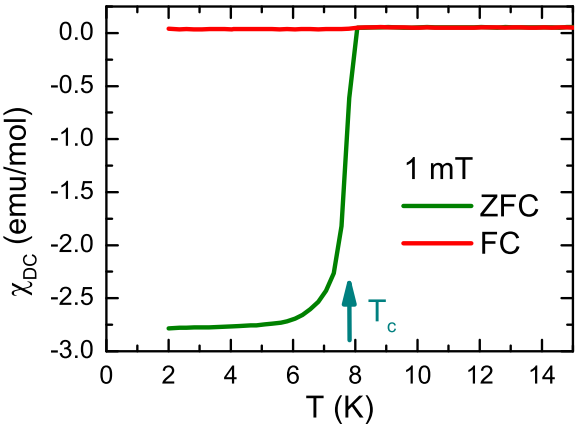

Figure 7.2.2: The sharp transition and strong diamagnetic signal in the ZFC measurement of the static susceptibility χ_{DC} confirm the high quality of the FeSe samples as well as the superconducting transition temperature $T_c = 8\,\mathrm{K}$.

7.2.2 Optical experiments

The reflectivity of FeSe was measured from the F^3IR to the VIS frequency range $(10 - 25\,000\,\mathrm{cm}^{-1})$ for temperatures $T = 3.4 - 300\,\mathrm{K}$ in the (001)-plane. The samples were cleaved prior to the optical measurements.

Qualitative discussion

First the spectra will be discussed on a qualitative level, in order to get an overview over the complex temperature dependence of the optical response of FeSe. Fig. 7.2.3 (a) displays the reflectivity $R(\omega)$ for temperatures above the structural transition at $T_s = 86\,\mathrm{K}$.

A continuous increase of the reflectivity in the FIR is observed, while in the MIR $R(\omega)$ is suppressed. The two ranges of opposite spectral evolution are separated by an isosbestic point at roughly $500\,\mathrm{cm}^{-1}$, where the reflectivity is temperature

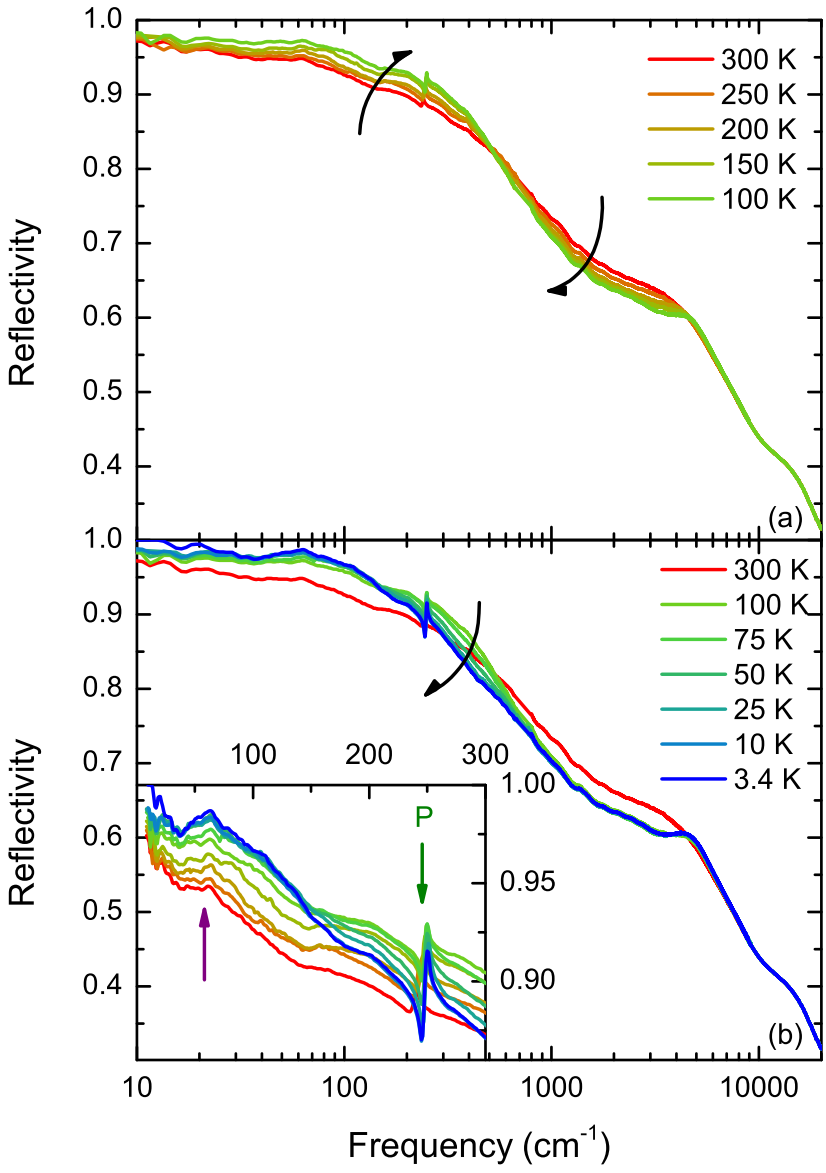

Figure 7.2.3: The reflectivity of FeSe over a wide frequency range for temperatures above (a) and below (b) the structural transition T_s. The temperature dynamics of the spectra for $T < T_s$ is completely different from the dynamics for $T > T_s$, as emphasized by the black arrows. The inset in panel (b) depicts an enlarged view of the FIR where a sharp phonon mode (P) is found. A second strong FIR mode is marked with a purple arrow in the inset. The reflectivity at $T = 3.4\,\mathrm{K}$ increases steeply to unity below $30\,\mathrm{cm}^{-1}$ which is the signature of a dirty limit superconducting state in the reflectivity in FeSe.

independent for $T > T_s$. This leads to the windmill like dynamics of the spectra emphasized with the black arrows.
The reflectivity below T_s depicted in Fig. 7.2.3 (b) does not follow the same trend. In the MIR the spectra for $T \leq 100\,\mathrm{K}$ fall on top of each other, and the metallic increase at low frequencies below T_s are small compared to the changes at higher temperatures. Instead, the reflectivity is suppressed in a range between $150\,\mathrm{cm}^{-1}$ and $700\,\mathrm{cm}^{-1}$ where the isosbestic point was located before.

At around $250\,\mathrm{cm}^{-1}$ a sharp phonon feature is resolved, marked with a green arrow and labeled with P in the inset of Fig. 7.2.3 (b). By symmetry considerations it is found that FeSe only hosts one infrared active E_u phonon mode that is visible in the in-plane geometry [159]. This phonon can be ascribed to in-plane displacements of Fe and Se atoms and was also reported in other optical studies on FeSe [236, 237], and is generally observed in the in-plane optical response of iron based superconductors (see e.g. [238–240]).
Another pronounced mode marked with a purple arrow is resolved below $100\,\mathrm{cm}^{-1}$ in the enlarged view of the reflectivity in the inset in Fig. 7.2.3 (b). In a recent optical study on FeSe single crystals any comparable feature was absent [237]. The origin of this low frequency mode in the optical data is likely not intrinsic, as will be discussed later.
The reflectivity at $T = 3.4\,\mathrm{K}$ exhibits a steep increase to unity below $30\,\mathrm{cm}^{-1}$ which is a direct hallmark of the superconducting state in FeSe. The manifestation of the superconducting state in the optical response of FeSe and its analysis will be discussed later in this chapter in a dedicated paragraph.
For frequencies above $8000\,\mathrm{cm}^{-1}$ the reflectivity is temperature independent.

The optical conductivity $\sigma_1(\omega)$ for $T > T_s$ is displayed in Fig. 7.2.4 (a). At low frequencies below $200\,\mathrm{cm}^{-1}$ the conductivity increases strongly towards lower temperatures. This behavior can be attributed to a growing Drude peak. This Drude peak is superposed by two distinct modes, one around $50\,\mathrm{cm}^{-1}$, and the second at $150\,\mathrm{cm}^{-1}$. At $200\,\mathrm{cm}^{-1}$, in the vicinity of the sharp phonon peak, $\sigma_1(\omega)$ also reveals an isosbestic point. For higher frequencies the spectra exhibit a temperature dynamics, that is typical for iron based superconductors. In the MIR the spectral weight is suppressed and transfered to high frequencies. This unconventional spectral weight redistribution in iron based superconductors is ascribed to the localization of itinerant carriers by Hund's rule coupling effects (see e.g. [241–243]).

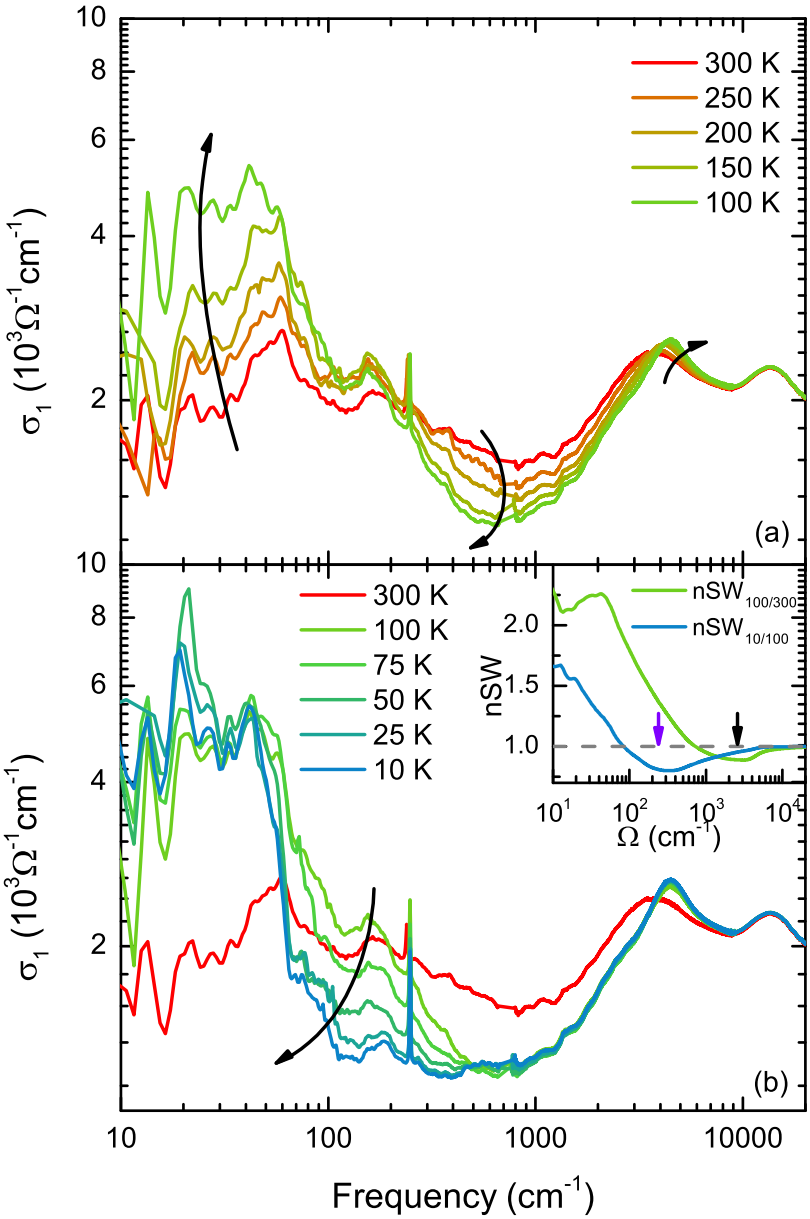

Figure 7.2.4: The optical conductivity above the structural transition at T_s (a) shows a similar behavior as is commonly observed in iron based superconductors. The low frequency part of the spectra exhibit a Drude like increase towards lower temperatures, while in the MIR the spectra get suppressed and the spectral weight gets transferred to higher energies. For $T < T_s$ $\sigma_1(\omega)$ diminishes in a range below $500\,\mathrm{cm}^{-1}$, while for higher frequencies the spectra are roughly temperature independent. The different energy scales of spectral weight suppression above and below the structural transition are emphasized in the normalized spectral weight $nSW = SW(\tilde{T})/SW(T > \tilde{T})$ depicted versus cutoff frequency Ω in the inset of panel (b).

The spectral weight redistribution from low to high energies is nicely uncovered by the normalized integrated spectral weight $nSW = SW(\tilde{T})/SW(T > \tilde{T})$, where the spectral weight $SW = \int_0^\Omega \sigma_1(\omega)d\omega$ of a given temperature $\tilde{T}$ is normalized to the SW at a higher temperature. The inset of Fig. 7.2.4 (a) depicts the nSW for $SW(100\,\mathrm{K})/SW(300\,\mathrm{K})$ versus the cutoff frequency Ω as green line. The black arrow marks the energy scale ($\approx 3000\,\mathrm{cm}^{-1}$), where the maximum loss of spectral weight is reached, and the spectra start to regain weight towards higher frequencies. At roughly $8000\,\mathrm{cm}^{-1}$ most of the lost spectral weight is recovered. The relevant energy scale in the $BaFe_2As_2$ compounds in the paramagnetic state is of the same order [243, 244]. Therefore the Hund's rule coupling energy J in FeSe can assumed to be comparable to the values found for the $BaFe_2As_2$ system ($J = 0.6-0.9\,\mathrm{eV}$ [243, 244]).

Just like in the reflectivity discussed above, the temperature dynamics of $\sigma_1(\omega)$ changes gears for $T < T_s$. The spectra for temperatures below the structural transition are roughly the same as the spectra at $T = 100\,\mathrm{K}$ for frequencies larger than $500\,\mathrm{cm}^{-1}$. For lower frequencies the optical conductivity gets drastically suppressed, emphasized by the black arrow in Fig. 7.2.4 (b). These dynamics can straightforwardly be assigned to the Fermi surface reconstruction below the structural transition.
The nSW for $SW(10\,\mathrm{K})/SW(100\,\mathrm{K})$ depicted in the inset of frame (b) as dark cyan line, reveals that the energy scale $\approx 300\,\mathrm{cm}^{-1}$ of this spectral weight redistribution marked with a purple arrow is much lower than the scale found for the Hund's rule correlations discussed above. The spectral suppression below T_s is reminiscent of the behavior found in the parent compounds of the 122-pnictides in the antiferromagnetic state [240, 243]. However, there the spectral suppression is always accompanied by a pile up of spectral weight around $1000\,\mathrm{cm}^{-1}$ which is completely absent in the data of FeSe presented in Fig. 7.2.4 (b).

The normal state

In order to analyze the optical data more quantitatively, the normal state spectra are fit with a series of Drude- and Lorentz terms. The fitting was conducted simultaneously on $\sigma_1(\omega)$, $\varepsilon_1(\omega)$ and $R(\omega)$.
The model that accounts best for all features in the spectra is depicted in Fig. 7.2.5 and contains two Drude terms (a narrow Drude ND and a broad Drude BD) and a series of Lorentz terms (L1-L7). The phonon (P) is also modeled with a Lorentz term and the temperature independent part of the spectra at high frequencies (HF)

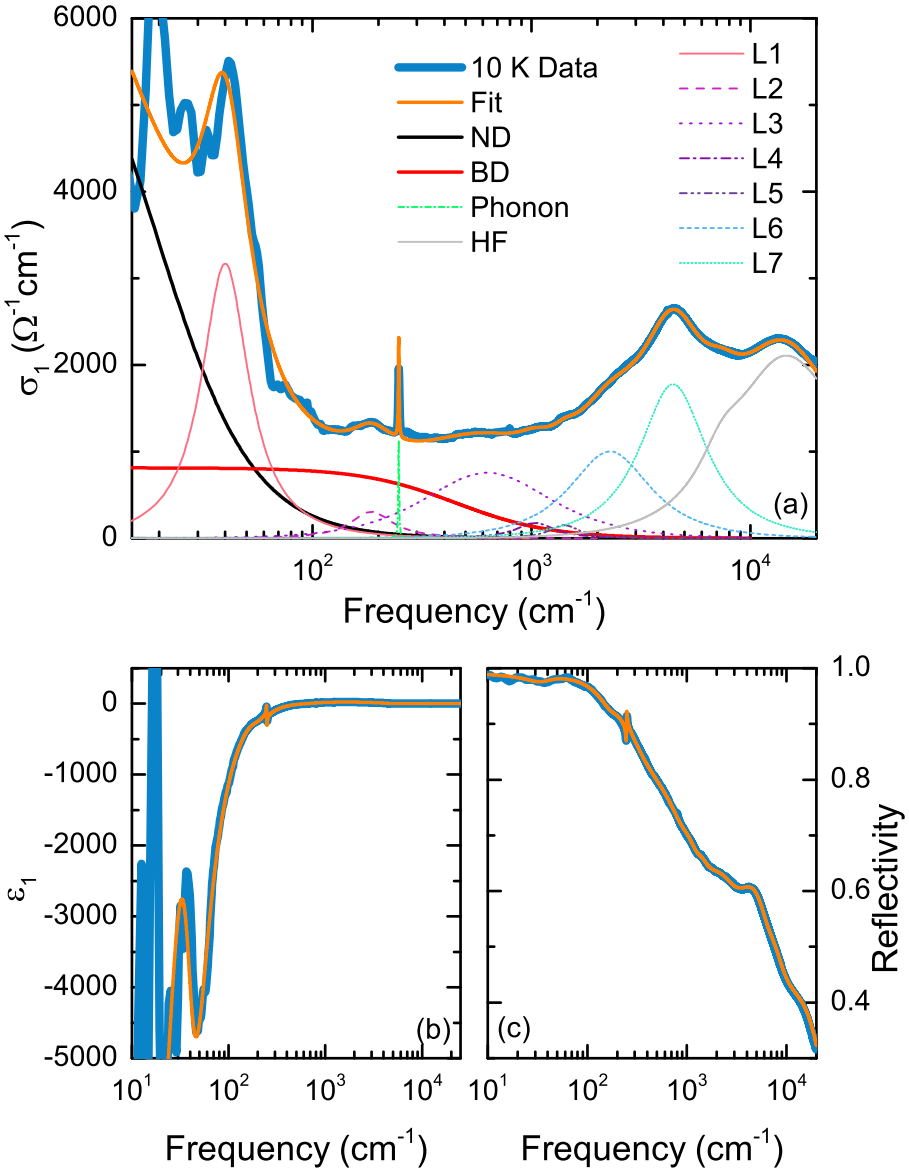

Figure 7.2.5: The Drude-Lorentz fit of $\sigma_1(\omega)$ (a), $\varepsilon_1(\omega)$ (b) and $R(\omega)$ (c) at 10 K. The fit contains two Drude terms and 7 temperature dependent Lorentz terms, as well as a series of T-independent high frequency Lorentzians. The single components are decomposed in frame (a).

by a series of Lorentzians. Panels (a-c) display the fit of $\sigma_1(\omega)$, $\varepsilon_1(\omega)$ and $R(\omega)$ at $T = 10\,\mathrm{K}$. The applied model nicely describes the spectra of these three optical response functions at all temperatures in the normal state, irrespective if $T > T_s$ or $T < T_s$. In Tab. 7.2.1 the center-frequencies ω_0 of the Lorentz terms L1-L7 at 10 K are listed.

Lorentz	L1	L2	L3	L4	L5	L6	L7
$\omega_0(\mathrm{cm}^{-1})$	40	186	628	1038	1416	2284	4433

Table 7.2.1: The center frequencies ω_0 of the Lorentz oscillators in the fit of the optical response functions at 10 K.

The comparably large number of Lorentz terms included in the fit to account for the all features in the spectra of FeSe calls for a closer look to identify their origin. The most pronounced temperature dependent absorption band L7 is generally observed in optical experiments on iron based superconductors (at slightly varying positions depending on the compound) [237, 240, 245–247]. In K-doped $BaFe_2As_2$ this absorption band was assigned to transition from Fe-d and As-p bands into Fe-d bands [245].
The relatively weak absorptions L4, L5 and L6 are reminiscent of low energy interband transitions found in the optical response of the 122-pnictides [248, 249]. The fact, that these aforementioned transitions L4-L7 are also found in the spectra of FeSe indicate, that on this energy scale the bandstructures of FeSe and 122-pnictides are similar.
The resonance frequency of L7 is temperature dependent, and the temperature evolution of ω_0 is depicted in Fig. 7.2.6 (f). The shift of L7 to higher energies follows the previously discussed transfer of spectral weight to high frequencies induced by Hund's rule coupling correlations. This effect is most prominent at temperatures $T > T_s$, where L7 shifts from $3960\,\mathrm{cm}^{-1}$ to $4400\,\mathrm{cm}^{-1}$. Below T_s the position of L7 remains rather constant.
Aside from L7, there are two more Lorentz terms that experience pronounced shifts of their resonance frequencies with temperature (the phonon is excluded here and will be discussed in a separate paragraph). The center frequency ω_0 of the absorption mode dubbed L3 remains constant down to 100 K as depicted in Fig. 7.2.6 (e). Below T_s in the spectra for $T \leq 75\,\mathrm{K}$ this mode experiences a considerable blue-shift. This is firm evidence, that mode L3 is related to interband transitions around the M-point, where the bands encounter substantial shifts at the structural transition [223, 250].

In contrast to L3, the lowest frequency mode L1 experiences a continuous red-shift when the temperature is lowered (see Fig. 7.2.6 (d)). Similar behavior of very low frequency modes was recently reported in Eu based 122-pnictides [112]. Following the interpretation of Ref. [112], the mode L1 is likely arising from impurity-localization effects. This interpretation is supported by the observation of a ferromagnetic impurity phase in our samples [235].
The origin of the remaining unidentified Lorentz-term L2 is yet unresolved.

In the zero frequency limit, the sum of the conductivities of the two Drude components should equal the measured DC-conductivity ($\sigma_{1,\mathrm{ND}}(\omega \to 0) + \sigma_{1,\mathrm{BD}}(\omega \to 0) = \sigma_{\mathrm{DC}}$). Fig. 7.2.6 (a) displays measured DC-conductivity σ_{DC} as blue solid line and the sum of the two Drude components in the zero frequency limit $\sigma_{1,\mathrm{D}}(\omega \to 0)$ as orange filled circles. For temperatures above T_s the agreement of the low frequency limit of the fit and the measured DC-conductivity is excellent. Below the structural transition, however a growing discrepancy between $\sigma_{1,\mathrm{D}}(\omega \to 0)$ and σ_{DC} is observed. This is strong evidence, that below T_s a new highly mobile carrier species emerges, with a scattering rate well below the lowest measured frequency. Similar observations were recently reported in magneto-transport data on FeSe [9, 40]. In accordance with reported experimental and theoretical evidence for Dirac carriers in FeSe [9, 10, 40, 220, 221, 234] the emergent high mobility carrier species in the present work can straightforwardly be assigned to arise from the Dirac like pockets around the M-point in the Brillouin zone.
To quantify the properties of this high mobility Dirac carriers the missing conductivity $\Delta\sigma = \sigma_{1,\mathrm{D}}(\omega \to 0) - \sigma_{\mathrm{DC}}$ is depicted as green stars in Fig. 7.2.6 (a). An upper limit of the scattering rate is obtained by adding a third Drude term (Dirac-Drude DD) with the DC-conductivity $\Delta\sigma$ in the model presented in Fig. 7.2.5 for $T < T_s$. All parameters of the model found before at each temperature are kept fixed. Only the scattering rate of the DD-term is increased as far as possible, without decreasing the overall the fit quality. The temperature dependence of the scattering rates γ of all three Drude terms are summarized in Fig. 7.2.6 (b). The BD-term has a scattering rate of the order $\gamma \approx 400\,\mathrm{cm}^{-1}$ which is roughly temperature independent. Similar quasi constant scattering rates on the broad Drude component was also reported in 122-pnictides [251, 252]. Note the large error bars, that arise because the BD-term shares a lot of spectral weight with the L3 Lorentz term.
In contrast the scattering rate of the narrow Drude exhibits a clear metallic behavior and decreases strongly upon cooling. The pink line in Fig. 7.2.6 (b) denotes a fit to the scattering rate of the narrow Drude according to $\gamma(T) = \gamma_0 + AT^2$

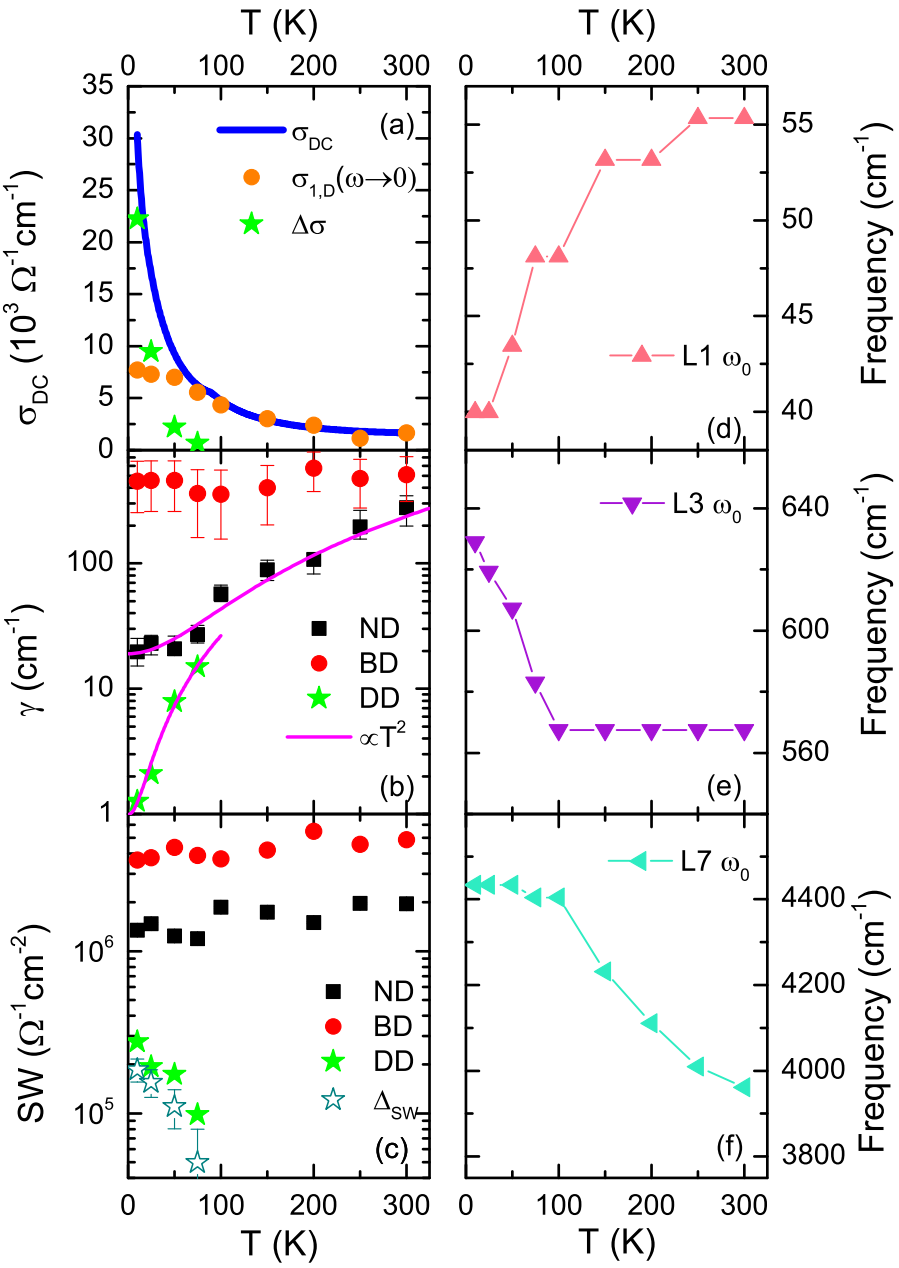

Figure 7.2.6: The fit parameters of the broad (BD) and narrow (ND) Drude components. The comparison of low frequency Drude conductivity $\sigma_{1,D}(\omega \to 0)$ and measured DC-conductivity σ_{DC} reveals the emergence of third carrier species (DD) for $T < T_s$ with large conductivity $\Delta\sigma$ (a) and low scattering rate γ (b). The spectral weight development indicates, that the emergent carriers gain weight from the FIR below 500 cm^{-1}. The center frequencies of the Lorentz terms L1, L3 and L7 are temperature dependent (d-f).

($\gamma_0 = 19\,\mathrm{cm}^{-1}$, $A = 2.42 \times 10^{-3}\,\mathrm{cm}^{-1}\,\mathrm{K}^{-2}$). The fit describes the T-dependence fairly well, indicating Fermi liquid behavior of the electronic subsystem described by the ND-component. The carriers described with the DD-term possess a very low scattering rate. As for the ND-term the T-dependence of the DD-term scattering rate can nicely be fit with the T^2 powerlaw ($\gamma_0 = 1\,\mathrm{cm}^{-1}$, $A = 2.54 \times 10^{-3}\,\mathrm{cm}^{-1}\,\mathrm{K}^{-2}$). Fermi liquid behavior of the Dirac carriers is predicted in for 2D [253], as well as for 3D linear dispersing bands [254]. Hence, the evolution of the DD-scattering rate is in line with the Dirac carrier interpretation.

The temperature dependence of the spectral weight of the Drude components $SW = \frac{\omega_p^2}{8} \propto \frac{N}{m^*}$, where ω_p is the plasma frequency, N the carrier density and m^* the effective carrier mass (see Sec.2.2), is depicted in Fig. 7.2.6 (c). The SW of the ND and BD components remains roughly temperature independent. This means, the carrier densities of these electronic subsystems remain constant (making the assumption that m^* is roughly T-independent). For $T < T_s$ the spectral weight of the DD component appears and strongly increases towards lower temperatures. The green open stars denote the spectral weight that is lost in the range in the FIR, where the spectra are stronly suppressed below T_s (see Fig. 7.2.4 (b)), calculated as $\Delta_{SW} = \int_0^{\Omega_c} [\sigma_1(100\,\mathrm{K}) - \sigma_1(T < T_s)]$. Here Ω_c denotes the cutoff frequency where the spectra merge together at high frequencies and is set to $500\,\mathrm{cm}^{-1}$. The loss of spectral weight Δ_{SW} goes hand in hand with the emergence of the DD-SW. This is evidence, that the carriers of the Dirac Drude previously contributed to the optical response above T_s as weakly bound carriers the range in the FIR below $500\,\mathrm{cm}^{-1}$.

The Dirac bands

To further elucidate the evidence for Dirac like carriers found above, it is desirable to trace down the Dirac interband transitions. The interband optical conductivity for 2D Dirac cones is well known from investigations on the flagship 2D Dirac material Graphene [12, 59–61, 255]. For a finite chemical potential, a step in $\sigma_{1,\mathrm{IB}}(\omega)$ at $|2\Delta_\mathrm{E}|$ marks the onset of the Dirac interband transitions, just as for the 3D case (see Sec. 2.6). Instead of increasing linear in frequency, for 2D Dirac materials the interband optical sheet conductivity $G_{1,\mathrm{IB}}(\omega)$ is frequency independent and solely determined by the conductance quantum $G_{1,\mathrm{IB}}(\omega) = G_0 = \frac{e^2}{4\hbar} = 6.08 \times 10^{-5}\,\Omega^{-1}$.
Since in FeSe the Dirac like band crossings only appear below T_s, an anomaly should appear in the $\sigma_1(\omega)$ spectra for $T < 100\,\mathrm{K}$. In the enlarged view of $\sigma_1(\omega)$ in Fig. 7.2.7 (a), a kink like structure is observed in the 10 K spectrum, encircled in orange, which

is absent in the 100 K spectrum. The difference spectra $\Delta\sigma_1(T) = \sigma_1(100\,\mathrm{K}) - \sigma_1(T)$ accentuate this anomaly as a pronounced peak structure, clearly visible for $T = 50, 25; 10\,\mathrm{K}$. For $T = 75\,\mathrm{K}$, close to T_s, the feature is strongly broadened, and shifted to higher frequencies.

From this spectral feature, the value for the distance of the Fermi energy E_F to the Dirac nodes is obtained as $\Delta_\mathrm{E} = 31\,\mathrm{cm}^{-1} = 3.8\,\mathrm{meV}$. This compares well with the report of $\Delta_\mathrm{E} \approx 10\,\mathrm{meV}$ in an ARPES study on FeSe thin films [10].

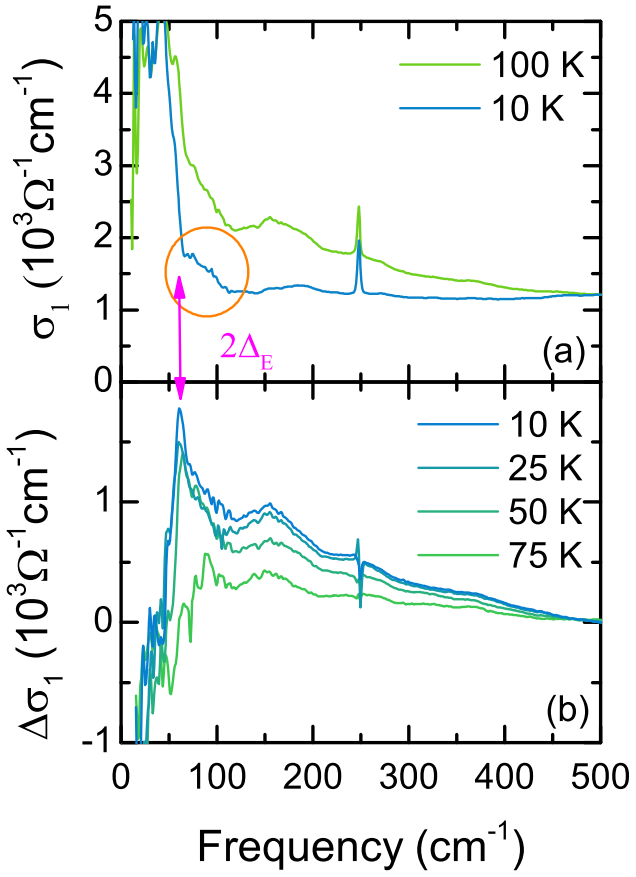

Figure 7.2.7: The $\sigma_1(\omega)$ spectra for $T < T_s$ exhibit a kink-like feature, associated with the onset of the interband transitions within the Dirac bands at $2\Delta_E$, which is absent in the spectra above the structural transition (a). In the subtracted spectra $\Delta\sigma_1(T) = \sigma_1(100\,\mathrm{K}) - \sigma_1(T)$ this onset is well resolved as a sharp peak at $2\Delta_E = 62\,\mathrm{cm}^{-1}$ (b).

For 2D Dirac carriers the chemical potential scales with the 2D carrier density N_2D as $\Delta_\mathrm{E} = \hbar v_\mathrm{F}\sqrt{\pi N_\mathrm{2D}}$ [255, 256]. From a mobility spectrum analysis a low carrier density of $N_\mathrm{3D} \approx 10^{18}\,\mathrm{cm}^{-3}$ is found for the high mobility carriers evolving below T_s in Ref. [9]. To extract the 2D carrier concentration per conducting sheet, the inter-layer distance (or lattice constant $c = 5.52\,\text{Å}$) of FeSe is utilized $N_\mathrm{2D} = N_\mathrm{3D} \cdot c$, which yields $N_\mathrm{2D} = 5.52 \times 10^{10}\,\mathrm{cm}^{-2}$. With N_2D and Δ_E the equation stated above yields a Fermi velocity for the Dirac bands in FeSe of $v_\mathrm{F} \approx 1.38 \times 10^5\,\mathrm{m\,s}^{-1}$, in good agreement with

the value reported in Ref. [40] ($9.1 \times 10^4\,\mathrm{m\,s^{-1}}$) and the value that can be estimated from the Dirac dispersion reported in Ref. [10] ($\approx 0.45\,\mathrm{eV\,\AA} = 6.8 \times 10^4\,\mathrm{m\,s^{-1}}$).
As stated above, for 2D Dirac fermions the interband conductivity is constant and adapts an universal value. To elucidate this issue in FeSe, the sheet conductance per layer is calculated as $G_1(\omega) = c\sigma_1(\omega)$, where c is the interlayer distance as before [12]. The resulting $G_1(\omega)$ is depicted in Fig. 7.2.8 in units of $G_0 = e^2/4\hbar$. The sheet conductance is roughly constant between $100\,\mathrm{cm^{-1}}$ and $500\,\mathrm{cm^{-1}}$ and of the order of G_0. The error bar points out the inaccuracy of the absolute value arising from the systematic uncertainty of the optical experiment and the data extrapolation. At frequencies below $100\,\mathrm{cm^{-1}}$ the interband sheet conductance is clearly perturbed by the steep increase arising from the intraband conductivity and the localization mode. Nevertheless, this quasi constant $G_1(\omega)$ in the FIR is striking evidence that 2D Dirac physics are of relevance in FeSe.

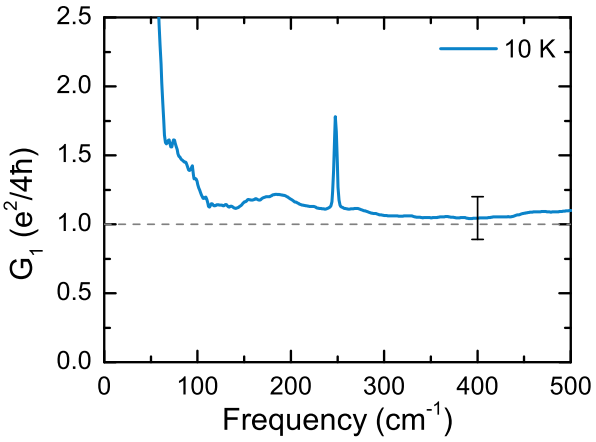

Figure 7.2.8: The sheet conductance of FeSe $G_1(\omega) = c\sigma_1(\omega)$ with the inter-layer distance $c = 5.52\,\mathrm{\AA}$ is quasi constant over an extended frequency range and of the order of $G_0 = \frac{e^2}{4\hbar} = 6.08 \times 10^{-5}\,\Omega^{-1}$. This reflects the two dimensional nature of the Dirac bands.

Phonon dynamics

The strong E_u phonon already discussed above exhibits a pronounced temperature dependence. Fig. 7.2.9 (a) depicts a stacked view of the optical conductivity around the phonon frequency. The clear blue shift of the center-frequency emphasized by the black arrow indicates sizable lattice hardening towards low temperatures in FeSe. Further insight into these dynamics is gained by plotting the resonance frequency ω_0 of the phonon Lorentz term versus the temperature (see Fig. 7.2.9 (b)). This reveals that ω_0 only shifts to higher frequencies for temperatures above T_s (dashed vertical violet line), while for $T < T_s$ ω_0 remains roughly constant. This is in stark contrast to the behavior of the E_u FeAs phonon in 122 iron pnictides which experiences

a jump in ω_0 at the magneto-structural transition in these compounds [238, 240]. Interestingly, the phonon frequency at 25 K in Fig. 7.2.9 (b) appears at a higher frequency. However, any interpretation of this behavior is rather speculative, because the shift in frequency ($\approx 1\,\mathrm{cm}^{-1}$) is just on the edge of the chosen frequency resolution in the FIR ($1\,\mathrm{cm}^{-1}$).

The FeAs phonon in 122 pnictides was found to drastically gain oscillator strength $\Omega = \omega_p^2$ below the magneto-structural transition [238]. In contrast, the temperature dependence of the oscillator strength Ω of the phonon Lorentz term in FeSe, depicted in Fig. 7.2.9 (c), exhibits a decrease for $T < T_s$. Note, that neither ω_0 nor Ω is affected, when the sample gets superconducting.

These observations indicate, that aside from the absence of magnetism, FeSe is also different from the other iron based superconductors in a structural point of view [224].

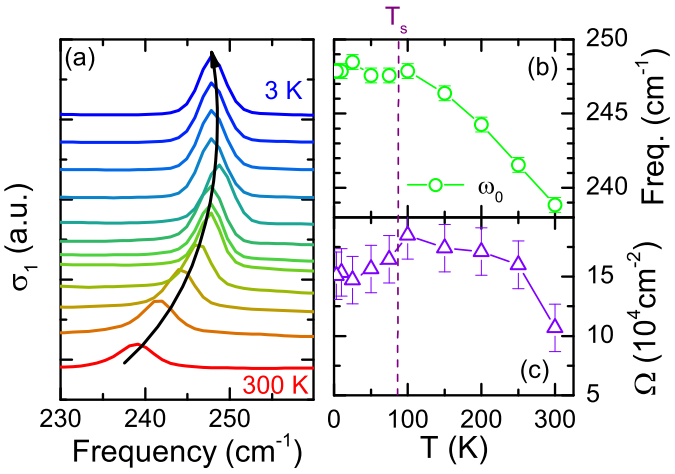

Figure 7.2.9: The E_u phonon identified in the spectra exhibits a considerable temperature dependence (a). The center frequency ω_0 is monotonously increasing towards lower temperatures and remains constant for $T < T_s$ (b). The oscillator strength reveals an anomalous decrease below the structural transition (c).

The superconducting state

Finally, the optical signatures of the superconducting state in FeSe will be discussed in this paragraph. Fig. 7.2.10 (a,b,c) depict the reflectivity $R(\omega)$, the relative reflectivity $R(T < T_c)/R(10\,\mathrm{K})$ and the optical conductivity, respectively, for $T = 3.4 - 10\,\mathrm{K}$. The reflectivity in panel (a) exhibits the typical behavior of a dirty limit superconductor (where the normal state scattering rate is larger than the superconducting gap $\gamma \gg 2\Delta$), meaning $R(\omega)$ exhibits a sharp upturn towards unity at low frequencies. Note, that the data is displayed as measured, and not smoothed. The relative reflectivity in panel (b) emphasizes the gradual development of the deviation from the normal state reflectivity with decreasing temperature.

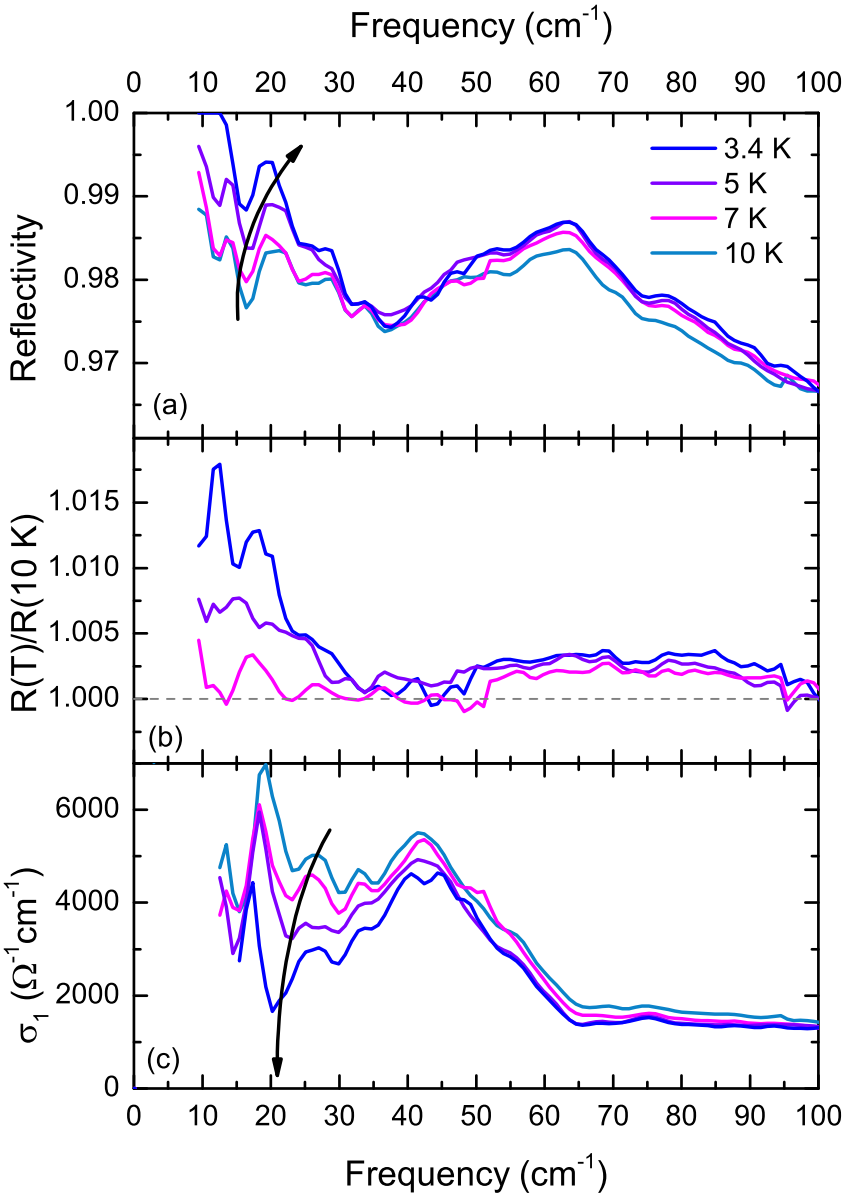

Figure 7.2.10: The reflectivity $R(\omega)$ (a) and relative reflectivity $R(T < T_c)/R(10\,\mathrm{K}$ show clear signatures of a dirty limit superconductor when FeSe is cooled below T_c. The optical conductivity is suppressed at low frequencies (c).

For low frequency extrapolation of the reflectivity in the superconducting state the Hagen-Rubens (see Sec. 2.3) is not applicable. The spectra at $T = 5; 7\,\mathrm{K}$ were instead extrapolated using $[1 - R(\omega)] \propto \omega^4$ and the reflectivity of the $T = 3.4\,\mathrm{K}$ spectrum was set to $R(\omega) = 1$ below the frequency, where it hits unity.
The resulting optical conductivity after Kramers-Kronig transformation, depicted in Fig. 7.2.10 (c), is suppressed below $100\,\mathrm{cm}^{-1}$. As discussed in Sec. 2.8, this loss of spectral weight is connected with the formation of a condensate.

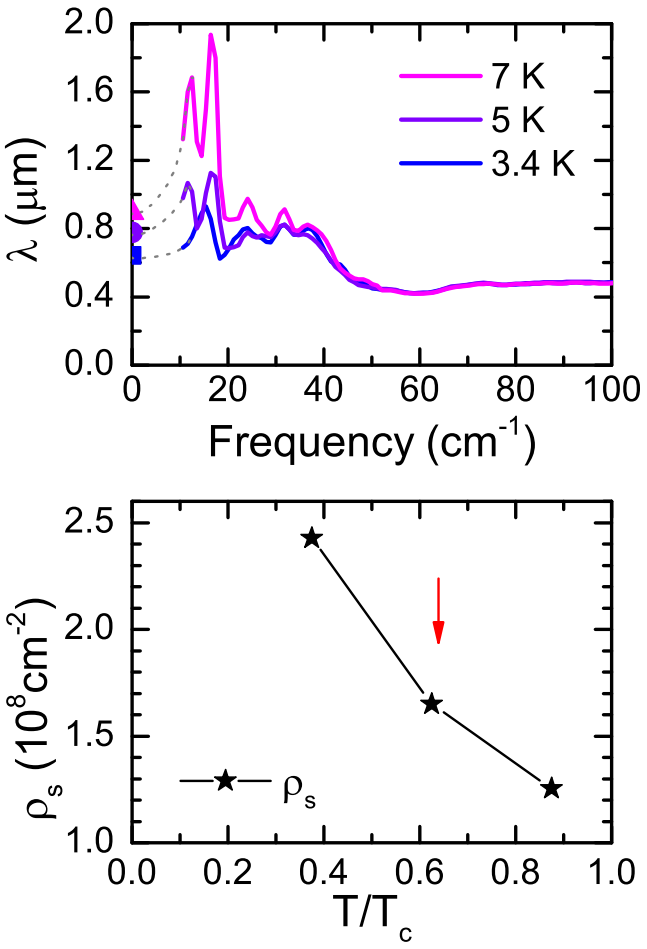

Figure 7.2.11: The frequency dependent penetration depth $\lambda(\omega)$ in the zero frequency limit and the penetration depth obtained from the FGT sum rule (symbols at $\omega = 0$) are in excellent agreement (a). Dotted gray lines represent the extrapolations. The concave development of the superfluid density (b) indicates the multiband nature of the superconducting state in FeSe.

The loss of low frequency spectral weight can be utilized to calculate superfluid density ρ_s and penetration depth λ via the FGT sum rule (see Sec. 2.8). The symbols at zero frequency in Fig. 7.2.11 (a) denote these values of λ for FeSe. The frequency dependent penetration depth $\lambda(\omega) = c/\left[4\pi\sigma_2(\omega)\right]^2$ calculated from the imaginary part of the optical conductivity is also displayed in this panel. The gray dashed lines represent the extrapolations. The values obtained from both methods reveal an excellent agreement, demonstrating the self consistency of the analysis. For $T = 3.4\,\mathrm{K}$

the penetration depth is $\lambda = 642\,\mathrm{nm}$, which compares well with previous reports [217, 257].
Fig. 7.2.11 (b) depicts the superfluid density $\rho_s = \omega_{p,s}^2 = c^2/\lambda^2$ versus the reduced temperature T/T_c. The flat, almost concave development of ρ_s, emphasized with the red arrow, is a hallmark of the multiband superconductivity in FeSe [257, 258].

For an estimation of the superconducting gap(s), the superconducting spectra are modeled. The two Drude terms that were utilized in the normal state are therefore replaced by two parametrized Mattis-Bardeen terms [109]. The parameters of all Lorentz terms were kept the same as in the normal state, as were the scattering rates and plasma frequencies. This reduces the free fit parameters down to two superconducting gaps Δ_1 and Δ_2.
The resulting fit for the $T = 3.4\,\mathrm{K}$ optical conductivity and reflectivity is depicted in Fig. 7.2.12 (a) and (b), respectively. The fit is decomposed into the two BCS terms and the background that was kept fixed from the normal state in panel (a). The evolution of the superconducting gaps with the temperature is depicted in panel (c). The temperature dependence of the energy gaps is fit (solid lines) by an expression that approximates the exact BCS temperature evolution $2\Delta(T) = 2\Delta(0)\tanh\{1.82\left[1.018(\frac{T_c}{T}-1)\right]^{0.51}\}$ [257, 259]. From the fit the gaps at zero temperature are estimated as $2\Delta_1(0) \approx 12\,\mathrm{cm}^{-1} \approx 1.5\,\mathrm{meV}$ and $2\Delta_2(0) \approx 34\,\mathrm{cm}^{-1} \approx 4.2\,\mathrm{meV}$, which is well in the spread of other reported values [217, 257, 260–262]. The gap ratios $2\Delta_1(0)/k_BT_c \approx 2.2$ and $2\Delta_2(0)/k_BT_c \approx 6$ indicate, that the smaller gap Δ_1 is likely anisotropic (but nodeless [258, 261, 263]), while the larger gap Δ_2 indicates strong coupling.

7.3 Conclusions

In conclusion, the intraband conductivity of the iron based superconductor FeSe indicates the emergence of a highly mobile carrier species below the structural transition at T_s. This carrier species is attributed to the Dirac pockets evolving in the bandstructure in the orthorhombic phase. The intraband transitions between the Dirac bands are found to start around $62\,\mathrm{cm}^{-1}$, which sets the chemical potential to $\Delta_\mathrm{E} = 3.8\,\mathrm{meV}$. The sheet conductance is quasi constant over an extended frequency range in the FIR and of the order of G_0. This indicates the 2D nature of the Dirac physics in FeSe.

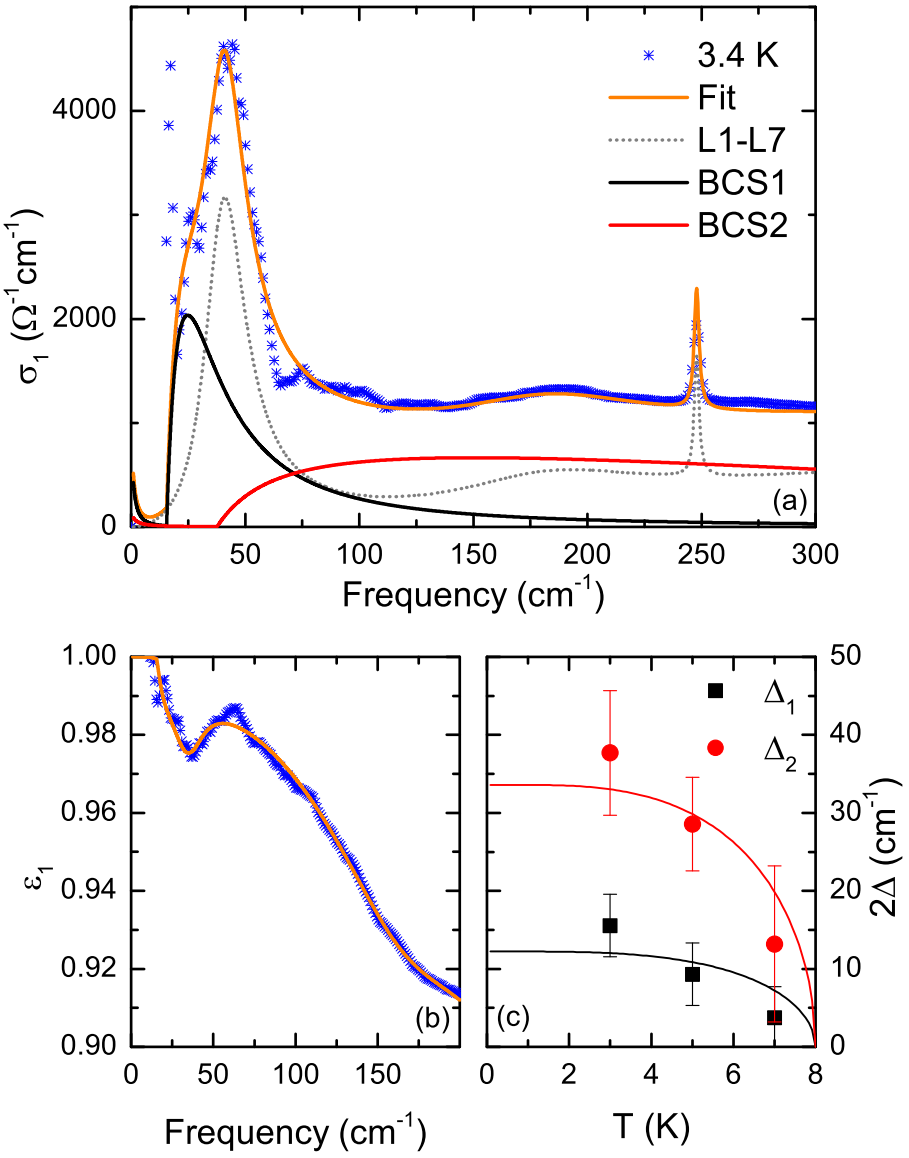

Figure 7.2.12: The optical response functions in the superconducting state can be nicely fit by replacing the two Drude components of the normal state with two BCS terms. The fit of the optical conductivity $\sigma_1(\omega)$ is decomposed into the background and the two BCS terms (a). The quality of the fit of the reflectivity is excellent (b). The values of the superconducting gaps $2\Delta_1$ and $2\Delta_2$ are following a BCS temperature dependence only very coarsly (lines) (c).

In the superconducting state the spectra demonstrate a behavior that is typical for dirty limit superconductors. The fit with two BCS terms gives access to the gap sizes. The BCS ratios $2\Delta/k_{\mathrm{B}}T_c$ indicate, that the smaller gap has to be considered anisotropic, in agreement with previous reports [258, 261, 263].
Tab. 7.3.1 summarizes the values relevant for the Dirac bands and the superconducting state found in this work. For comparison, published values for the same quantities are also listed.

RRR	T_s/T_c (K)	v_{F} ($10^5 \frac{\mathrm{m}}{\mathrm{s}}$)	Δ_E (meV)	$2\Delta_1/2\Delta_2$ (meV)	Ref.
20	86/8	1.38	3.8	1.5/4.2	this, O, T, M
33	86/9	0.91	-	-	[40], MT
-	125/−	0.68	10	-	[10], thin film, ARPES
40	90/9.5	-	-	5/7	[217], MT, STS
-	87/8.5	-	-	2.19	[264], MT, STS
-	−/9.4	-	-	0.8/6.6	[257], M
-	−/8.1	-	-	2.2/2.6	[261], SH
-	−/12	-	-	1.4/5.4	[265], polycrystal, AR

Table 7.3.1: Summary of the characteristic quantities of FeSe found in this work and extracted from references. The abbreviation (M)T, O, M, STS, SH, AR and ARPES stand for (magneto)-transport, optics, magnetization, scanning tunneling spectroscopy, specific heat, Andreev reflection and angle resolved photoemission spectroscopy, and point out, which technique was used to determine the values.

8. Summary and Outlook

The achievements of this work are dichotomous. First of all, the implementation of a novel installation in the lab enables to perform infrared spectroscopic measurements in reflection or transmission at high magnetic fields up to $B = 7\,\mathrm{T}$, low temperatures down to $T = 5\,\mathrm{K}$ in a frequency range $\omega = 40 - 2500\,\mathrm{cm}^{-1}$ on an everyday basis. The measurement accuracy in this range of frequencies in the new setup is excellent. It is comparable to the accuracy achieved in zero field measurements in the lab of the PI1, where the beam has a much shorter propagation path and the alignment is much easier.

Second and most important from the scientific point of view, the optical and magneto-optical investigations of Dirac and Weyl semimetals presented in this thesis enable a deep insight into the subtle details of the bandstructures of these materials. Four compounds have been investigated, and the key findings are listed in the following.

- Careful analysis of the interband optical conductivity of the 3D Dirac semimetal Cd_3As_2 reveals a peculiar shape of the Dirac bands in this materials. The Dirac cones narrow towards the nodes with a sublinear dispersion $\epsilon(k) \propto |k|^{0.6}$. The Fermi velocity at the nodes, estimated from the optical data is $v_\mathrm{F} = 7.6\,\mathrm{m\,s}^{-1}$. The chemical potential in the investigated, electron doped crystals with a carrier concentration of $N \approx 3 \times 10^{17}\,\mathrm{cm}^{-3}$ and a residual resistivity ratio of $RRR = 5.5$ is found to be situated at $\Delta_\mathrm{E} = 106\,\mathrm{meV}$ at low temperatures. The "Lifshitz gap" is directly seen in the spectra, and can be estimated as $E_\mathrm{L} \approx 370\,\mathrm{meV}$. The effective carrier mass is very small and of the order of $m^* \approx 0.03\,m_e$. 23 of the 30 E_u phonon modes are resolved in the in-plane spectra at low temperatures. In the intermediate frequency range, where neither Dirac interband transitions, nor the Drude intraband conductivity play a significant role, the anomalous spectral weight development indicates, that there must be two electronic subsystems contributing to the optical response. The exact origin of these contributions remains to be resolved.

- For the Weyl semimetal NbP, an excellent agreement between magneto-transport, optics, and magneto-optics is achieved. The carrier densities for the two carrier species (electrons and holes) deduced from the magneto-transport and optical data in the investigated samples with $RRR = 40$ are of the order $N_e = N_h \approx 3 \times 10^{19}\,\mathrm{cm}^{-3}$. The extremely high mobility of the holes reaches $\mu_h \approx 5 \times 10^5\,\mathrm{cm}^2\,\mathrm{V}^{-1}\,\mathrm{s}^{-1}$ at low temperatures and is larger than the electron mobility. From the zero-field optical spectra and from the inter Landau level transitions, the Fermi velocities of the two Weyl cone types W1 and W2 are found to be $v_{\mathrm{F,W1}} \approx 1.2\,\mathrm{m\,s}^{-1}$ and $v_{\mathrm{F,W2}} \approx 1.7\,\mathrm{m\,s}^{-1}$, and the positions of the nodes relative to the chemical potential are $\Delta_{\mathrm{E,W1}} = 27.6\,\mathrm{meV}$ and $\Delta_{\mathrm{E,W2}} = 27.6\,\mathrm{meV}$. The $\sqrt{B}$-dependence of all observed Landau level transitions proves the linearity of the bands in NbP. From the splitting of the screened plasma edge in magnetic fields, the cyclotron mass of the carriers is estimated as $m_c \approx 0.02\,m_e$. In the high magnetic field data indications are found, that the W1 cone enters the quantum limit only at 20 T, while the W2 cone is in the quantum limit already at very low fields.

- In TaAs, even though it belongs to the same family as NbP, the optical spectra look completely different. Nevertheless, a similar analysis as in NbP can be applied, which yields $v_{\mathrm{F,W1}} \approx 6.8\,\mathrm{m\,s}^{-1}$ and $v_{\mathrm{F,W2}} \approx 1.3\,\mathrm{m\,s}^{-1}$ for the Fermi velocities of the two types of Weyl cones. The Weyl nodes are closer to the Fermi energy as in NbP, and $\Delta_{\mathrm{E,W1}} = 10.7\,\mathrm{meV}$ and $\Delta_{\mathrm{E,W2}} = 4\,\mathrm{meV}$ are deduced from the fits of the spectra. The linearity of the Weyl bands in TaAs is also proven by the $\sqrt{B}$-dependence of the Landau level transitions. The cyclotron mass is estimated from the splitting of the screened plasma frequency in magnetic fields as $m_c \approx 0.004\,m_e$. An anomalous fourfold splitting of the lowest Landau level transition in high magnetic fields is observed. This can tentatively be assigned to the Zeeman splitting of the magnetic sub-levels in TaAs. From this splitting the effective magnetic g-factor is estimated to be $\overline{g} \approx 5 - 6$. For an in-depth understanding of this anomalous splitting in high magnetic fields, theoretical input is needed.

- For FeSe, strong evidence for 2D Dirac physics is found in the optical data. The investigated samples exhibit a transition from tetragonal to orthorhombic at $T_s = 86\,\mathrm{K}$ and enter a superconducting state at $T_c = 8\,\mathrm{K}$. One indicator for the development of Dirac bands, that form small pockets below T_s, is the emergence of a high mobility carrier species in the orthorhombic state evident

in the optical spectra. The quasi constant sheet conductance over a wide frequency range in the FIR of the order of the conductance quantum G_0 is the manifestation of the 2D type Dirac interband conductivity. From the spectra the chemical potential, $\Delta_{\mathrm{E}} = 3.8\,\mathrm{meV}$, and the Fermi velocity, $v_{\mathrm{F}} = 1.38\,\mathrm{m\,s^{-1}}$, of the Dirac bands are extracted. Below T_c, FeSe exhibits the typical behavior of a dirty limit superconductor. The penetration depth at 3.4 K is $\lambda = 642\,\mathrm{nm}$. From the BCS fit two gaps are extracted, with the magnitudes $2\Delta_1 = 1.5\,\mathrm{meV}$ and $2\Delta_2 = 4.5\,\mathrm{meV}$. The gap ratios $2\Delta_1/k_BT_c \approx 2.2$ and $2\Delta_2/k_BT_c \approx 6$ indicate, that the smaller gap Δ_1 is likely anisotropic, while the larger gap Δ_2 is isotropic and points out a strong coupling mechanism.

The work presented here demonstrates the relevance of optical and magneto-optical techniques for investigations on Dirac and Weyl semimetals, to gain a deep insight into the material properties and extract valuable information. The great self-consistency archived in the analysis of the zero field optical data, the Landau level transitions in magneto-optical spectra, and the magneto-transport data, yields the excellent agreement of all information extracted from data of different experimental origin.

Apart from the contribution of this thesis towards the understanding of Dirac and Weyl semimetals, this work paves the way for further experimental investigations in this field. The new upcoming materials dubbed Weyl type II semimetals, where the Weyl cones are strongly tilted due to a broken Lorentz invariance, are excellent candidates for further investigations in zero field, as well as in the novel installation for infrared optical measurements in high magnetic fields. Beyond the Weyl type II semimetals, it remains to be seen, which exotic quasiparticles emerging in theoretical suggestions for band crossings in multiple linear and quadratic fashions will eventually be realized in the form of crystalline materials [266].

Aside from the novel materials that are already existing or will be realized in the future, there also remain questions in the field of 'conventional' Dirac and Weyl semimetals. The observation of the Zeeman splitting in TaAs, for instance, calls for theoretical input and further investigations.

Finally, the 'Holy Grail' to observe the chiral anomaly in Weyl semimetals in parallel magnetic and electric fields with optical techniques is feasible with the novel magneto-optical installation in the PI1 lab. Technically still challenging, attempts to observe this purely quantum mechanical phenomenon are nevertheless highly desired. The pay-off in the form of information on scattering mechanisms and spectral weight redistribution is very valuable for the understanding of this anomaly [78].

A. Interband optical conductivity in the four-band model

In this chapter, the corner stones of the derivation of the interband optical conductivity $\sigma_{1,\mathrm{IB}}(\omega)$ in the four-band model (see Sec. 2.6.2) are presented. For the full derivation and argumentation see Ref. [74].

The starting point is the low energy Hamiltonian [17, 74, 93, 203]

$$\hat{H} = \hbar v_{\mathrm{F}} \hat{\tau}_x \boldsymbol{\sigma} \mathbf{k} + m\hat{\tau}_z + b\hat{\sigma}_z \tag{A.0.1}$$

with the material dependent Fermi velocity v_{F}, mass parameter m and intrinsic Zeeman-like term b. $\boldsymbol{\sigma}$ and $\boldsymbol{\tau}$ are 3D vectors of Pauli matrices, for the spin degree of freedom and for the pseudo-spins (e.g. sublattices, atomic orbitals), respectively [203].
The diagonalization yields the four energy bands with a dispersion as stated in Eq. 2.6.5.
To obtain the optical conductivity, Ref. [74] utilizes the real part Kubo formula at finite frequency in the one-loop approximation, which reads

$$\sigma_{\alpha\beta}(\Omega) = \frac{e^2\pi}{\hbar^2\Omega} \int_{-\infty}^{\infty} d\omega [f(\omega) - (\omega+\Omega)] \int \frac{d^3p}{(2\pi)^3} Tr[\hat{v}_\alpha \hat{A}(\mathbf{p},\omega) \hat{v}_\beta \hat{A}(\mathbf{p},\omega+\Omega)]. \tag{A.0.2}$$

$f(\omega) = [\exp(\beta[\omega-\mu])+1]^{-1}$ is the Fermi function with $\beta = 1/T$. Note, that here the usual notation for the chemical potential μ is utilized, in contrast to the rest of this work, to stay in line with the nomenclature in Ref. [74]. The velocity operator relates to the Hamiltonian as $\hat{v}_\alpha = \partial\hat{H}/\partial p_\alpha$ and the spectral function $\hat{A}$ relates to the Green's function via $\hat{G}(\mathbf{p},z) = \int_{-\infty}^{\infty} \frac{\hat{A}(\mathbf{p},\omega)}{z-\omega} d\omega$, where $\hat{G}^{-1}(\mathbf{p},z) = \hat{I}z - \hat{H}$ ($\hat{I}$ = identity matrix).

Utilizing the Hamiltonian Eq. A.0.1 and evaluating the elements of the spectral matrix $\hat{A}$ the expression for the interband optical conductivity

$$\sigma_{1,\mathrm{IB}}(\Omega) = \frac{e^2 v_\mathrm{F}^2 \pi}{\hbar^2} \sum_{s'=\pm} \int_{-\infty}^{\infty} d\omega \frac{[f(\omega) - (\omega + \Omega)]}{\Omega} \int \frac{d^3p}{(2\pi)^3} \left[1 + v_\mathrm{F}^2 \frac{p_z^2 - p^2}{2\epsilon_{+s'}^2}\right] \times[\delta(\omega - \epsilon_{+s'})\delta(\omega + \Omega + \epsilon_{+s'})][\delta(\omega + \epsilon_{+s'})\delta(\omega + \Omega - \epsilon_{+s'})] \tag{A.0.3}$$

is obtained in Ref. [74] ($k_\mathrm{B} = 1$).
In the end, after evaluating the sum and the integrals an analytic expression for $\sigma_{1,\mathrm{IB}}(\Omega)$ is obtained. The expression for the case where $b > m$, which describes a Weyl semimetal and is utilized in this work, reads

$$\begin{aligned}\sigma_{1,\mathrm{IB}}(\Omega) = \frac{e^2}{16\pi\hbar^2 v_\mathrm{F}} \frac{1}{\Omega} \frac{\sinh(\beta\Omega/2)}{\cosh(\beta\mu) + \cosh(\beta\Omega/2)} \\ \left[G_+\left(\sqrt{\left(\frac{\Omega}{2} - b\right)^2 - m^2}\right)\Theta\left(\frac{\Omega}{2} - b - m\right)\right. \\ +G_-\left(\sqrt{\left(\frac{\Omega}{2} + b\right)^2 - m^2}\right) \\ \left. -G_-\left(\sqrt{\left(\frac{\Omega}{2} - b\right)^2 - m^2}\right)\Theta\left(b - m - \frac{\Omega}{2}\right)\right]\end{aligned} \tag{A.0.4}$$

where,

$$\begin{aligned}G_\pm(x) = \left[\Omega + \frac{4}{\Omega}(m^2 + b^2)\right] x + \frac{4}{\Omega}\frac{x^3}{3} \\ \pm\frac{4b}{\Omega}\left(x\sqrt{m^2 + x^2} + m^2 \ln\left|\frac{x + \sqrt{x^2 + m^2}}{m}\right|\right).\end{aligned} \tag{A.0.5}$$

Note that Ω is the frequency in units of energy.

B. Magneto optical conductivity for a single isolated Weyl cone

This chapter, quotes the magneto-optical conductivity $\sigma_1(\omega, B)$ for a single isolated Weyl cone (see Sec. 2.7.2) from Ref. [86]. For the full derivation and argumentation see Ref. [86].

The starting point is the low energy Hamiltonian for an isolated Weyl point in a magnetic field, which reads

$$\hat{H} = \left[-i\nabla + \frac{e}{c}\mathbf{A}\right], \tag{B.0.1}$$

with the electron charge e and the speed of light c. Any Zeeman splitting is neglected in Eq. B.0.1. The Field is considered along z direction, and the gauge $A_y = A_z = 0$, $A_x = -By$ is used. Furthermore units are chosen such that, $\hbar = k_{\mathrm{B}} = v_{\mathrm{F}} = 1$ and the magnetic length $l_B^2 = \frac{c}{eB}$ is introduced.
Solving the eigenvalue problem $\hat{H}\psi = E\psi$ leads to the energy spectrum stated in Eqns. 2.7.3 and depicted in Fig. 2.7.2 (a).
The dynamical conductivity tensor is obtained in from the Kubo formula, and the real part of the diagonal element $\mathrm{Re}\sigma_{xx} = \sigma_1$ is obtained in scales where: $\overline{\omega} = l_B\omega$, $\overline{T} = l_B T$ (T=temperature), $\overline{\mu} = l_B\mu$ (again μ denotes the chemical potential to stay consistent with the nomenclature in Ref. [86]), and reads

$$\begin{aligned}\sigma_1(\overline{\omega}) = \frac{e^2}{8\pi l_B}\Bigg[&\frac{\sinh\left(\frac{2+\overline{\omega}^2}{2\overline{\omega}\overline{T}}\right)}{\cosh\left(\frac{\overline{\mu}}{\overline{T}}\right)+\cosh\left(\frac{2+\overline{\omega}^2}{2\overline{\omega}\overline{T}}\right)} - \frac{\sinh\left(\frac{2-\overline{\omega}^2}{2\overline{\omega}\overline{T}}\right)}{\cosh\left(\frac{\overline{\mu}}{\overline{T}}\right)+\cosh\left(\frac{2-\overline{\omega}^2}{2\overline{\omega}\overline{T}}\right)}\Bigg] \\ &\sum_{n=0}^{\left[\frac{(\overline{\omega}^2-2)^2}{8\overline{\omega}^2}\right]}\left[\frac{|2(2n+1)-\overline{\omega}^2|}{\overline{\omega}\sqrt{\overline{\omega}^4-4\overline{\omega}^2(2n+1)+4}}\Theta(|\sqrt{2}-\overline{\omega}|)\right].\end{aligned} \tag{B.0.2}$$

C. Influence of the extrapolation in Cd_3As_2

The influence of high frequency extrapolation on the powerlaw increase of the optical conductivity in Cd_3As_2 is presented in Fig. C.0.1. In panel (a) the high frequency extrapolations of the $R(\omega)$ are depicted up to $1 \times 10^5\,\mathrm{cm}^{-1}$. The black dotted line represents the case as described in Sec. 4.2, utilizing synchrotron data from from Refs. [135, 149] and the x-ray atomic scattering functions as described in Sec. 2.2 and Ref. [53]. The magenta line represents a simple free electron decay $\propto \omega^{-4}$ for frequencies beyond the accesible measurement range. Neglecting the spectral weight of the features above the measured range in the reflectivity, reduces the powerlaw in the optical conductivity $\sigma_1(\omega)$ from $\omega^{1.6}$ to $\omega^{1.4}$ as depicted in panel (b).

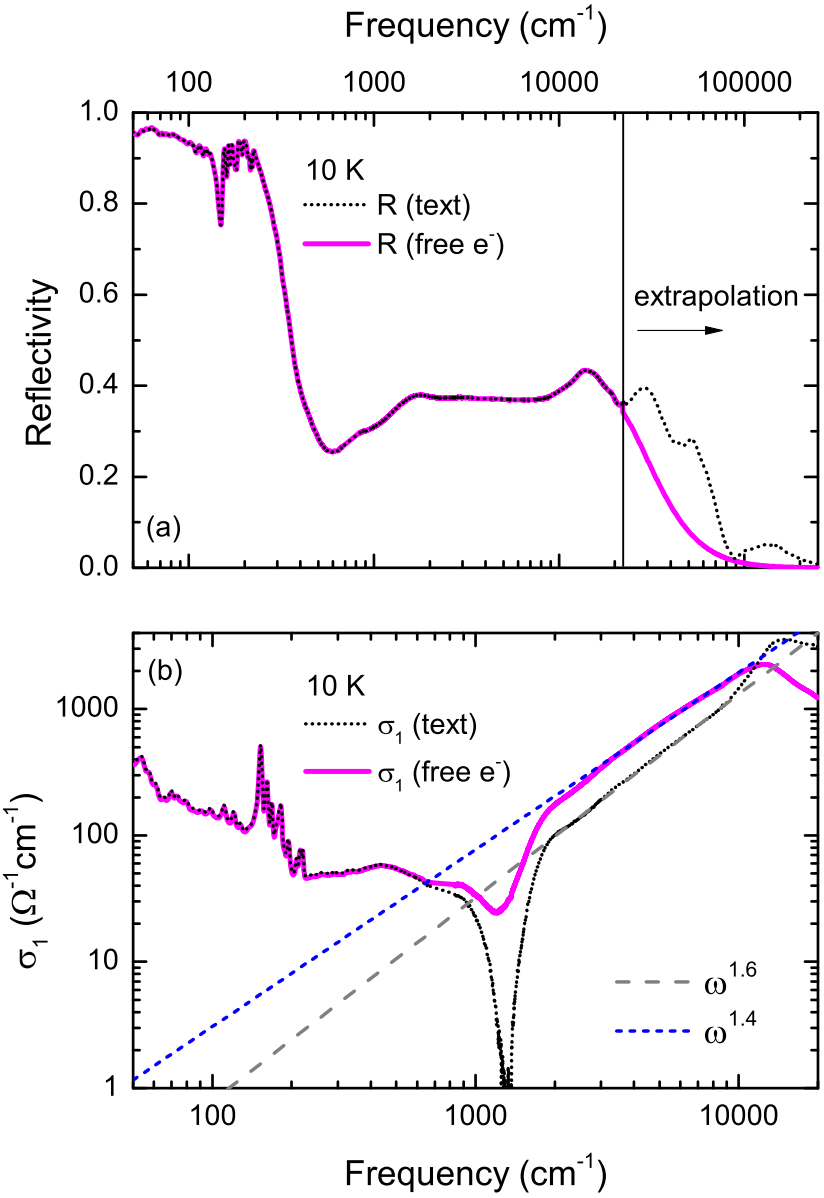

Figure C.0.1: Panel (a) depicts the reflectivity $R(\omega)$ of Cd_3As_2 measured at 10 K. Above 22 000 cm^{-1} spectra are extrapolated once as described in the text in Sec. 4.2 (black dotted line), and once with a free electron decay $\propto \omega^{-4}$ (magenta solid line). Neglecting the spectral weight in $R(\omega)$ in the second case, results in a decrease of the powerlaw in the optical conductivity $\sigma_1(\omega)$ from $\omega^{1.6}$ to $\omega^{1.4}$, respectively.

D. Magneto-optical setup - details

In this chapter relevant technical drawings, where crucial measures can be read out, as well as o-ring sizes (see Tab. D.0.1) of the magneto-optical installation are documented.

Part	Size (mm×mm)
Spectromag Windows	
seal to magnet	105×3
seal to window/adapter flanges	70×2.5
seal to optical box	120×3
Optical box	
front plate	254×4
side covers	348×4
top cover	651×5
wobble stick to front plate	18×2
wobble stick inside	5×1.75
KF- adapters on side covers	34×2
acrylic glass cover	175×4
Goldevaporation unit	52×2.5

Table D.0.1: O-ring sizes for the magneto-optical setup

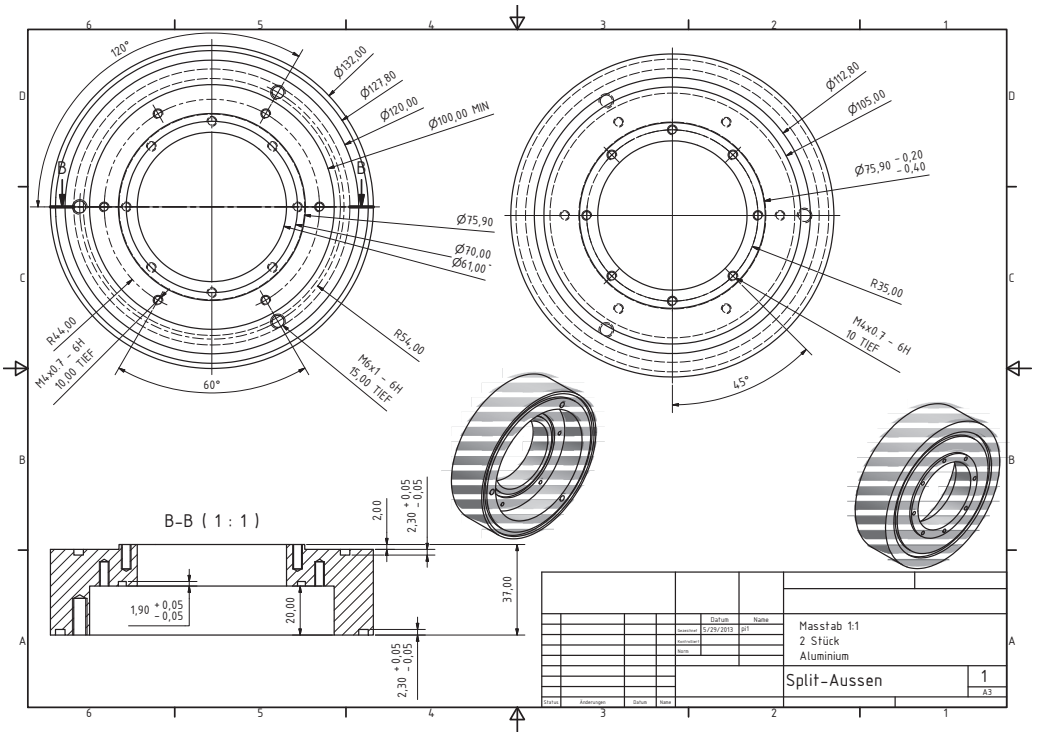

Figure D.0.1: Window adapter outside of Spectromag in split direction.

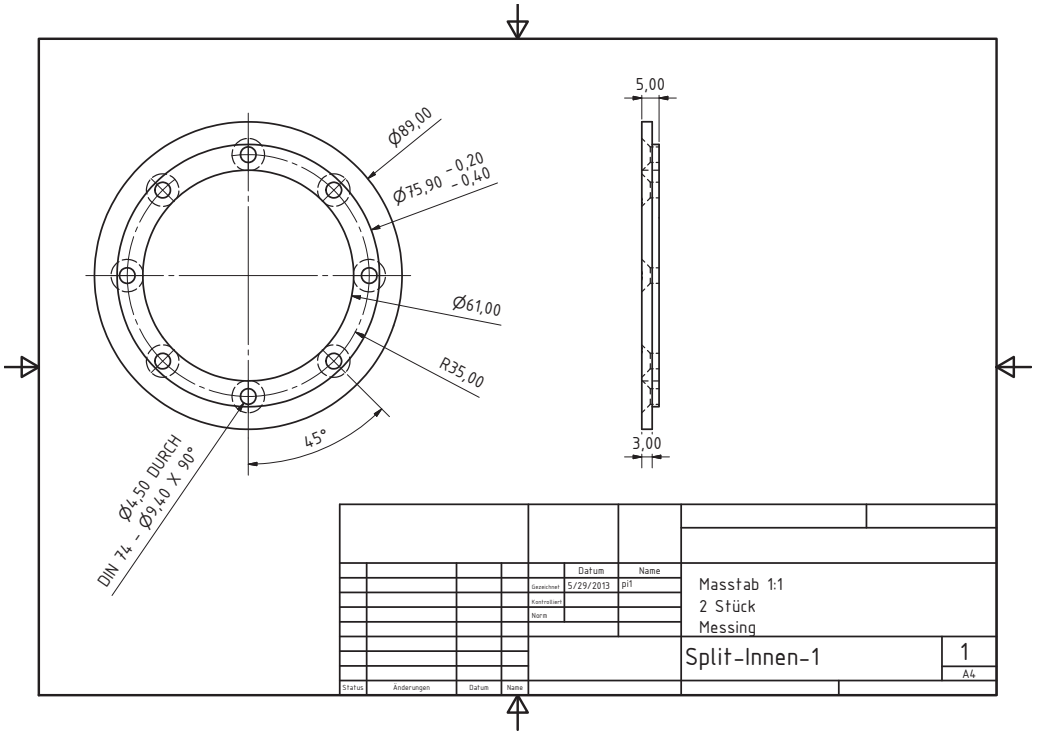

Figure D.0.2: Counterpart for the window adapter on the inside of the Spectromag bottom pot in split direction.

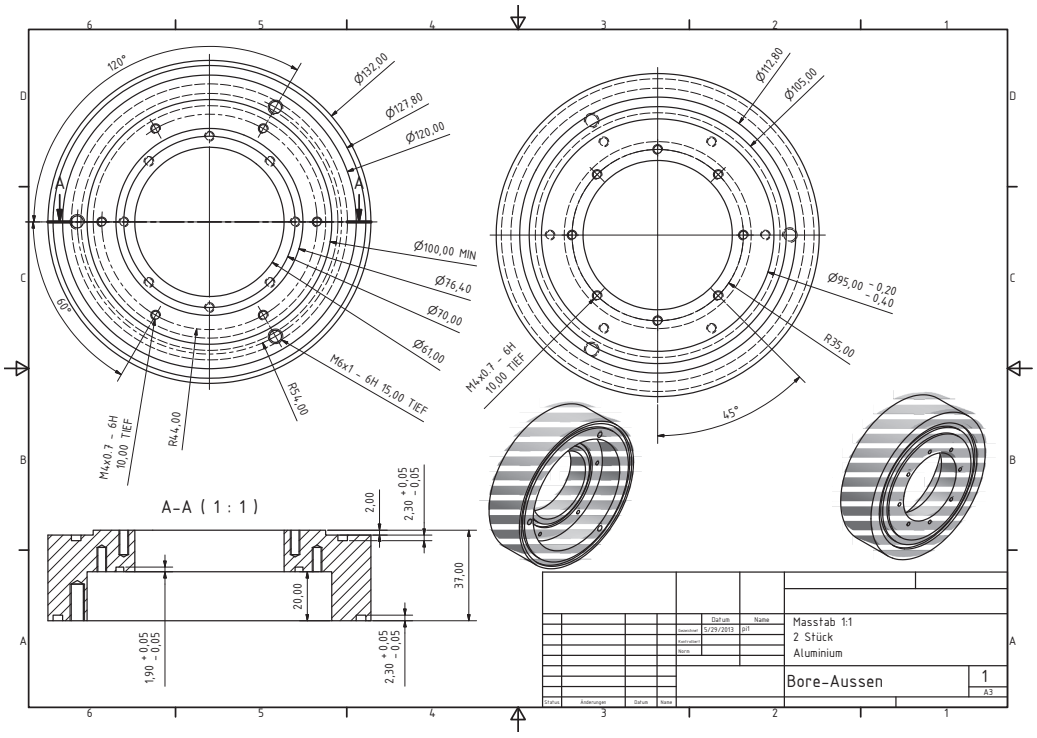

Figure D.0.3: Window adapter outside of Spectromag in bore direction.

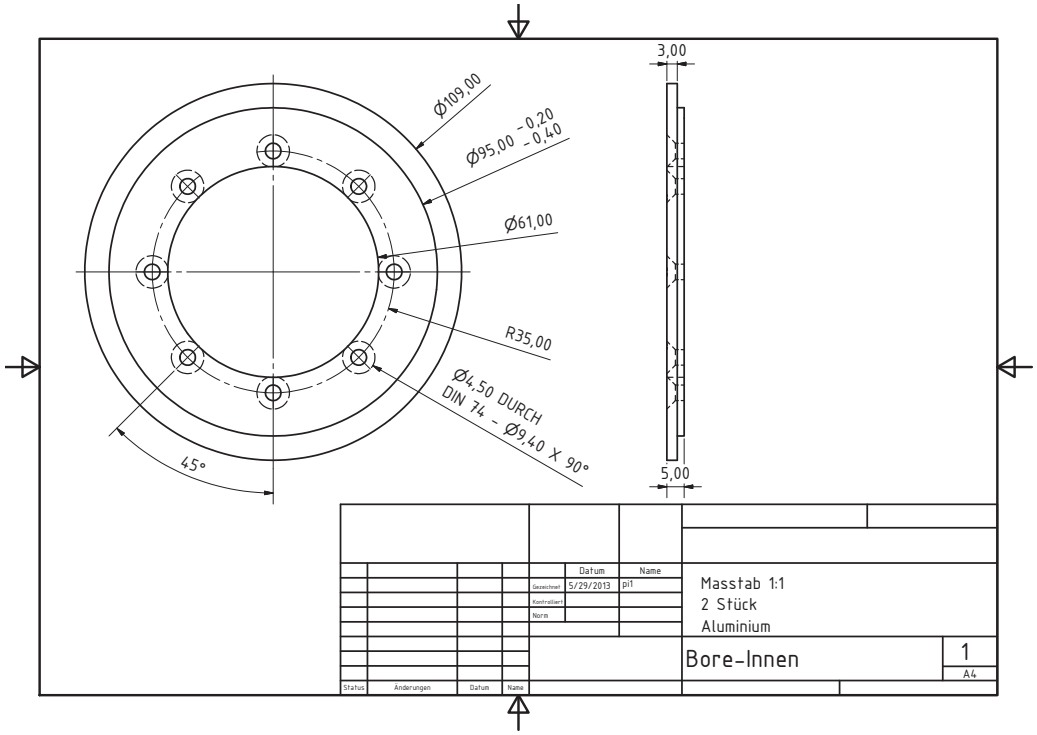

Figure D.0.4: Counterpart for the window adapter on the inside of the Spectromag bottom pot in bore direction.

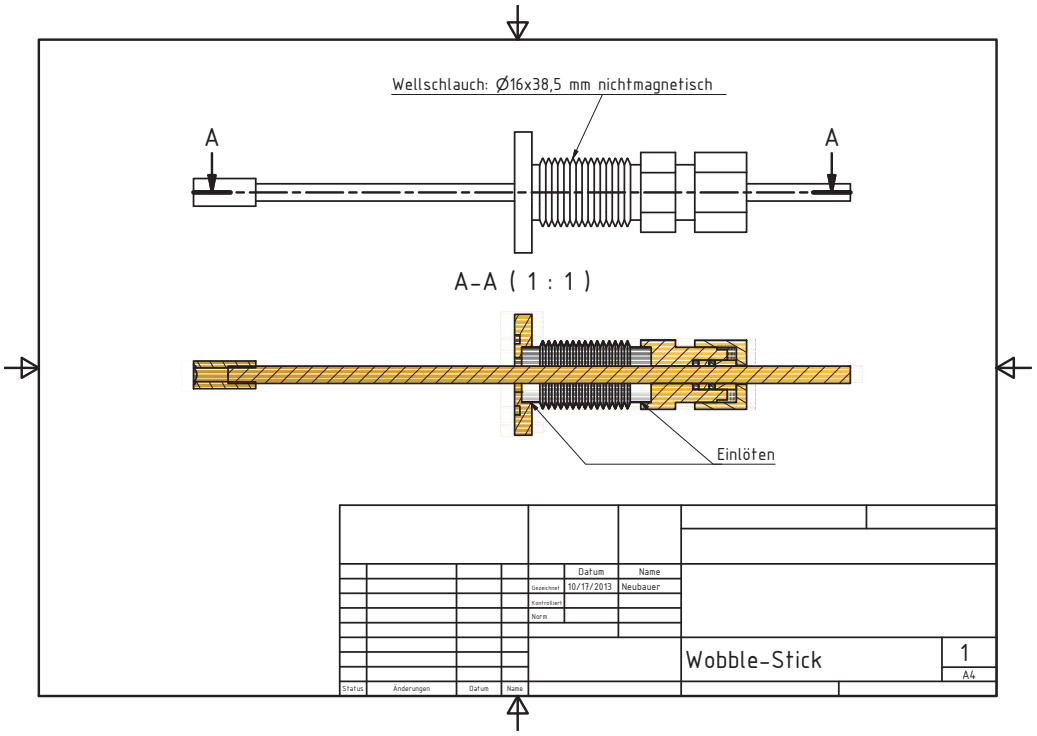

Figure D.0.5: Cut through the wobble stick revealing the working principle and sealing with two o-rings.

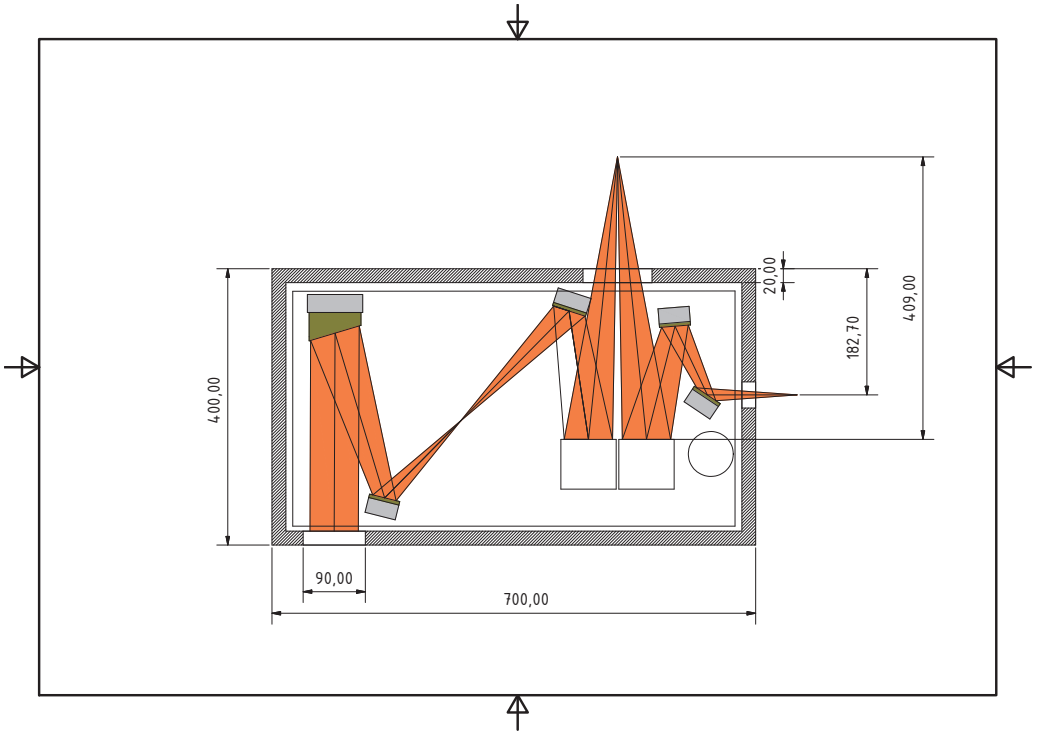

Figure D.0.6: Top view on the optical box and reflection beam path.

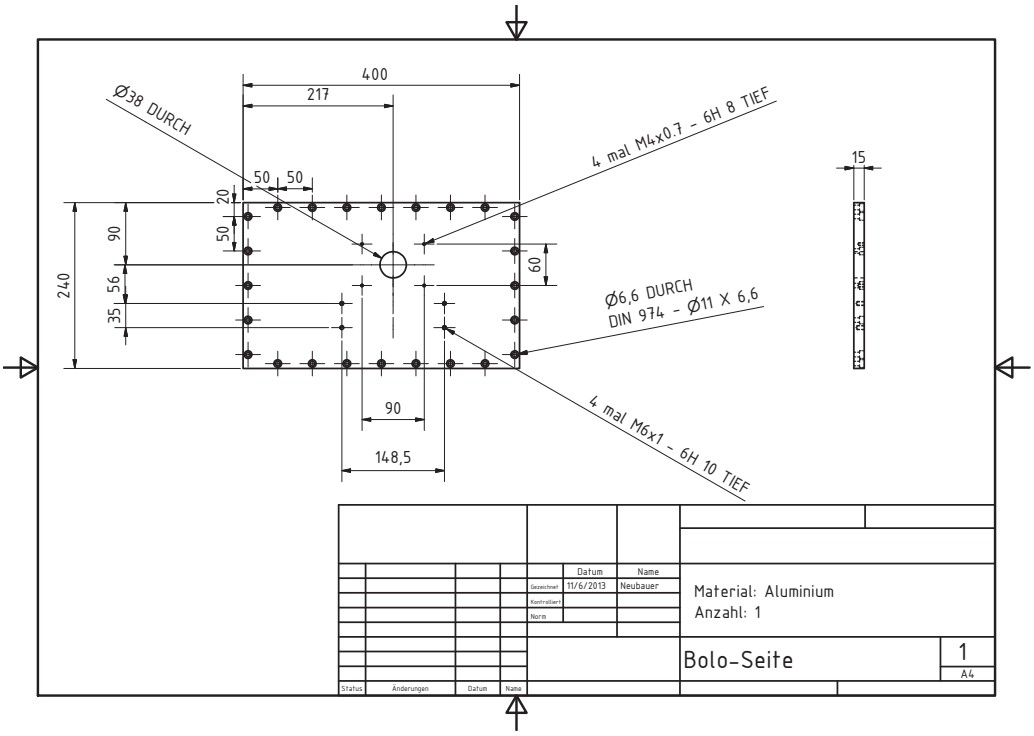

Figure D.0.7: Cover plate of the optical box on the bolometer side. The frames of screw holes are always 50 mm *spaced on all sides of the optical box.*

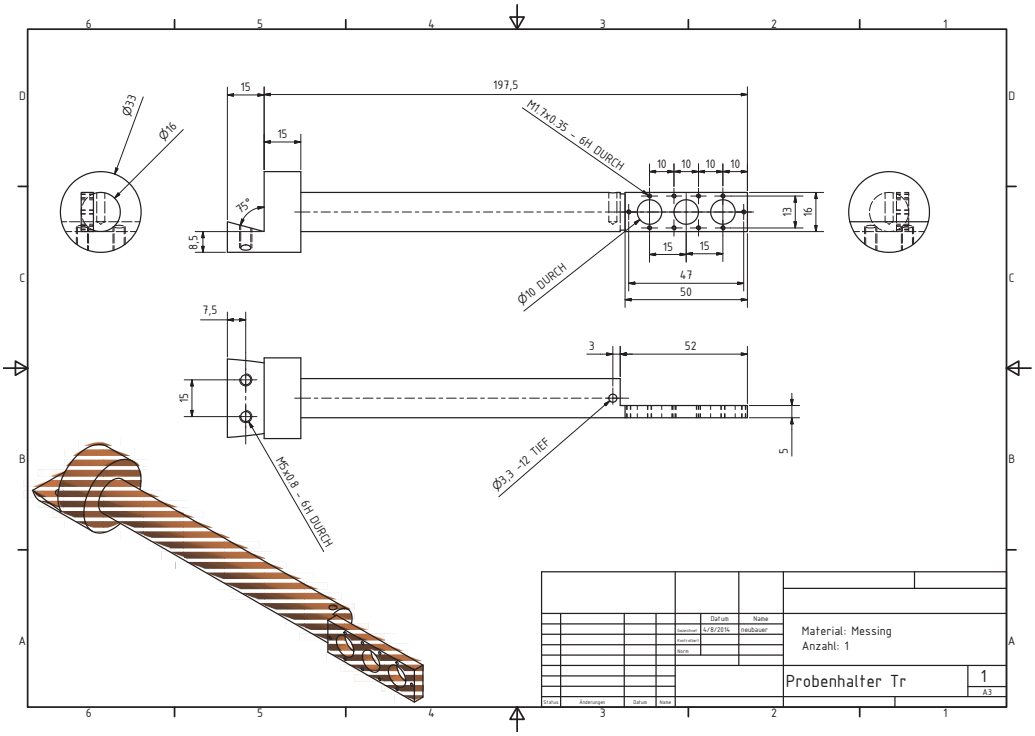

Figure D.0.8: Aperture sampleholder for transmission experiments.

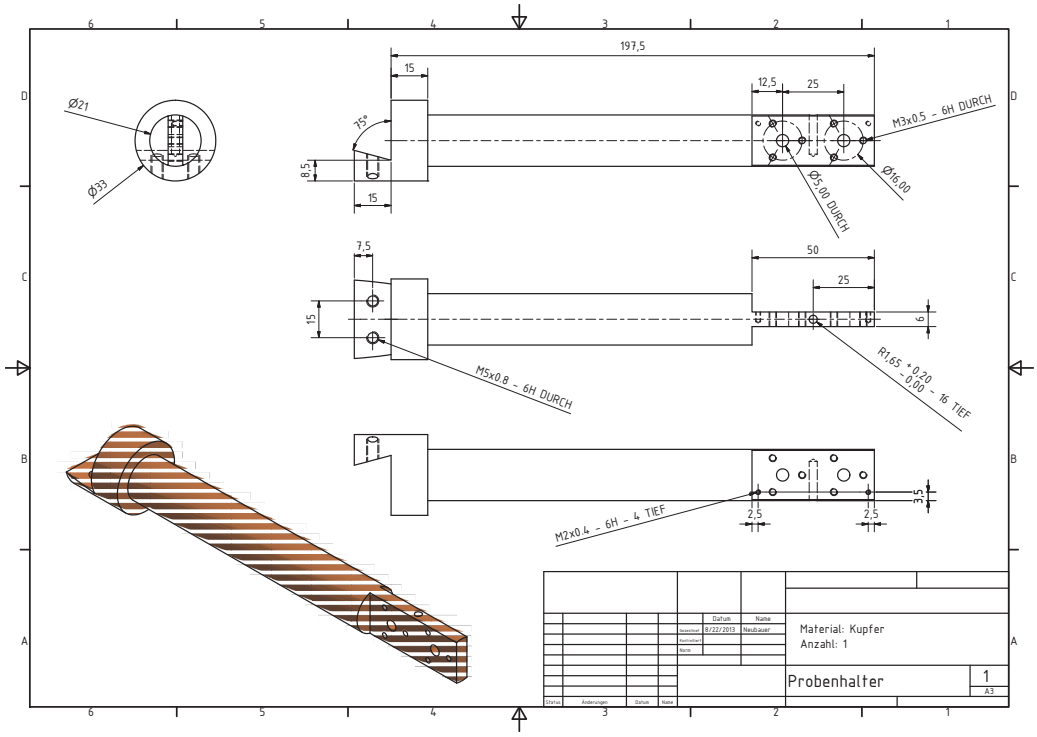

Figure D.0.9: Sampleholder for reflection experiments with the gold evaporation technique.

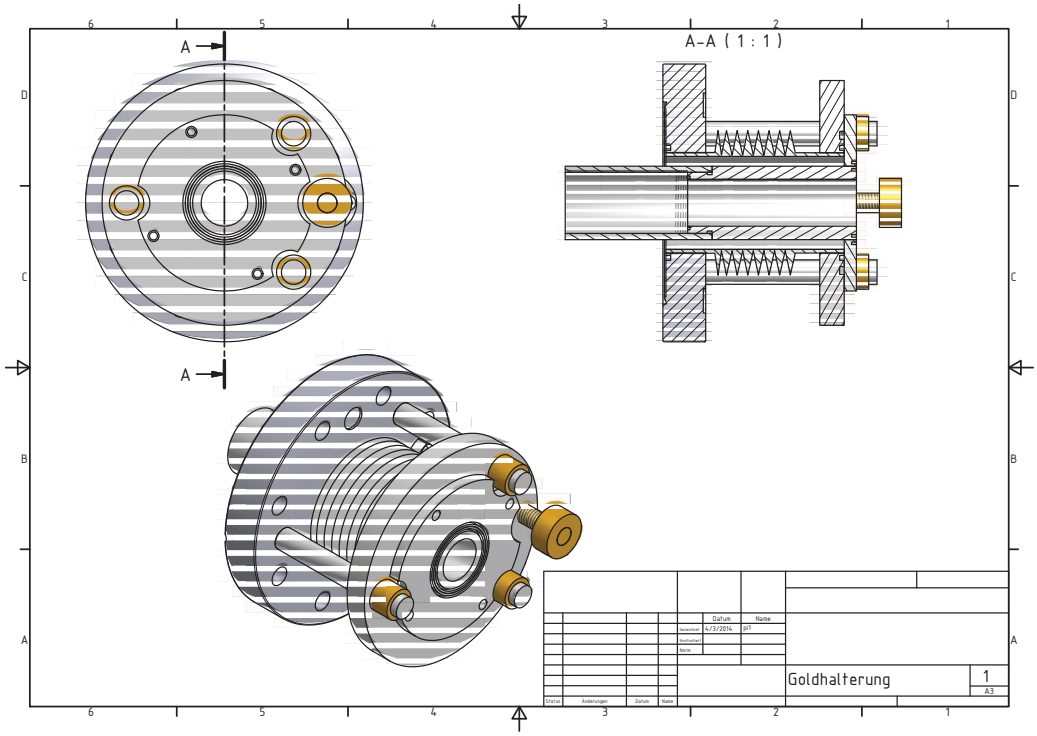

Figure D.0.10: Detail and sectional view of the gold evaporation unit.

E. Acknowledgments

At this point I would like to thank all the people who directly or indirectly contributed, or gave me support over the years.

- First of all I would like to thank my supervisor Prof. Dressel. I'm really grateful that you gave me the opportunity to dive into this fascinating field of superconductors and Dirac semimetals. Furthermore, thank you for having an open door and ear, whenever I needed your guidance.

- I also would like to thank Jun. Prof. Rost for agreeing to co-referee this work. Thank you also for your nice lecture on correlated electrons. I learned a lot there.

- I would like to thank Sina Zapf, who introduced me to the lab and gave me guidance in the first two years of my PhD work. I learned so many things from you that made this work possible. Furthermore, I would like to thank Artem Pronin, who took this 'job' in the second half of my PhD work. Thank you for encouraging me to change the topic of my thesis. That was the right thing to do.

- I deeply admire the technical and especially tactile capabilities of Gabi Untereiner! I can't imagine how many samples I would have destroyed without your help. Thank you! Many thanks also to Agni Schmidt for countless cases of help with administrative issues.

I also want to acknowledge all collaborators, people who provided samples and people who gave support building the magneto-optical setup:

- Even though they are barely discussed in this work, I would like the people who provided me samples of iron based superconductors, Sabine Wurmmehl and Saicharan Aswartham for the series of Ba-Eu 122 samples; Guang-Han Cao and Wen-He Jiao, as well as H. S. Jeevan and Prof. Gegenwart for the P substituted Eu pnictide samples; Thomas Wolf for KFe_2As_2 and FeSe.

- I would like to thank Alexandr Nateprov for providing the Cd_3As_2 samples.

- Ralph Hübner, thank you for providing NbP samples, and Claudia Felser, thank you for providing TaAs samples.

- I'm grateful for theoretical contributions by, and discussions with Jules Carbotte and Hongbin Zhang.

- I thank Dmyrto Kamenskyi and Andrea Marchese at the HFML in Nijmegen for their help with the measurements in Nijmegen.

- I would like to thank Prof. D. N. Basov and Kirk Post for enabling the visit in San Diego and introducing me to the magneto-optical setup there. This visit was highly inspirational for my construction works in Stuttgart.

- Thanks to Ralf Kamella and the whole mechanical workshop at the University of Stuttgart. I learned a lot about metal processing from all of you.

- Also many thanks to the low temperature workshop, not only for all the liquid helium (no helium, no low temperature physics), but also for countless advice concerning low temperature and vacuum instrumentation.

I want also to thank the people who supported and accompanied me over the years at the institute.

- I would like to thank the people of the IR-team not only for many fruitful discussions over the years, but also for the familiar athmosphere: Micha, Andrej, Andrea, Li, Tobi, Shuai, Rebecca, Tomislav, Elena

- The sidewinder never sleeps! Thank you Uwe, Conrad, Eric for all the nice time together. Uwe thank you for the discussions about many theoretical issues and the help with Mathematica simulations.

- Thank you Anja for contributing so many transport data to my work. Thank you Eva for introducing me to the DC-lab and helping with measurements.

- I would like to thank all my Bachelor and Master students: Johannes, Alina, Andreas, Bahar, Richard thank you for all your questions which made me think, and your contributions to this work.

- All other people of the institute for many on- and off-topic conversations over the years and the nice working atmosphere: Marc, Stefano, Roland, Bruno, Helga, Sabrina, Christian, Ievgen, Olga, Marcus, Mojtaba and all whom I have might forgot to mention here. Thank you!
- Thank you Ema for drinking so much espresso with me, which made me stay awake.

Much love and thanks to my parents and my sister who always supported me in following my dreams! Thanks to all my friends pushing me up whenever I felt down. Much love and thanks to my daughter Lilli, you enrich my life and motivate me to work and become a better person. Last but not least much love and thanks to Annika for proofreading through my thesis and motivating me.

Bibliography

[1] T. O. Wehling, A. M. Black-Schaffer, and A. V. Balatsky. „Dirac materials“. In: *Adv. Phys.* 63 (1) (2014), pp. 1–76.

[2] Oskar Vafek and Ashvin Vishwanath. „Dirac Fermions in Solids: From High-Tc Cuprates and Graphene to Topological Insulators and Weyl Semimetals“. In: *Annu. Rev. Condens. Matter Phys.* 5 (1) (2014), pp. 83–112.

[3] A. A. Burkov. „Topological semimetals“. In: *Nat. Mater.* 15 (11) (2016), pp. 1145–1148.

[4] Binghai Yan and Claudia Felser. „Topological Materials: Weyl Semimetals“. In: *Annu. Rev. Condens. Matter Phys.* 8 (1) (2017), pp. 031016–025458.

[5] S.-Y. Xu et al. „Discovery of a Weyl fermion semimetal and topological Fermi arcs“. In: *Science* 349 (6248) (2015), pp. 613–617.

[6] Xiaochun Huang et al. „Observation of the Chiral-Anomaly-Induced Negative Magnetoresistance in 3D Weyl Semimetal TaAs“. In: *Phys. Rev. X* 5 (3) (2015), p. 031023.

[7] Sergey Borisenko et al. „Experimental Realization of a Three-Dimensional Dirac Semimetal“. In: *Phys. Rev. Lett.* 113 (2) (2014), p. 027603.

[8] Z. K. Liu et al. „A stable three-dimensional topological Dirac semimetal Cd3As2“. In: *Nat. Mater.* 13 (7) (2014), pp. 677–681.

[9] K. K. Huynh et al. „Electric transport of a single-crystal iron chalcogenide FeSe superconductor: Evidence of symmetry-breakdown nematicity and additional ultrafast Dirac cone-like carriers“. In: *Phys. Rev. B* 90 (14) (2014), p. 144516.

[10] S. Y. Tan et al. „Observation of Dirac cone band dispersions in FeSe thin films by photoemission spectroscopy“. In: *Phys. Rev. B* 93 (10) (2016), p. 104513.

[11] K. S. Novoselov et al. „Two-dimensional gas of massless Dirac fermions in graphene“. In: *Nature* 438 (7065) (2005), pp. 197–200.

[12] A. B. Kuzmenko et al. „Universal Optical Conductance of Graphite“. In: *Phys. Rev. Lett.* 100 (11) (2008), p. 117401.

[13] Frank Wilczek. „Why Are There Analogies Between Condensed Matter and Particle Theory?“ In: *Phys. Today* 51 (1) (1998), pp. 11–13.

[14] M. I. Katsnelson and K. S. Novoselov. „Graphene: New bridge between condensed matter physics and quantum electrodynamics“. In: *Solid State Commun.* 143 (1-2) (2007), pp. 3–13.

[15] P. A. M. Dirac. „The Quantum Theory of the Electron“. In: *Proc. R. Soc. A Math. Phys. Eng. Sci.* 117 (778) (1928), pp. 610–624.

[16] Conyers Herring. „Accidental Degeneracy in the Energy Bands of Crystals“. In: *Phys. Rev.* 52 (4) (1937), pp. 365–373.

[17] A. A. Burkov, M. D. Hook, and Leon Balents. „Topological nodal semimetals“. In: *Phys. Rev. B* 84 (23) (2011), p. 235126.

[18] A. A. Zyuzin, Si Wu, and A. A. Burkov. „Weyl semimetal with broken time reversal and inversion symmetries“. In: *Phys. Rev. B* 85 (16) (2012), p. 165110.

[19] David Ciudad. „Weyl fermions: Massless yet real“. In: *Nat. Mater.* 14 (9) (2015), pp. 863–863.

[20] M. Zahid Hasan et al. „Discovery of Weyl Fermion Semimetals and Topological Fermi Arc States“. In: *Annu. Rev. Condens. Matter Phys.* 8 (1) (2017), pp. 031016–025225.

[21] S. M. Young et al. „Dirac semimetal in three dimensions“. In: *Phys. Rev. Lett.* 108 (14) (2012), p. 140405.

[22] Zhijun Wang et al. „Three-dimensional Dirac semimetal and quantum transport in Cd3As2“. In: *Phys. Rev. B* 88 (12) (2013), p. 125427.

[23] Xiangang Wan et al. „Topological semimetal and Fermi-arc surface states in the electronic structure of pyrochlore iridates“. In: *Phys. Rev. B* 83 (20) (2011), pp. 1–9.

[24] H. B. Nielsen and Masao Ninomiya. „The Adler-Bell-Jackiw anomaly and Weyl fermions in a crystal“. In: *Phys. Lett. B* 130 (6) (1983), pp. 389–396.

[25] Shuang Jia, Su-Yang Xu, and M. Zahid Hasan. „Weyl semimetals, Fermi arcs and chiral anomalies“. In: *Nat. Mater.* 15 (11) (2016), pp. 1140–1144.

[26] A. A. Burkov and Leon Balents. „Weyl Semimetal in a Topological Insulator Multilayer“. In: *Phys. Rev. Lett.* 107 (12) (2011), p. 127205.

[27] Gang Xu et al. „Chern Semimetal and the Quantized Anomalous Hall Effect in HgCr2Se4“. In: *Phys. Rev. Lett.* 107 (18) (2011), p. 186806.

[28] Hongming Weng et al. „Weyl Semimetal Phase in Noncentrosymmetric Transition-Metal Monophosphides“. In: *Phys. Rev. X* 5 (1) (2015), p. 011029.

[29] Shin-Ming Huang et al. „A Weyl Fermion semimetal with surface Fermi arcs in the transition metal monopnictide TaAs class“. In: *Nat. Commun.* 6 (2015), p. 7373.

[30] B. Q. Lv et al. „Observation of Weyl nodes in TaAs“. In: *Nat. Phys.* 11 (9) (2015), pp. 724–727.

[31] Chi Cheng-Long Zhang et al. „Signatures of the Adler-Bell-Jackiw chiral anomaly in a Weyl fermion semimetal“. In: *Nat. Commun.* 7 (2016), p. 10735.

[32] R. D. Dos Reis et al. „On the search for the chiral anomaly in Weyl semimetals: the negative longitudinal magnetoresistance“. In: *New J. Phys.* 18 (8) (2016), p. 085006.

[33] Madhab Neupane et al. „Observation of a three-dimensional topological Dirac semimetal phase in high-mobility Cd3As2“. In: *Nat. Commun.* 5 (May) (2014), p. 3786.

[34] Z. K. Liu et al. „Discovery of a Three-Dimensional Topological Dirac Semimetal, Na3Bi“. In: *Science* 343 (6173) (2014), pp. 864–867.

[35] Jun Xiong et al. „Evidence for the chiral anomaly in the Dirac semimetal Na3Bi“. In: *Science* 350 (6259) (2015), pp. 413–416.

[36] Philip J. W. Moll et al. „Transport evidence for Fermi-arc-mediated chirality transfer in the Dirac semimetal Cd3As2“. In: *Nature* 535 (7611) (2016), pp. 266–270.

[37] Zhi-Guo Chen et al. „Spectroscopic evidence for bulk-band inversion and three-dimensional massive Dirac fermions in ZrTe5“. In: *Proc. Natl. Acad. Sci.* 114 (5) (2017), pp. 816–821.

[38] P. Richard et al. „Observation of Dirac Cone Electronic Dispersion in BaFe2As2“. In: *Phys. Rev. Lett.* 104 (13) (2010), p. 137001.

[39] Sudhakar Pandey et al. „Spin Hall effect in iron-based superconductors: A Dirac-point effect“. In: *Phys. Rev. B* 86 (6) (2012), p. 060507.

[40] Yue Sun, Sunseng Pyon, and Tsuyoshi Tamegai. „Electron carriers with possible Dirac-cone-like dispersion in FeSe1-xSx (x=0 and 0.14) single crystals triggered by structural transition“. In: *Phys. Rev. B* 93 (10) (2016), p. 104502.

[41] Alexey A. Soluyanov et al. „Type-II Weyl semimetals“. In: *Nature* 527 (7579) (2015), pp. 495–498.

[42] Leslie M. Schoop et al. „Dirac Cone Protected by Non-Symmorphic Symmetry and 3D Dirac Line Node in ZrSiS“. In: *Nat. Commun.* 7 (9) (2015), p. 11696.

[43] Palash B. Pal. „Dirac, Majorana, and Weyl fermions“. In: *Am. J. Phys.* 79 (5) (2011), pp. 485–498.

[44] Frank Wilczek. „Majorana returns“. In: *Nat. Phys.* 5 (9) (2009), pp. 614–618.

[45] M. Z. Hasan and C. L. Kane. „Colloquium: Topological insulators“. In: *Rev. Mod. Phys.* 82 (2010), pp. 3045–3067.

[46] G. Bednik, A. A. Zyuzin, and A. A. Burkov. „Superconductivity in Weyl metals“. In: *Phys. Rev. B* 92 (3) (2015), p. 035153.

[47] Z. K. Liu et al. „Evolution of the Fermi surface of Weyl semimetals in the transition metal pnictide family“. In: *Nat. Mater.* 15 (1) (2015), pp. 27–31.

[48] L. P. He et al. „Quantum Transport Evidence for the Three-Dimensional Dirac Semimetal Phase in Cd3As2“. In: *Phys. Rev. Lett.* 113 (2014), p. 246402.

[49] J. Klotz et al. „Quantum oscillations and the Fermi surface topology of the Weyl semimetal NbP“. In: *Phys. Rev. B* 93 (12) (2016), p. 121105.

[50] Frank Arnold et al. „Chiral Weyl Pockets and Fermi Surface Topology of the Weyl Semimetal TaAs“. In: *Phys. Rev. Lett.* 117 (14) (2016), p. 146401.

[51] Martin Dressel and George Grüner. *Electrodynamics of Solids*. Cambridge: Cambridge University Press, 2002.

[52] Frederick Wooten. *Optical properties of solids*. New York, London: Academic press, 1972.

[53] D. B. Tanner. „Use of x-ray scattering functions in Kramers-Kronig analysis of reflectance“. In: *Phys. Rev. B* 91 (3) (2015), p. 035123.

[54] B. L. Henke, E. M. Gullikson, and J. C. Davis. „X-Ray Interactions: Photoabsorption, Scattering, Transmission, and Reflection at E = 50-30,000 eV, Z = 1-92“. In: *At. Data Nucl. Data Tables* 54 (2) (1993), pp. 181–342.

[55] Peter Y. Yu and Manuel Cardona. *Fundamentals of Semiconductors*. Graduate Texts in Physics. Springer Berlin Heidelberg, 2010, pp. 1829–1841.

[56] Marius Grundmann. *The Physics of Semiconductors*. Graduate Texts in Physics. Springer International Publishing, 2016.

[57] Hans Kuzmany. *Solid-State Spectroscopy*. Berlin, Heidelberg: Springer Berlin Heidelberg, 2009.

[58] K. S. Novoselov et al. „Electric Field Effect in Atomically Thin Carbon Films". In: *Science* 306 (5696) (2004), pp. 666–669.

[59] V. P. Gusynin, S. G. Sharapov, and J. P. Carbotte. „Unusual microwave response of dirac quasiparticles in graphene". In: *Phys. Rev. Lett.* 96 (25) (2006), p. 256802.

[60] Kin Fai Mak et al. „Measurement of the Optical Conductivity of Graphene". In: *Phys. Rev. Lett.* 101 (19) (2008), p. 196405.

[61] R. R. Nair et al. „Fine Structure Constant Defines Visual Transparency of Graphene". In: *Science* 320 (5881) (2008), pp. 1308–1308.

[62] Ádám Bácsi and Attila Virosztek. „Low-frequency optical conductivity in graphene and in other scale-invariant two-band systems". In: *Phys. Rev. B* 87 (12) (2013), p. 125425.

[63] T. Timusk et al. „Three-dimensional Dirac fermions in quasicrystals as seen via optical conductivity". In: *Phys. Rev. B* 87 (23) (2013), p. 235121.

[64] K. Ueda et al. „Variation of Charge Dynamics in the Course of Metal-Insulator Transition for Pyrochlore-Type Nd2Ir2O7". In: *Phys. Rev. Lett.* 109 (13) (2012), p. 136402.

[65] A. B. Sushkov et al. „Optical evidence for a Weyl semimetal state in pyrochlore Eu2Ir2O7". In: *Phys. Rev. B* 92 (24) (2015), p. 241108.

[66] R. Y. Chen et al. „Optical spectroscopy study of the three-dimensional Dirac semimetal ZrTe5". In: *Phys. Rev. B* 92 (7) (2015), p. 075107.

[67] B. Xu et al. „Optical spectroscopy of the Weyl semimetal TaAs". In: *Phys. Rev. B* 93 (12) (2016), p. 121110.

[68] D. Neubauer et al. „Interband optical conductivity of the [001]-oriented Dirac semimetal Cd3As2". In: *Phys. Rev. B* 93 (12) (2016), p. 121202.

[69] M. Orlita et al. „Observation of three-dimensional massless Kane fermions in a zinc-blende crystal". In: *Nat. Phys.* 10 (3) (2014), pp. 233–238.

[70] B. Rosenstein and M. Lewkowicz. „Dynamics of electric transport in interacting Weyl semimetals". In: *Phys. Rev. B* 88 (4) (2013), p. 045108.

[71] Phillip E . C. Ashby. „The optical conductivity of dirac materials“. PhD thesis. McMaster University, Hamilton, Ontario, 2013.

[72] Oleg V. Kotov and Yurii E. Lozovik. „Dielectric response and novel electromagnetic modes in three-dimensional Dirac semimetal films“. In: *Phys. Rev. B* 93 (23) (2016), p. 235417.

[73] Bitan Roy, Vladimir Juričić, and Sankar Das Sarma. „Universal optical conductivity of a disordered Weyl semimetal“. In: *Sci. Rep.* 6 (1) (2016), p. 32446.

[74] C. J. Tabert and J. P. Carbotte. „Optical conductivity of Weyl semimetals and signatures of the gapped semimetal phase transition“. In: *Phys. Rev. B* 93 (8) (2016), p. 085442.

[75] C. J. Tabert, J. P. Carbotte, and E. J. Nicol. „Optical and transport properties in three-dimensional Dirac and Weyl semimetals“. In: *Phys. Rev. B* 93 (8) (2016), p. 085426.

[76] J. P. Carbotte. „Dirac cone tilt on interband optical background of type-I and type-II Weyl semimetals“. In: *Phys. Rev. B* 94 (16) (2016), p. 165111.

[77] Pavan Hosur, S. A. Parameswaran, and Ashvin Vishwanath. „Charge Transport in Weyl Semimetals“. In: *Phys. Rev. Lett.* 108 (4) (2012), p. 046602.

[78] Phillip E. C. Ashby and J. P. Carbotte. „Chiral anomaly and optical absorption in Weyl semimetals“. In: *Phys. Rev. B* 89 (24) (2014), p. 245121.

[79] Takahiro Morimoto and Naoto Nagaosa. „Weyl Mott Insulator“. In: *Sci. Rep.* 6 (1) (2016), p. 19853.

[80] G. S. Jenkins et al. „Three-dimensional Dirac cone carrier dynamics in Na3Bi and Cd3As2“. In: *Phys. Rev. B* 94 (8) (2016), p. 085121.

[81] A. B. Pippard. *Magneto-resistance in metals*. Cambridge: Cambridge University Press, 1989.

[82] D. Schoenberg. *Magnetic oscillations in metals*. Cambridge. New York: Cambridge University Press, 2009.

[83] G. Landwehr and E. I. Rashba. *Landau level spectroscopy*. Ed. by G. Landwehr and E. I. Rashba. Modern Pro. North-Holland, 1991.

[84] Benjamin Lax and George B. Wright. „Magnetoplasma Reflection in Solids“. In: *Phys. Rev. Lett.* 4 (1) (1960), pp. 16–18.

[85] E. D. Palik and J. K. Furdyna. „Infrared and microwave magnetoplasma effects in semiconductors“. In: *Reports Prog. Phys.* 33 (3) (1970), p. 307.

[86] Phillip E. C. Ashby and J. P. Carbotte. „Magneto-optical conductivity of Weyl semimetals“. In: *Phys. Rev. B* 87 (24) (2013), p. 245131.

[87] Phillip E. C. Ashby and Jules P. Carbotte. „Theory of magnetic oscillations in Weyl semimetals“. In: *Eur. Phys. J. B* 87 (4) (2014), p. 92.

[88] J. M. Shao and G. W. Yang. „Magneto-optical conductivity of Weyl semimetals with quadratic term in momentum“. In: *AIP Adv.* 6 (2) (2016), p. 025312.

[89] V. P. Gusynin, S. G. Sharapov, and J. P. Carbotte. „Anomalous absorption line in the magneto-optical response of graphene“. In: *Phys. Rev. Lett.* 98 (15) (2007), p. 157402.

[90] Z. Jiang et al. „Infrared spectroscopy of landau levels of graphene“. In: *Phys. Rev. Lett.* 98 (19) (2007), p. 197403.

[91] V. P. Gusynin, S. G. Sharapov, and J. P. Carbotte. „Magneto-optical conductivity in graphene“. In: *J. Phys. Condens. Matter* 19 (2) (2007), p. 026222.

[92] M. Orlita et al. „Magneto-Optics of Massive Dirac Fermions in Bulk Bi2Se3“. In: *Phys. Rev. Lett.* 114 (18) (2015), p. 186401.

[93] R. Y. Chen et al. „Magnetoinfrared Spectroscopy of Landau Levels and Zeeman Splitting of Three-Dimensional Massless Dirac Fermions in ZrTe5“. In: *Phys. Rev. Lett.* 115 (17) (2015), p. 176404.

[94] Sándor Bordács et al. „Landau Level Spectroscopy of Dirac Electrons in a Polar Semiconductor with Giant Rashba Spin Splitting“. In: *Phys. Rev. Lett.* 111 (16) (2013), p. 166403.

[95] A. Akrap et al. „Magneto-Optical Signature of Massless Kane Electrons in Cd3As2“. In: *Phys. Rev. Lett.* 117 (13) (2016), p. 136401.

[96] A. A. Schafgans et al. „Landau level spectroscopy of surface states in the topological insulator Bi0.91Sb0.09 viamagneto-optics“. In: *Phys. Rev. B* 85 (19) (2012), p. 195440.

[97] A. Burkov. „Chiral anomaly without relativity“. In: *Science* 350 (6259) (2015), pp. 378–379.

[98] Heike Kamerlingh Onnes. „No Title“. In: *Leiden Commun.* 120b, 122b (1911).

[99] W. Meissner and R. Ochsenfeld. „Ein neuer Effekt bei Eintritt der Supraleitfähigkeit“. In: *Naturwissenschaften* 21 (44) (1933), pp. 787–788.

[100] J. Bardeen, L. N. Cooper, and J. R. Schrieffer. „Theory of superconductivity“. In: *Phys. Rev.* 108 (5) (1957), pp. 1175–1204.

[101] K. A. Müller and J. G. Bednorz. „The Discovery of a Class of High-Temperature Superconductors“. In: *Science* 237 (4819) (1987), pp. 1133–1139.

[102] F. Steglich et al. „Superconductivity in the Presence of Strong Pauli Paramagnetism: CeCu2Si2“. In: *Phys. Rev. Lett.* 43 (25) (1979), pp. 1892–1896.

[103] Yoichi Kamihara et al. „Iron-Based Layered Superconductor La[O1-xFx]FeAs (x=0.05-0.12) with Tc=26K“. In: *J. Am. Chem. Soc.* 130 (11) (2008), pp. 3296–3297.

[104] A. Charnukha et al. „Eliashberg approach to infrared anomalies induced by the superconducting state of Ba0.68K0.32Fe2As2 single crystals“. In: *Phys. Rev. B* 84 (17) (2011), p. 174511.

[105] L. Benfatto, E. Cappelluti, and C. Castellani. „Spectroscopic and thermodynamic properties in a four-band model for pnictides“. In: *Phys. Rev. B - Condens. Matter Mater. Phys.* 80 (2009), pp. 1–12.

[106] Michael Tinkham. *Introduction to superconductivity*. 2nd ed. McGraw-Hill Inc., 1996.

[107] F. London and H. London. „The Electromagnetic Equations of the Supraconductor“. In: *Proc. R. Soc. A Math. Phys. Eng. Sci.* 149 (866) (1935), pp. 71–88.

[108] D. C. Mattis and J. Bardeen. „Theory of the Anomalous Skin Effect in Normal and Superconducting Metals“. In: *Phys. Rev.* 111 (2) (1958), pp. 412–417.

[109] W. Zimmermann et al. „Optical conductivity of BCS superconductors with arbitrary purity“. In: *Phys. C Supercond.* 183 (1-3) (1991), pp. 99–104.

[110] K. Kamarás et al. „In a Clean High-Tc Superconductor You Do Not See the Gap“. In: *Phys. Rev. Lett.* 64 (1) (1990), pp. 84–87.

[111] R. P. S. M. Lobo et al. „Optical conductivity evidence of clean-limit superconductivity in LiFeAs“. In: *Phys. Rev. B* 91 (17) (2015), p. 174509.

[112] David Neubauer et al. „Optical properties of superconducting EuFe2(As1-xPx)2“. In: *Phys. status solidi* 254 (1) (2017), p. 1600148.

[113] D. N. Basov and T. Timusk. „Electrodynamics of high-Tc superconductors“. In: *Rev. Mod. Phys.* 77 (2) (2005), pp. 721–779.

[114] D. N. Basov et al. „Electrodynamics of correlated electron materials“. In: *Rev. Mod. Phys.* 83 (2) (2011), pp. 471–541.

[115] R. Dornhaus, G. Nimtz, and B. Schlicht. *Narrow-Gap Semiconductors*. Springer Berlin Heidelberg, 1983.

[116] George Grüner, ed. *Millimeter and Submillimeter Wave Spectroscopy of Solids*. Vol. 74. Topics in Applied Physics. Springer Berlin Heidelberg, 1998.

[117] Peter R. Griffiths and James A. de Haseth. *Fourier transform infrared spectrometry*. John Wiley & Sons, 2007.

[118] Ludwig Genzel. „Far-infrared fourier transform spectroscopy". In: *Millim. Submillim. Wave Spectrosc. Solids*. Springer Berlin Heidelberg, 1998, pp. 169–220.

[119] Bruker Optik GmbH. *IFS 113v Service Parts Manual*. 1992.

[120] Johannes Merz. „Infrarotspektroskopie an Eisenpniktieden". Bachelorarbeit. Universität Stuttgart, 2014.

[121] Andreas Baumgartner. „FTIR Spectroscopy and Magnetization Measurements on Europium-based Iron Pnictides". Master thesis. Universität Stuttgart, 2015.

[122] Christopher C. Homes et al. „Technique for measuring the reflectance of irregular, submillimeter-sized samples". In: *Appl. Opt.* 32 (16) (1993), p. 2976.

[123] Bruker Optik GmbH. *VERTEX 80v Benutzerhandbuch*. 2006.

[124] Stefan Kaiser. „Interplay of Charge Order and Superconductivity - Optical Properties of Quarter-Filled Two-Dimensional Organic Conductors and Superconductors." Dissertation. Universität Stuttgart, 2010.

[125] Bruker Optik GmbH. *HYPERION User Manual*. 2003.

[126] W. J. Padilla et al. „Broadband multi-interferometer spectroscopy in high magnetic fields: From THz to visible". In: *Rev. Sci. Instrum.* 75 (11) (2004), p. 4710.

[127] Oxford Instruments. *Spectromag 4000-7T Operator's Handbook; Project No: 37581.1*. 1993.

[128] Tobby Bert Brandt. „Optische Leitfähigkeit dünner Goldfilme im infraroten Spektralbereich Inhaltsverzeichnis". Dissertation. Universität Stuttgart, 2008.

[129] Daniel Faltermeier. „Optische Untersuchungen an niedrigdimensionalen organischen Supraleitern". Diplomarbeit. Universität Stuttgart, 2004.

[130] Robert C. Weast and Melvin J. Astle. *CRC Handbook of Chemistry and Physics*. 61st Editi. Baca Raton, Florida: CRC Press Inc., 1980.

[131] Mike McElfresh. *Fundamentals of magnetism and magnetic measurements featuring Quantum Design's magnetic property measurement system*. Quantum Design, 1994.

[132] Arthur J. Rosenberg and Theodore C. Harman. „Cd3As2 - A Noncubic Semiconductor with Unusually High Electron Mobility". In: *J. Appl. Phys.* 30 (10) (1959), p. 1621.

[133] W. J. Turner, A. S. Fischler, and W. E. Reese. „Physical properties of several II-V semiconductors". In: *Phys. Rev.* 121 (3) (1961), pp. 759–767.

[134] S. I. Radautsan, E. K. Arushanov, and G. P. Chuiko. „The conduction band of cadmium arsenide". In: *Phys. Status Solidi* 20 (1) (1973), pp. 221–226.

[135] Maury Zivitz. „THE OPTICAL PROPERTIES OF THE Cd3As2-Cd3P2 ALLOY SYSTEM". PhD thesis. Gorgia Institute of Technology, 1973.

[136] J. Stankiewicz, W. Giriat, and W. Dobrowolski. „Shubnikov de Haas Oscillations in Cd(v)Hg(1-v)Se". In: *Phys. Status Solidi* 61 (1) (1974).

[137] W. Zdanowicz and L. Zdanowicz. „Semiconducting Compounds of the AII BV Group". In: *Annu. Rev. Mater. Sci.* 5 (1) (1975), pp. 301–328.

[138] J. Bodnar. „Band structure of Cd3As2 fom Shubnikov de Haas and de Haas - van Alphen effects". In: *Phys. narrow gap Semicond. Proc. 3. internat. Conf. Warszawa, Sept. 12-15, 1977*. Ed. by J Raułuszkiewicz. Warszawa: PWN - Polish Scientific Publ., 1978, pp. 311–316.

[139] S. G. Bishop, W. J. Moore, and E. M. Swiggard. „OPTICALLY PUMPED Cd3P2 LASER". In: *Appl. Phys. Lett.* 16 (11) (1970), pp. 459–461.

[140] S. G. Bishop and P. L. Radoff. „Temperature dependence of photoluminescence in alloys". In: *Solid State Commun.* 9 (2) (1971), pp. 133–136.

[141] É. K. Arushanov et al. „Lasing of Cd3(AsxP1-x)2 solid solutions". In: *Sov. J. Quantum Electron.* 12 (9) (1982), pp. 1256–1258.

[142] Qinsheng Wang et al. „Ultrafast Broadband Photodetectors Based on Three-Dimensional Dirac Semimetal Cd3As2". In: *Nano Lett.* 17 (2) (2017), pp. 834–841.

[143] Hemian Yi et al. „Evidence of Topological Surface State in Three-Dimensional Dirac Semimetal Cd3As2". In: *Sci. Rep.* 4 (2014), p. 6106.

[144] Sangjun Jeon et al. „Landau quantization and quasiparticle interference in the three-dimensional DiracÂ semimetal Cd3As2.“ In: *Nat. Mater.* 13 (9) (2014), pp. 851–856.

[145] Mazhar N. Ali et al. „The Crystal and Electronic Structures of Cd3As2 , the Three-Dimensional Electronic Analogue of Graphene“. In: *Inorg. Chem.* 53 (8) (2014), pp. 4062–4067.

[146] Koichi Momma and Fujio Izumi. „VESTA 3 for three-dimensional visualization of crystal, volumetric and morphology data“. In: *J. Appl. Crystallogr.* 44 (6) (2011), pp. 1272–1276.

[147] C. P. Weber et al. „Transient reflectance of photoexcited Cd3As2“. In: *Appl. Phys. Lett.* 106 (23) (2015), pp. 1–5.

[148] Tian Liang et al. „Ultrahigh mobility and giant magnetoresistance in the Dirac semimetal Cd3As2“. In: *Nat. Mater.* 14 (3) (2014), pp. 280–284.

[149] M. Zivitz and J. R. Stevenson. „Optical properties of the Cd3As2-Cd3P2 semiconductor alloy system“. In: *Phys. Rev. B* 10 (6) (1974), pp. 2457–2468.

[150] M. J. Gelten. „Optical properties of cadmium phosphide and cadmium arsenide“. Dissertation. Eindhoven: Technische Hogeschool Eindhoven, 1985.

[151] D. Houde et al. „The infrared spectrum of Cd3As2“. In: *Solid State Commun.* 57 (4) (1986), pp. 247–248.

[152] Junzhi Cao et al. „Landau level splitting in Cd3As2 under high magnetic fields“. In: *Nat. Commun.* 6 (2015), p. 7779.

[153] L. G. Caron, J. P. Jay-Gerin, and M. J. Aubin. „Energy-band structure of Cd3As2 at low temperatures and the dependence of the direct gap on temperature and pressure“. In: *Phys. Rev. B* 15 (8) (1977), pp. 3879–3887.

[154] P. L. Radoff and S. G. Bishop. „Temperature Dependence of the Optical Transmission Edge in Cd3(As1-xPx)2 Alloys“. In: *Phys. Rev. B* 5 (2) (1972), pp. 442–448.

[155] Evan O. Kane. „Band structure of indium antimonide“. In: *J. Phys. Chem. Solids* 1 (4) (1957), pp. 249–261.

[156] M. Singh and P. R. Wallace. „High g-factors and Landau level crossing in the valence band of narrow gap semiconductors“. In: *Solid State Commun.* 53 (2) (1985), pp. 165–170.

[157] M. J. Aubin, L. G. Caron, and J. P. Jay-Gerin. „Band structure of cadmium arsenide at room temperature“. In: *Phys. Rev. B* 15 (8) (1977), pp. 3872–3878.

[158] J. M. Ziman. *Principles of the theory of solids*. 2nd ed. Cambridge: Cambridge University Press, 1972.

[159] E. Kroumova et al. „Bilbao Crystallographic Server : Useful Databases and Tools for Phase-Transition Studies“. In: *Phase Transitions* 76 (1-2) (2003), pp. 155–170.

[160] Ugo Fano. „Effects of Configuration Interaction on Intensities and Phase Shifts“. In: *Phys. Rev.* 124 (6) (1961), pp. 1866–1878.

[161] A. B. Kuzmenko et al. „Gate Tunable Infrared Phonon Anomalies in Bilayer Graphene“. In: *Phys. Rev. Lett.* 103 (11) (2009), p. 116804.

[162] B. Xu et al. „Temperature-tunable Fano resonance induced by strong coupling between Weyl fermions and phonons in TaAs“. In: *arXiv:1608.08160* (2016).

[163] Dong-Hun Chae et al. „Excitonic Fano Resonance in Free-Standing Graphene“. In: *Nano Lett.* 11 (3) (2011), pp. 1379–1382.

[164] A. Narayanan et al. „Linear Magnetoresistance Caused by Mobility Fluctuations in n-Doped Cd3As2“. In: *Phys. Rev. Lett.* 114 (11) (2015), p. 117201.

[165] J. Xu et al. „Crystal Structure, Electrical Transport, and Magnetic Properties of Niobium Monophosphide“. In: *Inorg. Chem.* 35 (4) (1996), pp. 845–849.

[166] K. V. Samokhin. „Spin-orbit coupling and semiclassical electron dynamics in noncentrosymmetric metals“. In: *Ann. Phys.* 324 (11) (2009), pp. 2385–2407.

[167] Kyo-Hoon Ahn, Kwan-Woo Lee, and Warren E. Pickett. „Spin-orbit interaction driven collective electron-hole excitations in a noncentrosymmetric nodal loop Weyl semimetal“. In: *Phys. Rev. B* 92 (11) (2015), p. 115149.

[168] Chi-Cheng Lee et al. „Fermi surface interconnectivity and topology in Weyl fermion semimetals TaAs, TaP, NbAs, and NbP“. In: *Phys. Rev. B* 92 (23) (2015), p. 235104.

[169] Yan Sun, Shu-Chun Wu, and Binghai Yan. „Topological surface states and Fermi arcs of the noncentrosymmetric Weyl semimetals TaAs, TaP, NbAs, and NbP“. In: *Phys. Rev. B* 92 (11) (2015), p. 115428.

[170] Chandra Shekhar et al. „Extremely large magnetoresistance and ultrahigh mobility in the topological Weyl semimetal candidate NbP“. In: *Nat. Phys.* 11 (8) (2015), pp. 645–649.

[171] S. Souma et al. „Direct observation of nonequivalent Fermi-arc states of opposite surfaces in the noncentrosymmetric Weyl semimetal NbP“. In: *Phys. Rev. B* 93 (16) (2016), p. 161112.

[172] Di-Fei Xu et al. „Observation of Fermi Arcs in Non-Centrosymmetric Weyl Semi-Metal Candidate NbP“. In: *Chinese Phys. Lett.* 32 (10) (2015), p. 107101.

[173] Anna Corinna Niemann et al. „Chiral magnetoresistance in the Weyl semimetal NbP“. In: *arXiv:1610.01413* (2016).

[174] Frank Arnold et al. „Negative magnetoresistance without well-defined chirality in the Weyl semimetal TaP“. In: *Nat. Commun.* 7 (8) (2016), p. 11615.

[175] Jun Xiong et al. „Anomalous conductivity tensor in the Dirac semimetal Na3Bi“. In: *EPL (Europhysics Lett.)* 114 (2) (2016), p. 27002.

[176] Chenglong Zhang et al. „Large magnetoresistance over an extended temperature regime in monophosphides of tantalum and niobium“. In: *Phys. Rev. B* 92 (4) (2015), p. 041203.

[177] Mazhar N. Ali et al. „Large, non-saturating magnetoresistance in WTe2“. In: *Nature* 514 (7521) (2014), pp. 205–208.

[178] Zhen Wang et al. „Helicity-protected ultrahigh mobility Weyl fermions in NbP“. In: *Phys. Rev. B* 93 (12) (2016), p. 121112.

[179] I. B. Ferreira et al. „The electrodynamics of the heavy fermion state of CeAl3“. In: *Solid State Commun.* 83 (1) (1992), pp. 27–31.

[180] Xiaojun Yang et al. „Observation of Negative Magnetoresistance and nontrivial pi Berrys phase in 3D Weyl semi-metal NbAs“. In: *arXiv:1506.02283* (2015).

[181] Zhujun Yuan et al. „Large magnetoresistance in compensated semimetals TaAs2 and NbAs2“. In: *Phys. Rev. B* 93 (18) (2016), p. 184405.

[182] Y. Kopelevich et al. „Universal magnetic-field-driven metal-insulator-metal transformations in graphite and bismuth“. In: *Phys. Rev. B* 73 (16) (2006), p. 165128.

[183] Yuke Li et al. „Resistivity plateau and negativemagnetoresistance in the topological semimetal TaSb2“. In: *Phys. Rev. B* 94 (12) (2016), p. 121115.

[184] F. F. Tafti et al. „Resistivity plateau and extreme magnetoresistance in LaSb“. In: *Nat. Phys.* 12 (3) (2015), pp. 272–277.

[185] Kefeng Wang et al. „Anisotropic giant magnetoresistance in NbSb2“. In: *Sci. Rep.* 4 (2014), p. 7328.

[186] Y. L. Wang et al. „Origin of the turn-on temperature behavior in WTe2“. In: *Phys. Rev. B* 92 (18) (2015), p. 180402.

[187] C. Michel et al. „Strong non-Arrhenius temperature dependence of the resistivity in the regime of traditional band transport“. In: *Appl. Phys. Lett.* 89 (11) (2006), p. 112116.

[188] D. V. Khveshchenko. „Magnetic-Field-Induced Insulating Behavior in Highly Oriented Pyrolitic Graphite“. In: *Phys. Rev. Lett.* 87 (20) (2001), p. 206401.

[189] Mazhar N. Ali et al. „Correlation of crystal quality and extreme magnetoresistance of WTe2“. In: *EPL (Europhysics Lett.)* 110 (6) (2015), p. 67002.

[190] Zengwei Zhu et al. „Quantum oscillations, thermoelectric coefficients, and the fermi surface of semimetallic WTe2“. In: *Phys. Rev. Lett.* 114 (17) (2015), p. 176601.

[191] P. L. Cai et al. „Drastic Pressure Effect on the Extremely Large Magnetoresistance in WTe2: Quantum Oscillation Study“. In: *Phys. Rev. Lett.* 115 (5) (2015), p. 057202.

[192] Chandra Shekhar, Vicky Süss, and Marcus Schmidt. „Mobility induced unsaturated high linear magnetoresistance in transition-metal monopnictides Weyl semimetals“. In: *arXiv:1606.06649* (2016).

[193] M. M. Parish and P. B. Littlewood. „Non-saturating magnetoresistance in heavily disordered semiconductors“. In: *Nature* 426 (6963) (2003), pp. 162–165.

[194] H. Takahashi et al. „Low-temperature magnetotransport of the narrow-gap semiconductor FeSb2“. In: *Phys. Rev. B* 84 (20) (2011), p. 205215.

[195] S. Ishiwata et al. „Extremely high electron mobility in a phonon-glass semimetal“. In: *Nat. Mater.* 12 (6) (2013), pp. 512–517.

[196] A. V. Pronin et al. „Direct observation of the superconducting energy gap developing in the conductivity spectra of niobium“. In: *Phys. Rev. B* 57 (22) (1998), pp. 14416–14421.

[197] H. W. Liu et al. „Raman study of lattice dynamics in the Weyl semimetal TaAs“. In: *Phys. Rev. B* 92 (6) (2015), p. 064302.

[198] H. W. Liu et al. „Comparative Raman study of Weyl semimetals TaAs, NbAs, TaP and NbP“. In: *J. Phys. Condens. Matter* 28 (29) (2016), p. 295401.

[199] M. Chinotti et al. „Electrodynamic response of the type-II Weyl semimetal YbMnBi2“. In: *Phys. Rev. B* 94 (24) (2016), p. 245101.

[200] Guohong Li and Eva Y. Andrei. „Observation of Landau levels of Dirac fermions in graphite“. In: *Nat. Phys.* 3 (9) (2007), pp. 623–627.

[201] A. M. Witowski et al. „Quasi-classical cyclotron resonance of Dirac fermions in highly doped graphene“. In: *Phys. Rev. B* 82 (16) (2010), p. 6.

[202] M. Orlita et al. „Classical to quantum crossover of the cyclotron resonance in graphene: a study of the strength of intraband absorption“. In: *New J. Phys.* 14 (9) (2012), p. 095008.

[203] Mikito Koshino and Intan Fatimah Hizbullah. „Magnetic susceptibility in three-dimensional nodal semimetals“. In: *Phys. Rev. B* 93 (4) (2016), p. 045201.

[204] Xiao Xiao, K. T. Law, and P. A. Lee. „Magneto-conductivities in Weyl semimetals: the effect of chemical potential and temperature“. In: *arXiv:1607.04943* (2016).

[205] Philip J. W. Moll et al. „Magnetic torque anomaly in the quantum limit of Weyl semimetals“. In: *Nat. Commun.* 7 (May) (2016), p. 12492.

[206] Philip Sergelius et al. „Berry phase and band structure analysis of the Weyl semimetal NbP“. In: *Sci. Rep.* 6 (1) (2016), p. 33859.

[207] Chenglong Zhang et al. „Tantalum Monoarsenide: an Exotic Compensated Semimetal“. In: *arXiv:1502.00251* (2015), pp. 1–14.

[208] Ching-Kai Chiu et al. „Classification of topological quantum matter with symmetries“. In: *Rev. Mod. Phys.* 88 (3) (2016), p. 035005.

[209] J. Hu et al. „pi Berry phase and Zeeman splitting of Weyl semimetal TaP“. In: *Sci. Rep.* 6 (1) (2016), p. 18674.

[210] David C. Johnston. „The puzzle of high temperature superconductivity in layered iron pnictides and chalcogenides“. In: *Adv. Phys.* 59 (6) (2010), pp. 803–1061.

[211] G. R. Stewart. „Superconductivity in iron compounds“. In: *Rev. Mod. Phys.* 83 (4) (2011), pp. 1589–1652.

[212] Johnpierre Paglione and Richard L. Greene. „High-temperature superconductivity in iron-based materials“. In: *Nat. Phys.* 6 (9) (2010), pp. 645–658.

[213] Hideo Hosono and Kazuhiko Kuroki. „Iron-based superconductors: Current status of materials and pairing mechanism“. In: *Phys. C* 514 (2015), pp. 399–422.

[214] Yoshikazu Mizuguchi and Yoshihiko Takano. „Review of Fe chalcogenides as the simplest Fe-based superconductor“. In: *J. Phys. Soc. Japan* 79 (10) (2010), p. 102001.

[215] Jian-Feng Ge et al. „Superconductivity above 100 K in single-layer FeSe films on doped SrTiO3“. In: *Nat. Mater.* 14 (3) (2014), pp. 285–289.

[216] S. Medvedev et al. „Electronic and magnetic phase diagram of Fe1.01Se with superconductivity at 36.7K under pressure“. In: *Nat. Mater.* 8 (8) (2009), pp. 630–633.

[217] Shigeru Kasahara et al. „Field-induced superconducting phase of FeSe in the BCS-BEC cross-over“. In: *Proc. Natl. Acad. Sci.* 111 (46) (2014), pp. 16309–16313.

[218] S. Kasahara et al. „Giant superconducting fluctuations in the compensated semimetal FeSe at the BCS-BEC crossover“. In: *Nat. Commun.* 7 (2016), p. 12843.

[219] J-X. Yin et al. „Observation of a robust zero-energy bound state in iron-based superconductor Fe(Te,Se)“. In: *Nat. Phys.* 11 (7) (2015), pp. 543–546.

[220] Kun Jiang et al. „Interatomic Coulomb interaction and electron nematic bond order in FeSe“. In: *Phys. Rev. B* 93 (11) (2016), p. 115138.

[221] Seiichiro Onari, Youichi Yamakawa, and Hiroshi Kontani. „Sign-Reversing Orbital Polarization in the Nematic Phase of FeSe due to the C2 Symmetry Breaking in the Self-Energy“. In: *Phys. Rev. Lett.* 116 (22) (2016), p. 227001.

[222] G. Garbarino et al. „High-temperature superconductivity (Tc onset at 34 K) in the high-pressure orthorhombic phase of FeSe“. In: *EPL (Europhysics Lett.)* 86 (2009), p. 27001.

[223] M. D. Watson et al. „Emergence of the nematic electronic state in FeSe“. In: *Phys. Rev. B* 91 (15) (2015), p. 155106.

[224] A. E. Böhmer et al. „Lack of coupling between superconductivity and orthorhombic distortion in stoichiometric single-crystalline FeSe“. In: *Phys. Rev. B* 87 (18) (2013), p. 180505.

[225] R. M. Fernandes, A. V. Chubukov, and J. Schmalian. „What drives nematic order in iron-based superconductors?“ In: *Nat. Phys.* 10 (2) (2014), pp. 97–104.

[226] S.-H. Baek et al. „Nematicity and in-plane anisotropy of superconductivity in beta-FeSe detected by 77Se nuclear magnetic resonance“. In: *Phys. Rev. B* 93 (18) (2016), p. 180502.

[227] A. E. Böhmer et al. „Origin of the Tetragonal-to-Orthorhombic Phase Transition in FeSe: A Combined Thermodynamic and NMR Study of Nematicity“. In: *Phys. Rev. Lett.* 114 (2) (2015), p. 027001.

[228] M. C. Rahn et al. „Strong (Pi,0) spin fluctuations in beta-FeSe observed by neutron spectroscopy“. In: *Phys. Rev. B* 91 (18) (2015), p. 180501.

[229] M. Bendele et al. „Coexistence of superconductivity and magnetism in FeSe1-x under pressure“. In: *Phys. Rev. B* 85 (6) (2012), p. 064517.

[230] J. P. Sun et al. „Dome-shaped magnetic order competing with high-temperature superconductivity at high pressures in FeSe“. In: *Nat. Commun.* 7 (2016), p. 12146.

[231] Taichi Terashima et al. „Pressure-Induced Antiferromagnetic Transition and Phase Diagram in FeSe“. In: *J. Phys. Soc. Japan* 84 (6) (2015), p. 063701.

[232] J. K. Glasbrenner et al. „Effect of magnetic frustration on nematicity and superconductivity in iron chalcogenides“. In: *Nat. Phys.* 11 (11) (2015), pp. 953–958.

[233] P. Zhang et al. „Observation of two distinct dxz/dyz band splittings in FeSe“. In: *Phys. Rev. B* 91 (21) (2015), p. 214503.

[234] Yue Sun et al. „Structural-transition-induced quasi-two-dimensional Fermi surface in FeSe“. In: *Phys. Rev. B* 94 (13) (2016), p. 134505.

[235] Baharak Heydari. „Pressure dependent resistivity measurements on iron based superconductors“. Master Thesis. Universität Stuttgart, 2016.

[236] R. H. Yuan et al. „In-plane optical spectroscopy study on FeSe epitaxial thin film grown on SrTiO3 substrate“. In: *Phys. Rev. B* 87 (14) (2013), p. 144517.

[237] Haipeng Wang et al. „Band structure reconstruction across nematic order in high quality FeSe single crystal as revealed by optical spectroscopy study“. In: *Sci. Bull.* 61 (14) (2016), pp. 1126–1131.

[238] A. Akrap et al. „Infrared phonon anomaly in BaFe2As2“. In: *Phys. Rev. B* 80 (18) (2009), p. 180502.

[239] C. Marini et al. „The optical phonon spectrum of SmFeAsO“. In: *EPL (Europhysics Lett.)* 84 (6) (2008), p. 67013.

[240] A. Charnukha et al. „Spin-density-wave-induced anomalies in the optical conductivity of AFe2As2,(A = Ca, Sr, Ba) single-crystalline iron pnictides“. In: *Phys. Rev. B* 88 (18) (2013), p. 184511.

[241] A. Charnukha. „Optical conductivity of iron-based superconductors“. In: *J. Phys. Condens. Matter* 26 (25) (2014), p. 253203.

[242] Z. P. Yin, K. Haule, and G. Kotliar. „Magnetism and charge dynamics in iron pnictides“. In: *Nat. Phys.* 7 (4) (2011), pp. 294–297.

[243] A. A. Schafgans et al. „Electronic Correlations and Unconventional Spectral Weight Transfer in the High-Temperature Pnictide BaFe2-xCoxAs2 Superconductor Using Infrared Spectroscopy“. In: *Phys. Rev. Lett.* 108 (14) (2012), p. 147002.

[244] N. L. Wang et al. „High energy pseudogap and its evolution with doping in Fe-based superconductors as revealed by optical spectroscopy“. In: *J. Phys. Condens. Matter* 24 (29) (2012), p. 294202.

[245] A. Charnukha et al. „Superconductivity-induced optical anomaly in an iron arsenide.“ In: *Nat. Commun.* 2 (2011), p. 219.

[246] Z. G. Chen et al. „Optical spectroscopy of single-crystalline LaFeAsO“. In: *Phys. Rev. B* 81 (10) (2010), p. 100502.

[247] Y. M. Dai et al. „Coexistence of clean- and dirty-limit superconductivity in LiFeAs“. In: *Phys. Rev. B* 93 (5) (2016), p. 054508.

[248] P. Marsik et al. „Low-energy interband transitions in the infrared response of Ba(Fe1-xCox)2As2“. In: *Phys. Rev. B* 88 (18) (2013), p. 180508.

[249] Sina Zapf et al. „Electronic scattering effects in europium-based iron pnictides“. In: *Comptes Rendus Phys.* 17 (1-2) (2015), pp. 188–196.

[250] Y. Suzuki et al. „Momentum-dependent sign inversion of orbital order in superconducting FeSe“. In: *Phys. Rev. B* 92 (20) (2015), p. 205117.

[251] Y. M. Dai et al. „Hidden T-Linear Scattering Rate in Ba0.6K0.4Fe2As2 Revealed by Optical Spectroscopy“. In: *Phys. Rev. Lett.* 111 (11) (2013), p. 117001.

[252] A. Lucarelli et al. „Charge dynamics of Co-doped BaFe2As2“. In: *New J. Phys.* 12 (7) (2010), p. 073036.

[253] S. Das Sarma, E. H. Hwang, and Wang-Kong Tse. „Many-body interaction effects in doped and undoped graphene: Fermi liquid versus non-Fermi liquid“. In: *Phys. Rev. B* 75 (12) (2007), p. 121406.

[254] Johannes Hofmann et al. „Interacting Dirac liquid in three-dimensional semimetals“. In: *Phys. Rev. B* 92 (4) (2015), p. 045104.

[255] Z. Q. Li et al. „Dirac charge dynamics in graphene by infrared spectroscopy“. In: *Nat. Phys.* 4 (7) (2008), pp. 532–535.

[256] Jason Horng et al. „Drude conductivity of Dirac fermions in graphene“. In: *Phys. Rev. B* 83 (16) (2011), p. 165113.

[257] M. Abdel-Hafiez et al. „Temperature dependence of lower critical field Hc1(T) shows nodeless superconductivity in FeSe“. In: *Phys. Rev. B* 88 (17) (2013), p. 174512.

[258] Meng Li et al. „Superfluid density and microwave conductivity of FeSe superconductor: ultra-long-lived quasiparticles and extended s-wave energy gap“. In: *New J. Phys.* 18 (8) (2016), p. 082001.

[259] A. Carrington and F. Manzano. „Magnetic penetration depth of MgB2“. In: *Phys. C Supercond.* 385 (1-2) (2003), pp. 205–214.

[260] C.-L. Song et al. „Direct Observation of Nodes and Twofold Symmetry in FeSe Superconductor“. In: *Science* 332 (6036) (2011), pp. 1410–1413.

[261] J.-Y. Lin et al. „Coexistence of isotropic and extended s-wave order parameters in FeSe as revealed by low-temperature specific heat“. In: *Phys. Rev. B* 84 (22) (2011), p. 220507.

[262] J. Maletz et al. „Unusual band renormalization in the simplest iron-based superconductor FeSe1-x“. In: *Phys. Rev. B* 89 (22) (2014), p. 220506.

[263] P. Bourgeois-Hope et al. „Thermal Conductivity of the Iron-Based Superconductor FeSe: Nodeless Gap with a Strong Two-Band Character“. In: *Phys. Rev. Lett.* 117 (9) (2016), p. 097003.

[264] Sahana Rößler et al. „Emergence of an incipient ordering mode in FeSe“. In: *Phys. Rev. B* 92 (6) (2015), p. 060505.

[265] Y. G. Ponomarev et al. „Andreev spectroscopy of FeSe: Evidence for two-gap superconductivity“. In: *J. Exp. Theor. Phys.* 113 (3) (2011), pp. 459–467.

[266] Barry Bradlyn et al. „Beyond Dirac and Weyl fermions: Unconventional quasiparticles in conventional crystals“. In: *Science* 353 (6299) (2016), p. 5037.

Declaration of originality

I hereby declare that this thesis and the work reported herein was composed by and originated entirely from me. Information derived from the published and unpublished work of others has been acknowledged in the text and references.

David Neubauer